Università degli Studi di Ferrara

Ph.D. degree in Physics - XXXVIII cycle

Reconstruction algorithms and particle detection performance of the electromagnetic calorimeter of SAND at DUNE near detector complex

Ph.D. candidate:
Denise Casazza

Supervisors:
Prof. Eleonora Luppi
Prof. Luca Tomassetti

Scientific-Disciplinary Sector (SDS): FIS/01

COORDINATOR Prof. Paolo Lenisa

Academic Years 2022/2025

Abstract

The Deep Underground Neutrino Experiment (DUNE) is a future long-baseline oscillation experiment designed to address long-standing open questions in neutrino physics. Its primary goals are to establish whether nature violates CP symmetry in the lepton sector and, if so, to measure the phase δ_{CP}, to determine the neutrino mass ordering, and to improve the precision on θ_{23} and its octant. DUNE will use a high-intensity muon (anti)neutrino beam, produced at Fermilab (FNAL), and will measure oscillations in both appearance and disappearance channels using two detectors located at near and far sites with respect to the beam production point.

The far detector, installed at the Sanford Underground Research Facility in South Dakota, will consist of a modular 68 kt liquid-argon time projection chamber detector. The near detector (ND) complex at FNAL will combine three complementary subsystems to measure the unoscillated neutrino flux and to constrain the interaction and flux systematics that currently limit the extrapolation of event rates from near to far.

SAND (System for on-Axis Neutrino Detection) is one of the three ND subdetectors and will be permanently located on-axis, acting as DUNE's primary beam monitor. It will host a 0.6 T superconducting magnet and a lead–scintillating fiber sampling electromagnetic calorimeter (ECal), both refurbished from the KLOE experiment. The ECal will provide nearly hermetic coverage of the inner volume, which will be instrumented with a low-density target–tracker system and a ~ 1 t liquid-argon detector, GRAIN (GRANular Argon for Interaction of Neutrinos), to image neutrino interactions via scintillation light.

SAND is expected to carry out a broad physics program, including measurements of (anti)neutrino fluxes using interactions on hydrogen, constraints on the systematic uncertainties entering the far-detector rate prediction, and measurements of ν–nucleus cross sections on several targets. The successful operation of the ECal in particle reconstruction and identification is therefore crucial.

This thesis develops a complete simulation-to-analysis chain for the SAND ECal, from the modeling of energy deposits in the scintillating fibers to high-level reconstructed clusters and their association with Monte Carlo truth. Dedicated digitization, clustering, and truth-matching algorithms are implemented and integrated in the SAND software framework, and the calorimeter response is characterized for both electromagnetic showers and muons. The active–to–total energy calibration factor and the energy resolution compatible with the performance achieved

by KLOE have been found, providing a quantitative validation of the ECal reconstruction chain and an infrastructure for future calibration, performance, and particle-identification studies.

Building on this framework, a dedicated selection procedure for neutron tagging in $\bar{\nu}_\mu + p \to \mu^+ + n$ channel on hydrogen in the SAND tracker targets is developed. The ECal signal efficiency, purity and non-hydrogen background rejection are quantified, yielding a neutron-tagged, hydrogen-enriched selection suitable for neutrino–hydrogen analyses and for constraints on flux and cross-section systematics in the DUNE oscillation program.

Contents

Introduction

Neutrinos are extremely light, electrically neutral particles that have been studied over the last decades, producing evidence of physics beyond the Standard Model. Experiments have shown that neutrinos change flavour as they propagate, implying that their mass states are different from their flavour states and that neutrinos have non-zero masses. Most oscillation parameters are now measured with good precision, and the focus of current and future facilities has shifted toward over-constraining the three-flavour framework and searching for deviations that could indicate new physics.

The Deep Underground Neutrino Experiment (DUNE) is designed to address several of the most pressing open questions in neutrino physics. By observing the oscillations of a high-intensity ν_μ and $\bar{\nu}_\mu$ beam over a baseline of about 1300 km, DUNE aims to determine the ordering of neutrino masses and to test whether charge-parity (CP) symmetry is violated in the leptonic sector. A significant CP-violating phase could provide a clue to understanding the matter-antimatter asymmetry of the Universe. In addition to its long-baseline program, DUNE will be sensitive to atmospheric neutrinos, search for proton decay and other rare processes, and record neutrinos from a potential core-collapse supernova, offering a broad physics program that extends beyond oscillation measurements.

To achieve these goals, the experiment will use a high intensity (anti)neutrino beam produced at Fermilab and directed toward a multi-kiloton liquid-argon time-projection chamber detector, located deep underground at the Sanford Underground Research Facility in South Dakota. A Near Detector system at Fermilab will measure the unoscillated beam and characterize neutrino interactions close to the source. Precise near-site measurements are essential both for monitoring the beam and for constraining neutrino interaction models, which in turn control many of the dominant systematic uncertainties in the oscillation analysis.

SAND (System for on-Axis Neutrino Detection) is one of the three detectors that constitute the DUNE Near Detector complex. Placed on-axis in the neutrino beam, SAND will provide a continuous monitor of the beam intensity, direction, and energy spectrum. Beyond this beam-monitoring role, SAND is a versatile neutrino interaction detector. It combines a magnetic low-mass gas-based tracking system with a high-performance surrounding electromagnetic calorimeter and hosts interchangeable nuclear targets, enabling detailed studies of ν and $\bar{\nu}$ interactions on different materials. A 1-ton active target for ν-Ar interactions, called GRAIN (GRanular Argon for Interaction of Neutrinos), is located in front of the tracker and is designed to image neutrino interactions using scintillation light produced in argon by charged particles, providing an on-axis argon target for cross-calibration with the other ND detectors and dedicated measurements of ν-Ar cross sections and nuclear effects.

In particular, by comparing interaction rates on hydrocarbon (CH_2) and graphite targets, SAND can isolate charged-current interactions on free protons in hydrogen through the so-called solid-hydrogen technique. The resulting hydrogen-enhanced samples, largely free of nuclear effects, can be used to constrain both the absolute

and relative neutrino and antineutrino fluxes and to measure cross sections on free nucleons. In combination with data on several nuclear and argon targets, these measurements allow SAND to quantify nuclear effects and final-state interactions and to reduce model uncertainties in the near-to-far extrapolation used in the DUNE oscillation analysis.

The magnetized tracking volume, together with the surrounding electromagnetic calorimeter, provides nearly 4π coverage, enabling precise tracking and calorimetric measurements of charged particles and photons, and allowing the reconstruction and tagging of final-state hadrons, including neutrons. A detailed understanding of the ECal response is therefore essential, both for the reconstruction of neutrino energy and for the kinematic selection of hydrogen events, used in flux and cross-section measurements. The work presented in this thesis develops a complete simulation–to–analysis chain for the SAND ECal, including realistic digitization of the scintillating-fiber signals, clustering, and truth-matching tools that are exploited to tune the reconstruction parameters, quantify the intrinsic energy resolution, and develop the strategy and tools for the complete particle identification in SAND. In addition, the neutron-induced activity in the calorimeter has been characterized, and the neutron-tagging selection has been performed and characterized for $\bar{\nu}_\mu p \to \mu^+ n$ interactions on hydrogen. These studies provide the first quantitative evaluation of the ECal performance needed for the solid-hydrogen program at SAND and for using exclusive ν and $\bar{\nu}$ interactions on hydrogen to obtain precise constraints on the neutrino flux and interaction models in the DUNE oscillation analysis.

The thesis is organized as follows:

- Chapter 1 introduces the basic concepts of neutrino oscillations and reviews the current status of neutrino physics.
- Chapter 2 presents the DUNE experiment, describing the LBNF beam, the Far Detector and the Near Detector complex, and summarizing the main physics goals that drive the detector design.
- Chapter 3 is devoted to the SAND detector. It describes the superconducting magnet, the electromagnetic calorimeter, the GRAIN liquid-argon target, and the options for the inner tracker with their modular nuclear targets. This chapter also outlines the SAND physics program, including beam monitoring, flux measurements, and studies of nuclear effects for interactions on hydrogen.
- Chapter 4 presents the simulation and reconstruction framework used in this thesis for the SAND ECal. It summarizes the `edep-sim` energy-deposit simulation and the digitization that converts the energy hits in the scintillating fibers into realistic electronic signals. In addition, it gives an overview of the existing reconstruction chains for the inner tracker and for GRAIN.

- Chapter 5 presents the reconstruction and truth-matching algorithms for the SAND ECal. It details the clustering procedure and introduces the `edep-reader` and backtracking tools that associate reconstructed clusters to Monte Carlo trajectories and build their truth counterparts. Using dedicated particle-gun and neutrino samples, the results of the reconstruction-truth chain validation are presented.
- Chapter 6 applies this framework to neutron detection in the SAND hydrogen program. The ECal neutron detection efficiency is quantified at hit and cluster level, then final-state neutron signals from $\bar{\nu}_\mu p \to \mu^+ n$ are characterized. The procedure for neutron tagging and evaluation of its efficiency, purity, non-H interaction rejection and impact on flux and cross-section measurements on hydrogen are presented.

Chapter 1

Neutrino physics

1.1 Neutrino introduction

The neutrino was first postulated by W. Pauli in 1930 as a neutral particle with spin-$\frac{1}{2}$, proposed as a "desperate remedy" to save energy conservation in β decay [1]. In 1933, E. Fermi developed a model to explain β decay in which the undetected particle was taken into account and called neutrino [2]. To account for the parity violation of the weak interactions, verified by the experiment performed in 1956 by C. S. Wu [3], the vector current in Fermi's theory was replaced by the V–A (vector minus axial) form [4, 5]. The nowadays-called Fermi theory, here reported for the beta decay,

$$\mathcal{L} = -\frac{G_F}{\sqrt{2}} \left[\bar{e}\,\gamma^\alpha(1-\gamma_5)\,\nu_e\right] \left[\bar{p}\,\gamma_\alpha(1-a\,\gamma_5)\,n\right] \;+\; \text{h.c.}, \tag{1.1}$$

with $a = 1.2695 \pm 0.0029$ and G_F the Fermi constant, describes the point-like interaction between four fermions and is the low-energy effective theory of the weak interactions. The results obtained by this effective theory are accurate only when the energies of the involved particles are much smaller than the weak scale, i.e. $E \ll M_W \simeq 80$ GeV with M_W the W-boson mass [6].

The first electron antineutrino ($\bar{\nu}_e$) was discovered by F. Reines and C. Cowan [7] in 1956 at the Savannah River reactor via the inverse-β decay process

$$\bar{\nu}_e + p \to e^+ + n\,.$$

The detector consisted of two water tanks doped with cadmium salts, each placed between liquid scintillator chambers [8]. The antineutrino interacts with a proton, producing a neutron and a positron. The positron promptly annihilates, emitting two back-to-back γ rays; the resulting Compton electrons are detected in the scintillators as a prompt coincident signal. The event signature is completed by the delayed γ rays from neutron capture on Cd (see also [8]).

B. Pontecorvo in 1959 [9] proposed that neutrinos produced in pion decay were different from those produced together with the electron in β decay. In 1962 the muon neutrino was discovered by L. Lederman, M. Schwartz, J. Steinberger and

collaborators [10] at Brookhaven National Laboratory. In their experiment, pions produced by a proton beam on a beryllium target decayed as

$$\pi^+ \to \mu^+ + \nu_\mu \qquad \text{and} \qquad \pi^- \to \mu^- + \bar{\nu}_\mu \,.$$

A series of ten modules, each composed of nine spark chambers, was exposed to the neutrino beam. The photographs were scanned, searching for muon tracks easily distinguishable from the electromagnetic showers produced by electrons. Many muon tracks were observed, but no electron events. The conclusion was that a neutrino produced in association with a muon yields muons in charged-current interactions (here with neutrons and protons),

$$\nu_\mu + n \to \mu^- + p, \qquad \bar{\nu}_\mu + p \to \mu^+ + n \,,$$

supporting the hypothesis of different neutrino types. Eventually, also the third neutrino family, with the first direct detection of the ν_τ was observed by the DONUT experiment at Fermilab in 2000 [11].

Compared to other particles, neutrinos have a much smaller probability of interacting with matter and, being neutral, cannot be detected via continuous ionization tracks as charged particles are. Neutrinos are never directly observed and different neutrino flavours can be distinguished only by the flavours of the charged lepton counterparts produced in the weak interactions. Despite the experimental difficulties, neutrino physics has attracted sustained attention since the discovery of lepton flavour change due to the phenomenon of flavour oscillations. Neutrino oscillations prove that neutrinos have mass, but the mechanism responsible for their mass generation has not yet been confirmed; consequently, the current effort of neutrino physics, with most measurements consistent with three-flavour oscillations, has shifted to precision determination of the mixing parameters and to establishing the absolute scale and nature of neutrino masses (see Section 1.3).

1.2 Neutrinos in the Standard Model

The Standard Model (SM) describes what is known and understood in particle physics. It is a gauge theory based on the symmetry group $SU(3)_C \times SU(2)_L \times U(1)_Y$. Particles are present as fermions and bosons, and the strong, weak and electromagnetic forces are described as an interaction term between the fermion fields and the corresponding spin 1 interaction boson field. The fermion content

of the theory can be written as

$$\begin{aligned} \text{quarks:} \quad & q_L^{(f)} = \begin{pmatrix} u_L^{(f)} \\ d_L^{(f)} \end{pmatrix}, \quad u_R^{(f)}, \quad d_R^{(f)}, \\ \text{leptons:} \quad & \ell_L^{(f)} = \begin{pmatrix} \nu_L^{(f)} \\ e_L^{(f)} \end{pmatrix}, \quad e_R^{(f)}, \end{aligned} \tag{1.2}$$

where the index f labels the three quark and lepton families. The fields have been split into left and right-handed chirality components. Left-handed fields are weak isospin doublets transforming as $SU(2)_L$ doublets, while right-handed fields are singlets; only left-handed fermions participate in charged-current weak interactions because of maximal parity violation. Right-handed neutrino is not present in the minimal SM because there is no experimental evidence of its existence.

Mass terms of the type $-m\,\bar{\psi}\psi$ cannot be added to the Lagrangian density as they would violate the required gauge invariances. Particle masses are instead generated by the spontaneous breaking of $SU(2)_L \times U(1)_Y$ via the Brout–Englert–Higgs mechanism, which postulates the existence of a complex scalar doublet ϕ. This field is an $SU(2)_L$ doublet with hypercharge $Y_\phi = +\frac{1}{2}$ fixed by the requirement that the zero-field configuration (the vacuum) is left unchanged by electromagnetic gauge transformations that correspond to the subgroup $U(1)_{\text{em}}$:

$$\phi \;=\; \frac{1}{\sqrt{2}} \begin{pmatrix} \phi^+ \\ \phi^0 \end{pmatrix}, \qquad \langle \phi \rangle \;=\; \frac{1}{\sqrt{2}} \begin{pmatrix} 0 \\ v \end{pmatrix}. \tag{1.3}$$

The interaction with the field ϕ generates Yukawa terms in the Lagrangian density that, after EWSB and in unitary gauge, for one family and restricting to the fermionic sector, can be written as

$$\begin{aligned} -\mathcal{L}_Y = m_e\,\bar{e}_R e_L + \frac{m_e}{v}\,h\,\bar{e}_R e_L + m_d\,\bar{d}_R d_L + \frac{m_d}{v}\,h\,\bar{d}_R d_L \\ + m_u\,\bar{u}_R u_L + \frac{m_u}{v}\,h\,\bar{u}_R u_L \;+\; \text{h.c.}, \end{aligned} \tag{1.4}$$

where v is the vacuum expectation value of ϕ, h is the physical Higgs field, $m_f = Y_f\,v/\sqrt{2}$, and Y_f is the Yukawa coupling for fermion f. It can be noticed that in the original formulation of the SM, neutrinos were taken to be massless because there was no evidence for neutrino masses, and no ν_R field or neutrino Yukawa term was included.

1.2.1 Extension to three families and V_{CKM}

The Lagrangian density extended to three families, without considering strong interactions, can be written as

$$\mathcal{L}_{SM} = \mathcal{L}_{YM} + \mathcal{L}_{\phi} + \mathcal{L}_{Fermions} + \mathcal{L}_{Yukawa}, \tag{1.5}$$

where

- $\mathcal{L}_{YM} = -\frac{1}{4} W^a_{\mu\nu} W^{a\,\mu\nu} \; - \; \frac{1}{4} B_{\mu\nu} B^{\mu\nu}$.
- $\mathcal{L}_{\phi} = (D_\mu \phi)^\dagger (D^\mu \phi) - V(\phi^\dagger \phi)$, with $D_\mu = \partial_\mu - ig \frac{\sigma^a}{2} W^a_\mu - ig' \frac{1}{2} B_\mu$ (for the Higgs with $Y_\phi = \frac{1}{2}$) and $V(\phi^\dagger \phi) = -\mu^2 \, \phi^\dagger \phi + \lambda (\phi^\dagger \phi)^2$.
- $\mathcal{L}_{Fermions} = \mathcal{L}_{kin} + \mathcal{L}_{em} + \mathcal{L}_{CC} + \mathcal{L}_{NC} = i \, \bar{L} \not{D} \, L + i \, \bar{Q} \not{D} \, Q + i \, \bar{U}_R \not{D} \, U_R + i \, \bar{D}_R \not{D} \, D_R + i \, \bar{E}_R \not{D} \, E_R$. Where $\mathcal{L}_{kin}$ are the kinetic terms, $\mathcal{L}_{em}$ are the electromagnetic interaction terms, $\mathcal{L}_{CC}$ and $\mathcal{L}_{NC}$ are the charged and neutral weak interaction terms.
- $\mathcal{L}_{Yukawa} = - Y_e \, \bar{E}_R \, \phi^\dagger L - Y_d \, \bar{D}_R \, \phi^\dagger Q - Y_u \, \bar{U}_R \, \tilde{\phi}^\dagger Q + \text{h.c.}$, with $\tilde{\phi} = i \sigma_2 \phi^*$ and Y_f are 3×3 matrices.

Particles are grouped as vectors in flavour space:

$$\begin{aligned} \text{quarks:} \quad & Q_{L,R} = \begin{pmatrix} q_{u\,L/R} \\ q_{c\,L/R} \\ q_{t\,L/R} \end{pmatrix}, \qquad U_{L,R} = \begin{pmatrix} u_{L/R} \\ c_{L/R} \\ t_{L/R} \end{pmatrix}, \qquad D_{L,R} = \begin{pmatrix} d_{L/R} \\ s_{L/R} \\ b_{L/R} \end{pmatrix}; \\ \text{leptons:} \quad & L = \begin{pmatrix} \ell_e \\ \ell_\mu \\ \ell_\tau \end{pmatrix}, \qquad E_{L,R} = \begin{pmatrix} e_{L/R} \\ \mu_{L/R} \\ \tau_{L/R} \end{pmatrix}, \qquad N_L = \begin{pmatrix} \nu_{eL} \\ \nu_{\mu L} \\ \nu_{\tau L} \end{pmatrix}. \end{aligned} \tag{1.6}$$

with

$$q_{u\,L} = \begin{pmatrix} u_L \\ d_L \end{pmatrix}, \quad q_{c\,L} = \begin{pmatrix} c_L \\ s_L \end{pmatrix}, \quad q_{t\,L} = \begin{pmatrix} t_L \\ b_L \end{pmatrix}, \qquad \ell_e = \begin{pmatrix} \nu_{eL} \\ e_L \end{pmatrix}, \; \ell_\mu = \begin{pmatrix} \nu_{\mu L} \\ \mu_L \end{pmatrix}, \; \ell_\tau = \begin{pmatrix} \nu_{\tau L} \\ \tau_L \end{pmatrix}.$$

After EWSB, the Yukawa term can be written as

$$\begin{aligned} \mathcal{L}_{Yukawa} = & - \; M_e \, \bar{E}_R E_L - M_d \, \bar{D}_R D_L - M_u \, \bar{U}_R U_L \; - \; \frac{M_e}{v} \, \bar{E}_R E_L \, h \\ & - \; \frac{M_d}{v} \, \bar{D}_R D_L \, h \; - \; \frac{M_u}{v} \, \bar{U}_R U_L \, h \; + \; \text{h.c.} \, , \end{aligned} \tag{1.7}$$

with $M_f = Y_f \, v / \sqrt{2}$. In the basis of the eigenstates of interaction, M_f are generic

non-diagonal 3×3 matrices, while $\not{D}$ is diagonal. Fields can be transformed as

$$\begin{array}{rclcrcl} E_L &=& V_e\, E'_L & & E_R &=& U_e\, E'_R \\ D_L &=& V_d\, D'_L, & & D_R &=& U_d\, D'_R, \\ U_L &=& V_u\, U'_L & & U_R &=& U_u\, U'_R \end{array} \tag{1.8}$$

Performing the bi-unitary transformations so that $V_f^\dagger M_f U_f = M_f^{diag}$, the Yukawa term becomes

$$\mathcal{L}_{Yukawa} \;\supset\; -\bar{E}'_R\, M_e^{diag} E'_L \;-\; \bar{D}'_R\, M_d^{diag} D'_L \;-\; \bar{U}'_R\, M_u^{diag} U'_L\,, \tag{1.9}$$

where M_f^{diag} are now diagonal.

All terms in $\mathcal{L}_{SM}$ remain unchanged except the charged–current term $\mathcal{L}^{CC} = \frac{g}{\sqrt{2}}\,[W_\mu^+ J^{-\mu} + W_\mu^- J^{+\mu}]$, in which, for example, $J^{-\mu} = \bar{N}_L \gamma^\mu E_L + \bar{U}_L \gamma^\mu D_L$ becomes

$$J^{-\mu} = \bar{N}_L \gamma^\mu V_e\, E'_L + \bar{U}'_L\, V_u^\dagger V_d\, \gamma^\mu D'_L\,. \tag{1.10}$$

There is no reason to rotate neutrinos (they are massless here), but they can be redefined as $N_L = V_e\, N'_L$, so that

$$J^{-\mu} = \bar{N}'_L V_e^\dagger V_e \gamma^\mu E'_L + U'_L V_u^\dagger V_d \gamma^\mu D'_L = \bar{N}'_L \gamma^\mu E'_L + \bar{U}'_L\, V_{CKM}\, \gamma^\mu D'_L\,, \tag{1.11}$$

where $V_{CKM} := V_u^\dagger V_d$ is the Cabibbo-Kobayashi-Maskawa matrix. Charged currents in the quark sector are not diagonal, so in the Standard Model, there is flavour changing in charged current, while charged currents in the leptonic sector are diagonal. If neutrinos had a non-zero mass, it would be necessary to make an independent transformation on N_L, and also for the leptonic sector, there would be flavour changing in charged current.

1.3 Neutrino masses

The evidence for the flavour oscillation phenomenon, discussed in Section 1.4, is in contrast with the massless nature of neutrinos. In this light, ν_R can be taken into account to build a Yukawa term

$$\mathcal{L}_{Yukawa} \;\supset\; -Y_\nu\, \bar{N}_R\, \tilde{\phi}^\dagger\, L \;+\; \text{h.c.} \tag{1.12}$$

which, after the EWSB, gives rise to a Dirac mass term $-M_\nu \bar{N}_R N_L$. To diagonalize M_ν it is necessary to operate a transformation on the fields

$$N_L = V_\nu N'_L\,, \qquad N_R = U_\nu N'_R\,, \tag{1.13}$$

that modify the charged currents

$$J^{-\mu} \supset \bar{N}_L \gamma^\mu L \rightarrow \bar{N}'_L\, V_\nu^\dagger V_e\, \gamma^\mu E'_L\,, \tag{1.14}$$

where $V_\nu^\dagger V_e$ is the U_{PMNS} (Pontecorvo–Maki–Nakagawa–Sakata) matrix. The introduction of neutrino masses generates flavour change in the charged current also in the leptonic sector.

There is another term that, given the null charge of neutrinos, is compatible with the gauge invariances of the $\mathcal{L}_{SM}$ and so it can be added to the Lagrangian density. It is a Majorana mass term, and it is written, for one family,

$$\frac{1}{2}\, M\, \bar{\nu}_R^c \nu_R + \text{h.c.}\ . \tag{1.15}$$

ν^c is obtained through

$$\psi^c = C\, \bar{\psi}^t \tag{1.16}$$

where C is the particle–antiparticle conjugation operator. Under the action of C all the quantum charges change their sign and in particular a left-handed field is transformed into a right-handed one, and vice versa. It is possible that the right-handed component of the neutrino field is equal to its C-conjugated left-handed field. If this possibility is verified then the neutrino is said to be a Majorana particle, while for a Dirac particle left- and right-handed components are completely independent.

An important point to underline is that M is a new mass scale introduced in the Standard Model and the introduction of this term is evidence of physics beyond the Standard Model. The Majorana mass term breaks the accidental lepton-number symmetry; this leads to two options: $\mathcal{L}_{SM}$ is invariant under the global lepton-number symmetry (so the Majorana term is not present) or $\mathcal{L}_{SM}$ is invariant only under gauge and Lorentz symmetries and the term must be taken into account.

If one assumes that the Dirac mass is the only mass for neutrinos, the Dirac mass term generated by the EWSB is somewhat unnatural because it gives rise to much smaller Yukawa couplings with respect to the couplings of the other particles,

$$\frac{Y_\nu}{Y_e} = \frac{m_\nu}{m_e} < 10^{-6}. \tag{1.17}$$

The introduction of M can represent a solution to this problem. Considering for one flavour the general Lagrangian density,

$$\mathcal{L} = -Y_\nu \frac{v}{\sqrt{2}} \bar{\nu}_R \nu_L \; + \; M \left(\bar{\nu}_R^c \nu_R + \bar{\nu}_R \nu_R^c\right) \tag{1.18}$$

with $Y_\nu \frac{v}{\sqrt{2}} = m_\nu = m_D$, this can be written as

$$-\frac{1}{2} \begin{pmatrix} \bar{\nu}_L^c & \bar{\nu}_R \end{pmatrix} \begin{pmatrix} 0 & m_D \\ m_D & M \end{pmatrix} \begin{pmatrix} \nu_L \\ \nu_R^c \end{pmatrix} \; + \; \text{h.c.}, \tag{1.19}$$

whose eigenvalues are $m_{1,2} = \dfrac{M \pm \sqrt{M^2 + 4m_D^2}}{2}$. Assuming $M \gg m_D$ it turns out that $m_1 \simeq -\dfrac{m_D^2}{M}$, $m_2 \simeq M$ and $\nu_1 \simeq \nu_L$, $\nu_2 \simeq \nu_R$; therefore, in this hypothesis, the introduction of the Majorana term leads to a light neutrino ν_1 which is essentially the observed particle ν_L. Thanks to the presence of M the smallness of the mass m_D is justified also with a Y_ν of the order of the Yukawa couplings of the other particles, being $\dfrac{m_D^2}{M} = \dfrac{Y_\nu^2 v^2}{2M}$.

The mechanism described above, which gives an explanation for the smallness of the neutrino mass with the introduction of the Majorana mass term, is called the see-saw mechanism. If the $\mathcal{L}_{SM}$ is seen as an effective theory, a composite operator

$$\theta^{d=5} = \left(\bar{\ell}_L^c \, \tilde{\phi}\right) \left(\tilde{\phi}^\dagger \, \ell_L\right)$$

with dimension 5 can be considered, as shown in Eq. (1.19):

$$\mathcal{L}_{SM} + \frac{C}{\Lambda} \theta^{d=5}. \tag{1.20}$$

The EWSB of this term gives rise in the $\mathcal{L}_{SM}$ to a Majorana term $M_L \, \bar{\nu}_L^c \nu_L$, where M_L is linked to the vacuum expectation value of ϕ. Depending on the choice of the propagator between the two interaction vertices there are three kinds of see-saw mechanisms, called I, II, III.

1.4 Neutrino oscillations

In the late 1960s the Homestake experiment [12] was testing the Standard Solar Model (SSM), which describes the Sun's behaviour, by measuring the predicted neutrino flux from the Sun. The experiment used a radiochemical technique to measure the flux of solar neutrinos by counting the number of ^{37}Ar atoms produced

in the charged–current capture

$$\nu_e + {}^{37}_{17}\mathrm{Cl} \rightarrow {}^{37}_{18}\mathrm{Ar} + e^-.$$

The number of interactions per day was expected to be 1.7, but the observed rate was only 0.48±0.04 neutrino interactions per day; this deficit became known as the solar neutrino problem. Gallium-based radiochemical experiments (SAGE [13] and GALLEX [14]) also measured a deficit of solar neutrinos. The Super–Kamiokande [15] water Cherenkov detector clearly observed the direction of solar neutrinos from the Sun, but the flux was about half the SSM expectation.

Could it be that the Standard Solar Model is not correct? The SNO experiment [16], a Cherenkov detector consisting of 10^6 kg of D_2O, could measure both the total and the electron–neutrino fluxes from the Sun. The SNO data demonstrated that the total flux of neutrinos from the Sun was consistent with the theoretical expectation, $\phi(\nu)_{\mathrm{model}} = (5.1 \pm 0.9) \times 10^6\ \mathrm{cm}^{-2}\,\mathrm{s}^{-1}$, but rather than consisting only of ν_e there was a large component of ν_μ and/or ν_τ; in particular,

$$\phi(\nu_\mu) + \phi(\nu_\tau) = (3.41 \pm 0.63) \times 10^6\ \mathrm{cm}^{-2}\,\mathrm{s}^{-1}.$$

These results confirmed that the number of ν_e produced at the source was correct and that the missing ν_e were actually converted into neutrinos of other flavours.

What is observed by the experiments can be explained by the phenomenon of neutrino oscillations, suggested by B. Pontecorvo in 1967 [17] and improved by V.N. Gribov and Pontecorvo in 1969 [18], then framed in the flavour–mass mixing scheme introduced by Z. Maki, M. Nakagawa, and S. Sakata in 1962 [19].

1.4.1 Oscillations in vacuum

The fundamental motivation of why neutrinos oscillate is that they are emitted in states with definite flavour which are not eigenstates of the free particle Hamiltonian (mass eigenstates), so when they propagate in vacuum they have to be decomposed into the basis of the mass eigenstates and the evolution of these must be considered separately.

Consider a neutrino beam of definite flavour, produced at some initial time $t = 0$, denoting with a Greek index the flavour eigenstates, and with a Roman index the mass eigenstates. The neutrino flavour eigenstates are related to the mass eigenstates by the unitary U_{PMNS} defined in Equation 1.14. Then we have:

$$\left|\nu_\alpha\right\rangle = \sum_{i=1}^{n} U^*_{\alpha i} \left|\nu_i\right\rangle, \tag{1.21}$$

where $U^*_{\alpha i}$ are the complex conjugates of the elements of the PMNS matrix. Since massive eigenstates $\big|\nu_i\big\rangle$ have definite mass and energy, they evolve in time as plane waves:

$$\big|\nu_i(t)\big\rangle = e^{-\,(iE_i - p_i L)}\,\big|\nu_i(0)\big\rangle, \tag{1.22}$$

where L is the distance travelled in the time interval t. Exploiting the fact that neutrinos are almost massless, this gives

$$L \simeq t \qquad ; \qquad E_i = \sqrt{p_i^2 + m_i^2} \simeq p_i + \frac{m_i^2}{2E}\,, \tag{1.23}$$

$E \simeq p_i \simeq p_j$[1]. Then,

$$\big|\nu_\alpha(L)\big\rangle \simeq \sum_i U^*_{\alpha i}\, e^{-\,i\,\frac{m_i^2}{2E}\,L}\,\big|\nu_i(0)\big\rangle. \tag{1.24}$$

The probability amplitude for observing a β flavour neutrino after the time t is

$$\langle\nu_\beta|\nu_\alpha(L)\rangle = \sum_{ij} U_{\beta j}\, U^*_{\alpha i}\, e^{-\,i\,\frac{m_i^2}{2E}\,L}\,\langle\nu_j|\nu_i\rangle = \sum_i U_{\beta i}\, U^*_{\alpha i}\, e^{-\,i\,\frac{m_i^2}{2E}\,L}\,. \tag{1.25}$$

The corresponding probability is given by

$$\begin{aligned} P_{\alpha\to\beta}(L) = \big|\langle\nu_\beta|\nu_\alpha(L)\rangle\big|^2 &= \left|\sum_j U_{\beta j}\, U^*_{\alpha j}\, e^{-\,i\,\frac{m_j^2}{2E}\,L}\right|^2 \\ &= \sum_{ij} \big(U_{\beta i} U^*_{\alpha i}\big)\,\big(U_{\beta j} U^*_{\alpha j}\big)^*\, e^{\,i\,\frac{m_j^2 - m_i^2}{2E}\,t}\,. \end{aligned} \tag{1.26}$$

Defining the squared–mass differences $\Delta m^2_{ij} \equiv m_i^2 - m_j^2$, the phases are

$$\Phi_{ij} \equiv -\,\frac{\Delta m^2_{ij}\, L}{2E}. \tag{1.27}$$

From Equations 1.26-1.27 it can be noticed that:

- the phases depend on the squared neutrino mass differences $m_i^2 - m_j^2$, implying neutrino flavor oscillations occurring only if at least two species of neutrinos have a nonzero mass and their masses are not all the same,

[1] The equal momentum assumption and the light-ray $L = t$ approximation are not justified in the formulation with plane waves, but are irrelevant or justified in the derivation of the oscillation probability with the wave packets treatment [20]

- both parameters that can be tuned in the experiment design as L, the source–detector distance and E, the neutrino energy, and physical constants Δm^2_{ij} are present in the oscillation probability phases,
- the amplitude of the oscillations is governed by the constant elements of the mixing matrix U_{PMNS},
- only information about the values of the squared-mass differences can be inferred from neutrino oscillations, but not on the absolute values of neutrino masses.

A useful formulation of Equation 1.26 is the one with separated real and imaginary parts, resulting in

$$\begin{aligned} P(\nu_\alpha \to \nu_\beta) = \delta_{\alpha\beta} &- 4 \sum_{i>j} \Re\{U^*_{\alpha i} U_{\beta i} U_{\alpha j} U^*_{\beta j}\} \sin^2 \Delta_{ij} \\ &+ 2 \sum_{i>j} \Im\{U^*_{\alpha i} U_{\beta i} U_{\alpha j} U^*_{\beta j}\} \sin(2\Delta_{ij}), \end{aligned} \tag{1.28}$$

with

$$\Delta_{ij} \equiv \frac{\Delta m^2_{ij} L}{4E}. \tag{1.29}$$

If $\alpha \neq \beta$ oscillation probabilities are called transition probabilities, while the oscillation probabilities of the channels with $\alpha = \beta$ are usually called survival probabilities. For survival channels ($\alpha = \beta$), the quartic products are real, giving the simple form:

$$P(\nu_\alpha \to \nu_\alpha) = 1 - 4 \sum_{i>j} |U_{\alpha i}|^2 |U_{\alpha j}|^2 \sin^2 \Delta_{ij}. \tag{1.30}$$

In practice, oscillations are observable only when the phase Δ_{ij} in Eq. (1.29) is of order unity; for $\Delta_{ij} \ll 1$ the modulation behaves as $\sin^2 \Delta_{ij} \simeq \Delta^2_{ij}$ and is too small, while for very large Δ_{ij} rapid oscillations are averaged by the L/E resolution.

Experiments therefore, choose L/E to target specific Δm^2 ranges, here reported some accelerator baseline (cf. Table 7.1 in [20]):

- **short-baseline**: $L \sim 1\,\text{km}$ and $E \sim 1\,\text{GeV}$ is sensitive to $\Delta m^2 \sim 1\,\text{eV}^2$, giving $\Delta_{ij} \approx 1.27$,
- **long-baseline**: $L \sim 10^3\,\text{km}$ and $E \sim 1\,\text{GeV}$ probes $\Delta m^2 \sim 10^{-3}\,\text{eV}^2$, again $\Delta_{ij} \approx 1.27$;
- **very-long-baseline**: $L \sim 10^4\,\text{km}$ and $E \sim 1\,\text{GeV}$ targets $\Delta m^2 \sim 10^{-4}\,\text{eV}^2$

with $\Delta_{ij} \approx 1.27$.

These choices place data near the first oscillation maximum and maximize visibility.

1.4.2 Two flavour approximation

Many situations are well described by an effective two–flavour framework in which only two flavour states (ν_α, ν_β) mix with two mass eigenstates (ν_1, ν_2). In this approximation

$$\begin{pmatrix} \nu_\alpha \\ \nu_\beta \end{pmatrix} = U \begin{pmatrix} \nu_1 \\ \nu_2 \end{pmatrix}, \qquad U = \begin{pmatrix} \cos\vartheta & \sin\vartheta \\ -\sin\vartheta & \cos\vartheta \end{pmatrix},$$

with mixing angle $0 \leq \vartheta \leq \pi/2$ and the squared–mass difference $\Delta m^2 \equiv \Delta m^2_{21} = m_2^2 - m_1^2$ (taking ν_1 as the lighter state so that $\Delta m^2 > 0$). The $\alpha \to \beta$ transition probability from Equations (1.26)–(1.29) is reduced to

$$P(\nu_\alpha \to \nu_\beta) = \tfrac{1}{2} \sin^2 2\vartheta \left[1 - \cos\left(\frac{\Delta m^2 L}{2E} \right) \right] = \sin^2 2\vartheta \, \sin^2\left(\frac{\Delta m^2 L}{4E} \right), \qquad (\alpha \neq \beta). \tag{1.31}$$

The survival probability is

$$P(\nu_\alpha \to \nu_\alpha) = 1 - P(\nu_\alpha \to \nu_\beta) = 1 - \sin^2 2\vartheta \, \sin^2\left(\frac{\Delta m^2 L}{4E} \right). \tag{1.32}$$

These expressions are consistent with the general three–flavour formulae when a single frequency dominates, so Δ_{ij} in Equation (1.29) reduces to $\Delta m^2 L/(4E)$ and the quartic products in Equation (1.28) collapse to $\sin^2 2\vartheta$.

1.4.3 Antineutrino formulation

For antineutrinos, flavour states are superpositions of massive antineutrinos, differing from the neutrino case by the use of U_{PMNS}. With the same conventions as Equation (1.21),

$$\left| \bar{\nu}_\alpha \right\rangle \; = \; \sum_i U_{\alpha i} \left| \bar{\nu}_i \right\rangle. \tag{1.33}$$

Using $\Delta_{ij} = \Delta m^2_{ij} L/(4E)$ from Equation (1.29) and the neutrino decomposition

in Eq. (1.28), the antineutrino probability is

$$P(\bar{\nu}_\alpha \to \bar{\nu}_\beta) = \delta_{\alpha\beta} - 4\sum_{i>j} \Re\{U^*_{\alpha i} U_{\beta i} U_{\alpha j} U^*_{\beta j}\} \sin^2 \Delta_{ij} - 2\sum_{i>j} \Im\{U^*_{\alpha i} U_{\beta i} U_{\alpha j} U^*_{\beta j}\} \sin(2\Delta_{ij}). \tag{1.34}$$

Comparing Equations (1.28) and (1.34) shows that the only difference between neutrino and antineutrino case in vacuum is the sign of the term proportional to the imaginary parts of the term

$$J^{ij}_{\alpha\beta} \equiv U^*_{\alpha i}\, U_{\beta i}\, U_{\alpha j}\, U^*_{\beta j}.$$

This sign flip comes from CP conjugation, which sends $U \to U^*$ while leaving the phase Δ_{ij} unchanged. Hence any neutrino–antineutrino difference arises from complex phases in U_{PMNS}.

1.4.4 CP violation in vacuum

Charge conjugation (C), parity (P) and time reversal (T) are discrete symmetries of space–time. The combined operation CPT is an exact symmetry of any local, Lorentz–invariant quantum field theory,

$$\mathrm{CPT} = \mathbb{I}. \tag{1.35}$$

In the neutrino context, a CP transformation interchanges neutrinos with antineutrinos and reverses the helicity [21], so that

$$\nu_\alpha \overset{\mathrm{CP}}{\longleftrightarrow} \bar{\nu}_\alpha. \tag{1.36}$$

Consequently, CP maps oscillation channels according to

$$\nu_\alpha \to \nu_\beta \overset{\mathrm{CP}}{\longleftrightarrow} \bar{\nu}_\alpha \to \bar{\nu}_\beta. \tag{1.37}$$

A T transformation exchanges the initial and final flavour states,

$$\nu_\alpha \to \nu_\beta \overset{\mathrm{T}}{\longleftrightarrow} \nu_\beta \to \nu_\alpha, \qquad \bar{\nu}_\alpha \to \bar{\nu}_\beta \overset{\mathrm{T}}{\longleftrightarrow} \bar{\nu}_\beta \to \bar{\nu}_\alpha. \tag{1.38}$$

Using CPT, one obtains the exact vacuum relation

$$P(\nu_\alpha \to \nu_\beta) = P(\bar{\nu}_\beta \to \bar{\nu}_\alpha). \tag{1.39}$$

A useful corollary is that survival probabilities are identical in vacuum as can be seen also using Equation (1.30),

$$P(\nu_\alpha \to \nu_\alpha) \;=\; P(\bar{\nu}_\alpha \to \bar{\nu}_\alpha). \tag{1.40}$$

The CP-asymmetry can be quantified as the difference between the two probabilities for neutrino and antineutrino in Equations (1.28) and (1.34):

$$\Delta P_{\alpha\beta} \;\equiv\; P(\nu_\alpha \to \nu_\beta) - P(\bar{\nu}_\alpha \to \bar{\nu}_\beta) \;=\; 4 \sum_{i>j} \Im\{J^{ij}_{\alpha\beta}\} \, \sin(2\Delta_{ij}). \tag{1.41}$$

In the three flavour case Equation (1.41) reduces to the Jarlskog form

$$\Delta P_{\alpha\beta} \;=\; 16\, J_{\alpha\beta} \, \sin\Delta_{21} \, \sin\Delta_{31} \, \sin\Delta_{32}, \qquad J_{\alpha\beta} = \pm J, \tag{1.42}$$

where

$$J \;=\; c_{12}\, s_{12}\, c_{23}\, s_{23}\, c_{13}^2\, s_{13} \, \sin\delta_{\rm CP} \tag{1.43}$$

is the Jarlskog invariant and the sign depends on the α and β permutation. Equation (1.42) makes clear that CP asymmetries vanish if any mixing angle is zero, if any Δm^2_{ij} is zero, or if $\delta_{\rm CP} = 0, \pi$.

A standard observable for CP violation is

$$A^{\alpha\beta}_{CP} = \frac{P(\nu_\alpha \to \nu_\beta) - P(\bar{\nu}_\alpha \to \bar{\nu}_\beta)}{P(\nu_\alpha \to \nu_\beta) + P(\bar{\nu}_\alpha \to \bar{\nu}_\beta)}\,, \tag{1.44}$$

which is different from zero in vacuum only for appearance channels ($\alpha \neq \beta$). For survival channels ($\alpha = \beta$) the CP sensitive term already vanishes in Equation (1.30), so in vacuum $P(\nu_\alpha \to \nu_\alpha) = P(\bar{\nu}_\alpha \to \bar{\nu}_\alpha)$.

The CP phase. In the standard three–flavour parameterization of $U_{\rm PMNS}$ there is a single physical Dirac phase $\delta_{\rm CP}$ controlling CP violation in oscillations. Its determination is a primary goal of current and future experiments: a nonzero value confirms CP violation in the lepton sector and may shed light on the observed matter–antimatter asymmetry of the Universe.

1.4.5 Oscillations in matter

Coherent matter effects. Neutrino oscillations in vacuuum arise from the phase differences among mass eigenstates discussed in Subsection 1.4.1. On the other hand when neutrinos propagate in matter, they can also interact with the

medium. Incoherent inelastic weak scatterings have the characteristic cross section

$$\sigma \;\simeq\; \frac{G_F^2\, s}{\pi} \;\approx\; 10^{-38}\ \mathrm{cm}^2\, \frac{E_\nu\, m_t}{\mathrm{GeV}^2},$$

[21] with s the Mandelstam variable, E_ν the neutrino energy, and m_t the target mass. The corresponding mean free path in a medium of number density N is

$$\ell \;\simeq\; \frac{1}{N\,\sigma} \;\approx\; \frac{10^{38}\ \mathrm{cm}}{(N/\mathrm{cm}^{-3})}\, \frac{\mathrm{GeV}^2}{E_\nu\, m_t},$$

so in ordinary matter ($N \sim N_A\,\mathrm{cm}^{-3}$, $m_t \sim 1\,\mathrm{GeV}$)

$$\ell_{\mathrm{matter}} \;\sim\; \frac{10^{14}\ \mathrm{cm}}{E_\nu/\mathrm{GeV}},$$

implying that the Earth becomes opaque only for $E_\nu \gtrsim 10^5$ GeV, below neutrinos absorption is negligible. The coherent forward elastic scattering can still happen, modifying the neutrino phase velocity instead of the intensity. Coherence means the medium remains unchanged and the neutrino forward–scattered wave interferes with the unscattered one, which can be encoded as an effective potential in the evolution equation. Coherent interactions, in which the medium remain unchanged, may occur via neutral currents (NC), which affect ν_e, ν_μ, ν_τ equally, and via charged currents (CC), which act mainly on the electron flavour that is the only one that matches the incoming lepton.

From two flavours in vacuum to matter. For simplicity, let's consider the two–flavour system described in Subsection 1.4.2 where the neutrino state can be written in the basis $\Psi = (\nu_e, \nu_x)^{\mathrm{T}}$, with ν_x orthogonal to ν_e. The state evolution in vacuum is described by the Schrödinger equation

$$i\,\frac{d}{dx}\,\Psi \;=\; H_{\mathrm{vac}}\,\Psi, \qquad H_{\mathrm{vac}} = \frac{1}{2E}\,U(\vartheta)\begin{pmatrix} m_1^2 & 0 \\ 0 & m_2^2 \end{pmatrix} U^\dagger(\vartheta) - \frac{m_1^2+m_2^2}{4E}\begin{pmatrix} 1 & 0 \\ 0 & 1 \end{pmatrix},$$

where E is the neutrino energy and $U(\vartheta)$ is the 2×2 mixing matrix,

$$U(\vartheta) = \begin{pmatrix} \cos\vartheta & \sin\vartheta \\ -\sin\vartheta & \cos\vartheta \end{pmatrix}, \qquad U^\dagger U = I.$$

Evaluating the product explicitly,

$$\frac{1}{2E}\,U\begin{pmatrix} m_1^2 & 0 \\ 0 & m_2^2 \end{pmatrix} U^\dagger = \frac{1}{2E}\begin{pmatrix} c^2 m_1^2 + s^2 m_2^2 & cs\,(m_2^2 - m_1^2) \\ cs\,(m_2^2 - m_1^2) & s^2 m_1^2 + c^2 m_2^2 \end{pmatrix},$$

with $c \equiv \cos\vartheta$, $s \equiv \sin\vartheta$. Subtracting the trace term $\frac{m_1^2+m_2^2}{4E}\begin{pmatrix}1&0\\0&1\end{pmatrix}$ gives

$$H_{\rm vac} = \frac{\Delta m^2}{4E}\begin{pmatrix}-\cos 2\vartheta & \sin 2\vartheta\\ \sin 2\vartheta & \cos 2\vartheta\end{pmatrix}, \qquad \Delta m^2 \equiv m_2^2 - m_1^2.$$

The evolution is

$$\Psi(L) = e^{-iH_{\rm vac}L}\,\Psi(0) = U\begin{pmatrix}e^{-i\frac{m_1^2 L}{2E}} & 0\\ 0 & e^{-i\frac{m_2^2 L}{2E}}\end{pmatrix}U^\dagger\,\Psi(0),$$

so oscillation probabilities result as $|\langle\nu_\beta|\nu_\alpha(L)\rangle|^2 = P(\nu_\alpha\to\nu_\beta)(L)$, reproducing Eqs. (1.31)–(1.32).

When neutrinos propagate in matter of constant, electrically neutral and unpolarised density, coherent forward scattering adds a diagonal potential $V = \mathrm{diag}(V_e, V_x)$ with

$$V_e \;=\; \sqrt{2}\,G_F\,N_e \;+\; V_{\rm NC}, \qquad V_x \;=\; V_{\rm NC}, \qquad V_{\rm NC} \;=\; -\frac{\sqrt{2}}{2}\,G_F\,N_n,$$

where N_e and N_n are the electron and neutron number densities. The neutral–current term is common to both flavours and cancels in probabilities, so one can use $V' = \mathrm{diag}(V_{\rm CC}, 0)$ with $V_{\rm CC} = \sqrt{2}G_F N_e$ and write the effective Hamiltonian in matter as

$$H_M \;=\; H_{\rm vac} + \mathrm{diag}(V_{\rm CC},\,0).$$

Re-diagonalising H_M gives the effective parameters

$$\Delta m^2_M = M\,\Delta m^2, \qquad \sin 2\vartheta_M = \frac{\sin 2\vartheta}{M},$$

with

$$M \;=\; \sqrt{(\cos 2\vartheta - \hat{A})^2 + \sin^2 2\vartheta}, \qquad \hat{A} \;=\; \pm\frac{2\sqrt{2}\,G_F\,N_e\,E}{\Delta m^2},$$

where the + sign holds for neutrinos and the − sign for antineutrinos. These medium–induced modifications of the effective mass splitting and mixing angle are known as the Mikheyev–Smirnov–Wolfenstein (MSW) effect [22, 23]. Using the effective parameters, the probabilities in matter take the same form as in vacuum with the replacements $\vartheta \to \vartheta_M$ and $\Delta m^2 \to \Delta m^2_M$, leading to

$$P(\nu_e\to\nu_x) = \sin^2 2\vartheta_M\,\sin^2\!\Big(\frac{\Delta m^2_M\,L}{4E}\Big), \qquad P(\nu_e\to\nu_e) = 1-\sin^2 2\vartheta_M\,\sin^2\!\Big(\frac{\Delta m^2_M\,L}{4E}\Big).$$

The MSW resonance occurs when the matter potential compensates the vacuum term in the effective mixing angle, namely

$$\hat{A} = \cos 2\vartheta \quad \Longleftrightarrow \quad 2\sqrt{2}\, G_F\, N_e\, E = \Delta m^2 \cos 2\vartheta.$$

At this point one has $\vartheta_M = \pi/4$ and therefore $\sin^2 2\vartheta_M = 1$: even if the vacuum mixing ϑ is small, oscillations in matter can become maximal and the flavour–conversion probability is strongly enhanced.

Because the matter term enters through $\hat{A}$ with opposite sign for neutrinos and antineutrinos, the effective mixing parameters in matter are different for ν and $\bar{\nu}$ even if the CP phase is zero. Neutrinos usually propagate into matter that contains electrons but essentially no positrons, so ν_e interact with a positive charged–current potential while $\bar{\nu}_e$ with an equal and opposite one. The resulting difference between $P(\nu_\alpha \to \nu_\beta)$ and $P(\bar{\nu}_\alpha \to \bar{\nu}_\beta)$ is a matter–induced CP asymmetry: it is generated by propagation in an asymmetric medium rather than by CP violation in the mixing matrix.

Because $\hat{A} \propto \text{sign}(\Delta m^2)$, the resonance condition can be satisfied only for one sign of Δm^2 in a given channel. This dependence on the sign of Δm^2 links the MSW effect to the neutrino mass ordering and can be exploited in long–baseline neutrino experiments such as DUNE (see Chapter 2) to determine the hierarchy.

Matter effects are negligible when $|\hat{A}| \ll 1$, so that $\vartheta_M \simeq \vartheta$ and $\Delta m^2_M \simeq \Delta m^2$. In addition, oscillations are experimentally invisible if the phase in matter is minimal, $\Delta m^2_M L/(4E) \ll 1$ as discussed in 1.4.1, even in the presence of a matter potential. Observable MSW effects therefore require both a sufficiently large matter term and an experimental baseline such that $\Delta m^2_M L/(4E) \sim \mathcal{O}(1)$.

1.5 Measurement of the neutrino oscillation parameters

Neutrino oscillations are studied experimentally using a variety of neutrino sources and detector technologies. By measuring the probabilities for a given flavour to appear or disappear, one can constrain the elements of the PMNS matrix U_{PMNS} (see Equation 1.14) together with the neutrino mass–squared differences.

The PMNS matrix can be described in terms of four physical parameters: three mixing angles θ_{12}, θ_{23}, θ_{13} and one CP–violating phase δ_{CP}. In general, a 3×3 unitary matrix is specified by nine complex numbers, but the unitarity condition $UU^\dagger = 1$ imposes nine real constraints, leaving nine real free parameters. These can be organised as three real rotation angles and six complex phases of the

form $\mathrm{e}^{i\phi}$. Five of those phases are unphysical, since they can be absorbed into redefinitions of the charged–lepton and neutrino fields, so that only one phase remains observable.

A convenient parametrisation expresses U_{PMNS} as the product of three effective two–flavour rotations,

$$U_{\mathrm{PMNS}} = \underbrace{\begin{pmatrix} 1 & 0 & 0 \\ 0 & c_{23} & s_{23} \\ 0 & -s_{23} & c_{23} \end{pmatrix}}_{\text{“atmospheric”}} \underbrace{\begin{pmatrix} c_{13} & 0 & \mathrm{e}^{i\delta_{\mathrm{CP}}} s_{13} \\ 0 & 1 & 0 \\ -\mathrm{e}^{i\delta_{\mathrm{CP}}} s_{13} & 0 & c_{13} \end{pmatrix}}_{\text{“accelerator/reactor”}} \underbrace{\begin{pmatrix} c_{12} & s_{12} & 0 \\ -s_{12} & c_{12} & 0 \\ 0 & 0 & 1 \end{pmatrix}}_{\text{“solar”}}, \quad (1.45)$$

where $c_{ij} \equiv \cos\theta_{ij}$ and $s_{ij} \equiv \sin\theta_{ij}$.

The mixing angles θ_{ij} can, without loss of generality, be chosen in the first quadrant, $\theta_{ij} \in [0, \pi/2]$, while the CP phase is taken in the range $\delta_{\mathrm{CP}} \in [0, 2\pi]$. Different classes of experiments are mainly sensitive to different subsets of these parameters. Atmospheric and long–baseline accelerator experiments constrain θ_{23} and $|\Delta m^2_{31}|$, solar–neutrino and long–baseline reactor measurements determine θ_{12} and Δm^2_{21}, and short–baseline reactor experiments probe θ_{13}. Together, they provide complementary information on the full structure of the mixing matrix.

In the standard three–flavour framework, neutrino oscillations therefore depend on six independent parameters: the three mixing angles, the CP–violating phase and two independent mass–squared differences, which can be chosen as

$$\theta_{12}, \quad \theta_{23}, \quad \theta_{13}, \quad \delta_{\mathrm{CP}}, \quad \Delta m^2_{21}, \quad \Delta m^2_{32}. \quad (1.46)$$

The third mass–squared difference is not independent, since $\Delta m^2_{31} = \Delta m^2_{32} + \Delta m^2_{21}$. By convention, the mass eigenstates are ordered so that $\Delta m^2_{21} > 0$, while the sign of Δm^2_{32} determines whether the spectrum follows the normal or inverted mass ordering (see 1.5.0.4).

Neutrinos used in oscillation experiments originate from several sources: the Sun, interactions of cosmic rays in the atmosphere, nuclear reactors, and accelerator beams. Each source is characterised by typical neutrino energies E and baselines L, and thus by a different sensitivity to the mass–splitting scales Δm^2. As a result, different experimental setups are designed to exploit specific sources and to probe different regions of the oscillation parameter space.

Two main strategies are used to measure oscillations:

- **Appearance** measurements, which look for a neutrino flavour ν_β in a beam

produced initially as ν_α ($\alpha \neq \beta$). In the three–flavour framework and in vacuum, the transition probability is the one defined in Equation 1.28. Since the final flavour may be very suppressed or absent with respect to the original flux, backgrounds can be small, and appearance channels are particularly sensitive to small mixing angles and to CP–violating effects.

- **Disappearance** measurements, which determine the survival probability (see Equation 1.30)of a given flavour ν_α by comparing the observed interaction rate to the expectation in the absence of oscillations. Because interaction rates are affected by statistical fluctuations, small deficits in the event rate are harder to detect, and disappearance channels are generally less suited to measure very small mixing angles.

In both cases, a controlled neutrino source is required. Many experiments deploy a near detector close to the source in order to characterize the initial flux and interaction rates, while a far detector measures the flux after the propagation distance L. Appearance measurements then compare the rate of a different flavour ν_β at the far detector to the initial ν_α flux, whereas disappearance measurements compare the ν_α rate at near and far sites.

In the following sections, the current picture of different kinds of neutrino experiments and their results within the oscillation framework is summarized.

1.5.0.1 Solar neutrinos and θ_{12}

As discussed in Section 1.4, a long series of solar neutrino experiments established the solar neutrino deficit and demonstrated that it is due to flavour conversion rather than to a failure of the Standard Solar Model (SSM) [12, 13, 14, 15, 16]. Building on this evidence, solar neutrino data now provide some of the most precise constraints on the mixing angle θ_{12} and on the "solar" mass–squared splitting Δm^2_{21}, especially when combined with long–baseline reactor antineutrino measurements from KamLAND [24, 25].

For solar neutrinos, the relevant observable is the survival probability $P(\nu_e \to \nu_e)$. In the three–flavour framework, the oscillations driven by $|\Delta m^2_{31}|$ are averaged out because of the large Sun–Earth distance, so that the survival probability can be written as

$$P^{3\nu}(\nu_e \to \nu_e) \;\simeq\; \sin^4\theta_{13} + \cos^4\theta_{13}\, P^{2\nu}(\nu_e \to \nu_e)(\Delta m^2_{21}, \theta_{12}), \tag{1.47}$$

where $P^{2\nu}(\nu_e \to \nu_e)$ is the two–flavour survival probability for the (ν_e, ν_x) system, evaluated including matter effects. Since θ_{13} is small and precisely measured by reactor experiments, the dependence on θ_{13} does not prevent a clean determination

of $\sin^2\theta_{12}$ from solar data.

The KamLAND reactor experiment probes the same mass–splitting Δm^2_{21} using $\bar{\nu}_e$ over a baseline of $\mathcal{O}(100\text{ km})$. In this case matter effects are negligible and the survival probability is well described by the two–flavour vacuum expression

$$P^{2\nu}_{\text{KamLAND}}(\bar{\nu}_e \to \bar{\nu}_e) \;=\; 1 - \sin^2 2\theta_{12}\,\sin^2\!\left(\frac{\Delta m^2_{21}\,L}{4E}\right), \tag{1.48}$$

analogous to the disappearance probability in Eq. (1.32). The reactor antineutrino spectrum observed by KamLAND yields a very precise determination of Δm^2_{21}, while solar data constrain θ_{12} through Equation (1.47). The combination of solar and KamLAND results lead to MSW as the solution for the correct description of the solar neutrino problem.

The Borexino experiment has performed a precision measurement of the ^{7}Be solar neutrino interaction rate, providing a direct determination of the survival probability [26], and has subsequently measured most of the main components of the pp–chain solar neutrino flux. More recently, Borexino has reported the first experimental evidence of solar neutrinos produced in the CNO fusion cycle [27].

1.5.0.2 Atmospheric/accelerator neutrinos and θ_{23}

Atmospheric neutrinos are produced in showers initiated by cosmic rays interacting with nuclei in the atmosphere. Charged pions and kaons present in the cascades, decay predominantly as

$$\pi^\pm \to \mu^\pm + \nu_\mu(\bar{\nu}_\mu), \tag{1.49}$$
$$\mu^\pm \to e^\pm + \nu_e(\bar{\nu}_e) + \bar{\nu}_\mu(\nu_\mu), \tag{1.50}$$

so that both electron and muon (anti)neutrinos are produced, with an expected flavour ratio $(\nu_\mu + \bar{\nu}_\mu)/(\nu_e + \bar{\nu}_e) \simeq 2$ in the sub–GeV range [20, 21]. For a given energy, the neutrino path length L spans from a few tens of kilometres (downward–going events) up to the Earth's diameter ($L \simeq 1.3 \times 10^4\,\text{km}$) for upward–going events, allowing oscillation studies.

The first indications of an anomaly in the atmospheric ν_μ flux were reported by the Kamiokande and IMB water–Cherenkov detectors [28, 29]. Super–Kamiokande then observed a clear zenith–angle dependent deficit of muon–like events, interpreted as ν_μ oscillations with $|\Delta m^2_{32}| \sim 10^{-3}\,\text{eV}^2$ and nearly maximal mixing $\sin^2 2\theta_{23} \simeq 1$ [30]. These results have been corroborated by other atmospheric neutrino experiments such as Soudan 2 and MACRO [31, 32], and more recently by neutrino telescopes like ANTARES and IceCube, which extend the measure-

ment of ν_μ disappearance to higher energies and longer baselines in the multi–GeV to TeV range [33, 34].

In the atmospheric sector, the dominant transition is $\nu_\mu \to \nu_\tau$, governed by the mixing angle θ_{23} and the mass–squared splitting Δm^2_{32}. The muon–neutrino survival probability can be written as

$$P(\nu_\mu \to \nu_\mu) \simeq 1 - \cos^4\theta_{13}\,\sin^2 2\theta_{23}\,\sin^2\left(\frac{\Delta m^2_{32} L}{4E}\right) + \mathcal{O}(\alpha, s^2_{13}), \tag{1.51}$$

where $\alpha \equiv \Delta m^2_{21}/\Delta m^2_{32}$ and $s_{13} \equiv \sin\theta_{13}$ [20, 21, 35]. Atmospheric data provide constraints on $|\Delta m^2_{32}|$ and on the size of $\sin^2 2\theta_{23}$, including whether θ_{23} lies below or above $\pi/4$ (the "octant" problem) [36, 37].

Long–baseline accelerator experiments probe the same parameters with neutrino beams. Measurements were performed by K2K and MINOS using ν_μ disappearance [38] and later combining ν_μ disappearance and ν_e appearance in a full three–flavour framework [39]. More recently, T2K and NOvA have provided high–precision measurements of $|\Delta m^2_{32}|$ and θ_{23}, together with sensitivity to the leptonic CP–violating phase δ_{CP}, through the observation of ν_e and $\bar{\nu}_e$ appearance in a ν_μ or $\bar{\nu}_\mu$ beam [40, 41, 42, 43].

For accelerator beams with energies of a few GeV and baselines of several hundred kilometres, matter effects are moderate and can be treated in the constant–density approximation. The ν_μ survival probability has the same form of Equation (1.51), while the appearance probability can be expressed as

$$\begin{aligned} P(\nu_\mu(\bar{\nu}_\mu) \to \nu_e(\bar{\nu}_e)) \simeq \sin^2\theta_{23}\,\sin^2 2\theta_{13}\,\frac{\sin^2\!\left[(1-\hat{A})\,\Delta_{31}\right]}{(1-\hat{A})^2} \\ + \text{subleading terms in } \alpha \text{ and } s_{13}, \end{aligned} \tag{1.52}$$

where $\Delta_{31} \equiv \Delta m^2_{31} L/(4E)$ and $\hat{A} \equiv 2\sqrt{2}\,G_F N_e E/\Delta m^2_{31}$ is the dimensionless matter parameter introduced in Subsection 1.4.5. The leading term shows explicitly that accelerator appearance measurements are primarily sensitive to θ_{13} and θ_{23}, while the subleading contributions have the dependence on α, the CP–violating phase δ_{CP}, and the sign of Δm^2_{31}. The combination of atmospheric and long–baseline data provides constraints on $|\Delta m^2_{32}|$ and θ_{23}, and plays a central role in the determination of the neutrino mass ordering and in searches for leptonic CP violation [36, 37, 42, 43, 35].

1.5.0.3 Reactor/accelerator neutrinos and θ_{13}

The discoveries of atmospheric and solar neutrino oscillations naturally motivated a precise measurement of the remaining mixing angle θ_{13}, which global fits had previously constrained to be much smaller than the other mixing angles, and even compatible with zero within uncertainties.

Nuclear reactors produce intense fluxes of electron antineutrinos $\bar{\nu}_e$ with typical energies below $\sim$ 10 MeV. In this energy range, $\bar{\nu}_e$ disappearance is the only oscillation channel accessible, and for baselines of order $L \sim 1$ km the effects driven by Δm^2_{21} are negligible. Medium–baseline reactor experiments therefore provide an almost direct measurement of $\sin^2\theta_{13}$. The detection channel is inverse beta decay,

$$\bar{\nu}_e + p \to e^+ + n,$$

identified experimentally through the coincidence between the prompt signal from the positron and the delayed signal from neutron capture (often on gadolinium) in a liquid scintillator detector.

For such medium–baseline reactor experiments, the electron–antineutrino survival probability can be approximated as

$$P_{\bar{\nu}_e \to \bar{\nu}_e}(L, E) \;\simeq\; 1 - \sin^2 2\theta_{13}\, \sin^2\!\left(\frac{\Delta m^2_{ee}\, L}{4E}\right) + \mathcal{O}(\alpha^2), \tag{1.53}$$

where $\alpha \equiv \Delta m^2_{21}/\Delta m^2_{31}$ and

$$\Delta m^2_{ee} \;=\; \cos^2\theta_{12}\, \Delta m^2_{31} + \sin^2\theta_{12}\, \Delta m^2_{32} \tag{1.54}$$

is the effective mass–squared splitting relevant for electron–flavour oscillations [20, 35]. In this regime the dependence on the other oscillation parameters is strongly suppressed, so that the oscillation amplitude is essentially governed by $\sin^2 2\theta_{13}$.

Sensitivity to Δm^2_{21} requires much longer baselines, $L \sim 100$ km, where oscillation experiments can measure mass splittings down to $\Delta m^2_{21} \sim 10^{-5}\,\mathrm{eV}^2$. This is the case of KamLAND, a reactor $\bar{\nu}_e$ experiment that played a key role in establishing the solar oscillation parameters and confirming the MSW solution to the solar neutrino problem [25].

Long–baseline accelerator experiments with the appearance channel $\nu_\mu \to \nu_e$ probed θ_{13}, with the first indication of a non–zero value was reported by the T2K experiment [40]. Dedicated reactor experiments such as Daya Bay, RENO, and Double Chooz also precisely measured $\bar{\nu}_e$ disappearance providing the most accurate determination of this mixing angle to date [44, 45, 46].

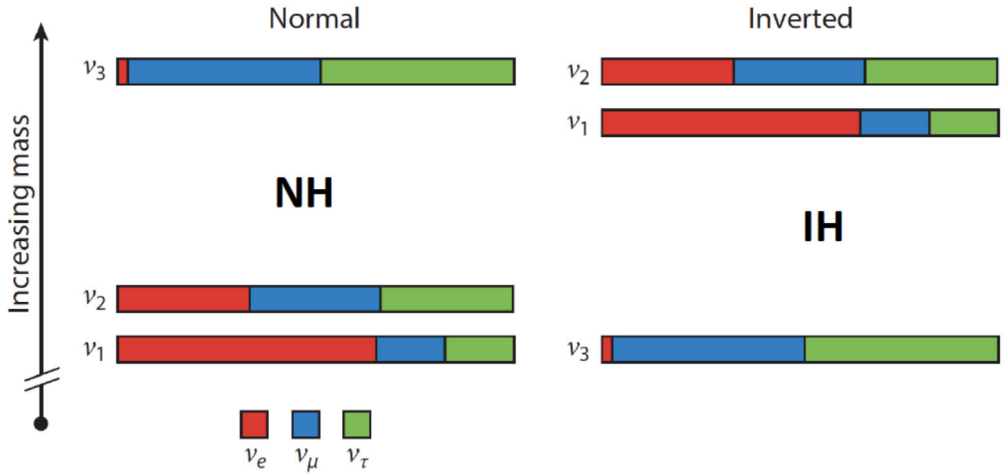

Figure 1.1: Schematic illustration of the normal (NH) and inverted (IH) neutrino mass ordering, with the flavour composition of each mass eigenstate. Image from [47].

1.5.0.4 Mass ordering

In Section 1.5 the three-flavour oscillation framework was introduced in terms of the mixing angles, the CP-violating phase and two independent mass-squared splittings, chosen as Δm^2_{21} and Δm^2_{32} in 1.46. By convention, the mass eigenstates are labelled so that $\Delta m^2_{21} > 0$, while the sign of Δm^2_{32} is still unknown. As a consequence, current data allow two distinct patterns for the spectrum of mass eigenstates, usually referred to as the normal and inverted mass ordering:

- **Normal ordering (NO):** $m_1 < m_2 < m_3$, corresponding to $\Delta m^2_{32} > 0$;
- **Inverted ordering (IO):** $m_3 < m_1 < m_2$, corresponding to $\Delta m^2_{32} < 0$.

Figure 1.1 sketches the two possibilities in which each horizontal bar represents one mass eigenstate ν_i, with its vertical position indicating the relative mass (the absolute scale is unknown), showing the flavour content of that state with different colors. Different fractions $|U_{ei}|^2$, $|U_{\mu i}|^2$ and $|U_{\tau i}|^2$ are associated with ν_e (red), ν_μ (blue) and ν_τ (green), respectively. In the normal ordering, ν_1 and ν_2 contain a large ν_e component, while ν_3 is mostly a mixture of ν_μ and ν_τ with only a small ν_e admixture. In the inverted ordering, the lightest state ν_3 has negligible ν_e content, and the two heavier states ν_1 and ν_2.

Determining the mass ordering is one of the main open questions in neutrino

physics, with important implications for neutrinoless double beta decay and for cosmological constraints on the sum of neutrino masses [48]. Sensitivity to the mass ordering arises from matter effects in long-baseline and atmospheric neutrino oscillations, and from precision measurements of the atmospheric splitting in reactor experiments. Recent global fits that combine accelerator, reactor and atmospheric data indicate that both NO and IO still give an acceptable description of the data, with only a mild preference for normal ordering. The NuFIT 6.0 analysis, which includes long-baseline, reactor and IceCube atmospheric samples, finds that NO and IO provide almost equally good fits; the inclusion of the Super-Kamiokande data leads to a preference for NO [49]. Nowadays, the ordering is not yet established, although NO is slightly favoured.

A definitive determination of the mass ordering is expected from the next generation of oscillation experiments. The medium-baseline reactor experiment JUNO aims at a stand-alone sensitivity of about 3σ, while future long-baseline facilities such as DUNE (see Chapter 2) and Hyper-Kamiokande, together with high-statistics atmospheric-neutrino measurements, will exploit matter effects. Combined analyses of JUNO with long-baseline and atmospheric data are expected to enhance the overall sensitivity, and could resolve the mass ordering at the 5σ level within the coming decade [50, 51].

1.6 Status of global three–flavour fits

As discussed in Section 1.5, neutrino oscillations in the three–flavour framework are described by six independent parameters whose determination requires a global analysis combining the data from the different experiemnts. In this Section results and figures are quoted from the latest NuFIT 6.0 analysis [49], and are consistent with the summary presented in the PDG review of neutrino mixing [48]. Independent global analyses reach very similar conclusions [51].

Figure 1.2 summarises the present status of the oscillation parameters as obtained by the NuFIT 6.0 global analysis. For each mass ordering the table reports the best–fit values together with their 1σ uncertainties and 3σ ranges. At 3σ the four best–constrained parameters are already known with $\mathcal{O}(10\%)$ relative precision or better: θ_{12} is determined to about 13%, θ_{13} to $\sim 8\%$, Δm^2_{21} to $\sim 15\%$ and $|\Delta m^2_{3\ell}|$ to $\sim 6\%$, where $\Delta m^2_{3\ell} \equiv \Delta m^2_{31}$ for NO and $\Delta m^2_{3\ell} \equiv \Delta m^2_{32}$ for IO, following the NuFIT convention [49]. θ_{23} and $\delta_{\rm CP}$ remain less precisely determined, and their allowed regions exhibit a strong dependence on the assumed data set and mass ordering [49, 51].

Figure 1.3 shows two–dimensional projections of the NuFIT 6.0 global fit. In each

NuFIT 6.0 (2024)

		Normal Ordering ($\Delta\chi^2 = 0.6$)		Inverted Ordering (best fit)	
		bfp $\pm 1\sigma$	3σ range	bfp $\pm 1\sigma$	3σ range
IC19 without SK atmospheric data	$\sin^2\theta_{12}$	$0.307^{+0.012}_{-0.011}$	$0.275 \to 0.345$	$0.308^{+0.012}_{-0.011}$	$0.275 \to 0.345$
	$\theta_{12}/^\circ$	$33.68^{+0.73}_{-0.70}$	$31.63 \to 35.95$	$33.68^{+0.73}_{-0.70}$	$31.63 \to 35.95$
	$\sin^2\theta_{23}$	$0.561^{+0.012}_{-0.015}$	$0.430 \to 0.596$	$0.562^{+0.012}_{-0.015}$	$0.437 \to 0.597$
	$\theta_{23}/^\circ$	$48.5^{+0.7}_{-0.9}$	$41.0 \to 50.5$	$48.6^{+0.7}_{-0.9}$	$41.4 \to 50.6$
	$\sin^2\theta_{13}$	$0.02195^{+0.00054}_{-0.00058}$	$0.02023 \to 0.02376$	$0.02224^{+0.00056}_{-0.00057}$	$0.02053 \to 0.02397$
	$\theta_{13}/^\circ$	$8.52^{+0.11}_{-0.11}$	$8.18 \to 8.87$	$8.58^{+0.11}_{-0.11}$	$8.24 \to 8.91$
	$\delta_{\rm CP}/^\circ$	177^{+19}_{-20}	$96 \to 422$	285^{+25}_{-28}	$201 \to 348$
	$\frac{\Delta m^2_{21}}{10^{-5}\ \text{eV}^2}$	$7.49^{+0.19}_{-0.19}$	$6.92 \to 8.05$	$7.49^{+0.19}_{-0.19}$	$6.92 \to 8.05$
	$\frac{\Delta m^2_{3\ell}}{10^{-3}\ \text{eV}^2}$	$+2.534^{+0.025}_{-0.023}$	$+2.463 \to +2.606$	$-2.510^{+0.024}_{-0.025}$	$-2.584 \to -2.438$
		Normal Ordering (best fit)		Inverted Ordering ($\Delta\chi^2 = 6.1$)	
		bfp $\pm 1\sigma$	3σ range	bfp $\pm 1\sigma$	3σ range
IC24 with SK atmospheric data	$\sin^2\theta_{12}$	$0.308^{+0.012}_{-0.011}$	$0.275 \to 0.345$	$0.308^{+0.012}_{-0.011}$	$0.275 \to 0.345$
	$\theta_{12}/^\circ$	$33.68^{+0.73}_{-0.70}$	$31.63 \to 35.95$	$33.68^{+0.73}_{-0.70}$	$31.63 \to 35.95$
	$\sin^2\theta_{23}$	$0.470^{+0.017}_{-0.013}$	$0.435 \to 0.585$	$0.550^{+0.012}_{-0.015}$	$0.440 \to 0.584$
	$\theta_{23}/^\circ$	$43.3^{+1.0}_{-0.8}$	$41.3 \to 49.9$	$47.9^{+0.7}_{-0.9}$	$41.5 \to 49.8$
	$\sin^2\theta_{13}$	$0.02215^{+0.00056}_{-0.00058}$	$0.02030 \to 0.02388$	$0.02231^{+0.00056}_{-0.00056}$	$0.02060 \to 0.02409$
	$\theta_{13}/^\circ$	$8.56^{+0.11}_{-0.11}$	$8.19 \to 8.89$	$8.59^{+0.11}_{-0.11}$	$8.25 \to 8.93$
	$\delta_{\rm CP}/^\circ$	212^{+26}_{-41}	$124 \to 364$	274^{+22}_{-25}	$201 \to 335$
	$\frac{\Delta m^2_{21}}{10^{-5}\ \text{eV}^2}$	$7.49^{+0.19}_{-0.19}$	$6.92 \to 8.05$	$7.49^{+0.19}_{-0.19}$	$6.92 \to 8.05$
	$\frac{\Delta m^2_{3\ell}}{10^{-3}\ \text{eV}^2}$	$+2.513^{+0.021}_{-0.019}$	$+2.451 \to +2.578$	$-2.484^{+0.020}_{-0.020}$	$-2.547 \to -2.421$

Figure 1.2: Global three-flavour oscillation parameters from the NuFIT 6.0 analysis [49]. The upper panel ("IC without SK-atm") corresponds to the fit including IceCube data but excluding Super-Kamiokande atmospheric neutrinos, while the lower one ("IC24 with SK-atm") includes both the latest IceCube and Super-Kamiokande atmospheric samples. The values quoted in this Section refer to the "IC24 with SK-atm" fit.

panel, two oscillation parameters are displayed on the axes, while the remaining ones (and, when applicable, the mass ordering) are varied to minimize the global χ^2. The contours therefore represent the regions allowed by the full six–parameter fit, projected onto these planes.

The panel in the ($\sin^2\theta_{12}$, Δm^2_{21}) plane illustrates the high precision reached in the solar sector, largely driven by the combination of solar and KamLAND data.

The panel involving $\sin^2\theta_{13}$ and $|\Delta m^2_{3\ell}|$ reflects the constraints from medium–baseline reactor experiments, which contrain the reactor angle and the atmospheric mass splitting with percent-level accuracy.

The ($\sin^2\theta_{13}$, $\delta_{\rm CP}$) panel highlights the present status of the CP–violating phase: the allowed region is very narrow in $\sin^2\theta_{13}$, confirming the precise reactor determination of this angle, but remains broad in $\delta_{\rm CP}$, indicating that the phase is still only weakly constrained. The ($\sin^2\theta_{23}$, $\delta_{\rm CP}$) panel further shows the interplay between the atmospheric mixing angle and the CP phase: solutions with θ_{23} in the first and second octant are both allowed, and they are associated with different preferred ranges of $\delta_{\rm CP}$, leading to the multiple disconnected islands and non-Gaussian shape visible in this plane. Finally, the panel in the (Δm^2_{31}, Δm^2_{32}) plane shows that the two atmospheric mass–squared splittings are tightly constrained and strongly correlated, clustering around $|\Delta m^2_{3\ell}| \simeq 2.5 \times 10^{-3}\,\mathrm{eV}^2$ for both mass orderings, as expected from the relation $\Delta m^2_{31} = \Delta m^2_{32} + \Delta m^2_{21}$.

Concerning the mass ordering, present global fits provide an indication in favour of the normal spectrum. Including Super-Kamiokande atmospheric neutrinos and the latest IceCube data, the NuFIT 6.0 analysis finds a difference $\Delta\chi^2 \simeq 6$ between NO and IO, corresponding to a preference of about 2.5σ [49]. If SK atmospheric data are omitted, the sensitivity to the ordering is substantially reduced. Independent global analyses reach similar conclusions, with a preference for NO at the level of ~ 2–2.5σ; a more detailed discussion is given in 1.5.0.4 [51].

The status of the CP–violating phase is even less conclusive. In the NuFIT 6.0 global fit with SK–atm and IceCube, the best–fit values are $\delta_{\rm CP} \simeq 210^\circ$ for NO and $\delta_{\rm CP} \simeq 270^\circ$ for IO, with broad allowed intervals at 3σ [49]. For the normal ordering, CP–conserving values $\delta_{\rm CP} = 0, \pi$ are well within the currently allowed region, so there is at present no statistically significant indication of leptonic CP violation. For the inverted ordering, values of $\delta_{\rm CP}$ near 270° are preferred and CP conservation is disfavoured at the level of a few standard deviations, but this conclusion depends on the mass ordering which is itself disfavoured and should therefore be interpreted with caution [49, 48].

The information from global fits can be also shown as the leptonic unitarity triangles, defined by the conditions of the PMNS matrix:

$$\sum_{i=1}^{3} U_{\alpha i}\, U^*_{\beta i} \;=\; 0 \qquad (\alpha \neq \beta), \tag{1.55}$$

which correspond to six triangles in the complex plane, one for each pair of flavour indices (α, β). Figure 1.4 shows the triangle constructed from the first and third columns of $U_{\rm PMNS}$, plotted using the NuFIT 6.0 allowed ranges and taken from the PDG review of neutrino mixing [48]. After an appropriate rescaling and rotation, two vertices are fixed at $(0, 0)$ and $(1, 0)$, while the third vertex is given by

$$z \;=\; -\,\frac{U_{e1}U_{e3}^{*}}{U_{\mu 1}U_{\mu 3}^{*}}. \tag{1.56}$$

In the absence of CP violation the triangle would be flat, $\mathrm{Im}(z) = 0$, and its area (proportional to the Jarlskog invariant $J_{\rm CP}$) would vanish. The coloured allowed band in Figure 1.4 shows that current data favour a non-zero area, corresponding to a non-zero best–fit value $J_{\rm CP} \simeq -0.009$, but the region still crosses the real axis so CP conservation remains allowed at the $\sim 2\sigma$ level and no definitive observation of leptonic CP violation can yet be claimed [48].

In summary, four of the six oscillation parameters $(\theta_{12}, \theta_{13}, \Delta m^2_{21}, |\Delta m^2_{3\ell}|)$ are now known at the few–percent level, while the atmospheric mixing angle θ_{23}, the CP–violating phase $\delta_{\rm CP}$ and the sign of the atmospheric splitting $\Delta m^2_{3\ell}$ remain the main open questions to be addressed by the next generation of oscillation experiments.

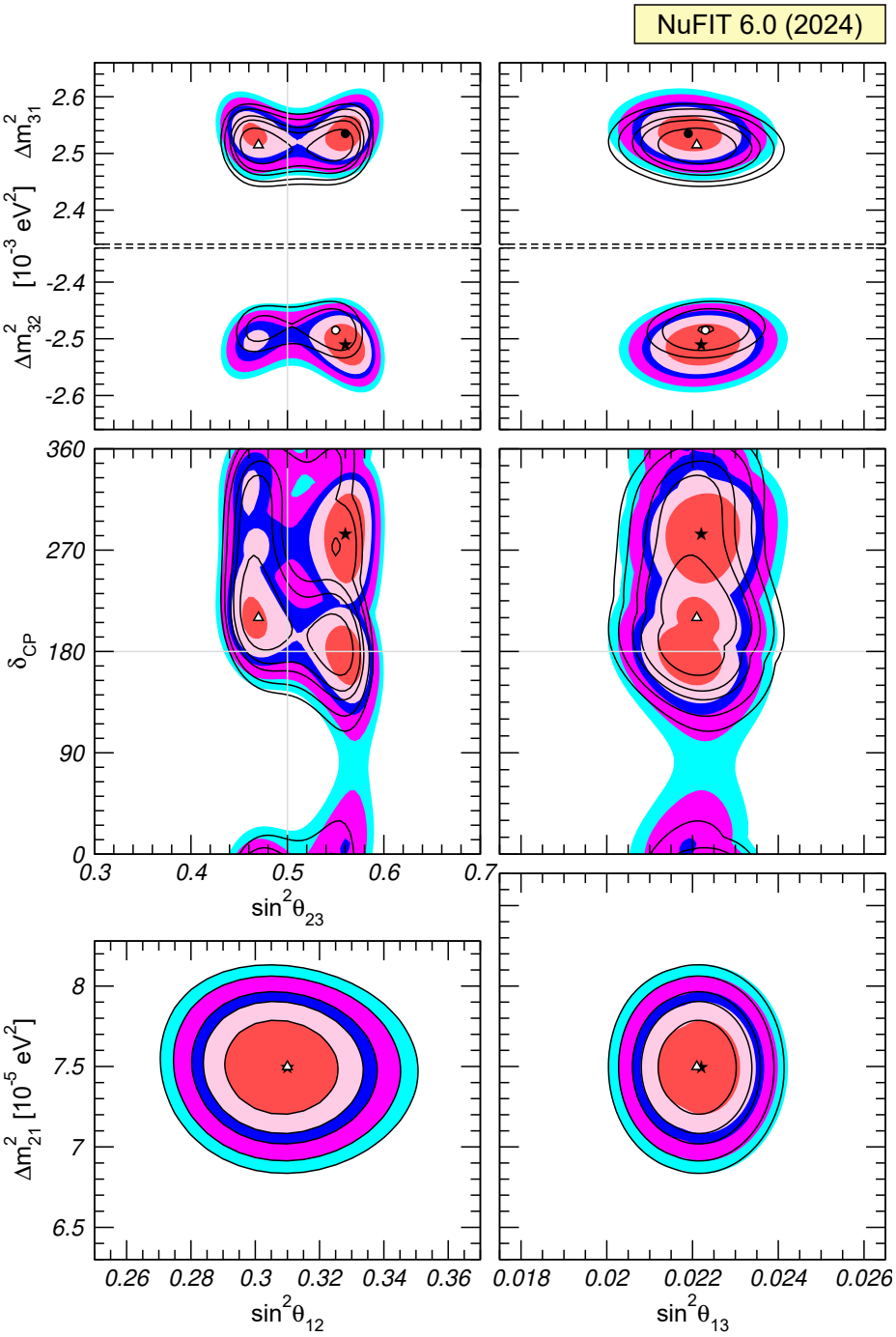

Figure 1.3: Two–dimensional projections of the allowed region from the NuFIT 6.0 global three–flavour analysis, showing the correlations between selected pairs of oscillation parameters for both normal and inverted mass ordering. In each panel the remaining parameters are minimised over. The contours correspond to 1σ, 90%, 2σ, 99% and 3σ confidence levels. Figure taken from Ref. [49].

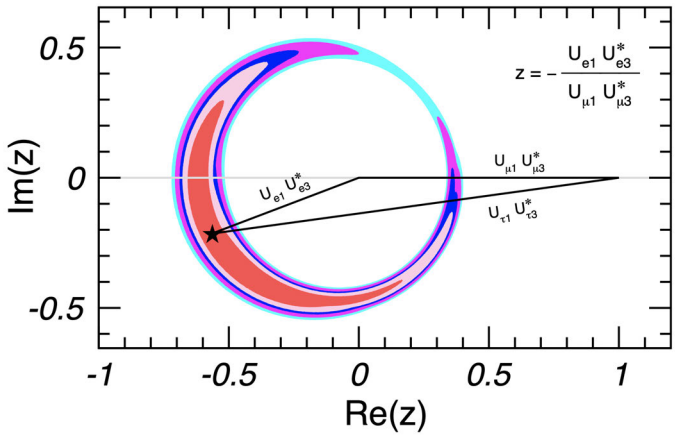

Figure 1.4: Leptonic unitarity triangle for the first and third columns of the PMNS matrix, constructed from the NuFIT 6.0 allowed ranges of the mixing parameters. The coloured regions show the 1σ, 90%, 2σ, 99% and 3σ allowed domain of the third vertex in the complex plane. Figure adapted from Ref. [48], Fig. 14.9.

Chapter 2

The Deep Underground Neutrino Experiment (DUNE)

The Deep Underground Neutrino Experiment (DUNE) [52, 53] is a next–generation long-baseline neutrino oscillation experiment that will operate in the United States. Its primary goals are to measure with high precision the parameters governing neutrino and antineutrino oscillations, in particular the leptonic CP-violating phase δ_{CP} and the neutrino mass ordering, while also detect and measure ν_e from a core-collapse supernova within the Milky Way and search for signals of physics beyond the Standard Model such as proton decay.

DUNE will use the high-intensity, wide-band Long-Baseline Neutrino Facility (LBNF) beam located at Fermilab, capable of operating in both neutrino and antineutrino modes. A modular near-detector (ND) complex will be installed roughly 600 m downstream the neutrino production point to characterize the neutrino flux before the oscillations take place, providing precise constraints on interaction cross sections, and pursue an independent program of beyond-the-Standard-Model measurements. Neutrinos will then propagate about 1300 km through the Earth's crust to reach a multi-module, 1.5 km underground far detector (FD), based on liquid-argon time-projection chamber (LArTPC) technology at the Sanford Underground Research Facility (SURF), with a total fiducial mass of order 40 kt.

DUNE will take data in two stages: an initial Phase I configuration with a reduced ND complex, two FD modules and a 1.2 MW beam, followed by a Phase II upgrade to four FD modules and a 2.4 MW beam and an improved ND complex, providing the sensitivity required to determine the mass ordering and to measure δ_{CP} with few-percent precision. A schematic view of the facility is shown in Figure 2.1, and comprehensive descriptions of the design and science program will be given in the next sections.

2.1 DUNE physics program

Central to DUNE program are the determination of CP violation in neutrino oscillations, through a measurement of the leptonic phase δ_{CP}, the identification

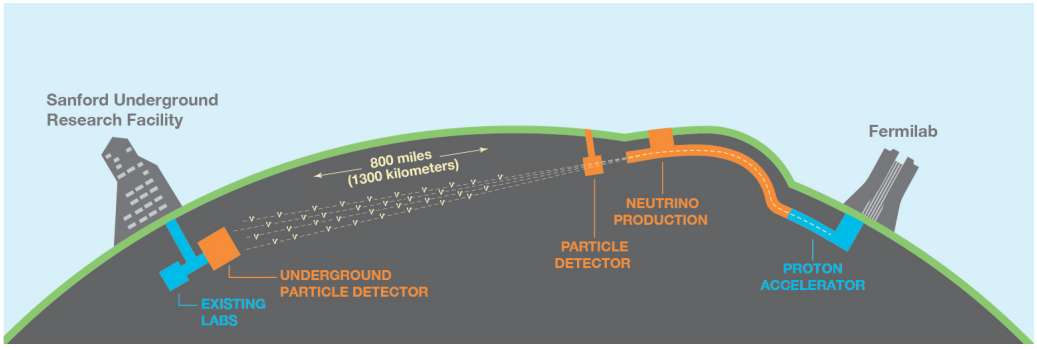

Figure 2.1: Schematic representation of the LBNF beamline and the DUNE experiment. Image from [52].

of the neutrino mass ordering (i.e. the sign of Δm^2_{31}), and the resolution of the octant in which the atmospheric mixing angle θ_{23} lies.

Other key goals of the experiment include sensitive searches for proton decay in several possible decay modes, and the detection and detailed measurement of neutrinos from a core–collapse supernova, should such an event occur during the data taking of the experiment. DUNE will also have a broad program of secondary measurements, such as searches for physics beyond the Standard Model and precision studies of neutrino oscillations using atmospheric neutrinos. All these topics are introduced in this section. The DUNE near detector will in addition pursue its own complementary physics program, that is discussed separately in Sec. **??**.

2.1.1 Neutrino Oscillations: Masses, Mixing Angles, and CP Violation

The primary scientific goal of DUNE is to perform long-baseline neutrino oscillation measurements with high–intensity ν_μ and $\bar{\nu}_\mu$ beams delivered by the LBNF accelerator complex at Fermilab [52]. These measurements exploit both $\nu_\mu \to \nu_\mu$ ($\bar{\nu}_\mu \to \bar{\nu}_\mu$) disappearance and $\nu_\mu \to \nu_e$ ($\bar{\nu}_\mu \to \bar{\nu}_e$) appearance channels to address some of the central open questions in neutrino physics: the leptonic CP–violating phase $\delta_{\rm CP}$, the neutrino mass ordering, and the octant of the atmospheric mixing angle θ_{23}. In addition, DUNE aims to improve the precision on the other oscillation parameters within the three–flavour framework and to provide stringent consistency tests of the PMNS paradigm.

The appearance probabilities $P(\nu_\mu \to \nu_e)$ and $P(\bar{\nu}_\mu \to \bar{\nu}_e)$ at a baseline of $L \simeq$ 1300 km are strongly affected by both matter effects and CP violation.

Their dependence on the neutrino energy and on $\delta_{\rm CP}$ is illustrated in Figure 2.2

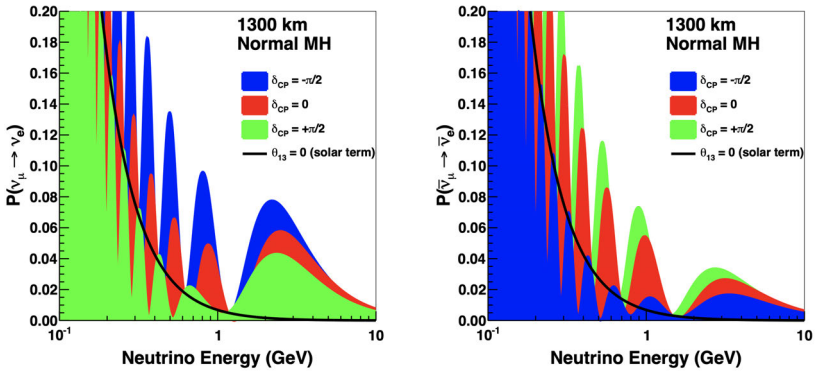

Figure 2.2: Electron neutrino (left) and antineutrino (right) appearance probabilities at a baseline of 1300 km as a function of neutrino energy, for several values of $\delta_{\rm CP}$, assuming normal mass ordering. Figure from Ref. [52].

for several values of $\delta_{\rm CP}$ and assuming normal ordering. Expressions for these probabilities in constant-density matter are given in Eq. (1.52). In the usual perturbative expansion in $\alpha \equiv \Delta m^2_{21}/\Delta m^2_{31}$ and s_{13}, the appearance probabilities can be written schematically as $P(\nu_\mu \to \nu_e) = P_0 + P_1 \cos\delta_{\rm CP} + P_2 \sin\delta_{\rm CP}$, whereas for antineutrinos one has $P(\bar{\nu}_\mu \to \bar{\nu}_e) = P_0 + P_1 \cos\delta_{\rm CP} - P_2 \sin\delta_{\rm CP}$. The term proportional to $\sin\delta_{\rm CP}$ changes sign between neutrinos and antineutrinos, giving rise to the CP asymmetry $A^{\mu e}_{CP}$ introduced in the general definition of Equation (1.44).

At the same time, the coherent forward scattering of electron neutrinos in matter induces an additional $\nu/\bar{\nu}$ asymmetry through the matter potential, whose magnitude and sign depend on the neutrino mass ordering. For the DUNE baseline, the matter–induced difference between the $\nu_\mu \to \nu_e$ and $\bar{\nu}_\mu \to \bar{\nu}_e$ appearance probabilities in the region of the first oscillation maximum corresponds to a $\nu/\bar{\nu}$ asymmetry of order 40%, much larger than the maximal CP–violating asymmetry in vacuum. Because the sign of the matter–induced asymmetry is fixed by the mass ordering, while the CP–violating contribution changes sign with $\sin\delta_{\rm CP}$, the combined measurement of ν_e and $\bar{\nu}_e$ appearance spectra over a wide energy range allows DUNE to disentangle matter and CP effects and to determine the ordering of the mass eigenstates.

These considerations led the choice of a wide–band beam with an energy coverage from 0.5 to 5 GeV, peaking around 2–3 GeV, where the first oscillation maximum occurs at $L \simeq 1300$ km. Measuring the energy dependence of the appearance probabilities over several oscillation nodes is particularly powerful: it constrains the oscillation parameters through both rate and spectral information and helps to resolve degeneracies among $\delta_{\rm CP}$, the mass ordering and the mixing angles.

In addition to the appearance channels, DUNE will exploit ν_μ and $\bar{\nu}_\mu$ disappearance measurements, which are mainly sensitive to $\sin^2 2\theta_{23}$ and Δm^2_{32}. Combining appearance and disappearance information for both neutrinos and antineutrinos provides constraints on the three–flavour oscillation framework and enhances the sensitivity to the θ_{23} octant.

For exposures of a few hundred kt·MW·years in the Phase II configuration, DUNE is expected to determine the neutrino mass ordering with a significance exceeding 5σ over essentially the entire δ_{CP} range, as illustrated in Figure 2.3(a). The evolution of this sensitivity with the total exposure is shown in Figure 2.3(b).

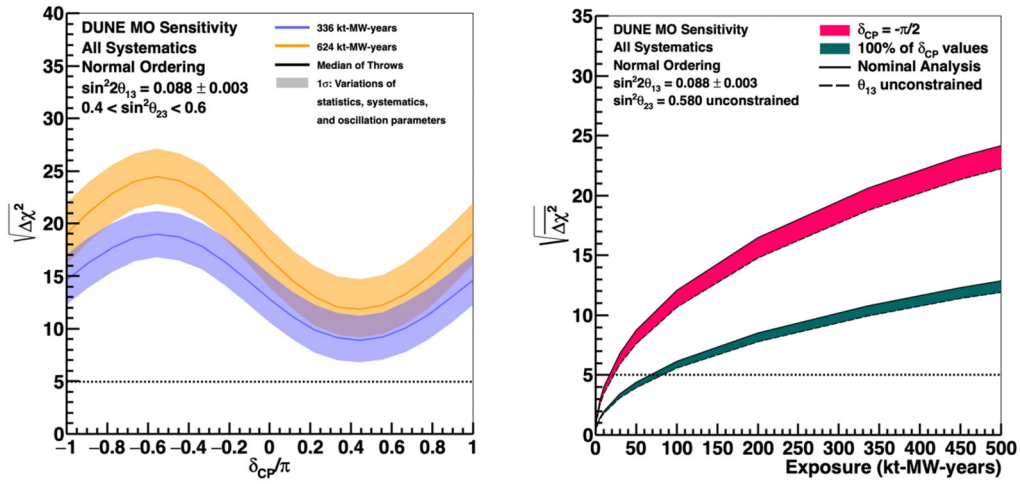

(a) (b)

Figure 2.3: DUNE sensitivity to the neutrino mass ordering, from Ref. [54]. In both panels the vertical axis shows $\sqrt{\Delta\chi^2_{\mathrm{MO}}}$, with $\Delta\chi^2_{\mathrm{MO}} = \chi^2_{\text{wrong ordering}} - \chi^2_{\text{true ordering}}$, interpreted as the significance for rejecting the wrong ordering. Panel (a) shows the sensitivity as a function of the true value of δ_{CP} for two exposures, 336 and 624 kt·MW·years. Panel (b) shows the sensitivity as a function of exposure for the maximally CP–violating value $\delta_{\mathrm{CP}} = -\pi/2$ and for different fractions of the δ_{CP} parameter space. The coloured bands indicate the range of sensitivities obtained when varying oscillation parameters and systematic uncertainties in the simulations.

The same exposures provide strong sensitivity to CP violation and the relevant sensitivities are shown in Figure 2.4 [54]. For exposures of a few hundred kt·MW·years, DUNE is expected to reach a 5σ discovery of CP violation for half of the possible values of δ_{CP}, and at least a 3σ sensitivity for most of the parameter space, as illustrated in Figure 2.4(a). Figure 2.4(b) shows how the CP-violation discovery significance increases with exposure, both for the value

$\delta_{CP} = -\pi/2$ and for the fractions of 50% and 75% of all possible δ_{CP} values. The corresponding evolution of these sensitivities as a function of the data taking years in Phase I is shown in Figure 2.18.

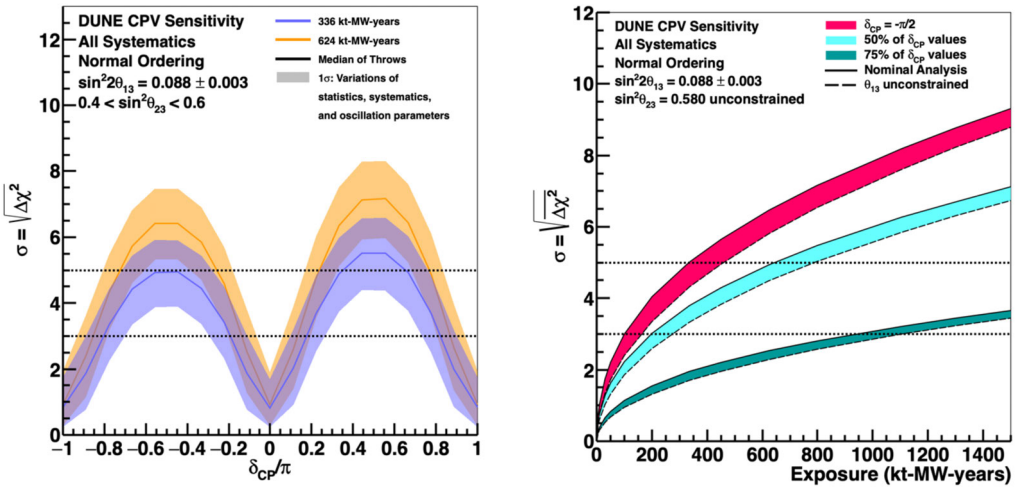

(a) (b)

Figure 2.4: DUNE sensitivity to leptonic CP violation, from Ref. [54]. In both panels the vertical axis shows $\sigma = \sqrt{\Delta\chi^2_{\mathrm{CPV}}}$, where $\Delta\chi^2_{\mathrm{CPV}}$ is the difference between the best–fit χ^2 for the CP–conserving hypotheses $\delta_{CP} = 0, \pm\pi$ and that for the true value of δ_{CP}. Panel (a) shows the significance as a function of the true δ_{CP} for the same exposures as in Figure 2.3. Panel (b) shows the expected significance as a function of exposure for the maximally CP-violating value $\delta_{CP} = -\pi/2$ (magenta band), and for the fractions of 50% and 75% of all possible δ_{CP} values (cyan bands).

Precise measurements of the mixing angles and mass splittings are a second major objective of the DUNE oscillation program. By combining ν_μ disappearance and ν_e appearance data, DUNE will significantly improve the precision on $\sin^2\theta_{23}$ and help resolve whether θ_{23} lies in the lower or upper octant. Representative sensitivities are shown in Figure 2.5: panel (a) gives the significance $\sqrt{\Delta\chi^2}$ for rejecting the wrong octant as a function of the true value of $\sin^2\theta_{23}$ for exposures of 10 and 15 years, while panel (b) shows the expected 1σ resolution on $\sin^2 2\theta_{23}$ as a function of the total exposure. Exposures of a few hundred kt·MW·years yield percent-level precision on $\sin^2 2\theta_{23}$ and robust sensitivity to non-maximal mixing. The same analysis also provides an independent determination of θ_{13} and Δm^2_{32} that is competitive with, and complementary to, the constraints from reactor and other long-baseline experiments [55].

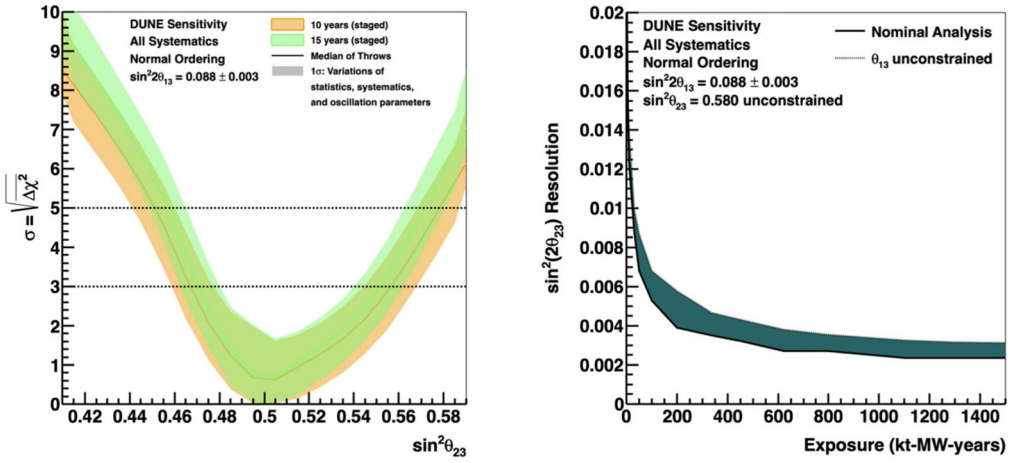

(a) (b)

Figure 2.5: DUNE sensitivity to θ_{23}, from [55]. Panel (a) shows the significance $\sqrt{\Delta\chi^2}$ for excluding the wrong octant as a function of the true value of $\sin^2\theta_{23}$ for two exposures, 10 and 15 years. Panel (b) shows the expected 1σ resolution on $\sin^2(2\theta_{23})$ versus the total exposure in kt·MW·years. The shaded bands indicate the impact of variations in statistics, systematics and oscillation parameters in the sensitivity study.

2.1.2 Supernova, solar, and other low-energy neutrinos

Core–collapse supernovae happen when the iron core of a massive star approaches the Chandrasekhar mass and collapses to supranuclear densities. Most of the released gravitational binding energy is emitted as $\sim 10^{58}$ neutrinos and antineutrinos of all flavours with typical energies of a few tens of MeV [56, 57]. In a core–collapse event, the neutrino signal starts with a short "neutronization" burst lasting a few milliseconds and dominated by ν_e, followed by an accretion phase of a few hundred milliseconds and a cooling phase of order 10 s during which the proto–neutron star radiates away most of its energy and the three flavours are equalized. The time, energy and flavour structure of this signal can give information on the progenitor, the collapse and explosion dynamics, the nature of the remnant, and possible non–standard neutrino properties.

The importance of supernova neutrinos was first demonstrated by the observation of a few dozen $\bar{\nu}_e$ events from SN 1987A in water Cherenkov and scintillator detectors, which provided a qualitative confirmation of the core–collapse picture. Core–collapse events in the Milky Way are expected at a rate of a few per century, with a comparable rate in the Andromeda galaxy at a distance of about 780 kpc; over the multi–decade lifetime of DUNE there is therefore a realistic chance that

at least one nearby supernova will be observed with high statistics.

From the detector point of view, the supernova burst is challenging because the neutrino energies are below the charged–current thresholds for ν_μ, $\bar{\nu}_\mu$, ν_τ and $\bar{\nu}_\tau$, so these flavours are accessible mainly via neutral–current interactions. Present large detectors are primarily sensitive to $\bar{\nu}_e$ through inverse beta decay. DUNE, instead, will be uniquely sensitive to the ν_e component of the burst. In liquid argon, the dominant interaction in the few–tens–of–MeV regime is the charged–current absorption of electron neutrinos on argon,

$$\nu_e + {}^{40}\mathrm{Ar} \rightarrow e^- + {}^{40}\mathrm{K}^*, \tag{2.1}$$

for which the observable signature consists of a short electron track followed by de–excitation γ rays and other secondaries from the excited ${}^{40}\mathrm{K}^*$ state [53, 58]. This channel dominates the event rate in argon and gives DUNE a unique capability among current and planned detectors to measure the ν_e flux from a core–collapse burst, particularly during the early neutronization phase, which is essentially inaccessible to water Cherenkov and liquid–scintillator experiments.

The same low–energy capabilities that enable supernova–burst physics also make DUNE sensitive to other astrophysical neutrino sources. In particular, the large ν_e charged–current cross section on argon and the excellent imaging capabilities of the LArTPC open the possibility of observing solar neutrinos, which are expected to produce of order 10^2 events per day in a final far–detector fiducial mass of 40 kt [59], and the diffuse supernova neutrino background (DSNB), once radiological and cosmogenic backgrounds are sufficiently controlled [58].

These measurements would extend the DUNE physics into the few–MeV energy domain and provide information on both astrophysical sources and neutrino parameters that is complementary to that obtained with the other detector technologies.

2.1.3 Beyond Standard Model searches

Sterile neutrino mixing Experimental anomalies in tension with the standard three–flavour framework can be interpreted as mixing between the known active neutrinos and one or more light sterile states [60]. DUNE will search for deviations from the standard oscillation pattern in both charged–current and neutral–current samples. The combination of the long baseline and the near detector one gives sensitivity to a broad range of sterile–neutrino mass splittings and mixing angles [61].

Non–unitarity of the PMNS matrix Many extensions of the Standard Model

that explain neutrino masses introduce heavy neutral leptons in addition to the three light states. In this case, the PMNS matrix describing light–neutrino mixing need not be exactly unitary. Deviations from unitarity modify both the overall event rates and the flavour composition observed at the ND and FD. Thanks to its precise flux and cross–section constraints at the ND and its high–statistics oscillation measurements at the FD, DUNE can test such non–unitarity at the percent level, providing constraints that are complementary to those from flavour physics and electroweak precision observables [61].

Non–standard interactions (NSI) Non–standard neutrino interactions are effective four–fermion couplings that modify neutrino production, detection or propagation in matter [62]. In long–baseline experiments they mainly appear as additional terms in the matter potential and can distort the oscillation probabilities, potentially mimicking or obscuring CP violation and mass–ordering effects. The very long baseline and wide–band beam give DUNE excellent sensitivity to such effects, allowing it to improve bounds on several NSI parameters [61].

Neutrino trident production at the ND Neutrino trident production is a rare electroweak process in which a neutrino interacts coherently with the electromagnetic field of a heavy nucleus, leaving the nucleus intact while producing a charged–lepton pair in the final state. The intense neutrino flux and the capability of the near detector will allow DUNE to record an unprecedented sample of trident events, particularly $\nu_\mu \to \nu_\mu \mu^+ \mu^-$ interactions [63]. Measuring the trident cross section with good precision will provide a test of the Standard Model and a sensitive probe of new gauge bosons [63, 61].

Proton decay and baryon–number violation Grand Unified Theories generically predict baryon number violating processes such as proton decay. With its large fiducial mass, low backgrounds and excellent imaging capabilities, the DUNE far detector will search for channels like $p \to K^+ \bar{\nu}$ and $p \to e^+ \pi^0$, where the kaon or pion and their decay products can be fully reconstructed [53]. With exposures of a few hundred kt·yr, DUNE is expected to improve the current Super–Kamiokande limits by an order of magnitude, or to observe proton decay [61]. Similar techniques can be applied to other baryon–number–violating processes such as neutron decay and neutron–antineutron oscillations.

Dark sector and boosted dark matter The DUNE detectors will probe dark sectors. Light dark matter produced in the LBNF beamline via a vector ("dark photon") mediator could travel to the ND and interact via elastic scattering with electrons or nuclei in the detector. The high beam intensity and the DUNE–PRISM program increase the sensitivity to sub–GeV dark matter in regions of parameter space that are difficult to access with traditional direct de-

tection experiments [64, 61]. At the FD, DUNE could be sensitive to boosted dark matter arising in scenarios where a heavier dark matter species, χ_1, which composes the dominant component of the Galactic halo or is captured in the Sun, annihilates into a lighter state χ_2 that is produced with a relativistic boost and can reach the detector. In such cases, χ_2 would be observed through its scattering on electrons or nuclei rather than via secondary neutrinos. Inelastic scattering of such boosted particles, followed by the decay of an excited dark state, can produce characteristic multi lepton or lepton/nucleon signatures that can be reconstructed with the LArTPC technology [65, 61].

2.2 DUNE components and design

In this section a brief overview is given of the main components of the DUNE experiment, namely the high–power neutrino beamline, the Near Detector (ND) complex and the Far Detector (FD).

In Phase I DUNE will deploy two LArTPC FD modules at the Sanford Underground Research Facility. Each module contains an liquid argon mass of about 17 kt, corresponding to a fiducial mass of ~ 10 kt, and uses one of the two readout technologies: a single–phase horizontal–drift (HD) design and a vertical–drift (VD) design [66, 67]. The Phase I ND complex will consist of a modular liquid–argon TPC (ND–LAr), The Muon Spectrometer (TMS) located downstream of ND–LAr, and the System for on–Axis Neutrino Detection (SAND). ND–LAr provides a near–detector implementation of the LArTPC technology used at the FD, while SAND is permanently on–axis to monitor the neutrino beam and to constrain flux and cross–section systematics (see Chapter 3) [68, 69]. The TMS is a magnetized muon spectrometer that measures the momentum and charge of muons exiting ND–LAr.

In Phase–II upgrade on the FD side, two additional LArTPC modules will be installed, enhancing the total liquid–argon mass to 70 kt and the fiducial mass to $\gtrsim 40$ kt [70]. The LBNF beam power will be increased from the initial design value of 1.2 MW to an enhanced power of about 2.1 MW, providing substantially larger exposures at the oscillation maximum [70]. In the ND complex, the TMS will be replaced by ND–GAr, a high–pressure gaseous–argon TPC surrounded by electromagnetic calorimetry inside a magnetic field, which will deliver precise measurements of charged particle kinematics and additional control of neutrino–interaction systematics [71, 70]. A more detailed discussion of all the components will be done in the next subsections.

2.2.1 The LBNF beamline

The intense neutrino flux for DUNE will be produced by LBNF beamline at Fermilab, designed to deliver one of the most powerful neutrino beams in the energy range relevant for long–baseline oscillation studies.[52, 53, 72] The facility reuses the existing Main Injector (MI) accelerator complex, originally developed for the Tevatron collider, to provide a proton beam that is directed towards the DUNE Far Detector at SURF in South Dakota at a baseline of 1300 km. The beamline is optimized to cover the first and second oscillation maxima at $E_\nu \simeq 2.5$ and 0.8 GeV, respectively, which motivates a wide-band beam spanning approximately 0.5–5 GeV.[73]

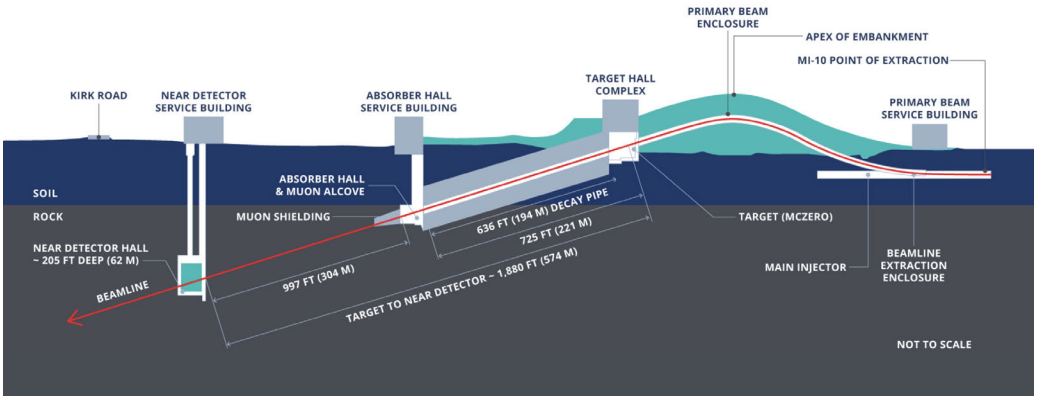

Figure 2.6: Longitudinal view of the LBNF beamline facilities at Fermilab, showing the extraction of the primary proton beam from the Main Injector, target hall complex, decay pipe and the Near Detector hall located about 62 m underground and $\sim$ 574 m downstream of the target. The illustration is not to scale. Figure from the official LBNF/DUNE web page on the neutrino beam [74].

With the commissioning of the PIP II (Proton Improvement Plan II), proton production for LBNF will begin in a new superconducting linear accelerator, which accelerates H^- ions to 800 MeV before injection into the Booster synchrotron.[75] The Booster accelerates the protons to 8 GeV, after which they are transferred to the MI and accelerated to energies between 60 and 120 GeV, depending on the running configuration. The baseline operating point for DUNE Phase I corresponds to a proton beam power of 1.2 MW on the LBNF target, with about 7.5×10^{13} protons per extraction and roughly 1.1×10^{21} protons on target (POT) per year.[73, 72] The accelerator cycle time is approximately 1.2 s, and each spill lasts about 10 μs and contains six Booster batches, The main parameters of the Phase I beam are summarized in Table 2.1. each made of 84 bunches separated

Table 2.1: Nominal primary-beam parameters for the LBNF facility in DUNE Phase I. Values correspond to an 80–120 GeV Main Injector beam delivering 1.2 MW on the LBNF target.[73, 72]

Parameter	Value
Protons per cycle	7.5×10^{13}
Proton kinetic energy	80–120 GeV
Beam power on target	1.2 MW
POT per year	1.1×10^{21}
Accelerator cycle time	1.2 s
Spill duration	10 μs
Booster batches per spill	6
Batch duration	1.6 μs
Bunches per batch	84
RMS bunch length	1 ns
Bunch spacing	19 ns (last 2–3 empty)

by $\sim$ 19 ns with a bunch length of $\sim$ 1 ns. A further upgrade of the accelerator complex beyond PIP II (often referred to as PIP III) is being studied to increase the available beam power to beyond 2 MW for DUNE Phase II, while keeping the same energy range[76, 70].

Once the primary proton beam reaches the desired energy in the MI, it is extracted and downward bended to point the neutrino beam towards SURF (see Figure 2.6). The beam is steered onto a solid graphite or graphite–beryllium production target housed in the target hall complex. Secondary hadrons, predominantly pions and kaons, are produced and focused by two magnetic horns into a decay pipe of length $\sim$ 200 m, where they decay into muons and neutrinos.[72]. Downstream of the decay region, a massive absorber is used to remove the residual hadrons and muons. In the reference design, roughly 40% of the beam power is deposited in the target and surrounding shielding, 30% in the decay pipe and 30% in the absorber.[77]

The polarity of the horns determines the sign of the focused hadrons and thus the running mode of the beam. When the horns focus positively charged mesons, the resulting secondary beam is dominated by ν_μ; this configuration is referred to as forward horn current (FHC) or neutrino mode. Reversing the horn polarity focuses negatively charged mesons and produces a beam dominated by $\bar{\nu}_\mu$, known as reverse horn current (RHC) or antineutrino mode. In both modes the focusing system provides a high-purity beam, with wrong-sign contamination in the oscillation energy region kept at the level of $\mathcal{O}(10\%)$ or below, and with intrinsic ν_e and $\bar{\nu}_e$ components at the percent level.[53, 68] The fluxes at the Far Detector for

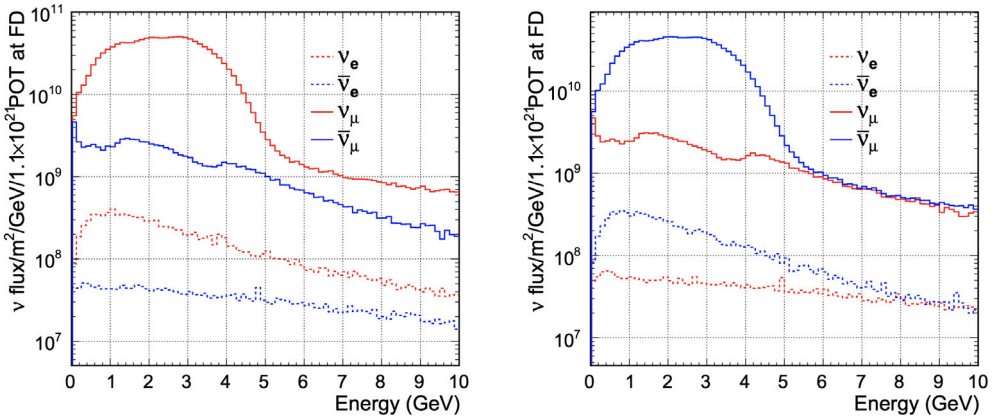

Figure 2.7: Predicted neutrino fluxes at the DUNE Far Detector for one year of operation with 1.1×10^{21} POT in forward horn current (neutrino) mode (left) and reverse horn current (antineutrino) mode (right). The contributions from ν_μ, $\bar{\nu}_\mu$, ν_e and $\bar{\nu}_e$ are shown separately. The spectra correspond to the nominal 1.2 MW LBNF beam at a 1300 km baseline. Figure from [53].

FHC and RHC operation, are shown in Figure 2.7.

2.3 Far detectors

The underground infrastructure that will host the DUNE Far Detector (FD) complex at the Sanford Underground Research Facility (SURF) in South Dakota consists of two large detector caverns, each designed to house two cryostats, and a central utility cavern for the cryogenics and services, as sketched in Figure 2.8.[52, 78] The FD complex sits about 1.5 km underground along a baseline of 1300 km from Fermilab.

Each FD module is a LArTPC installed inside a membrane cryostat. The cryostats have external dimensions of roughly 65.8 m (L) ×18.9 m (W) ×17.8 m (H) and internal dimensions of about 62 m × 15.1 m × 14 m, containing a total liquid-argon mass of ∼ 17 kt per module.[52, 66, 67] The caverns are sized to host up to four such modules, corresponding to a total liquid-argon mass of about 70 kt and a fiducial mass of at least 40 kt when all modules are instrumented.[70, 79]

The LArTPC technology was chosen for its excellent tracking and calorimetric performance and for its scalability to multi-kiloton volumes.[53] Charged particles produced in neutrino interaction final states ionize and excite argon atoms along their paths. The resulting ionization electrons are drifted in a uniform electric field towards anodes, while the de-excitation of argon dimers produces scintillation light

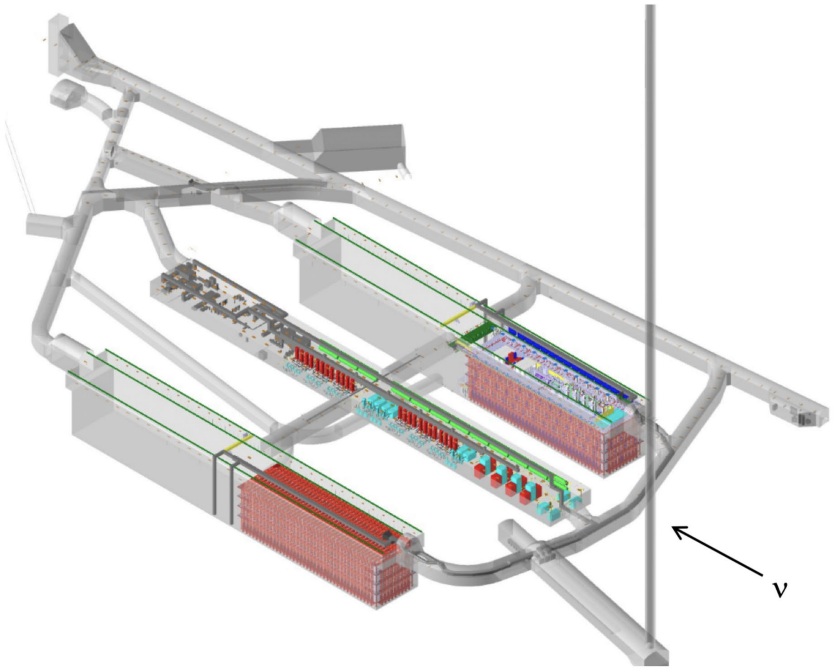

Figure 2.8: Three-dimensional view of the underground caverns at SURF hosting the DUNE far detector cryostats and cryogenic systems. Two large detector caverns accommodate up to four LArTPC modules, while a central cavern contains the cryogenic and support infrastructure. The arrow indicates the incoming neutrino beam direction. Figure from [52].

at ~ 128 nm. Dedicated photon detectors, based on X-ARAPUCA light collectors coupled to silicon photomultipliers (SiPMs), record this scintillation light. The prompt light signal provides an absolute time reference t_0, which, combined with the measured electron drift time, allows for reconstructing the coordinate along the drift direction. Together with the segmented anode readout in the transverse plane, this enables full three-dimensional reconstruction of neutrino interactions over an energy range extending from a few MeV to several GeV.[66, 67]

During Phase I, two single-phase LArTPC implementations will be employed in the FD: a horizontal-drift (HD) and a vertical-drift (VD) design.

Horizontal-drift design. In the HD configuration, the active volume is subdivided into four drift regions by alternating Anode Plane Assemblies (APAs) and Cathode Plane Assemblies (CPAs), arranged in an A–C–A–C–A pattern along the beam direction, as illustrated in Figure 2.9.[66] Ionization electrons drift hor-

izontally over distances of up to about 3.6 m towards the APA walls, guided by a field cage that surrounds the drift volumes on the top, bottom, and end walls. Each APA hosts four wire planes: an electrostatic grid, two induction planes and a collection plane. The induction wires are inclined at ±35°–40° with respect to the vertical, while the collection wires are vertical, as sketched in Figure 2.10.[66] The typical wire pitch is of order 5 mm, and the planes are closely spaced. Signals induced on the three instrumented wire planes provide three complementary two-dimensional projections, which can be combined to form a detailed three-dimensional image of the event with mm-scale granularity.

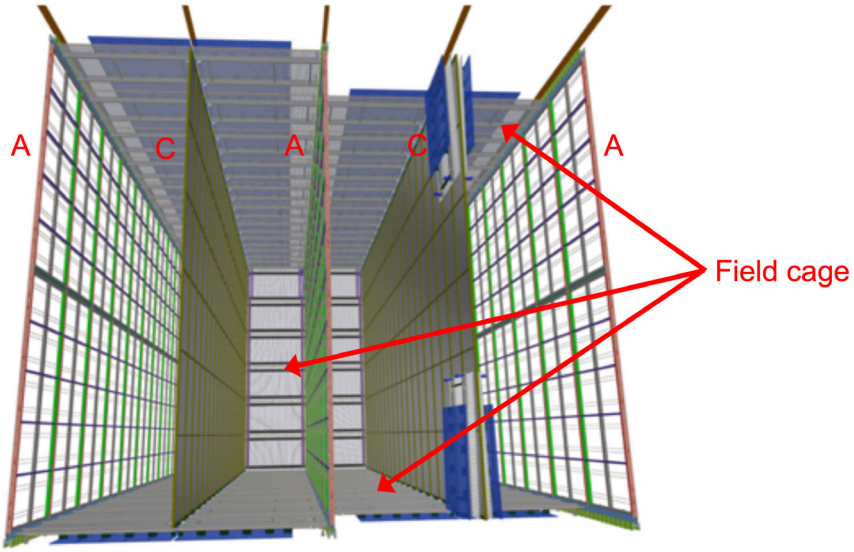

Figure 2.9: Layout for a horizontal-drift (HD) far-detector module. The active LAr volume is divided into four drift regions by alternating anode (A) and cathode (C) walls, with a surrounding field cage that shapes the electric field. Figure from [66].

Vertical-drift design. The VD configuration adopts a different field geometry to increase the maximum drift distance and to simplify the mechanical integration of the readout.[67] A horizontal cathode plane, realized with resistive panels, is suspended at mid-height of the active volume and divides the detector into two drift regions. In each region, ionization electrons drift over a vertical distance of about 6.25 m towards modular Charge Readout Planes (CRPs) located close to the top and bottom of the cryostat, as illustrated in Figure 2.11.

The anode is built from perforated printed-circuit-board (PCB) layers with copper strips arranged in two orthogonal views, providing two-dimensional charge readout with $\sim$ mm pitch.

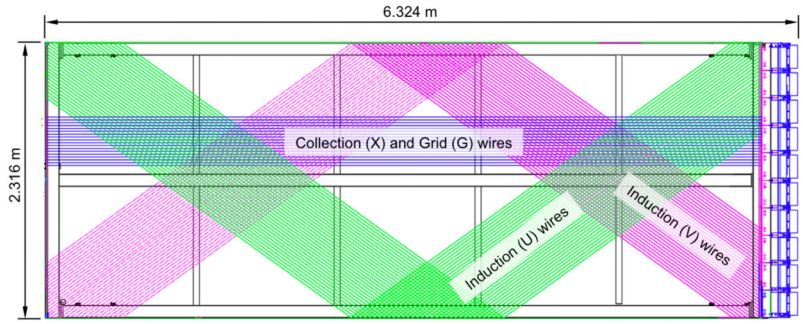

Figure 2.10: Schematic of an APA in the horizontal-drift design, showing the three wire views: induction U and V wires at ± angles with respect to the vertical, and the collection X (and grid G) wires. The overlapping wire planes provide three complementary projective views for three-dimensional reconstruction.[66]

As in the HD design, the VD module is equipped with a dedicated photon detection system that records the 128 nm argon scintillation light. In this case, X-ARAPUCA devices are installed on the central cathode plane and on the side walls (Figure 2.11), providing a uniform light coverage of the active volume and enhancing the sensitivity to low-energy events such as supernova and solar neutrino interactions[80, 81].

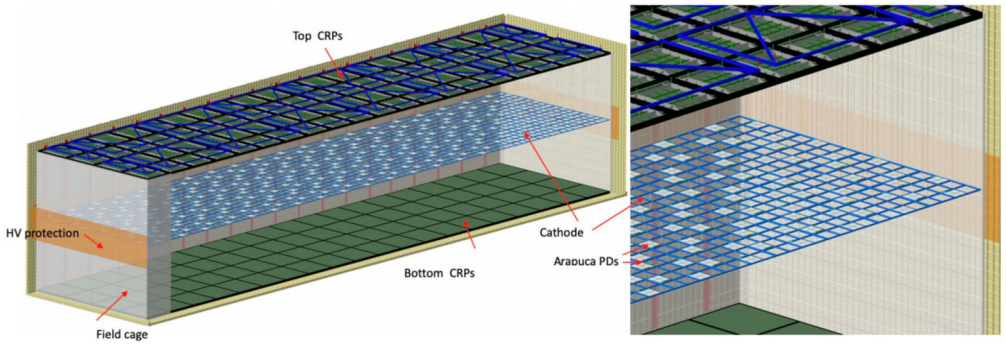

Figure 2.11: Conceptual design of a DUNE far-detector module based on the vertical-drift (VD) technology. A horizontal cathode divides the active liquid-argon volume into two drift regions. Ionization electrons drift vertically towards modular Charge Readout Planes (CRPs) located at the top and bottom of the cryostat. ARAPUCA photon detectors (PDs) are embedded near the cathode plane and on the walls to collect the scintillation light. Figure adapted from [67].

2.4 Near Detector

The DUNE ND complex will be located at Fermilab, about 60 m underground and approximately 574 m downstream of the neutrino production target in the LBNF beamline. ND will measure the energy spectrum and composition of the neutrino beam before oscillations develop both on-axis and at varying off-axis angles, and will provide high-precision inputs to the neutrino interaction model, through cross-section and final-state topology measurements.[68]

The ND complex consists of three complementary detectors:

- **ND-LAr**, a modular and optically segmented LArTPC with a pixelated charge readout based on the ArgonCube concept. [82] Using the same target nucleus as the FD and a similar detection technology reduces cross section and detector systematic uncertainties in the oscillation analysis when extrapolating to the FD.
- **TMS/ND-GAr**, a magnetized muon spectrometer directly downstream of ND-LAr to measure the energy and charge of the exiting muons. In Phase I, this role is covered by The Muon Spectrometer (TMS), in Phase II, will be replaced by ND-GAr, a magnetized high-pressure gaseous-argon TPC surrounded by an electromagnetic calorimeter, which, in addition, will provide further ν–Ar interaction measurements with capabilities that exceed those of ND-LAr due to the lower threshold for hadrons.[68]
- **SAND**, the System for on-Axis Neutrino Detection, a magnetized on-axis beam monitor that provides determination of the neutrino flux and performs cross-section measurements on different target nuclei, thereby further constraining the interaction model.[69] SAND design and physics program will be discussed further in Chapter 3.

Figure 2.12 illustrates the configuration of the ND hall for Phases I and II. In Phase I, ND-LAr and TMS are installed on a movable platform allowing the detectors to be moved up to 28.5 m off the beam axis, while SAND remains permanently on axis in a dedicated alcove. In Phase II, TMS is replaced by ND-GAr in the downstream position. A more detailed view of the Phase II hall layout is shown in Figure 2.13.

The capability of moving ND-LAr together with TMS/ND-GAr off-axis is known as DUNE-PRISM (Precision Reaction-Independent Spectrum Measurement). As the detectors move off-axis, the incident neutrino spectrum becomes narrower, and its mean energy decreases, approaching a quasi-monochromatic distribution. Off-axis measurements at different positions thus provide a set of neutrino beams

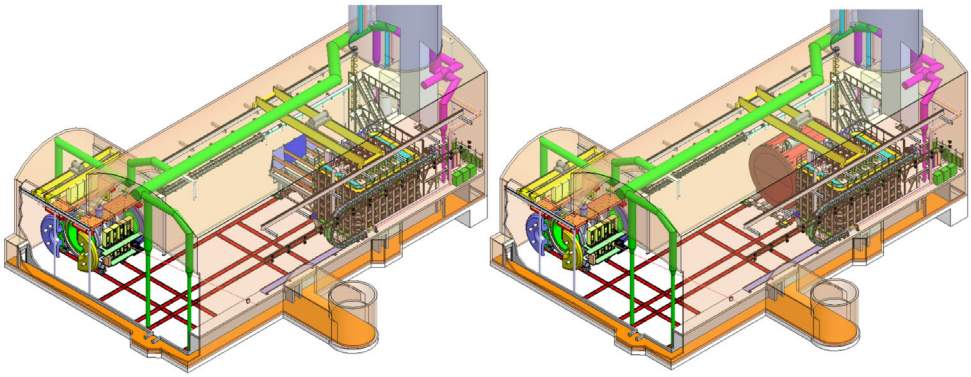

Figure 2.12: Schematic representation of the DUNE Near Detector complex in Phase I (left) and Phase II (right). In Phase I, the movable detectors are ND-LAr (front) and TMS (back), while SAND sits in an on-axis alcove. In Phase II, TMS is replaced by ND-GAr. The neutrino beam enters from the lower right. Figure adapted from Ref. [68].

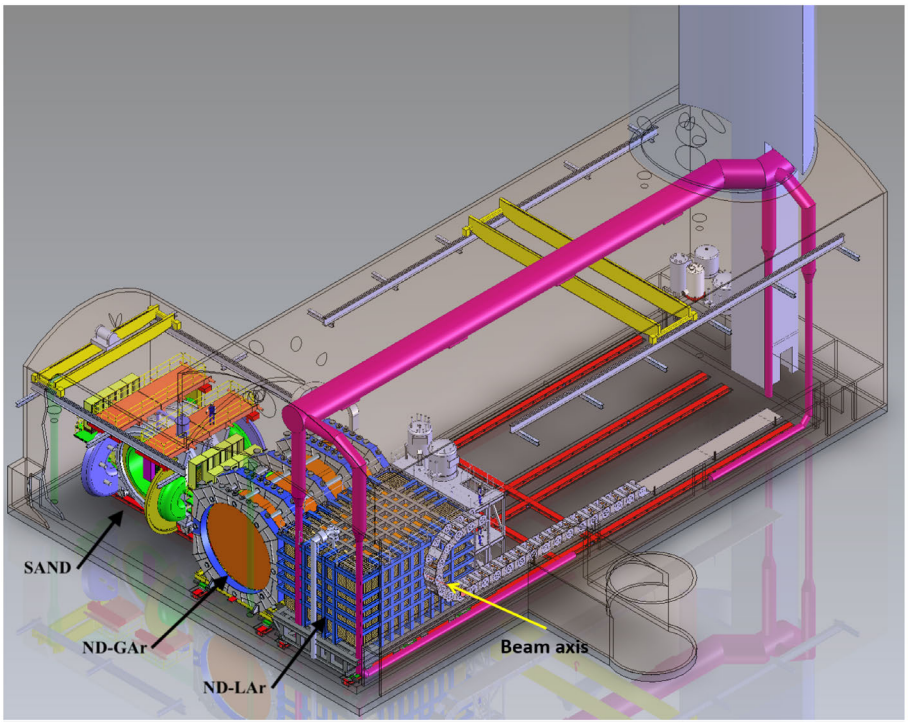

Figure 2.13: Representation of the ND hall in Phase II, showing ND-LAr, ND-GAr and SAND from right to left in the beam direction. Figure adapted from Ref. [68].

with different energy spectra, enabling a largely data-driven mapping between reconstructed and true neutrino energy. The muon–neutrino flux as a function of the off-axis angle is illustrated in Figure 2.14. By linearly combining the off-axis spectra, it is possible to make projections of near-detector samples that mimic the oscillated spectra at the FD, reducing the dependence on interaction models in the oscillation analysis.[83]

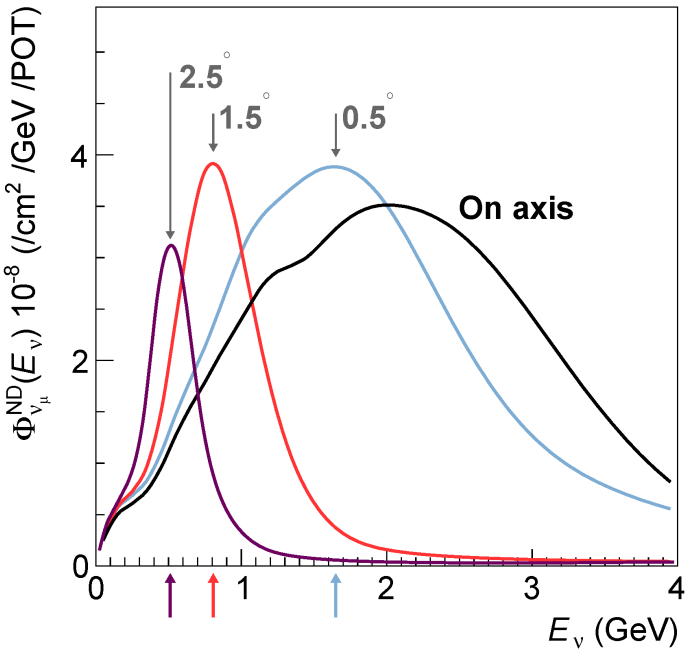

Figure 2.14: Predicted muon–neutrino flux at the ND for the on-axis configuration (black) and for off-axis positions corresponding to 0.5°, 1.5° and 2.5° with respect to the beam axis, illustrating the DUNE-PRISM concept. Figure from [68].

Apart from its primary role in the long-baseline oscillation analysis, the large neutrino interaction samples and the variety of detector technologies in the ND complex enable a rich physics program, including precision cross-section measurements and searches for heavy neutral leptons, dark photons, and other exotic signatures [54].

2.4.1 ND-LAr

ND-LAr is a modular LArTPC that provides a high-granularity, high-rate neutrino target based on the ArgonCube concept. [82] It consists of 35 optically isolated TPC modules arranged in a 7×5 matrix and housed in a common cryostat, resulting in an active volume of approximately $7 \times 5 \times 3$ m^3 and a fiducial mass

of about 67 t. A schematic view of a single ArgonCube module and its main components is shown in Figure 2.15.

Each module is further divided into two TPC volumes by a central cathode, yielding a total of 70 drift regions. The pixelated anode plane provides true three-dimensional charge readout with a pitch $\sim$ mm. At the same time, the optical system, based on segmented light collectors inside the drift volume, delivers precise event timing and helps to mitigate pile-up.

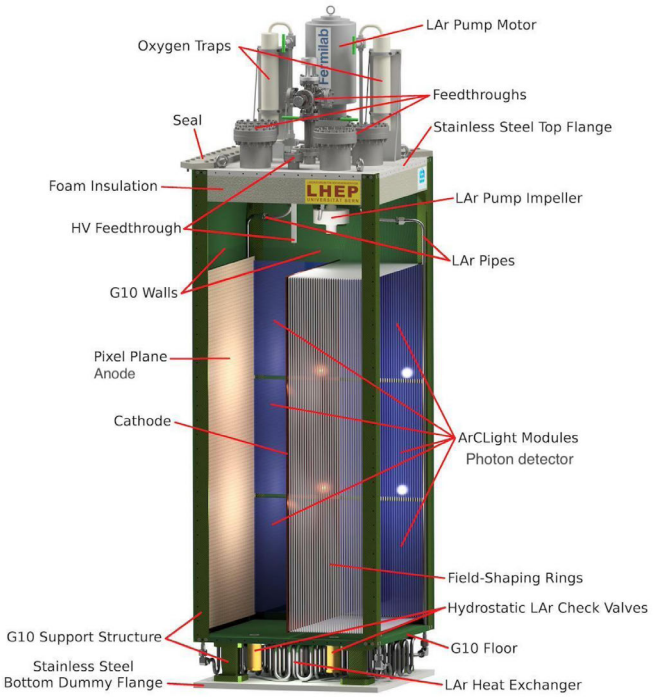

Figure 2.15: Detailed view of a single ArgonCube module used in ND-LAr, showing the main components. Figure from [82].

The modular design allows ND-LAr to deal with the high event rates at the ND location, of order 10^2 neutrino interactions per 10 μs spill.[68] With its transverse size, it can contain most of the hadronic activity produced in the neutrino interactions, while muons with momenta above 0.7 GeV typically exit the detector and are detected in the downstream spectrometer.

2.4.2 TMS and ND-GAr

A good reconstruction of the neutrino kinematics requires, in particular, a measurement of the momentum and charge of muons exiting ND-LAr. In DUNE Phase I, this is provided by The Muon Spectrometer (TMS), a magnetized steel

scintillator spectrometer installed immediately downstream of ND-LAr. Measuring range and curvature of muons that leave the ND-LAr volume, TMS extends the acceptance of ND-LAr and allows the combined system to reach a muon momentum resolution of order $\delta p/p \sim 5\%$ in the few-GeV region. [68] The information on the charge sign, unavailable in ND-LAr alone, is particularly important for the δ_{CP} measurement, especially in reverse horn current running, where there is a large contamination of neutrino interactions comparable to the desired antineutrino interactions.

TMS is composed of three longitudinal modules built from alternating layers of magnetized steel and plastic scintillator, as schematically illustrated in Fig. 2.16. The steel plates act both as an absorber and as a magnetic yoke, being magnetized by external coils mounted around the detector. Each scintillator module contains long strips arranged in two stereo views (U and V), providing segmented tracking information through the range stack. The muon momentum is primarily determined from the traversed thickness of steel, while the sign of the charge is obtained from the curvature of the track in the magnetic field. The scintillator readout supplies precise hit positions and energy deposits, which help identify stopping muons and refine the range-based momentum estimate.

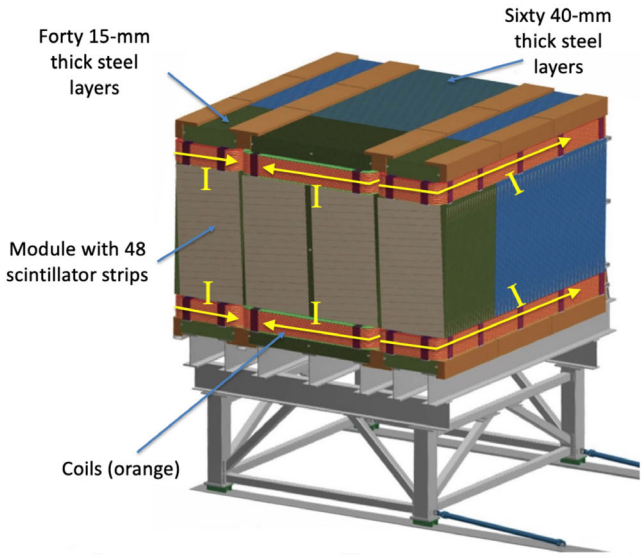

Figure 2.16: Schematic view of The Muon Spectrometer (TMS), highlighting its main components: magnetized steel absorber, scintillator modules and magnet coils. Figure adapted from Ref. [84].

In Phase II, where the uncertainties will no longer be dominated by the lack of statistics, systematic effects become more important, and DUNE design foresees

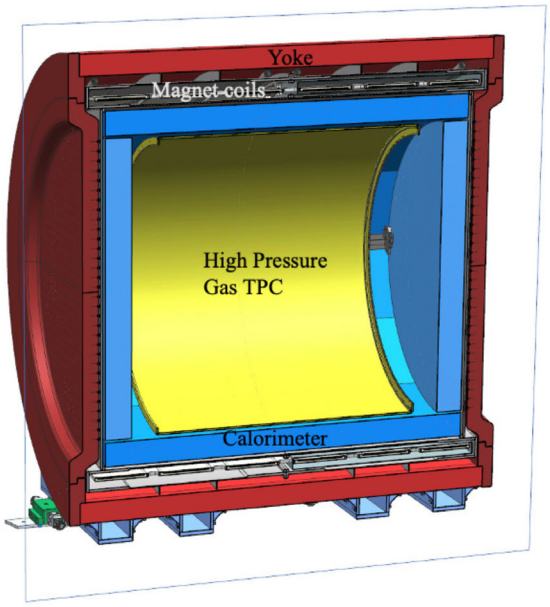

Figure 2.17: Cross section of the ND-GAr detector, showing the high-pressure gas TPC (HPgTPC) and the surrounding electromagnetic calorimeter. Figure from [70].

replacing TMS with a more capable downstream detector, ND-GAr, which also provides its own neutrino target. [70]

ND-GAr is a magnetized gaseous-argon detector based on a high-pressure gaseous-argon time-projection chamber (HPgTPC) surrounded by an electromagnetic calorimeter (ECAL), as shown in Figure 2.17. The HPgTPC operates at several tens of bars, so that charged particles leave ionization clusters while still having relatively long ranges. This configuration gives a very low momentum threshold and excellent tracking resolution for protons, pions, and muons. Combining precise curvature measurements in the magnetic field with dE/dx information in the HPgTPC and energy deposits in the ECAL, particle identification is performed, in particular for pion-proton separation and for distinguishing different hadronic final states.

ND-GAr will measure the charge and momentum of muons exiting the LAr target with improved resolution and lower systematic uncertainties compared to TMS. At the same time, neutrino interactions in the HPgTPC and ECAL provide an independent, high-precision sample on argon gas, with much lower tracking thresholds for hadrons than in a LArTPC. By combining measurements from ND-LAr and ND-GAr, DUNE will be able to constrain neutrino-argon interactions over a wide

energy range and significantly reduce flux and cross-section uncertainties.

2.4.3 PRISM

As discussed above, the DUNE-PRISM concept exploits the dependence of the neutrino energy spectrum on the off-axis angle of observation. The peak energy of the neutrino flux decreases, and the spectrum becomes narrower as the detector is moved to larger off-axis angles. Similar strategies have been used in other long-baseline experiments, such as T2K and NOvA experiments, to obtain a narrow-band beam centered on the oscillation maximum.[85, 86]

Within DUNE-PRISM, ND-LAr and the downstream muon spectrometer (TMS in Phase I, ND-GAr in Phase II) can be moved with respect to the beam direction transversely up to about 28.5 m, corresponding to off-axis angles of approximately 3°[68, 83]. Off-axis data at multiple positions provide a set of fluxes that can be linearly combined to approximate the full oscillated spectrum at the FD and to build near-detector samples with a peaked true neutrino energy. This approach allows the oscillation analysis to rely much more directly on data, with greatly reduced dependence on neutrino-nucleus interaction models.[83]

2.4.4 SAND

SAND will monitor the stability and the absolute normalization of the neutrino beam by continuously measuring the on-axis neutrino energy spectra. Because ND-LAr and its downstream spectrometer spend a significant fraction of the running time in off-axis positions during DUNE-PRISM data-taking, SAND provides a permanently on-axis reference. A stable and well-understood beam configuration and a rapid modeling of possible distortions are critical. SAND will also perform independent flux measurements and neutrino cross-section studies on different nuclei (argon, carbon, hydrogen), complementing ND-LAr and ND-GAr measurements and providing additional constraints on interaction models.

SAND will exploit the 0.6 T superconducting solenoid and the lead-scintillating fiber electromagnetic calorimeter from the KLOE experiment[69]. The inner magnetized volume hosts a low-density tracking system based on straw tubes as the default design, interleaved with thin passive targets, together with a liquid argon detector of about 1 t with an optical readout system that allows particle reconstruction using scintillation light called GRAIN.

2.4.5 Role of the Near Detector

To measure the oscillation probability $P_{\nu_\alpha \to \nu_\beta}(E_\nu)$ DUNE records neutrino interactions of different flavors as a function of the reconstructed energy in the Near and the Far Detectors, and infers the oscillation parameters from these event spectra. For both detectors, the observed number of events is a convolution of the neutrino flux, the interaction cross section, and the detector response. Many of the effects entering this convolution do not cancel simply between ND and FD, so a ratio of event rates is not sufficient to recover the oscillation probability.

The expected number of reconstructed ν_μ events in the ND and ν_x, with $x = e, \mu$, events in the FD, as a function of reconstructed neutrino energy E_{rec}, can be written as

$$N^{\text{ND}}_{\nu_\mu}(E_{\text{rec}}) = \int dE_\nu \, \Phi^{\text{ND}}_{\nu_\mu}(E_\nu) \, \sigma^{m}_{\nu_\mu}(E_\nu) \, R^{m,\nu_\mu}_{\text{phys}}(E_\nu, E_{\text{vis}}) \, R^{\text{ND}}_{\text{det}}(E_{\text{vis}}, E_{\text{rec}}), \tag{2.2}$$

$$N^{\text{FD}}_{\nu_x}(E_{\text{rec}}) = \int dE_\nu \, \Phi^{\text{FD}}_{\nu_\mu}(E_\nu) \, P_{\nu_\mu \to \nu_x}(E_\nu) \, \sigma^{\text{Ar}}_{\nu_x}(E_\nu) \, R^{\text{Ar},\nu_x}_{\text{phys}}(E_\nu, E_{\text{vis}}) \, R^{\text{FD}}_{\text{det}}(E_{\text{vis}}, E_{\text{rec}}). \tag{2.3}$$

The unoscillated flux at the FD is related to that at the ND through the flux ratio between near and far $R(E_\nu)$,

$$\Phi^{\text{FD}}_{\nu_\mu}(E_\nu) = R(E_\nu) \, \Phi^{\text{ND}}_{\nu_\mu}(E_\nu). \tag{2.4}$$

In these expressions:

- $\Phi(E_\nu)$ is the unoscillated neutrino flux. It is different at ND and FD because of the beamline geometry and, at the FD, the effect of oscillations. The ratio $R(E_\nu)$ can be constrained using hadron–production data and a detailed simulation of the beamline.
- $\sigma^{m}_{\nu_\mu}(E_\nu)$ is the interaction cross section for ν_μ scattering on the ND target material m (for example C, CH_2 or Ar), while $\sigma^{\text{Ar}}_{\nu_x}$ is the corresponding cross section on argon for the FD.
- $P_{\nu_\mu \to \nu_x}(E_\nu)$ is the oscillation probability, which is the quantity to be extracted from the data.
- $R_{\text{phys}}(E_\nu, E_{\text{vis}})$ is the physics response function. It describes how the true neutrino energy E_ν, target nucleus, and interaction mode translate into a visible final state with energy E_{vis}, including nuclear effects and final–state interactions. It is different for the various flavors, targets, and interaction channels.

- $R_{\mathrm{det}}(E_{\mathrm{vis}}, E_{\mathrm{rec}})$ is the detector response function, which maps the visible energy E_{vis}, that could in principle be observed in the detector, to the reconstructed energy E_{rec}, used in the oscillation analysis. This function differs between ND and FD because of their different designs and operating conditions.

Equations (2.2)–(2.4) make clear that even after taking into account the flux ratio between far and near, the simple ratio of reconstructed event spectra does not directly give the oscillation probability:

$$\frac{N^{\mathrm{FD}}_{\nu_x}(E_{\mathrm{rec}})}{N^{\mathrm{ND}}_{\nu_\mu}(E_{\mathrm{rec}})} \neq R(E_\nu)\, P_{\nu_\mu \to \nu_x}(E_\nu). \tag{2.5}$$

This is because the mapping between true and reconstructed quantities depends on the interaction channel, the target nucleus, and the detector, and is therefore different for the ND and FD. In addition, effects that can not be eliminated arise from backgrounds, intrinsic beam contamination, and the different acceptances of the two detectors. All of these must be modeled and constrained before comparing the spectra.

To fully exploit the FD statistics, DUNE must reduce the uncertainties from the flux prediction, the neutrino interaction model, and the detector response to the level of a few per cent, comparable to the FD statistical error for the expected exposure.[55, 68] Experience from current long–baseline experiments demonstrates that a near detector is essential, in fact, in the T2K experiment, the ND280 near detector constraint reduces the flux and interaction–model uncertainties on the far detector event prediction from about 11–14% to 2.5–4%[87]. In the NOvA experiment, the uncertainty on the ν_e appearance signal rate arising from cross–section modeling would be of order 12% without using the ND, but is reduced to about 5% once the near–detector data are included in the fit.[88, 68]

The DUNE Near Detector complex's primary role for oscillation physics is to perform high–statistics measurements of neutrino interactions on argon, matching the FD target, with a detector technology closely related to that of the FD. At the same time, the ND provides complementary measurements on other targets and with different detector technologies, which are essential to constrain interaction models and to study nuclear effects.

As the on–axis component, SAND (System for on-Axis Neutrino Detection) continuously monitors the neutrino beam and measures neutrino interactions on several targets (C, CH_2, Ar) with a different detector technology. By directly comparing data taken on different nuclei within the same beam, SAND helps to constrain

the flux prediction and to tune the interaction model, in particular, the nuclear effects in argon that are critical for extrapolating the ND constraints to the FD.

The PRISM concept addresses another key limitation: the strong dependence of the FD oscillation signal on the shape of the unoscillated flux. By moving ND-LAr and ND-GAr off-axis, DUNE can collect ND data sets with significantly different neutrino energy spectra. Linear combinations of these off–axis samples can be used to build effective ND spectra that approximate the oscillated FD flux for a wide range of oscillation parameters. This allows to reduce model dependence in the mapping from reconstructed observables to neutrino energy and to separately study flux and cross–section systematics.

The DUNE sensitivity to the neutrino mass ordering and to CP violation as a function of the years of data taking in Phase I is shown in Figure 2.18. In this configuration, the significance for determining the mass ordering reaches 5σ for all values of δ_{CP} with an exposure of about 70 kt $\cdot$ MW $\cdot$ years, corresponding to roughly 3–5 years of running depending on the beam scenario. For a maximally CP–violating phase $\delta_{\mathrm{CP}} = -\pi/2$ in the Phase I configuration a CP–violation sensitivity of about 3σ with an exposure of $\sim$ 100 kt $\cdot$ MW $\cdot$ years is reached, corresponding to approximately 4–6 years. These results are consistent with the sensitivities as a function of exposure discussed in Section 2.1.1 and shown in Figures 2.3 and 2.4: exposures of a few hundred kt·MW·years achievable in the full Phase II configuration, provide a 5σ determination of the mass ordering and a 3–5σ discovery of CP violation for a large fraction of the δ_{CP} parameter space. Extending the CP–violation discovery reach to such a large fraction of δ_{CP} values therefore requires the Phase II configuration with limited systematics. In Phase II a high performance near–detector complex, including ND-GAr, becomes essential to control flux and cross–section systematics and to reach the CP–violation physics goals of DUNE.[55, 54, 68]

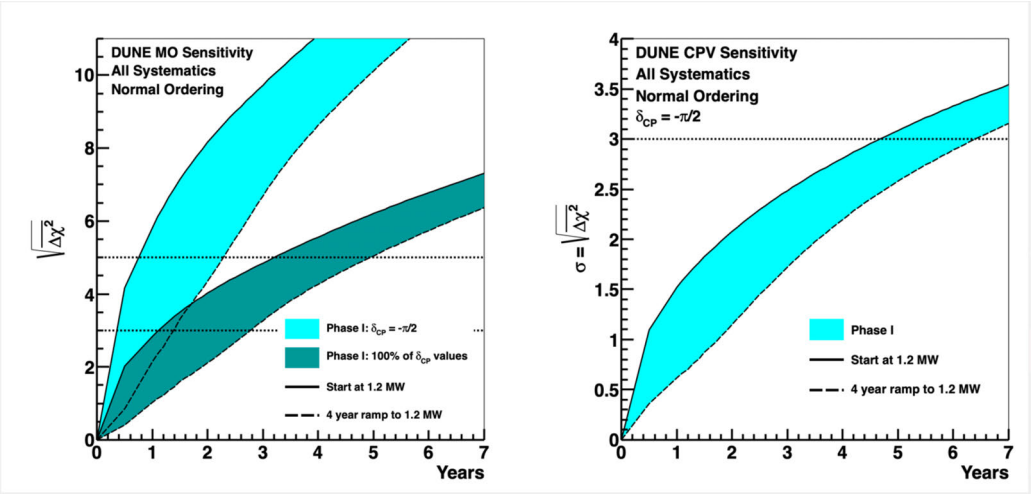

Figure 2.18: Expected DUNE Phase I sensitivity to the neutrino mass ordering (left) and to CP violation for $\delta_{\mathrm{CP}} = -\pi/2$ (right) as a function of years of data taking, from [54]. The light-blue bands show the sensitivity for $\delta_{\mathrm{CP}} = -\pi/2$; in the left panel the darker band indicates the sensitivity required to cover 100% of possible δ_{CP} values. The width of each band reflects different assumptions on the beam power. The solid line corresponds to starting immediately at the nominal 1.2 MW beam power, while the lower dashed line assumes a 4-year ramp to the same power. Horizontal lines at 3σ and 5σ show the discovery thresholds.

Chapter 3

SAND - System of on-Axis Neutrino Detection

The System for on-Axis Neutrino Detection (SAND) is one of the three components of the DUNE Near Detector complex, and is the only one permanently located on the beam axis. From this position, SAND continuously monitors the beam, providing a high-precision measurement of the spectra and detecting beam variations. When ND-LAr and ND-GAr are in off-axis positions, as part of the DUNE-PRISM program, SAND records the on-axis flux, diagnosing changes caused by beamline parameters and cross-checking flux predictions used in the oscillation analysis.

SAND is a multipurpose detector capable of precision tracking and calorimetry and can record neutrino interactions on a variety of target materials, including argon, carbon, and hydrocarbons (CH_2). The detector volume is surrounded by a 0.6 T superconducting solenoidal magnet, originally operated in the KLOE experiment at the DAΦNE ϕ-factory at INFN LNF.[89] Within the magnetic volume, SAND houses a lead-scintillating fiber electromagnetic calorimeter (ECal), also from KLOE, together with with an inner tracking and target system and a compact liquid-argon detector (GRAIN). The magnet and ECal together provide an almost 4π hermetic, instrumented volume with well-understood performance, while the inner tracker is tailored to the DUNE Near Detector physics program, balancing the need for a large target mass with that for good detector resolution. A sketch of the detector can be found in Figure 3.1

The standard design for the inner tracker of SAND is a low-density straw-tube target tracker (STT). The STT is composed of modular units that combine thin passive targets with four planes of small-diameter straw tubes arranged in an XXYY configuration. In each module, the first two planes (X views) have straws oriented parallel to the y axis and measure the x coordinate, while the following two planes (Y views) have straws rotated by 90° and measure the y coordinate. The duplicated X and Y views provide a two-dimensional view with redundancy, improving pattern recognition and spatial resolution. The targets are composed of different materials, allowing the possibility of using many nuclear targets beyond argon, in particular graphite and plastic (CH_2), so that interactions on several

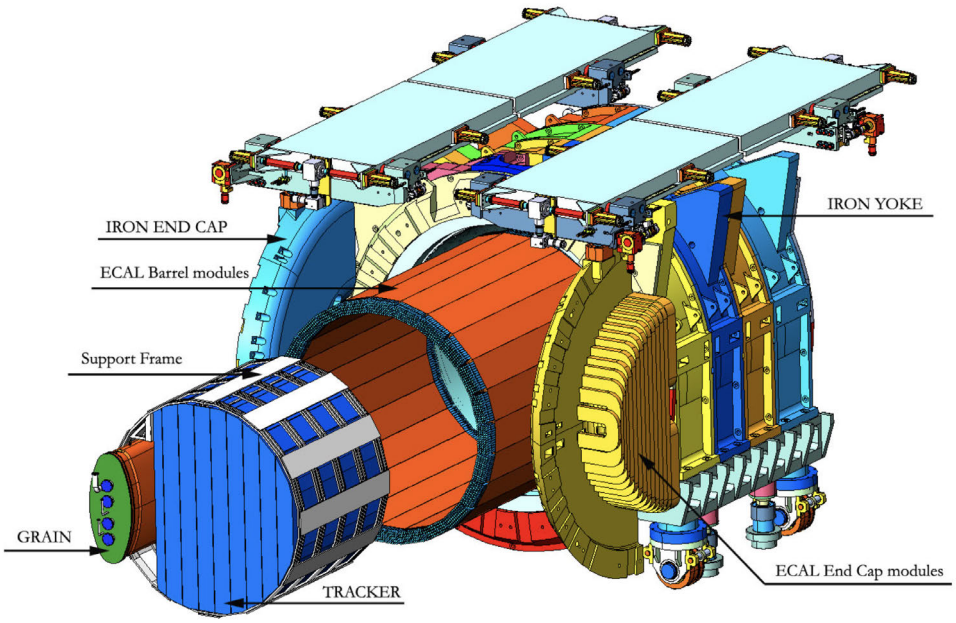

Figure 3.1: Exploded engineering view of the SAND detector. The main components are shown: GRAIN, the inner tracker with the targets, the surrounding electromagnetic calorimeter (ECal) with both barrel and endcap modules, and the iron yoke.

nuclei, including hydrogen, can be studied within the same detector. The low density of the tracker limits multiple scattering while maintaining sufficient target mass, and the high granularity of the straw geometry provides tracking with sub-millimeter spatial resolution and a few-percent momentum resolution for charged particles.

A drift-chamber tracker with a reduced number of channels is being investigated as an alternative option for the inner tracker. This configuration uses planes of sense wires separated by thin mechanical supports, providing a complementary technology with different systematic uncertainties and material budget, while maintaining the ability to employ various nuclear targets. The final layout will balance these options to optimize tracking performance, target mass, and control of systematic effects.

A dedicated LAr active target is located upstream of the target, known as GRAIN (GRanular Argon for Interactions of Neutrinos). GRAIN is a $\mathcal{O}(1\ \mathrm{t})$ liquid-argon detector that exploits a novel optical readout concept: neutrino interactions are reconstructed using scintillation light collected by SiPM-based cameras, rather

than by the drift of charge typical of the time-projection chamber detector. This approach is tuned to the high event rates expected at the Near Detector and offers excellent timing capabilities, high-rate operation in a magnetic field and a compact cryostat design. GRAIN provides an on-axis argon target that is permanently available for cross-calibration with ND-LAr and for dedicated measurements of neutrino-argon interactions, reducing flux and interaction-model systematics [90].

Beyond its beam-monitoring role, SAND is designed to independently measure the neutrino flux using many methods described in Section 3.2, to provide high-statistics measurements of neutrino interactions on argon, hydrogen, carbon, and composite targets, and to constrain nuclear effects and final-state interactions that enter the oscillation analysis. Furthermore, the low-density tracking region and excellent timing open opportunities for searches for physics beyond the Standard Model, such as heavy neutral leptons and other exotic signatures, making SAND a key element of the DUNE Near Detector physics program. [68, 69]

3.1 Design

3.1.1 Superconducting magnet and iron return yoke

The SAND detector exploits the superconducting solenoid and iron return yoke originally deployed in the KLOE experiment. The system was designed to provide a uniform axial field of 0.6 T over a cylindrical tracking volume about 4.3 m long and 4.8 m in diameter, surrounding the central tracking and ECal detectors. The main magnet specifications are summarized in Table 3.1.

The superconducting coil is housed in an aluminum cryostat and cooled with liquid and gaseous helium using a thermo-siphon circuit. It operates at a nominal current of 2902 A, corresponding to a stored energy of 14.3 MJ. The iron return yoke, with a total mass of 5×10^2 t, surrounds the cryostat and provides both the magnetic return path and mechanical support for the ECal modules. It is divided into a barrel and two endcaps, segmented to allow opening for detector installation and maintenance.

The magnetic field was mapped before the KLOE operation, indicating that the longitudinal component, $B_z \simeq 0.6$ T, is nearly uniform over the central tracking volume, and drops steeply beyond the ends of the coil, in the region where the field lines close inside the endcap iron and return yoke.

Table 3.1: Main specifications of the SAND superconducting magnet. [91].

Central magnetic field	0.6 T
Useful field volume (L × D)	4.3 m × 4.8 m
Vacuum case length	4.4 m
Vacuum case inner diameter	4.86 m
Cold mass	10 t
Iron return yoke mass	$\sim 5 \times 10^2$ t
Stored energy at full field	14.3 MJ

3.1.2 Electromagnetic calorimeter

The SAND electromagnetic calorimeter (ECal) is a lead–scintillating–fiber sampling calorimeter, reused from the KLOE detector operating at INFN - Laboratori Nazionali di Frascati in Italy.[89] It surrounds the SAND inner volume inside the superconducting solenoid and iron yoke (Section 3.1.1), providing almost 4π coverage. An overview of the ECal detector is given in Figure 3.2, where in panel (a) a photograph of one of the two endcap side open showing the inner volume and the barrel modules can be seen, while panel (b) displays a sketch of the vertical cross section of the detector geometry.

3.1.2.1 Geometry and segmentation

The calorimeter is composed of a cylindrical barrel and two endcaps. The barrel consists of 24 modules with a trapezoidal cross-section, located on the inner wall of the coil cryostat. Each barrel module is 4.3 m long, 23 cm thick corresponding to about $15\,X_0$ and the inner diameter of the barrel volume is about 4 m. The two endcaps, each consisting of 32 "C-shaped" modules of different widths, are mounted on the movable end doors of the iron yoke, thus providing access to the inner detector volume.

Scintillating fibers run parallel to the cylinder axis for the length in the barrel modules, and almost completely perpendicular to it in the endcaps, so that for neutrino interactions originating inside the inner tracker in which final state particles are predominantly forward-going along the beam direction, this geometry still ensures that clusters in the ECal cross the fibers largely transversely for most of the solid angle, limiting channeling effects and reducing sampling fluctuations.

Each module is segmented transversely into cells of roughly 4.4×4.4 cm^2, grouped into five planes along the radial direction. The first four layers have a thickness of about 4.4 cm, while the outermost plane is slightly thicker ($\sim$ 5.2 cm). The full calorimeter comprises 2440 cells, each read out at both ends, for a total of 4880

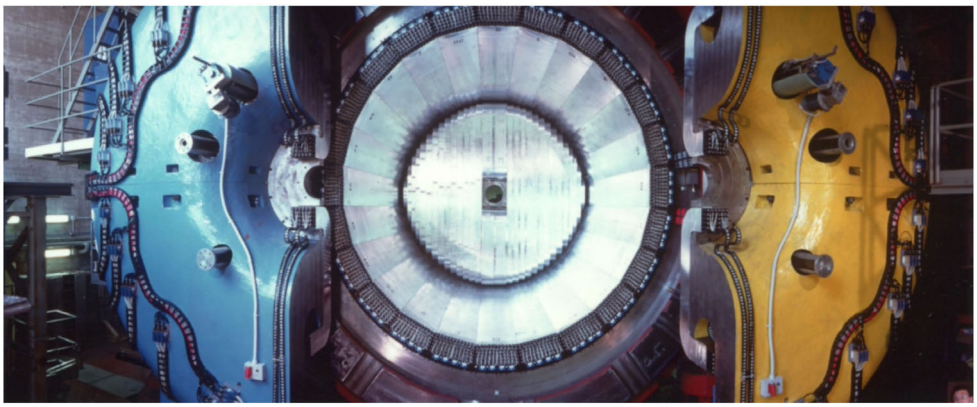

(a) Photo of the detector showing the two end doors of the iron return yoke (blue and yellow) that close around the inner volume, the superconducting solenoid cryostat is also visible. The endcap is open, showing barrel modules running for the detector length. Photo from the KLOE collaboration.

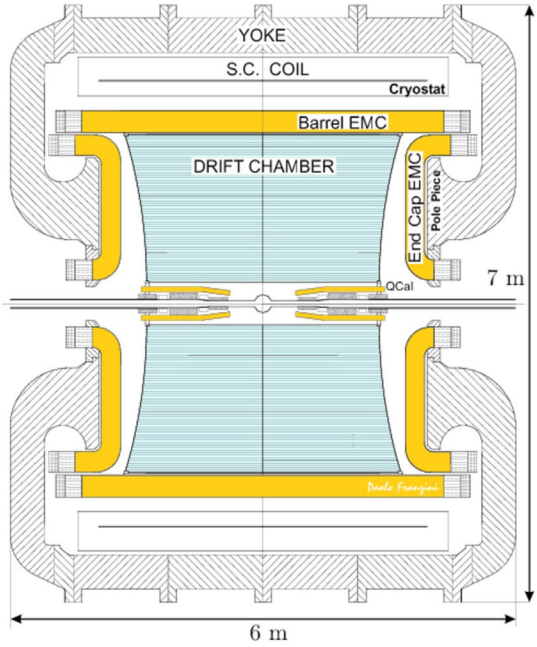

(b) Vertical cross section of the KLOE configuration, showing the KLOE drift chamber configuration, surrounded by the barrel and endcap ECal modules inside the superconducting coil and iron yoke.

Figure 3.2: Overview of the ECal detector: (a) photograph of the apparatus and (b) schematic cross-section highlighting the position of the ECAL with respect to the tracker and magnet.

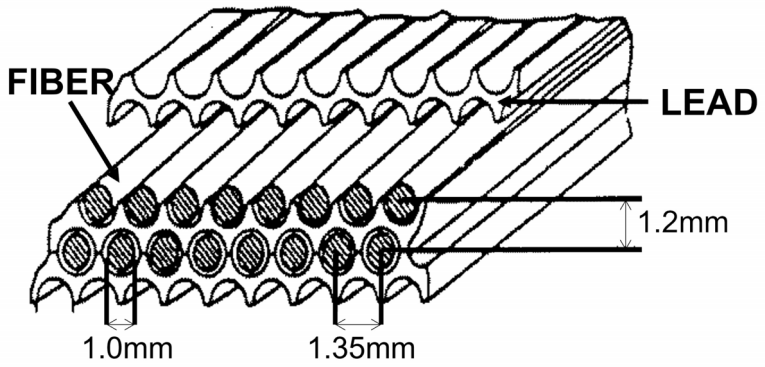

Figure 3.3: Schematic view of the sampling structure of an ECal module. Alternating layers of grooved lead foils and 1 mm-diameter scintillating fibers are shown with the pitch and dimensions of the scintillating fibers.

electronic channels. Barrel modules provide 60 channels per side, while endcap modules have 10, 15, or 30 channels per side, depending on their width.

3.1.2.2 Sampling structure and scintillating fibers

The internal structure of an ECal module consists of about 200 layers of 1 mm-diameter plastic scintillating fibers between 200 grooved lead foils of 0.5 mm thickness. The grooves on the two faces of each foil are shifted by half a pitch so that the fibers lie at the vertices of quasi-equilateral triangles of side ~ 1.35 mm (Figure 3.3). This geometry results in an almost uniform fiber distribution and mechanical stability of the composite structure.

The volume ratio of fiber:lead:glue is approximately 48 : 42 : 10, yielding an average density of about 5 g/cm^3 and an effective radiation length $X_0 \simeq 1.5$ cm. The total thickness of a module corresponds to roughly $15\,X_0$. [92] The thinness of the individual lead foils ($\lesssim 0.1\,X_0$) ensures a high conversion probability and good efficiency also for low energy photons.

Two types of scintillating fibers are used in the calorimeter (Kuraray SCSF-81 and Pol.Hi.Tech 0046), with a total length of about 1.5×10^4 km. The Kuraray fibers, which have slightly higher light yield and longer attenuation length, are installed in the inner half of the modules, while the Pol.Hi.Tech fibers are used elsewhere. Typical attenuation lengths are 3–5 m, and the light yield is of the order of one photoelectron at the photomultiplier for a 1 mm path length in a single fiber at a distance of 2 m from the readout. The emission spectrum peaks around $\lambda \simeq 460$ nm, well matched to the quantum efficiency of the photomultiplier

tubes employed.[89]

3.1.2.3 Optical readout and photomultiplier tubes

Fibers belonging to a given cell are optically coupled to light guides at each end of the module, so that the cell segmentation is defined by the readout only. The fibers from each cell terminate on a light guide, which is shaped to match the square cell area to the circular photocathode of the photomultiplier, ensuring efficient optical coupling. The light guides reduce the effective area by about a factor of four, while still transmitting more than 80% of the collected light. The arrangement of the photomultiplier tubes at the end of a barrel module, together with the routing of the high-voltage and signal cables, is shown in Figure 3.4.

Figure 3.4: View of one end side of an ECal barrel module showing the array of photomultiplier tubes. Photo from [93].

Each calorimeter cell is read out by a fine-mesh photomultiplier tube (Hamamatsu R5946/01, 1.5″ diameter), chosen for its ability to operate in the magnetic field of the SAND solenoid with only a modest gain reduction[89].

3.1.2.4 Performance and calibration

In KLOE, the calorimeter calibration was based on a combination of cosmic-ray muons, Bhabha events, and tagged photons and electrons from radiative and hadronic ϕ decays. The energy resolution for photons and electrons was parameterized as

$$\frac{\sigma_E}{E} \simeq \frac{5.7\%}{\sqrt{E\,[\mathrm{GeV}]}} \oplus b, \qquad b \lesssim 1\%, \tag{3.1}$$

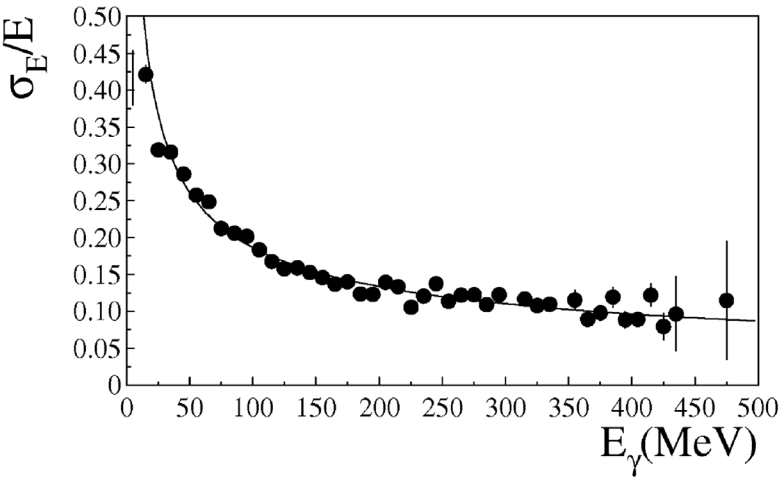

Figure 3.5: Energy resolution of the KLOE electromagnetic calorimeter for photons as a function of the incident photon energy E_γ. The points show data from test beams and in-situ calibrations; the curve represents a fit of the form $\sigma_E/E = (5.7\%)/\sqrt{E_\gamma\,[\mathrm{GeV}]} \oplus b$ with a small constant term b. Figure from [89].

while the time resolution could be written as

$$\sigma_t(E) \simeq \frac{57 \text{ ps}}{\sqrt{E\,[\mathrm{GeV}]}} \oplus 100 \text{ ps}, \tag{3.2}$$

where E is the deposited energy in the calorimeter. [89] Figure 3.5 shows the measured σ_E/E for photons as a function of the incident photon energy E_γ together with a fit of the form in Eq. (3.1). This result as been used in Chapter 5 as the reference for the comparison with the energy resolution obtained for SAND configuration from dedicated simulations of electron particle guns and from neutrino interactions.

The electromagnetic energy resolution for the SAND configuration has been evaluated with the new reconstruction chain, and it is presented in Chapter 5. There, electron-gun samples and the Monte Carlo backtracking clusters are used to derive an active-to-total calibration factor and to measure the stochastic and constant terms of σ_E/E for neutrino interactions. The fit is found to be close to the KLOE one, as discussed in Subsection 5.6.

The response of a KLOE calorimeter prototype to neutrons with kinetic energies between 22 and 174 MeV was also measured in a dedicated test beam at The Svedberg Laboratory, using a single KLOE-like Pb–Pb-scintillating fiber module prototype, read out by two photomultipliers on each side. The two signals on

a given side were summed and discriminated, and a neutron was detected when the analog sums on both sides of the module exceeded a threshold expressed in electron–equivalent energy.[94] In these conditions, the overall neutron detection efficiency of the prototype was found to be of order 30–50%, depending on neutron energy and threshold. This efficiency is significantly larger than the expectation from scintillator thickness alone. In fact, a lead-scintillation fiber calorimeter, neutrons interact predominantly in the lead absorber, producing secondary charged particles. These secondaries then enter the scintillating fibers and deposit visible energy, effectively increasing the probability that a neutron interaction leads to a detectable signal in the active material.

The corresponding Monte Carlo hit and reconstructed cluster-level neutron efficiencies in the new configuration of the SAND ECal are evaluated in this thesis in Chapter 6. Using a full detector Monte Carlo with realistic geometry, upstream tracker-target material, digitization, and thresholds as described in Chapter 4, the ECal shows a Monte Carlo hit efficiency of about 77% and a reconstructed-cluster efficiency of about 30% for final-state neutrons in the 100–1000 MeV range arising from neutrino interactions by the LBNF beam. In this analysis, a calorimeter cell is required to be complete, that means to have both photosensors above the discriminator threshold, and only clusters built from complete cells are considered, so cells with only one photo-signal above threshold are discarded. The KLOE test-beam measurement, instead, corresponds to an efficiency based on the analog sums of the signals and does not impose any per-cell completeness requirement. The SAND cluster efficiency is therefore consistent with the KLOE test-beam results once the more restrictive clustering conditions and realistic photo-sensor thresholds are taken into account.

Per-cell reconstruction of position, time and energy. The three-dimensional position of a signal in a calorimeter cell is reconstructed by combining the position of the fired cell in the transverse plane of the module with the difference between the signal arrival times at the two ends of the module for the longitudinal coordinate along the cell length. For each fired cell, two time-to-digital converter (TDC) measurements $T_{A,B}$ and two analog-to-digital converter (ADC) amplitudes $S_{A,B}$ are recorded from the photomultipliers located at the ends of the fibers. The TDC counts are converted into times via calibration constants $c_{A,B}$ and time offsets $t^0_{A,B}$:

$$t_A = c_A\, T_A + t^0_A, \qquad t_B = c_B\, T_B + t^0_B. \tag{3.3}$$

The corresponding simulation of the digitized signal is described in Section 4.2.

Taking the center of the module as $s = 0$, the coordinate s along the module length, and the signal hit time t is reconstructed as

$$s = \frac{v_{\text{fiber}}}{2}\left(t_A - t_B\right), \tag{3.4}$$

$$t = \frac{1}{2}\left(t_A + t_B\right) - \frac{L}{2v_{\text{fiber}}}, \tag{3.5}$$

where L is the cell length and v_{fiber} the effective light propagation speed in the fibers. The other two coordinates are given by the known geometrical center of the cell in the transverse plane (projected along y, z for barrel cells and x, z for endcap cells). In the clustering algorithm developed in this work in Chapter 5, the same procedure for reconstruction of the time and position is implemented.

For each cell, the photomultiplier amplitudes $S_{A,B}$ in ADC counts are converted into energies after pedestal subtraction and calibration. Denoting by $S_{0,i}$ the zero-offset (pedestal) and by $S_{M,i}$ the response to a minimum ionizing particle crossing the center of cell i, the energy measured on side A of cell i can be written as

$$E_{A,i}(\text{MeV}) = \left(S_{A,i} - S_{0,i}\right)\,\frac{k_E}{S_{M,i}}\,\frac{1}{A_l(d_A)}, \tag{3.6}$$

and analogously for $E_{B,i}$. Where k_E is the global energy-scale factor (MeV per MIP deposition) determined from electrons and photons of known energy, and $A_l(d_A)$ is the attenuation factor along the light path d_A, measured as in Equation (4.2), obtained from dedicated attenuation measurements. The cell energy is then taken as the average of the two sides,

$$E_i = \frac{1}{2}\left(E_{A,i} + E_{B,i}\right). \tag{3.7}$$

From the separated measurements, an average number of about 35 photoelectrons per PMT is obtained for a minimum ionizing particle crossing the module center, corresponding to a light yield of approximately 1 photoelectron per MeV of deposited energy at the module center.[89]

The digitization and reconstruction chain adopted for the SAND simulations in Chapters 4 and 5 follow the same structure. In the digitization step (Section 4.2), the deposited energy dE of each `edep-sim` hit in a cell is converted into a mean number of photoelectrons on each side via

$$\mu_{pe}^{A,B} = dE\, A_l(d_{1,2})\, E_{pe}, \tag{3.8}$$

where A_l is the attenuation factor of Equation (4.2) and E_{pe} is set such that a

MIP crossing the module center yields $\simeq 1$ photoelectron per MeV, consistent with the KLOE measurement.

The actual number of photoelectrons is then Poisson-fluctuated and converted to ADC counts as

$$S^{A,B} = N_{pe}^{A,B} \times ADC_{\text{photo-electron}}, \tag{3.9}$$

with $ADC_{\text{photo-electron}} = 4$. Pedestals on the ADC amplitudes are not simulated, so that $S_{0,i} = 0$ by construction, and a single $ADC_{\text{photo-electron}}$ is an already scaled for a MIP response $S_{M,i}$.

The electronic and photo-sensor time uncertainty is instead included in the digitization through the Gaussian smearing term Gauss(1 ns) in Equation (4.3), which models a 1 ns timing jitter on the TDC measurement.

In the clustering reconstruction (see Section 5.1), the digitized amplitudes are converted back into energy following the same structure of Equations (3.6)–(3.7). For a complete cell with ADC values $(\mathrm{S}_A, \mathrm{S}_B)$ and attenuation factors $A_l(d_{A,B})$, the reconstructed energy is

$$E = \frac{1}{2}\left(\frac{\mathrm{S}_A}{A_l(d_A)} + \frac{\mathrm{S}_B}{A_l(d_B)}\right) \Bigg/ \left(f_{\text{att,tot}}\, E_{pe}\, \text{peADC}\right), \tag{3.10}$$

where E_{pe} is the light yield in photoelectrons per MeV, peADC is the number of ADC counts per photoelectron and $f_{\text{att, tot}}$ is the active–to–total correction factor that is discussed in Section 5.5.

3.1.3 The GRAIN detector

GRAIN (GRanular Argon for Interactions of Neutrinos) is a $\mathcal{O}(1\ \text{t})$ liquid-argon target designed to be installed upstream of the tracking system, as illustrated in Figure 3.6. GRAIN will measure ν-Ar interactions for nuclear-effect studies, and it will also act as a complementary argon target for cross-calibration with the other near-detector detectors. Being subject to different systematics than ND-LAr, GRAIN will contribute in an independent way to constrain the neutrino flux and neutrino-argon cross sections.

The GRAIN cryostat consists of an inner vessel, containing the liquid argon, housed inside a vacuum vessel that provides thermal insulation and mechanical support, both with an elliptical transverse shape. The inner vessel is fabricated from stainless steel and has an elliptical cross-section with axes of approximately 49 cm and 148 cm and a longitudinal length of 150 cm. The vacuum vessel operates at room temperature and is built as a carbon-fiber reinforced plastic

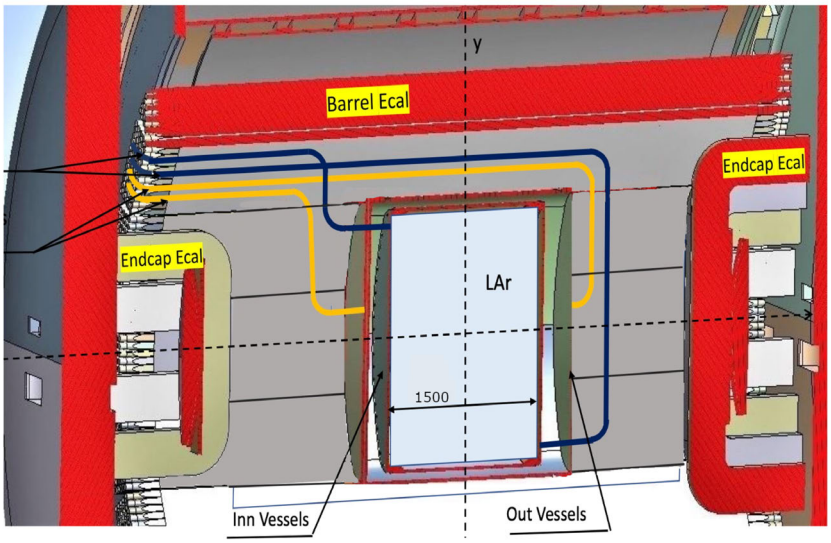

Figure 3.6: Cross-section view of the GRAIN cryostat inside the magnetic volume of SAND. GRAIN is installed upstream of the tracker, in proximity to the ECal barrel (see Figure 3.1).

sandwich around a Nomex honeycomb core, with an aluminum inner liner to ensure vacuum tightness. The elliptical geometry has been chosen to follow the curvature of the SAND barrel ECal, allowing efficient use of the available space and reducing the amount of passive material between GRAIN and the surrounding calorimeter. A sketch of GRAIN can be found in Figure 3.7.

If GRAIN were sufficiently thin along the neutrino beam axis, particles produced in ν-Ar interactions would typically exit the LAr volume, and their momenta could be reconstructed downstream by the tracker. However, the cryostat must contain approximately 1 ton of liquid argon, implying a thickness of several tens of centimeters in the beam direction. On the other hand, low-energy particles that stop in the LAr or in the cryostat walls, as well as particles exiting at large angles with respect to the beam, often fall outside the tracker acceptance. This leads to potential biases in topological selection and to missing energy in the neutrino reconstruction.

To mitigate these effects, the LAr volume in GRAIN will be actively instrumented with arrays of silicon photomultipliers (SiPMs) coupled to dedicated optical systems. The light readout provides a precise time reference for the interaction and a calorimetric measurement of the total energy deposited in the target. Two R&D programs are underway to develop an optical imaging system capable of reconstructing tracks and interaction vertices from scintillation light. GRAIN is

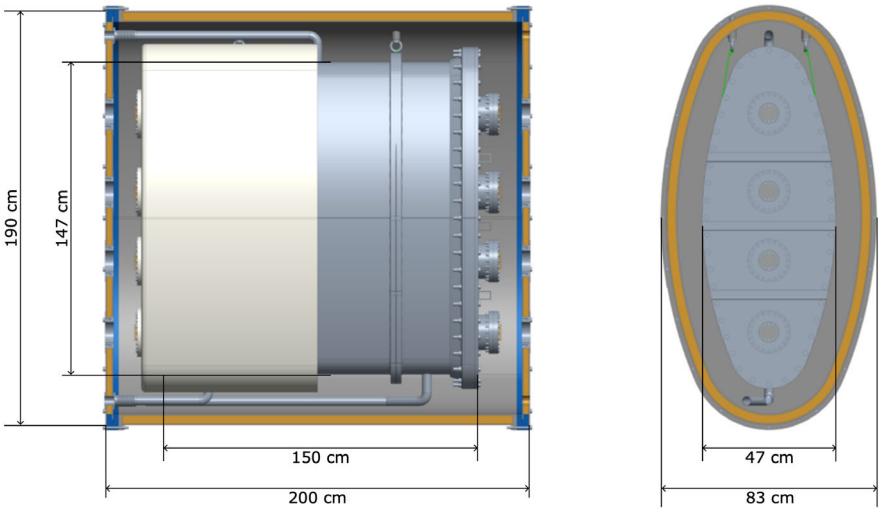

Figure 3.7: Engineering model of the GRAIN cryostat. Left: longitudinal section. Right: transverse elliptical cross-section. The inner vessel (light gray) contains the 1 t LAr volume, while the vacuum vessel (orange) provides vacuum insulation. The overall external dimensions are about 2.0 m (length), 1.9 m (height), and 0.83 m (width).

instrumented with imaging cameras based on matrices of cryogenic SiPMs, read out by a dedicated ASIC. Each camera combines a finely segmented SiPM focal plane with an optical system that projects the three-dimensional light distribution in the LAr volume into a set of two-dimensional images.

Two complementary imaging technologies are under study: lens-based cameras and coded aperture mask cameras [90]. In the lens-based option, shown in Figure 3.8, scintillation photons are focused onto the SiPM matrix by a VUV lens system. The current design employs a doublet of plane–convex fused-silica lenses with an effective diameter of 60 mm and a focal length of about 9 cm in xenon-doped LAr, which shifts the emission wavelength from 127 nm to $\sim$ 174 nm and improves the lens transmissivity.

In the alternative coded-aperture mask option, the optical element is a perforated mask placed a few centimeters in front of the SiPM matrix. A coded-aperture mask is a thin aluminum sheet with an array of open and closed cells aligned with the sensor pixels and an overall open fraction of about 50%. As illustrated in Figure 3.10, each point-like source in the LAr volume produces a shifted copy of the mask transmission pattern on the focal plane, with alternating illuminated and blocked regions. The original light distribution can then be reconstructed

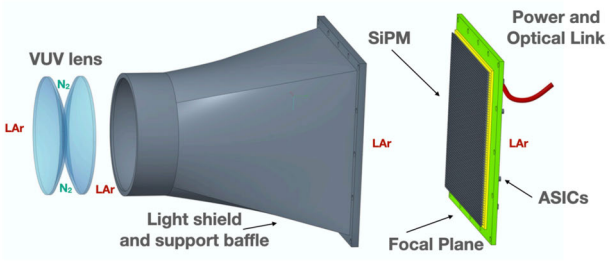

Figure 3.8: Exploded view of a lens-based camera for GRAIN, showing the VUV lens doublet and the SiPM focal plane with its front-end electronics.

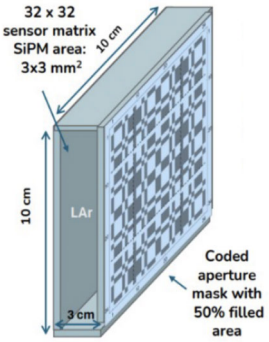

Figure 3.9: Schematic coded-aperture camera for GRAIN. A 32×32 SiPM matrix with $\sim 3 \times 3$ mm^2 pixels (active area $\sim 10 \times 10$ cm^2) is placed ~ 3 cm behind a perforated aluminum mask with a 50% open fraction.

using deconvolution techniques [95]. In the GRAIN implementation, the mask is located at a distance of about 3 cm from the SiPM focal plane, as sketched in Figure 3.9. The detector volume between the mask and sensor is filled with LAr, so the optical transmission depends only on the mask open fraction and is essentially independent of wavelength.

Detector layouts optimized for lens-based and coded-aperture mask cameras are being studied in parallel. For lens-based optics, a configuration with 53 cameras distributed on the elliptical walls and on the top and bottom of the inner vessel is under evaluation, providing overlapping fields of view that cover most of the 1 t fiducial volume. A corresponding layout with 60 coded-aperture cameras is also being developed.

The SiPM matrices will be coated with a wavelength shifter to match their spectral response to the shifted scintillation light: this coating is required irrespective of whether the optics are based on lenses (with xenon-doped LAr) or on masks. The

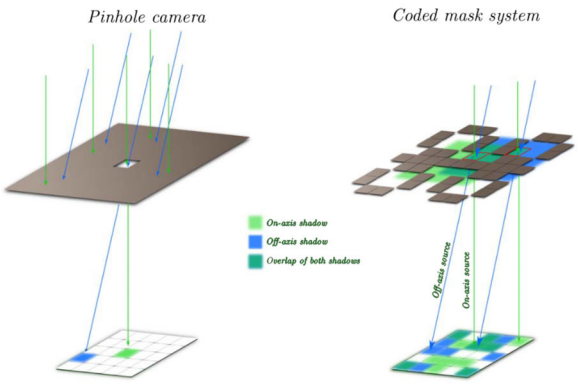

Figure 3.10: Imaging principle of a coded-aperture camera compared with a pinhole camera. Left: a pinhole camera, where the detector plane records a low-efficiency image of the source field. Right: a coded mask camera, where multiple overlapping shadows of the mask are recorded and later decoded to recover the original light distribution.

final solution may combine both technologies, exploiting the higher light-collection efficiency of the lenses and the robustness and wavelength-independence of the coded masks.

3.1.4 The inner tracker

The low-mass gas-based inner tracker of SAND provides both the neutrino interaction target and the charged–particle tracking in the magnetic field. Its design is driven by four main requirements: (i) a precisely known and tunable target mass, with the possibility of using different nuclei; (ii) high–precision tracking in three dimensions with good momentum resolution in the 0.5–5GeV range; (iii) a low average density, so that final state particles are only minimally affected by secondary interactions; and (iv) the possibility to select ν–H interactions with the "solid hydrogen" technique discussed in Subsection 3.2.2.2. To satisfy these conditions, the active tracking elements are as light as possible and are separated from the neutrino targets, so that the latter dominate the mass percentage and can be controlled with high accuracy.

The tracker is located in the central region of SAND and it is surrounded by the ECal, while the upstream area is occupied by GRAIN liquid-argon, as illustrated in Figure 3.11.

The tracker configuration is based on a sequence of modules, each consisting of a target slab closely followed by a tracking station. Two implementations of the tracking system are under study: a Straw Tube Tracker (STT) based on

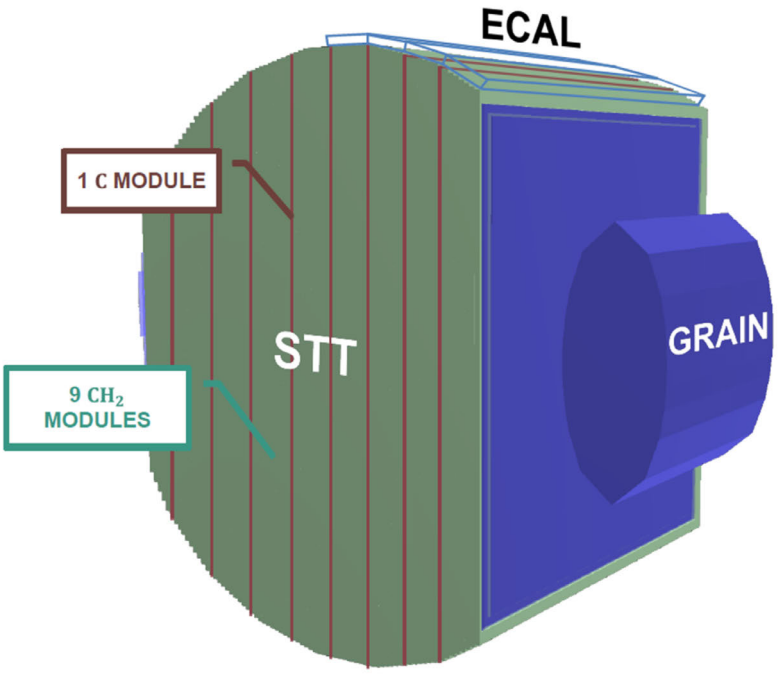

Figure 3.11: SAND inner volume geometry showing the alternating sequence of C and CH_2 modules in the tracker, in red and green, respectively. The first and last five modules are tracking-only (blue). GRAIN is located upstream of the tracker, and the beam is coming from right to left. Figure adapted from DUNE Collaboration documentation.

cylindrical drift tubes, and a drift-chamber tracker based on wire planes. Both options share the same external geometry and target configuration, so that the overall acceptance and target masses are comparable.

3.1.4.1 Modular target and tracker layout

The basic module of the tracker consists of a target slab, typically 5 mm thick followed by a compact tracking station. In the standard configuration targets are slabs of polypropylene (CH_2) or graphite (C), which can be weighed before installation in order to check the fiducial mass at the percent level. The tracking elements contribute only a small fraction of the radiation length ($\sim$ 1-2% X_0) and of the total mass, so that the average density of the tracker can be tuned by changing the number and composition of the target slabs.

The reference configuration is composed of 90 modules: 78 standard CH_2 target modules, 7 modules equipped with graphite targets, and 5 tracking-only modules without target. The different module types are shown in Figures 3.12 and 3.13.

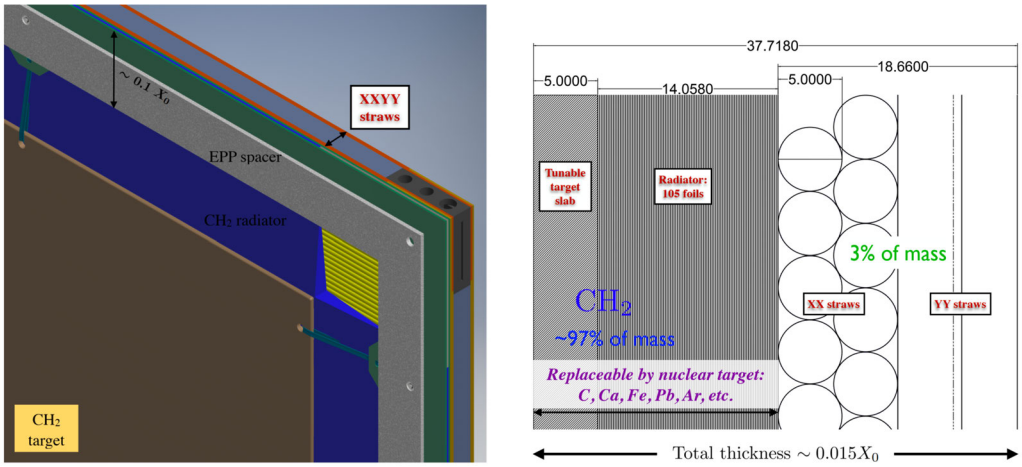

(a) CAD model (b) Detailed drawing

Figure 3.12: Left: 3D engineering CAD model of one STT module equipped with a CH_2 target slab (brown) and a radiator (blue). Right: detailed drawing of an STT module, showing target, radiator and the four straw layers (XXYY, with the beam along the z axis and the magnetic field along the x axis). Figure from DUNE Collaboration.

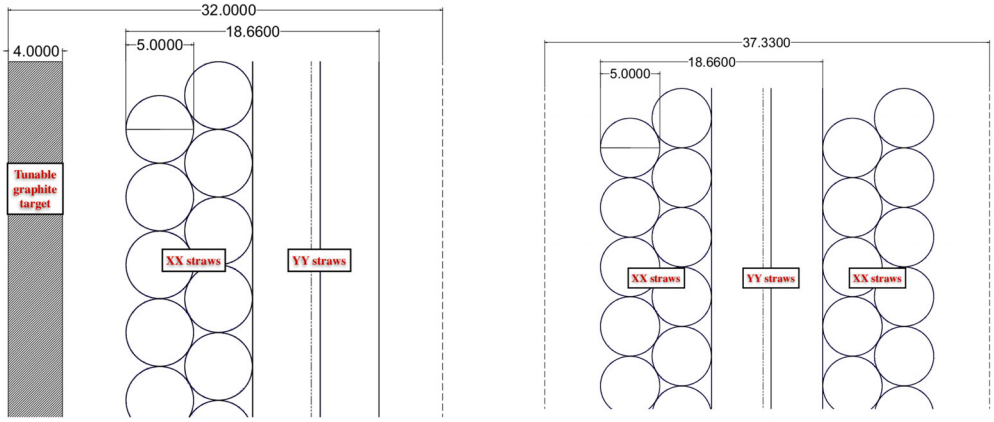

(a) C module (b) Tracking module

Figure 3.13: Detailed drawings of a graphite module (left) and a tracking-only module (right). Figure from DUNE Collaboration.

Standard modules host a CH_2 slab together with a transition-radiation detector and a tracking station; graphite modules replace the CH_2 target with a C slab matching the same radiation length; tracking modules contain only the tracking station and are used to instrument the upstream and downstream areas of the tracker region.

The 90 modules are grouped into seven super-modules that can be inserted and extracted from the detector as independent units. Each super-module contains one graphite module followed by a sequence of CH_2 modules, for a total of 10-12 target modules per super-module. Starting from the upstream side, the baseline geometry consists of one tracking-only module, the seven super-modules, and four additional tracking-only modules downstream. The presence of CH_2 and C modules allows to apply the "solid-hydrogen" technique, while the upstream and downstream tracking modules improve the reconstruction of tracks entering or leaving the tracker region. The overall thickness of the tracker along the beam direction is about 1.3 X_0, including all targets and tracking material. A three-dimensional rendering of one super-module inside the ECal and its transverse cross-section are shown in Figure 3.14.

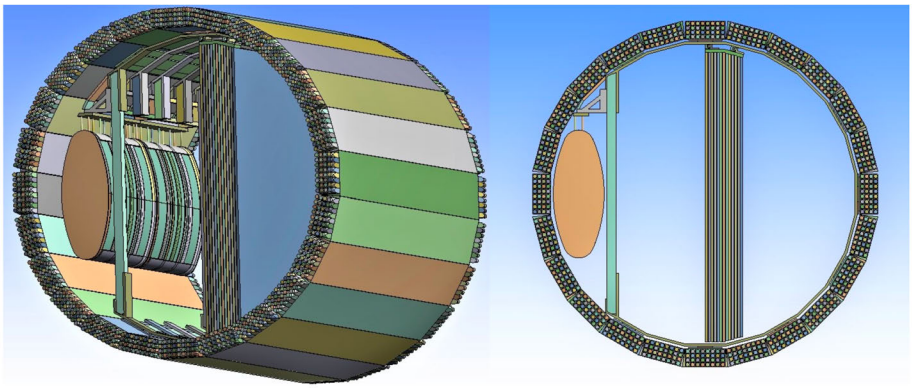

Figure 3.14: Preliminary engineering drawings of the STT configuration. Left: 3D view of the tracker inside the ECal barrel modules. Right: 2D transverse projection. For simplicity, a single super-module is shown, but all the volume will be filled with modules of different lengths. The upstream region is reserved for GRAIN (see Section 3.1.3). The beam is coming from left to right. Figure from DUNE Collaboration.

3.1.4.2 Straw Tube Tracker

In the STT option, the tracking stations are made of gas-filled cylindrical straw tubes with a conductive inner coating as the cathode and a thin anode wire along the axis of each straw. An electric field between the wire and the straw wall separates electrons and positive ions produced by the ionization of the charged particle along its trajectory. Electrons drift towards the wire, where the electric field is large enough to trigger an avalanche multiplication, producing a proportional signal on the anode. The operating gas is a Xe/CO_2 (70/30) mixture at a slight overpressure; typical gains are of the order of 10^4-10^5.

Each tracking station consists of four layers of 5 mm diameter straws arranged in an XXYY configuration, with two stereo views orthogonal to each other and transverse to the beam direction. The single-hit spatial resolution is expected to be better than 200 µm so that for tracks that traverse about 1 m in the 0.6 T magnetic field, the track curvature and hence the momentum can be determined with a resolution better than 5%. The longitudinal coordinate along a straw is obtained by comparing the signals read out at the two ends: both the asymmetry in the collected charge and the difference in arrival time are converted into a position along the tube. Hits in the orthogonal straw layers provide a second, independent view of the track, and are used to match the corresponding track segments and resolve ambiguities when several tracks cross the same region.

In standard CH_2 modules (Figure 3.12) the straw planes are preceded by a polypropylene radiator composed of about one hundred thin foils (thickness $\sim 20\,\mu m$) separated by gas gaps. Transition radiation photons produced by ultra-relativistic electrons in the radiator convert in the gas and are detected in the straws, providing e/π discrimination over a broad momentum range. The combination of low-density tracking, precise momentum measurement, and particle identification makes the STT option particularly suited for reconstructing neutrino final states.

3.1.4.3 Drift Chamber

As an alternative to the STT, a tracker based on planar drift chambers (DCs) is under development as a backup solution for the SAND inner tracker. [96]

Drift chambers are a well-established technology, providing precise tracking, fast time response and robust operation in high-rate environments. The DC option is designed to have the same performance and to the STT one, while reducing the number of readout channels and the overall mechanical and production complexity. The chambers are operated with an Ar/CO_2 gas mixture at a pressure close to atmospheric, requiring only a few millibars of overpressure to circulate the gas.

The layout closely follows that of the STT discussed in Section 3.1.4.1: the modules with graphite and CH_2 targets are arranged in super-modules. At the same time, the transition-radiation detector present in the STT baseline is removed in the DC configuration. Ten modules (nine with CH_2 targets and one with graphite) form a super-module about 35 cm thick along the beam direction, and the full tracker comprises roughly 240 DC planes. In this way, the total target mass and average radiation length are essentially identical for the STT and DC options, allowing a direct comparison of their physics sensitivities.

The active part of a DC module consists of three sense wire planes interleaved

with thin Mylar cathode foils, as sketched in Figure 3.15. Each drift cell is defined by a central anode wire, made of gold-plated tungsten with a diameter of 20 µm, enclosed between two cathode planes of bi-aluminised Mylar (20 µm thick with a 70 nm aluminium coating on each side). Two additional field-shaping wires, complete the cell and delimit the drift volume. The use of continuous cathode planes, together with field wires, yields an electric-field configuration similar to that of a straw tube while reducing the number of readout channels, since only the sense wires are instrumented. The chambers operate with typical drift times of a few hundred nanoseconds for the maximum drift distance.

Each wire plane in a module is oriented at a different angle with respect to the magnetic-field axis to enable 3D reconstruction of tracks. A stereo angle of about $\pm 5^\circ$ has been adopted: the three wire planes are oriented at approximately $+5^\circ$, 0° and -5°.

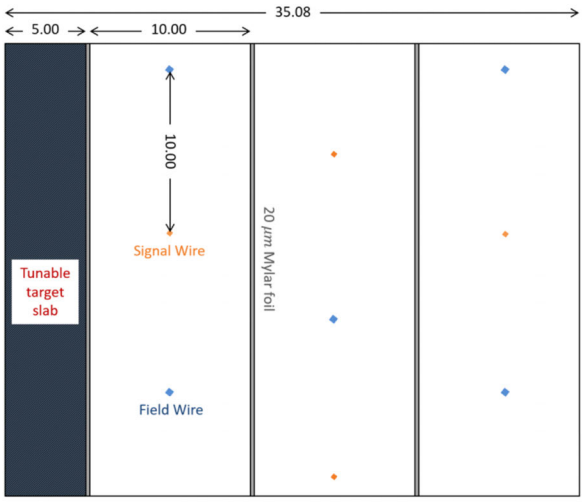

Figure 3.15: Schematic cross-section of one drift-chamber module of the tracker. A drift region follows a tunable target slab instrumented with a central signal wire and surrounding field wires, separated by Mylar cathode foils of thickness 20 µm. The horizontal dimensions (in mm) indicate the thickness of the target slab (5 mm), the characteristic size of a drift gap (10 mm) and the total thickness of the module (35.08 mm) along the beam direction. Figure from [96].

The drift-chamber option therefore, has the light target concept of the STT while offering a simpler mechanical structure and a well-established readout technology, at the price of a lower longitudinal sampling and the absence of transition-radiation e/π separation.

3.2 SAND physics program

As mentioned above, SAND's primary role is to monitor the LBNF neutrino beam in real time and to provide complementary neutrino interaction measurements. To do so, SAND must continuously measure the charge and momentum of muons produced in neutrino interactions, reconstruct interaction vertices with centimeter-scale precision, and operate in a high-rate environment, also rejecting cosmic and beam-induced backgrounds. By combining information from the low-density inner tracker, the GRAIN liquid-argon target detector, and the surrounding electromagnetic calorimeter, SAND can track muons and charged hadrons, perform particle identification via $\mathrm{d}E/\mathrm{d}x$ and by combining different sub-detector signatures, measure the energies of particles reaching the ECal, and identify neutrons. These capabilities allow measurements of the on-axis neutrino fluxes and the detection of variations in the beam spectrum.

Beyond beam monitoring, SAND has a broad neutrino interaction program that strengthens the DUNE oscillation physics goal. The combination of hydrocarbon, pure carbon and argon targets allows measurements on multiple nuclei and the "solid-hydrogen" technique application, in which interactions on free protons are isolated using transverse kinematic imbalance techniques. This allows the constraining of nuclear effects and cross-section models, reducing systematic uncertainties in the near-to-far rate extrapolation. The low-density, magnetized tracking volume and high-resolution calorimetry also allow for searches for rare and Beyond-the-Standard-Model processes, such as heavy neutral lepton decays. In the following subsections, a more detailed discussion of the SAND physics goals is presented.

3.2.1 Beam monitoring

Beam monitoring is based on inclusive $\nu_\mu/\bar{\nu}_\mu$ charged-current (CC) interactions reconstructed in the inner tracker and ECAL, from which the neutrino energy and interaction vertex can be measured. This information is used to detect variations in the intensity, energy spectrum and transverse profile of the beam on time scales of order one week.

The expected sensitivity has been studied in dedicated SAND beam-monitoring simulations by the DUNE Collaboration, using one week of exposure in FHC mode, corresponding to 3.78×10^{19} protons on target [97, 68]. Events are selected by requiring at least one reconstructed charged track in the bending plane of the inner tracker, with the muon momentum and calorimetric hadronic energy used to reconstruct the neutrino energy. For each assumed variation of the beamline

Table 3.2: Sensitivity to variations of the main beam parameters with respect to the nominal FHC beam settings, for one week of data taking. The "1σ variation" column lists the size of the change applied to each beam parameter in the sensitivity study, chosen to be representative of realistic fluctuations expected in LBNF operation. The last two columns give the sensitivity expressed as $\sqrt{\Delta\chi^2}$ when using the true neutrino energy E_ν^{true} and the reconstructed energy E_ν^{rec}, respectively. Values taken from the SAND beam-monitoring studies of the DUNE Collaboration [97, 68].

Beam parameter	1σ variation	$\sqrt{\Delta\chi^2(E_\nu^{\text{true}})}$	$\sqrt{\Delta\chi^2(E_\nu^{\text{rec}})}$
Horn current	+3 kA	12.57	9.44
Water layer thickness	+0.5 mm	4.69	3.58
Proton target density	+2%	5.28	4.07
Proton beam radius	+0.1 mm	4.41	3.53
Proton beam offset X	+0.45 mm	5.11	3.54
Proton beam θ, ϕ	0.07 mrad, 1.57 mrad	0.62	0.28
Proton beam θ	0.070 mrad	0.91	0.58
Horn 1 X shift	+0.5 mm	4.70	3.42
Horn 1 Y shift	+0.5 mm	5.27	3.87
Horn 2 X shift	+0.5 mm	1.18	0.69
Horn 2 Y shift	+0.5 mm	1.31	0.77

parameters, a varied sample of neutrino interactions is obtained and compared to the nominal configuration using the test statistic

$$T \equiv \Delta\chi^2 = \sum_{i=1}^{N} \frac{\left(N_i^{\text{nom}} - N_i^{\text{var}}\right)^2}{N_i^{\text{nom}}}\,, \tag{3.11}$$

where N_i^{nom} and N_i^{var} are the expected event in bin i for the nominal and varied beam, respectively. The quantity $\sqrt{\Delta\chi^2}$ is the significance for rejecting the varied hypothesis.

Table 3.2 summarizes the sensitivity for a representative set of 1σ variations of the main beam parameters around the nominal FHC configuration. Results are given both using the true neutrino energy and the reconstructed energy obtained from smeared detector observables. For most variations (horn current, target and horn alignment, proton beam profile) SAND achieves $\sqrt{\Delta\chi^2} \gtrsim 3$ within one week, being able to detect these changes with a significance of at least about 3σ.

In addition to monitoring the energy spectrum, SAND is also sensitive to changes in the transverse position of the beam. This is studied by applying artificial shifts to the position of the beam axis along the X direction and comparing the nominal and shifted samples using Eq. (3.11). Different observables can be

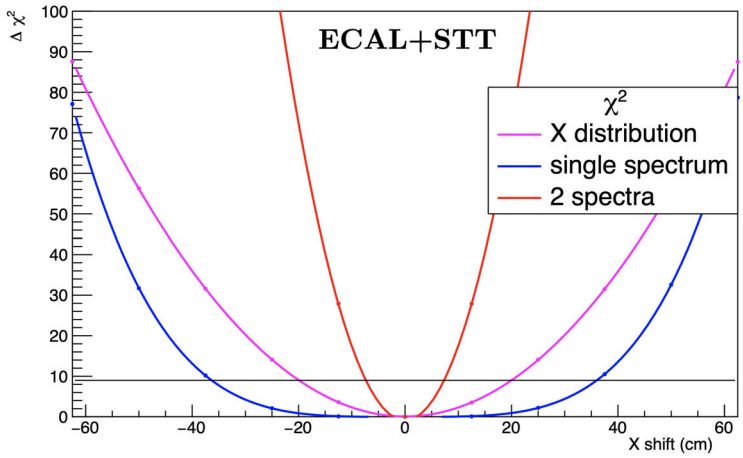

Figure 3.16: Sensitivity of the ECAL+STT configuration to a shift of the neutrino beam axis along the X direction, expressed as $\Delta\chi^2$ as a function of the applied shift. Three observables are compared: the distribution of the reconstructed interaction-vertex coordinate X (magenta curve), a single inclusive reconstructed neutrino-energy spectrum (blue curve), and two separate E_ν^{rec} spectra for events with $X < 0$ and $X > 0$ (red curve). The horizontal line indicates $\Delta\chi^2 = 9$, corresponding to a $\sim 3\sigma$ significance. Figure from [68].

used: the distribution of the reconstructed X coordinate of the interaction vertex, a single inclusive E_ν^{rec} spectrum, or two separate E_ν^{rec} spectra for events whose reconstructed interaction vertex lies at $X_{\text{vtx}} < 0$ and $X_{\text{vtx}} > 0$, respectively. The corresponding sensitivities are shown in Figure 3.16. Using only the vertex distribution gives limited sensitivity because the beam profile at the ND site is wider than the transverse size of SAND, while a single inclusive E_ν^{rec} spectrum further dilutes the effect of a transverse shift. The best performance is obtained when the cylindrical symmetry is broken by constructing separate spectra for $X_{\text{vtx}} < 0$ and $X_{\text{vtx}} > 0$, which enhances the sensitivity to a lateral displacement of the beam axis; in this configuration shifts down to 8.4 cm can be detected with $\Delta\chi^2 > 9$.

Overall, these studies show that SAND provides sufficient sensitivity to detect percent-level variations in the beam intensity and spectral shape and to control beam pointing at the level of a few centimetres on a weekly basis.

3.2.2 Flux measurements

The determination of the oscillation probability at the Far Detector requires an accurate knowledge of the unoscillated neutrino flux at the near site. SAND

is designed to provide an independent measurement of the interaction rate and energy spectra of the ν_μ, $\bar{\nu}_\mu$, ν_e and $\bar{\nu}_e$ beam components, exploiting its low-density tracker, the GRAIN liquid-argon target and the surrounding ECal. The ability to identify and reconstruct a variety of exclusive topologies on hydrogen, carbon and argon enables several complementary strategies to determine both the absolute normalization and the energy dependence of the flux, and to measure flux ratios relevant for the oscillation analysis, such as ν_e/ν_μ, $\bar{\nu}_e/\bar{\nu}_\mu$ and $\bar{\nu}_\mu/\nu_\mu$.

Several channels are under study for flux measurements in SAND that will be discussed in a the following.

3.2.2.1 ν-e elastic scattering

Elastic scattering of neutrinos on atomic electrons,

$$\nu_\ell + e^- \to \nu_\ell + e^- \,, \tag{3.12}$$

with $\ell = \mu, e$, is a purely electroweak process whose cross section is predicted by the Standard Model with sub-percent uncertainties and is free from nuclear effects. For an accelerator neutrino beam this channel therefore provides a direct and theoretically clean handle on the absolute neutrino flux normalization, limited mainly by statistics and detector systematics rather than by the theoretical description of the interaction.[55]

The experimental signature in SAND is a single, isolated electron emerging at small angle with respect to the beam direction and no hadronic activity above threshold. For scattering on an electron at rest, the electron energy E_e and scattering angle θ satisfy the kinematic relation

$$1 - \cos\theta \simeq \frac{m_e(1-y)}{E_e} \,, \tag{3.13}$$

where m_e is the electron mass and $y = E_e/E_\nu$ is the fraction of the neutrino energy transferred to the electron. For DUNE beam energies $E_\nu \gg m_e$ the electron is ultra-relativistic and the scattering angle is typically a few mrad, such that $E_e\theta^2 \lesssim 2m_e$. The measured (E_e, θ) distribution can therefore be related to the incident neutrino energy spectrum with minimal model dependence, and can be used to extract the flux normalization and, in combination with external constraints on the beam composition, information on the energy dependence of the on-axis flux.

Dedicated studies based on the DUNE Near Detector flux and detector simulations indicate that a ν-e sample selected in the straw-tube tracker with requirements on the electron energy ($E_e \gtrsim 0.15$ GeV), isolation, and on the kinematic variable $E_e\theta_e^2$

can be obtained with an efficiency of $\sim$ 80-85% and total background contamination at the level of a few percent, dominated by ν_e charged-current interactions without visible hadrons and neutral-current π^0 production. A complementary ν-e sample can be selected in ND-LAr, which features a larger fiducial mass but higher background levels, combining the two detectors improves the overall statistical precision and provides important cross-checks of detector systematics.

Under these conditions, the ν-e elastic scattering channel in SAND is expected to constrain the absolute normalization of the (predominantly ν_μ) on-axis flux at the few-percent level. When combined with external constraints on the beam composition and with other interaction channels in the near detectors, the ν-e sample also contributes to constraining the energy dependence of the flux in a largely model-independent way.

3.2.2.2 Solid-hydrogen technique and interactions on H

The flexible design of the SAND tracker (STT) offers the possibility to isolate charged-current (CC) interactions on hydrogen (H) by comparing samples of events interacting on polypropylene (CH_2) and graphite (C) targets interleaved in the tracker.[68, 98, 97]

Because the two targets are exposed to the same beam and are measured by the same detector, many detector-related effects cancel in the subtraction of the C sample from the CH_2 sample, leaving an H-enriched sample whose residual C background can be constrained directly from data.[99, 100, 101] This data-driven procedure, often referred to as the *solid-hydrogen* (solid-H) technique is adopted as the baseline strategy for SAND. The solid-H method exploits the kinematic symmetry of CC quasi-elastic (CCQE) scattering on a free proton at rest.

For $\bar{\nu}_\mu p \to \mu^+ n$ on hydrogen, the muon and neutron are nearly back-to-back in the plane transverse to the beam direction, so that the missing transverse momentum $\delta p_T^m = \|\vec{p}_T^{\,\mu} + \vec{p}_T^{\,H}\|$ is strongly peaked near zero. For bound protons in C, Fermi motion and final-state interactions broaden this distribution, producing a tail to higher δp_T^m.[99, 100] By comparing the CH_2 and C samples bin-by-bin in δp_T^m and other kinematic variables, and subtracting the appropriately normalized C distributions from the CH_2 ones, one obtains a hydrogen-enhanced sample in which the residual nuclear background is constrained directly from the data.[101] Interactions on free protons can be used for flux measurements because they are free from nuclear effects so that the cross section depends only on nucleon form factors and radiative corrections and is not affected by nuclear modeling uncertainties.[100, 101]

CC interactions on H thus offer a way to determine the absolute and relative neutrino (and antineutrino) flux normalization and spectrum and to study cross-section models for more complex nuclei.[99, 100] The simplest topology considered for neutrino configuration is the single-pion channel

$$\nu_\mu p \to \mu^- p \pi^+ \,. \tag{3.14}$$

In charged–current events, the hadronic energy $E_{\rm had}$ is the part of the final-state energy carried by hadrons rather than by the outgoing charged lepton. Experimentally, it is reconstructed as the calorimetric sum of the visible energy of all hadronic particles, or as the difference between the reconstructed neutrino energy and the muon energy, $E_{\rm had} \simeq E_\nu - E_\mu$. For the $\nu_\mu p \to \mu^- p \pi^+$ process on hydrogen, events are selected at low hadronic energy transfer, $E_{\rm had} < 0.5$ GeV.

In this regime the hadronic system is dominated by the exclusive $p\pi^+$ final state, with little additional hadronic activity. On the theory side, the corresponding cross section is mainly dependent by the form factors that parameterize the CC interaction on the free proton; on the experimental side, the leading systematics arise from the muon energy scale and from the overall hadronic energy calibration. The low-$E_{\rm had}$ requirement mitigates both types of uncertainties and at the same time, it suppresses backgrounds from interactions on carbon: even at the same neutrino energy, CC events on a nuclear target typically produce additional nucleons and pions and undergo final-state interactions inside the nucleus, so that the visible hadronic energy is significantly higher. As a consequence, the $E_{\rm had} < 0.5$ GeV select a sample enriched in interactions on free protons relative to those on carbon.[68, 98, 99]

For antineutrino running is studied the quasi-elastic process

$$\bar{\nu}_\mu p \to \mu^+ n \,. \tag{3.15}$$

At four-momentum transfer $Q^2 \to 0$ the corresponding CCQE cross section is theoretically known with an uncertainty well below 1%.[99, 100] By selecting events with reconstructed $Q^2 \lesssim 0.05$ GeV^2, one obtains a hydrogen sample for which the cross section becomes effectively independent of the neutrino energy and is known to high precision.[99, 101] In SAND, the $\nu_\mu p \to \mu^- p \pi^+$ and $\bar{\nu}_\mu p \to \mu^+ n$ samples in neutrino and antineutrino mode, respectively, provide complementary channels for the flux determination and for validating the CC interaction models used in the oscillation analysis. In the antineutrino sample used in this thesis in Chapter 6, about 7.8% of all interactions in the tracker volume are CCQE with a $\mu^+ n$ final state, and $\sim$ 17% of these are on hydrogen, the rest being domi-

nated by carbon (see Table 6.1). This composition implies that the $\bar{\nu}_\mu p \to \mu^+ n$ signal has a background of interactions on nuclear targets that can be isolated by combining a dedicated event selection with the solid-H CH_2–C subtraction. In this context, the ECal provides the key experimental handle, since it is the only SAND sub-detector capable of tagging the final-state neutron in $\bar{\nu}_\mu p \to \mu^+ n$ events. Chapter 6 presents a detailed simulation study of neutron detection in the ECal and of its impact on the hydrogen sample. For neutrons produced anywhere in the tracker volume, about 30% of those that reach the calorimeter form at least one reconstructed ECal cluster, with a cluster efficiency that is broadly flat in the true neutron kinetic-energy range $T_n^{\text{true}} \simeq$ 100–1000 MeV (see Section 6.1). For CCQE events with final state $\mu^+ n$, the kinematics of the neutron can be predicted from the measured muon under the free-proton hypothesis; the corresponding "flight line" and time-of-flight are then compared to the reconstructed ECal clusters using the spatial and timing residuals (Δr, Δt) (Section 6.4). By varying the ($|\Delta t|, \Delta r$) requirements, Chapter 6 defines working points that trade neutron-tag efficiency against cluster purity and non-H rejection. Approximately 20% of true $\mu^+ n$ events on hydrogen can be tagged by at least one neutron cluster, while about 80% of CCQE($\mu^+ n$) events on non-H targets are rejected before applying the CH_2–C subtraction. This demonstrates that SAND can select a hydrogen-enriched $\bar{\nu}_\mu p \to \mu^+ n$ sample with controllable non-H contamination and a well-quantified selection efficiency. When combined with the solid-H technique in the tracker, such a hydrogen-enhanced and neutron-tagged $\bar{\nu}_\mu p \to \mu^+ n$ sample provides the necessary ingredients to turn the precisely known low-Q^2 CCQE cross section on hydrogen into a constraint on the (anti)neutrino flux: the observed event rate in the selected sample is, up to residual detector systematics, directly proportional to the incident flux. The study carried out in this thesis therefore constitutes a quantitative assessment of the ECal neutron-tagging performance required for a future precision flux determination with SAND, and shows that the detector design is compatible with this physics goal.[99, 100, 101, 68]

3.2.3 Nuclear effects and cross-section measurements

As discussed in Section 2.4.5, the event rates are the result of the convolution of the on-axis neutrino flux with the interaction cross sections on the various target nuclei and with the detector response. The flux normalization and shape can be constrained with the ν-e channel and with hydrogen-enhanced samples, as described in 3.2.2, but a dedicated program of cross-section and nuclear-effect measurements in SAND is still required to control the remaining model dependence in the oscillation analysis.[68, 79] The SAND configuration addresses this problem by combining hydrocarbon and pure carbon targets in the tracker

and a liquid-argon target in GRAIN, all exposed to the same beam.[68, 97, 90] As discussed in 3.1.4.1 in the modular target-tracker the passive material can be tuned (e.g. CH_2, C and, in future, additional nuclei), while GRAIN provides complementary measurements on argon with a different reconstruction.

Cross-section measurements. In both neutrino and antineutrino running, SAND exploits exclusive charged-current interactions on hydrogen, following the solid-H program [99, 100, 101]. Key channels include

$$\nu_\mu p \to \mu^- p \pi^+ \,, \tag{3.16}$$

$$\bar{\nu}_\mu p \to \mu^+ n \,, \tag{3.17}$$

$$\bar{\nu}_\mu p \to \mu^+ p \pi^- \,. \tag{3.18}$$

Additional channels with higher hadronic multiplicity (e.g. $\bar{\nu}_\mu p \to \mu^+ n \pi^0$ or $\nu_\mu p \to \mu^- p \pi^+ X$) and CC-inclusive samples can also be used.

Once the hydrogen component is isolated via the CH_2-C subtraction and transverse kinematic-imbalance variables, as discussed in Section 3.2.2.2, the differential cross section on hydrogen can be estimated from the data as $d\sigma_{\mathrm{H}}/d\vec{x}$, where $\vec{x}$ denotes a vector of observables defining the analysis phase space, for example

$$\vec{x} \equiv (E_\nu^{\mathrm{rec}},\, Q^2_{\mathrm{rec}},\, p_T^\mu,\, p_T^H) \,.$$

Here E_ν^{rec} is the reconstructed neutrino energy, Q^2_{rec} is the reconstructed four-momentum transfer, p_T^μ is the muon transverse momentum with respect to the beam direction, and p_T^H is the magnitude of the transverse momentum carried by the hadronic system.

In each bin i of $\vec{x}$, the number of events on H N_i^{H} is obtained by subtracting the appropriately normalized C sample from the CH_2 sample and correcting for selection efficiency and acceptance. After unfolding detector smearing (for instance with a bin-by-bin or matrix-based procedure) and dividing by the effective number of target protons T_{H} and by the integrated neutrino flux Φ, an estimator for the binned differential cross section can be obtained as

$$\left(\frac{d\sigma_{\mathrm{H}}}{d\vec{x}}\right)_i \simeq \frac{1}{T_{\mathrm{H}}\,\Phi}\frac{N_i^{\mathrm{H,\,corr}}}{\Delta\vec{x}_i} \,, \tag{3.19}$$

where $N_i^{\mathrm{H,\,corr}}$ denotes the corrected number of events in bin i, $\Delta\vec{x}_i$ is the bin width in observable space, and T_{H} is the effective number of free protons in the fiducial hydrogen target, computed from the target mass and chemical composition.[99, 100, 101] Because the target is hydrogen, this extraction is free from uncertainties

related to nuclear structure and intranuclear rescattering; the remaining model dependence arises mainly through the unfolding and acceptance corrections.

An analogous procedure can be applied also to the antineutrino quasi-elastic process $\bar{\nu}_\mu p \to \mu^+ n$ at low four-momentum transfer Q^2, which cross section on free protons is theoretically known with an uncertainty well below 1%.[99, 100] As discussed in Chapter 6, SAND can select a hydrogen-enriched $\mu^+ n$ sample using the solid-H method and neutron tagging in the ECAL, with a well-quantified efficiency and non-H background rejection. This provides the necessary ingredients for a future measurement of the CCQE cross section on hydrogen.

Nuclear effects. Nuclear effects modify both the total and differential cross sections and distort the kinematics of the outgoing leptons and hadrons via Fermi motion, nucleon correlations, and final-state interactions (FSI).[102] Incomplete modeling of these effects is one of the dominant sources of systematic uncertainty in present long-baseline experiments and is expected to be a limiting factor for next-generation measurements if not controlled at the few-percent level. This is illustrated in Figure 3.17, which shows the distribution of reconstructed-to-true neutrino energy $E_\nu^{\mathrm{rec}}/E_\nu^{\mathrm{true}}$ for inclusive ν_μ CC interactions on hydrogen and on argon in FHC mode, for different assumptions on the argon nuclear model. While the hydrogen distribution is centered close to unity, argon exhibits a much broader smearing in the main oscillation region, with clear dependence on the nuclear model.[98]

Because the solid targets in the tracker are exposed to the same beam and are measured with a common tracking and calorimetric acceptance, cross-section ratios between different nuclei can be calculated with reduced sensitivity to the flux and to many detector-systematic uncertainties. The hydrogen samples obtained with the solid-H technique (Section 3.2.2.2) provide a reference free of nuclear effects, against which the nuclear responses of any target material in the tracker can be compared in the same exclusive topologies. For a nuclear target of mass number A (for example C with $A = 12$, or a different target in the target modules), a differential cross section per nucleus $d\sigma_A/d\vec{x}$ can be extracted as a function of the same observable vector $\vec{x}$ used for hydrogen. Ratios of the form

$$R_{\mathrm{nuc}}^A(\vec{x}) = \frac{1}{A}\frac{d\sigma_A/d\vec{x}}{d\sigma_{\mathrm{H}}/d\vec{x}}\,, \tag{3.20}$$

compare the per-nucleon response of a nucleus with mass number A to that of free protons in hydrogen. In these ratios the flux Φ and many effect related to the reconstruction representing systematic effects cancel out, since the hydrogen and nuclear targets in the tracker are exposed to the same beam and reconstructed

in the same way as well. The denominator $d\sigma_{\mathrm{H}}/d\vec{x}$ provides a reference measurement on free nucleons, so that deviations of $R^{A}_{\mathrm{nuc}}(\vec{x})$ from unity as a function of $\vec{x}$ directly show the impact of Fermi motion, binding, multinucleon contributions and FSI in the nuclear target.[102] Complementary information on argon is provided by GRAIN (and ND-LAr), which sample the beam with a different detector technology, allowing consistency checks of nuclear models on Ar within the DUNE near-detector complex.[68, 90]

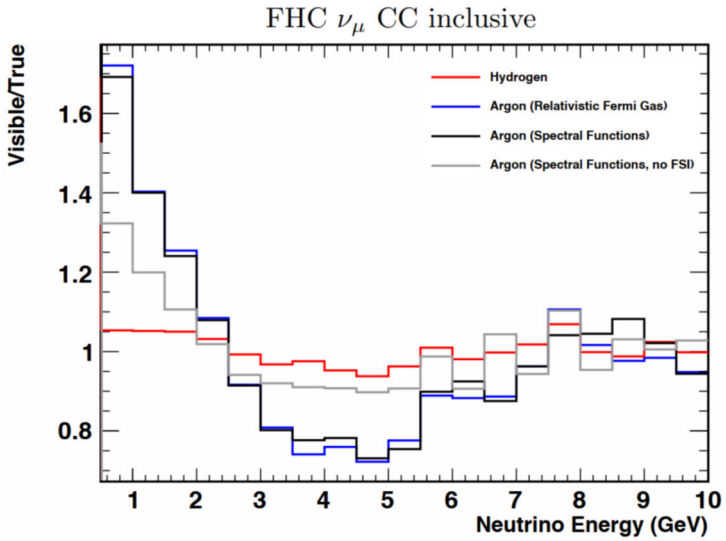

Figure 3.17: Ratio of reconstructed to true neutrino energy in inclusive ν_μ charged-current interactions on hydrogen (red) and argon (blue, black and grey) in FHC mode, obtained with different assumptions for the argon nuclear model (relativistic Fermi gas, spectral functions with and without FSI). The much larger nuclear smearing in argon in the main oscillation region (0.5 GeV $< E_\nu <$ 5 GeV) can be constrained using hydrogen events in the tracker as a reference. Figure from [98].

Chapter 4

SAND simulation and reconstruction framework

The studies presented in this thesis are based on a full simulation and reconstruction chain for SAND, from the neutrino interaction in the detector materials to high-level reconstructed objects and analysis variables. This chapter aims to summarize the structure of this chain and to define the interfaces between its main components. Particular emphasis is placed on the parts that have been developed or substantially extended in the context of this work: the SAND ECal digitization, described in this chapter, and the ECal clustering and Monte Carlo backtracking algorithms presented in Chapter 5. The GRAIN liquid-argon detector, which shares the common ND simulation chain but uses a dedicated optical readout, is discussed in Section 4.3.

The SAND workflow is organized into two main blocks. On the simulation side, the DUNE Near Detector (ND) simulation infrastructure provides the LBNF neutrino flux prediction at the SAND location and generates neutrino interactions in the SAND detector geometry using the GENIE neutrino event generator [103]. Final-state particles are then transported through the detector with the `edep-sim` energy-deposition simulation [104] discussed in Section 4.1, which records the detailed truth information and the energy deposits in all active media in a `TG4Event TTree` populated with `TG4Trajectory` and `TG4HitSegment` objects.

From the point of view of the reconstruction framework, this simulation chain is summarized by two main Monte Carlo inputs to the reconstruction code `sandreco`:

- the SAND detector geometry in GDML format, produced with the `dunendggd` package [105]. The latter is based on the DUNE Geometry Description Generator (GeGeDe), a Python tool that converts a high-level, modular description of the detector into a detailed GDML geometry where information on active volumes and readout channels is attached through dedicated auxiliary tags and is later used by `edep-sim` and `sandreco` to identify the sensitive elements of each subdetector.
- the `edep-sim` output ROOT file, which contains the `TG4Event TTree` with the list of simulated trajectories and the corresponding energy deposits

(`TG4HitSegment` objects) in all sensitive volumes (Section 4.1).

This `edep-sim` output provides the standard energy-deposit samples for all ND components and is used as the common input to the various detector-specific reconstruction packages. For SAND, the same GDML geometry and `edep-sim` file constitute the inputs to `sandreco`, which uses them to perform the detector digitization and event reconstruction. For GRAIN, the `edep-sim` energy deposits in liquid argon are additionally passed to a dedicated Geant4-based optical simulation module (`OptMen`), which propagates individual scintillation photons to the imaging cameras.

On the reconstruction side, the `sandreco` framework [106] reads the detector geometry and the `edep-sim` output, simulates the detector response (digitization) for each subdetector, and reconstructs tracks and calorimetric clusters using different executables:

- `Digitize`: reads the `EDepSimEvents` `TTree` and the `EDepSimGeometry` `TGeoManager` written by `edep-sim` and simulates the detector response, producing digitized signals for the inner tracker (straw tubes or drift chambers) and for the ECal in a ROOT format that mimics the DAQ output. The executable builds a `tDigit` `TTree` containing vectors of tracker wires and ECal digitized cells.

  For the ECal, each energy-deposit hit (`TG4HitSegment` object, see Section 4.1) in the ECal is mapped to the corresponding ECal cell, and its deposited energy in the active volume is attenuated along the two fiber halves and converted into an average number of photoelectrons. For each photoelectron, an arrival time at the PMT is generated by adding the scintillation emission time, the propagation time along the fiber, and an electronic jitter. Photoelectrons are then integrated in the acquisition window with a dead time, and only signals above threshold are kept. The total number of photoelectrons in the window is converted to ADC counts, while the TDC time is obtained either with a constant-fraction algorithm or with a fixed photoelectron threshold, emulating different timing discriminators. The digitization model used in this thesis is described in detail in Section 4.2.

  For the tracker, the hit segments are first grouped by straw tube (STT option) or by drift cell (drift-chamber option). For each wire, the code determines the point of closest approach between the hit segment and the sense wire, computes the drift time and the signal propagation time along the wire using the configured drift and signal velocities, and assigns to the wire a TDC time smeared with the intrinsic timing resolution, together with

an ADC value proportional to the total energy deposit.

- `SANDECALClustering`: reconstructs ECal clusters starting from the digitized cells `dg_cell`, which after the digitization step contain one or more photo-signals. The executable takes as input the digitization output `tDigit TTree` and produces a `tCluster TTree` containing a vector of reconstructed clusters for each event. The full clustering and Monte Carlo backtracking chain is described in Sections 5.1, 5.2 and 5.3.

- Additional reconstruction executables implement the full track reconstruction in the inner tracker. In particular, the `Reconstruct` program takes as input the tracker digits, performs pattern recognition by grouping digits into 2D clusters, fits circles in the bending plane and straight lines in the non-bending plane, and can optionally refine the helix parameters with a dedicated Kalman filter that includes the effect of the magnetic field, multiple scattering and energy loss along the track.

  Different configurations are available at the moment of this thesis writing for the tracker reconstruction. In the two *fast* modes (`fast_only_primaries` and `fast`), tracker digits are linked to Monte Carlo trajectories using information provided by `edep-sim`, so that no pattern-recognition step is performed. The two modes differ only in which trajectories are allowed to seed a reconstructed track: in `fast_only_primaries` the loop is restricted to primary trajectories exiting directly from the vertex, whereas in `fast` the same truth-based association is used but all trajectories with at least one matched tracker digit are reconstructed. The *full* mode instead performs pattern recognition without using MC truth: the interaction vertex is first estimated from the distributions of hit positions along the tracker, and track candidates are then built by clustering hits into local segments in each module and linking them across successive modules on the basis of geometrical consistency.

  In the `primary_only_kf` configuration, the reconstruction is driven by a Kalman filter. Tracker digits are first grouped into 3D clusters and local "tracklets", which provide position and direction estimates at each tracker station. These "tracklets" are then used as measurements in a global Kalman fit that propagates the track state through the magnetic field, including process noise from multiple scattering and energy loss, and updates it at each layer. The smoothed state at the downstream end is finally converted into the helix parameters stored in the final track objects.

When needed for both SAND-level and DUNE-wide oscillation analyses, the re-

constructed information is finally exported to the Common Analysis File (CAF) with the ND CAFMaker package [107].

4.1 edep-sim tool

The `edep-sim` package is an energy-deposition simulation built as a generic wrapper around GEANT4 and it is used by the DUNE collaboration for the official productions for all the ND detectors.[104] Its role is to simulate particle transport and interactions in the full SAND geometry and to provide a standard, geometry-aware truth description of each event in a ROOT file, which is then used by the SAND downstream algorithms as digitization and reconstruction.

Geometry and event generation. The SAND geometry is described in `gdml` format and loaded into `edep-sim` . Primary particles can be provided either by a neutrino interaction generator (GENIE `RooTracker` files for the beam samples) or by simple particle guns used for calibration and performance studies (e.g. the muon and electron guns of Section 5.4.1 and the samples of Section 5.5). In all cases, the particle transport and the physics processes are handled by GEANT4, while `edep-sim` records a compact summary of the simulated event.

Output file The standard output of `edep-sim` is a ROOT file containing:

- a `TGeoManager` stored as `EDepSimGeometry`, which stores the full detector geometry used in the simulation
- a tree `EDepSimEvents` with a single branch `Event` of type `TG4Event`.[104]

All kinematic and geometry quantities in `TG4Event` are stored in CLHEP units: distances in millimetres, energies in MeV and times in nanoseconds, with a global coordinate system defined by the input GDML. These conventions are assumed throughout the digitization and reconstruction codes and in the truth-level comparisons of Chapter 5.

Truth data model: `TG4Event`. The `TG4Event` object summarises the GEANT4 simulation for one event, that in the context of this thesis means one neutrino interaction. Only the elements used in this thesis are recalled here:

- **Primary vertices.** The `Primaries` vector holds the `TG4PrimaryVertex` instances corresponding to neutrino interactions. Each vertex stores the interaction position and the list of outgoing particles, together with generator information (reaction code, event weight, etc.) used in the flux and hydrogen analyses.

- **Trajectories.** The `Trajectories` vector contains one `TG4Trajectory` per GEANT4 track. For each trajectory, the track and parent identifiers (`TrackId`, `ParentId`), PDG code and initial four-momentum are stored, together with a sequence of `TG4TrajectoryPoint` objects describing the particle path. The parent-child relations contain the information for build the family tree and are later used for Monte Carlo backtracking in Section 5.3.
- **Energy depositions.** The `SegmentDetectors` map associates, to each sensitive detector name (e.g. tracker, ECal, GRAIN), a vector of `TG4HitSegment` objects. Each segment represents the energy deposited along a finite step and stores the start and end positions, the deposited energy and the identifiers of the contributing tracks. For the ECal, the segments in the calorimeter sensitive volumes are the only truth input to the digitization and backtracking algorithms.

Use in the SAND ECal simulation and backtracking. For the electromagnetic calorimeter, the `TG4HitSegment` objects associated with the ECal sensitive volumes represent the microscopic energy depositions in the scintillating fibers and absorber. The ECal digitization step (Section 4.2) uses these segments as input, maps each segment to a cell and converts the deposited energy, position and time into digitized ADC/TDC values for the two photosensors at the cell ends. The resulting digitized cells are then used as input by the clustering algorithm of Section 5.1.

The `TG4Event` objects are accessed by the `edep-reader` library introduced in Section 5.2, which wraps trajectories and hit segments into the `EDEPTree` and `EDEPTrajectory` classes used for Monte Carlo backtracking. Hit segments from `SegmentDetectors` are grouped per trajectory and per detector component, while the parent-child relations between `TG4Trajectory` objects are used to build the `EDEPTree`. The backtracking algorithm of Section 5.3 exploits this structure to identify, for each reconstructed cluster, the set of the so called generator trajectories that deposited energy in its cells and to compute the corresponding true quantities and to define the correspondent true cluster, used in the performance studies of Chapter 5 and in the analysis in Chapter 6.

4.2 ECal digitization

The ECal simulation chain starts from the energy deposited hits simulated by `edep-sim` and stored as `TG4HitSegment` objects in the `EDepSimEvents` tree of the `TG4Event` output (Section 4.1). The digitization step consists of a C++ module integrated in the `sandreco` framework which takes these energy deposits and

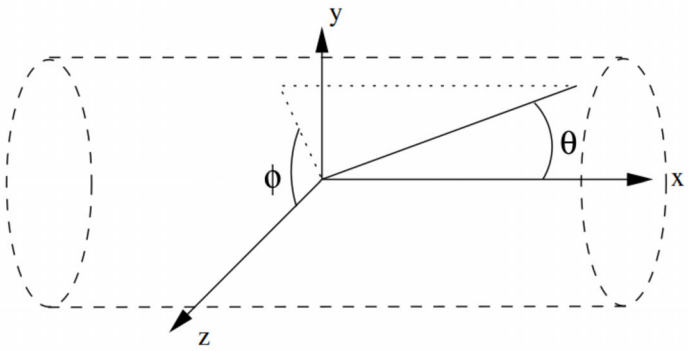

Figure 4.1: Definition of the SAND coordinate system and of the polar (θ) and azimuthal (ϕ) angles. The origin is at the center of the detector; the x axis points along the barrel module length direction, the y axis vertically upwards, and the z axis is along the neutrino beam. Module positions are parameterized by (θ, ϕ) in this frame.

converts them into digitized photo-detector signals, stored in a ROOT `tDigit TTree`. The resulting digits are the only ECal inputs used by the clustering and Monte Carlo backtracking tools described in Secs. 5.1, 5.2 and 5.3 in Chapter 5.

The digitization reproduces the calorimeter segmentation, the light production in the scintillating fibers, the propagation of light to the two photosensors at the cell ends and the formation and digitization of the corresponding electronic signals.

In the barrel, each of the 24 modules is segmented radially into five sampling layers; within each layer twelve cells are present, so that every barrel module contains 60 readout cells per side, independent of its position around the azimuth. The segmentation of a single barrel module into layers and readout cells is illustrated in Figure 4.2.

In the endcaps, the segmentation also consists of five layers, but the number of cells per layer is not constant: all modules share the same readout cell width, while the number of columns (and hence the total cell count) varies module by module, the geometry of the barrel and endcap modules is shown in Figure 4.3 in which the endcap modules have different dimensions and so a different number of columns. The azimuthal position of each module and the definition of the polar and azimuthal angles follow the SAND reference frame shown in Figure 4.1.

Each ECal cell is labeled by a unique integer identifier that encodes the detector (barrel or endcap), the module, the layer and the cell index within the layer, and this convention is used consistently throughout the digitization, clustering (Section 5.1) and backtracking (Section 5.3) chain.

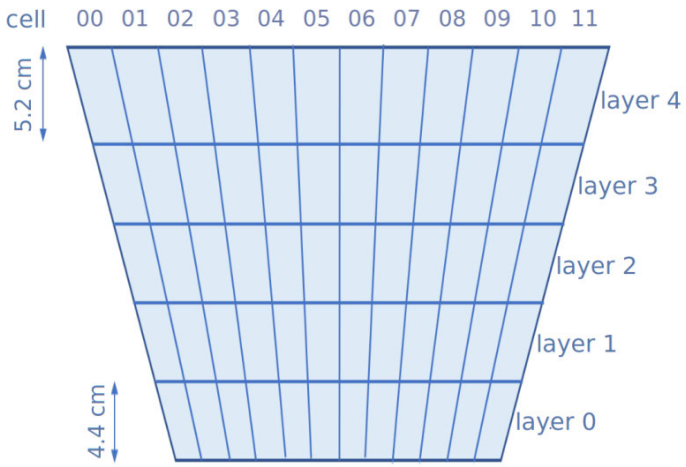

Figure 4.2: Segmentation of a single barrel ECal module into five readout layers (labelled 0-4) and twelve cells per layer. The cell height is 4.4 cm in layers 0-3 and increases to 5.2 cm in layer 4, while the cell width is constant in all layers. All barrel modules share this readout pattern, so that each module contains 60 cells per side, independent of its azimuthal position.

For each `TG4HitSegment` in the ECal scintillator volumes, the digitization module first determines the cell and the corresponding cell geometry along the readout fibers. The hit position is mapped to a global cell identifier through the `SANDGeoManager` utilities, which also compute the distances d_1 and d_2 from the hit point to the two photosensors along the fiber path inside the cell. The deposited energy dE of the segment is then associated with this cell and shared between the two sides according to a parametrized attenuation law.

The average number of photo-electrons produced at each photosensor is written as

$$\mu_{pe}^{(1,2)} = dE\, A_\ell(d_{1,2}, \ell)\, E_{pe}, \tag{4.1}$$

where $A_\ell(d_{1,2}, \ell)$ is the light attenuation factor along the fiber for a hit at distances $d_{1,2}$ from the two ends in layer ℓ, and E_{pe} is the energy-to-photoelectron conversion factor. The attenuation factor implements the double-exponential parametrization used in KLOE,

$$A_\ell(d) = p_1 \exp\left(-\frac{d}{L_1}\right) + (1 - p_1) \exp\left(-\frac{d}{L_2(\ell)}\right), \tag{4.2}$$

with $p_1 = 0.35$, $L_1 = 50\,\text{cm}$ and a layer-dependent long attenuation length $L_2(\ell)$ equal to 430 cm for the innermost layers $\ell = 0, 1$, 380 cm for $\ell = 2$ and 330 cm for

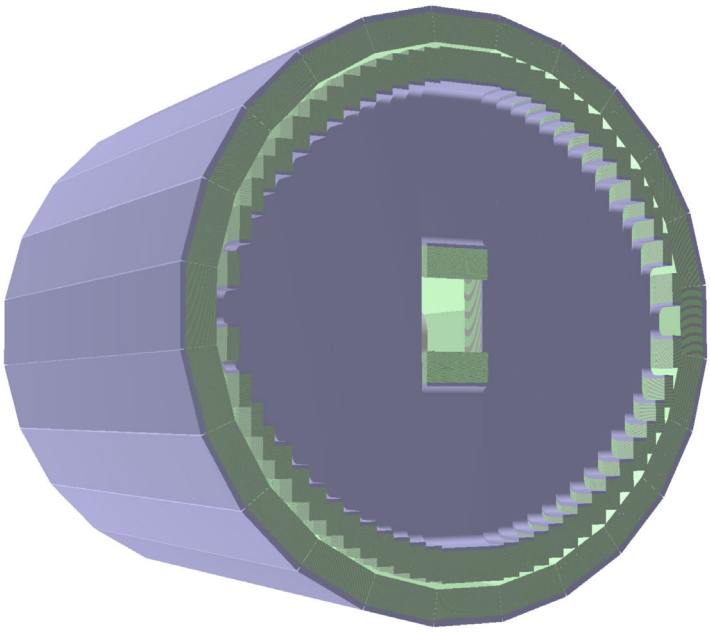

Figure 4.3: Three-dimensional view of the SAND electromagnetic calorimeter geometry as implemented in the `gdml` description. The system consists of 24 barrel modules and two endcaps with 32 modules each. All barrel modules have the same length in the x coordinate and share the same granularity, with twelve cells per layer (60 cells per module side), so that only their azimuthal positions differ. In the endcaps, instead, the physical length and width of the individual modules change with the polar angle, and the number of cells per module varies accordingly.

the outer layers $\ell = 3, 4$. This mild layer dependence of $L_2(\ell)$ reflects the different scintillating-fiber populations used in the inner and outer parts of the modules, which exhibit slightly different effective long attenuation lengths. The conversion factor E_{pe} is tuned such that a minimum-ionizing particle crossing the cell at its center produces, on average one photo-electron per MeV at each side, consistent with the KLOE calibration measurements.[89]

For each side of the cell, the actual number of photo-electrons N_{pe} is then extracted from a Poisson distribution with mean $\mu_{pe}^{(1,2)}$. Each photo-electron is assigned an arrival time at the corresponding photosensor according to

$$t_{\mathrm{pe}} = t_{\mathrm{cross}} + t_{\mathrm{scint}} + t_{\mathrm{prop}}(d_{1,2}) + \delta t_{\mathrm{elec}}, \tag{4.3}$$

where t_{cross} is the time of the particle crossing the cell as provided by `edep-sim`, t_{scint} is sampled from the scintillation time distribution of the fiber (with param-

eters tuned to reproduce the KLOE time response), $t_{\mathrm{prop}}(d_{1,2})$ is the light propagation time along the fiber and δt_{elec} is a Gaussian smearing term with a width of order 1 ns that accounts for the intrinsic timing resolution of the photosensors and front-end electronics. The propagation time is modelled as

$$t_{\mathrm{prop}}(d) = v_{\mathrm{fib}}\, d, \tag{4.4}$$

with an effective propagation constant $v_{\mathrm{fib}} \simeq 5.85\,\mathrm{ns\,m^{-1}}$, which corresponds to a group velocity of about $17\,\mathrm{cm\,ns^{-1}}$ for light in the scintillating fibers, in agreement with the KLOE measurements.[89]

For each cell side, all generated photo-electrons are collected and sorted by arrival time. The electronics response is then simulated by integrating the photons in a fixed acquisition window of duration Δt_{int} and applying a dead time Δt_{dead} after each accepted pulse. Only integration windows containing more than a minimum number of photo-electrons N_{pe}^{thr} are promoted to digitized signals. For each such pulse, the total charge is converted into an ADC value

$$S^{(1,2)} = N_{pe}\,\mathrm{ADC_{pe}}, \tag{4.5}$$

with $\mathrm{ADC_{pe}} = 4$ ADC counts per photo-electron, while the TDC time is defined by a simple model of the discriminator behaviour. Two options are implemented: a constant-fraction discriminator, in which the TDC value corresponds to the time of the photo-electron at a fixed fraction $0 < f < 1$ of the total charge in the pulse, and a fixed-threshold mode in which the TDC is given by the time of the photo-electron that brings the integrated charge above a configurable threshold. In the studies presented in this thesis the constant-fraction configuration is used, with $f = 0.15$, to mimic the timing scheme adopted in KLOE.[89]

The output of the ECal digitization consists of a collection of digitized cells, stored in the `tDigit` tree. For each digitized cell, the following quantities are recorded:

- the unique cell identifier;
- the position of the cell center in the global SAND reference frame and the effective cell length along the fibers;
- the indices of the detector, module, layer and cell within the layer.

For each of the two photosensors coupled to the cell, the digitization stores:

- the module side identifier;
- the TDC value defined by the chosen discriminator logic;

- the list of simulated photo-electrons contributing to the pulse, with their arrival times and the index of the underlying `TG4HitSegment` in the `EDepSimEvents` tree (Section 4.1).

These digitized cells are the starting point of the ECal clustering algorithm (Section 5.1). In the reconstruction, the same attenuation model and propagation constant are used to convert ADC and TDC values back into reconstructed hit energy, time and position via the parametrizations discussed in Chapter 5. The explicit link to the original `TG4HitSegment` indices is then exploited by the `edep-reader` library (Section 5.2) and by the backtracking tools of Section 5.3 to associate reconstructed clusters with the simulated particle trajectories that generated them.

4.3 Tracker and GRAIN reconstruction

4.3.1 GRAIN

Neutrino interactions that produce activity in GRAIN are processed by two independent reconstruction chains. The first is the inner tracker chain, which reconstructs charged particles from the tracker digitized signals into three-dimensional tracks and vertices, and extrapolates the track parameters and covariance matrices to the entrance of the GRAIN cryostat. The second is a dedicated optical chain, in which the GRAIN cameras reconstruct the three-dimensional pattern of scintillation light in the liquid argon volume. The long-term goal is to match tracks reconstructed in GRAIN to tracker tracks and eventually to clusters from the surrounding ECal, providing a global description of each event.

GRAIN optical simulation and reconstruction are implemented in a standalone framework, separate from the `sandreco` executables used for the tracker and ECal. Both reconstruction chains (`sandreco` and GRAIN) take as input the same `edep-sim` energy deposit tree and GDML geometry, but all steps from optical photon production to "camera digits" and optical track reconstruction are performed by dedicated codes outside the standard SAND reconstruction.

In both optical readout options considered for GRAIN, lens based and coded aperture mask cameras, the optical chain is organized in two stages. In a first digitization stage, the energy deposits from `edep-sim` in the GRAIN volume are converted into scintillation photons by a dedicated GEANT4 based simulation of liquid argon scintillation and transport. A standalone detector response simulation then models the SiPM photon detection efficiency, dark noise, optical crosstalk, afterpulses and the response of time over threshold or charge integration readout ASICs. The result is, for each camera, a set of "camera digits" describing, for every SiPM

pixel, the number of detected photons and, when available, the leading edge time, defined as the time at which the pixel signal crosses a fixed threshold on the rising edge of the pulse, and optionally the full sampled waveform. These camera digits form the input to the reconstruction algorithms described below.

Lenses option In the lens based configuration, each camera forms a two-dimensional image of the scintillation light on the sensor. Track reconstruction relies on a pattern recognition algorithm based on the Hough transform, which searches the pixel intensity maps for straight line structures and groups the pixels belonging to each structure into two-dimensional clusters, defined as contiguous sets of active pixels associated with the projection of a single track or track segment. To obtain a three-dimensional description of the tracks inside GRAIN, the liquid argon volume is discretized into small three-dimensional cells (voxels). For each camera, voxels whose projection onto the sensor plane falls within a given cluster are marked as compatible with that track, and voxels seen consistently in multiple cameras are then fitted with straight lines, forming three-dimensional track parameters.

Coded aperture mask option In the coded aperture mask configuration, the lens is replaced by a patterned mask in front of the sensor, so that each camera records, in its SiPM pixels, a superposition of shadowgrams rather than a direct image of the event. The three-dimensional light distribution in GRAIN is reconstructed by solving an inverse problem with a maximum likelihood expectation-maximization algorithm, which uses precomputed response matrices to estimate the light yield in each voxel from the measured pixel counts. These response matrices store, for every voxel in the GRAIN volume and every sensor pixel, the probability that a scintillation photon produced in that voxel is detected by that pixel. They are computed once from the detector geometry and optical simulation and then kept fixed during reconstruction. The reconstruction is performed using the information from all cameras at once, and the resulting voxel maps represent the best estimate of the three-dimensional light distribution in the active volume. [108]

In both the options, the reconstructed three-dimensional light distribution is then converted into track candidates by selecting voxels with a reconstructed light yield above a suitable threshold, grouping neighbour-selected voxels forming three-dimensional clusters, and eventually fitted with a straight line. The resulting line parameters define the reconstructed track segments in GRAIN.

Finally, the optical readout can be exploited for calorimetry. For each reconstructed track, and for each camera, the total number of detected photons is obtained by summing all image pixels or voxels that have been assigned to that

track. After corrections for the geometrical acceptance and light collection efficiency of each camera, the total number of scintillation photons produced by the track is estimated and converted into an energy deposit using the light yield of liquid Argon. A first implementation of this procedure, tested on single muon tracks generated inside GRAIN and reconstructed with the lens-based option, achieves a mean energy resolution of order $\sigma_E/E \simeq 18\%$ for forward going tracks, showing that the optical system can provide an independent calorimetric measurement of the energy deposited in GRAIN. [90]

4.3.2 Tracker

As introduced in Chapter 3, the SAND inner tracker has two designs currently under development. A straw-tube tracker (STT), and a drift-chamber (DC). In both cases, the reconstruction chain starts from the digitized wire hits produced by the `Digitize` executable, which for each fired wire stores a TDC time and an ADC proportional to the collected charge. These digits are written to the `tDigit TTree` as `dg_wire` objects and are used as the input to the `Reconstruct` program. In the SAND reference frame, the solenoidal magnetic field is oriented along the x axis, so that charged particles bend in the transverse (y, z) plane, while the x direction is approximately non-bending.

In the two *fast* modes of reconstruction (`fast_only_primaries` and `fast`), pattern recognition is bypassed and digits are associated directly to Monte Carlo trajectories using the information provided by `edep-sim`. The simulated trajectories in the `TG4Event` are analyzed and if the digits whose hit segments are compatible in position and direction with a given trajectory, the corresponding reconstructed `track` object is filled with ordered lists of hits in the two tracker projections. The `fast_only_primaries` configuration restricts this procedure to primary trajectories exiting from the neutrino vertex, while `fast` applies the same truth-based association to all charged trajectories with at least one matched digit.

In both cases, the three-dimensional helix parameters of the trajectory are obtained by a two-step least-squares fit: a circle is first fitted in the bending (y, z) plane and a straight line is then fitted in the track longitudinal coordinate. This corresponds to a χ^2 minimization of the distance between the helix and the measured hit positions and is used for both the straw-tube and drift-chamber options.

The *full* mode instead performs pattern recognition without using MC truth. The interaction vertex is first estimated by scanning the tracker along z (beam direction) and, for each tracker module, computing the mean and RMS of the hit positions in x and y. The vertex z position is taken as the module where the transverse spread of hits is minimal, i.e. where the hits are most concentrated in

clusters in the (x, y) plane. Starting from this vertex estimate (z_V, y_V), the hits in the bending plane are transformed from the (z, y) coordinates to an auxiliary (u, v) space where tracks emerging from the vertex map into straight lines. The corresponding angle $\phi = \arctan(v/u)$ is used as a one-dimensional pattern-recognition variable: peaks in the ϕ distribution identify track candidates, and hits contributing to each peak are grouped into clusters in successive tracker modules. Clusters in the two projections are then matched in z to form three-dimensional tracks, which are finally fitted with the same circle and line χ^2 helix fit described above.

Two additional configurations are available for studies of advanced fitting techniques. In the `primary_only_kf` mode, the digits are first organized per tracker module and grouped into three-dimensional clusters of adjacent fired tracker cells. For each cluster, a local straight-line fit is performed and a "tracklet" is returned, i.e. a 3D segment characterised by a position, a direction and a fit quality at the correspondent module z position. Only tracklets with good χ^2 are kept and stored as a map of z-ordered measurements, which are then used as inputs to the extended Kalman filter [109]. The Kalman filter propagates the track state through the magnetic field, including multiple scattering and energy loss as process noise, and updates the state at each measurement tracker plane. The smoothed state at the downstream end is then converted into the helix parameters stored in the final `track` structure.

The algorithms outlined in this subsection define the nominal tracking performance expected for the SAND inner tracker. In the analyses presented in this thesis, however, the detailed tracker reconstruction output is not used directly. Whenever tracker information is required, the true kinematic quantities from the `edep-sim` output are used.

Chapter 5

Reconstruction algorithms for the SAND ECal

5.1 ECal clustering

Particle reconstruction in the ECal is performed with a C++ clustering algorithm integrated in the ECal reconstruction framework. The algorithm takes as input the ROOT file produced by the digitization step (Section 4.2), which contains the digitized cells, and produces a ROOT TTree of reconstructed clusters. Each cluster groups together spatially and time adjacent ECal cells that are consistent with originating from the same particle.

Complete vs. incomplete cells and multi photo-signals. Each digitized cell is classified as complete or incomplete. A complete cell has a photo-signal on both photosensors at the two ends of the module; an incomplete cell carries a signal on only one end. If multiple photo-signals per side are present creating pile-up, the algorithm pairs signals across the two ends when the absolute time difference is below a tolerance

$$|\Delta t| \; < \; \delta \equiv L \, \frac{1}{v_{\text{eff}}}, \tag{5.1}$$

where L is the cell length and v_{eff} is the effective light propagation speed in the fibers [89]. Each successful pairing is stored as a complete cell instance with one photo-signal per side. Unpaired signals are kept as single-ended incomplete cells. The clustering stage initially uses only the complete cells.

Pre-clustering by spatial adjacency. Starting from one of the complete cells of the event as a seed, neighbor cells are recursively added to a growing pre-cluster. Adjacency is defined by Euclidean distances in the appropriate module plane and differs for barrel and endcap so as not to connect cells across modules:

- Endcaps: cells are neighbors if $\sqrt{(x_i - x_j)^2 + (z_i - z_j)^2} < 65.70\,\text{mm}$.
- Barrel: cells are neighbors if $\sqrt{(y_i - y_j)^2 + (z_i - z_j)^2} < 72.36\,\text{mm}$,

where the numbers cited are the maximum distance that two cell central points can have in the "non reconstructed" plane, taking into account different layer heights, in endcap and barrel respectively (see Section 4.2). The procedure proceeds until no further complete neighbor cells are found; then a new seed is chosen among the remaining complete cells, and the process repeats.

Per-cell reconstruction. For each paired complete cell with photo-signal times (t_A, t_B)[1] and ADC signals $(\mathrm{S}_A, \mathrm{S}_B)$:

- **Energy**: The energy for each cell is reconstructed according to

$$E = \frac{1}{2}\left(\mathrm{S}_A/A_{l,A} + \mathrm{S}_B/A_{l,B}\right) / \left(f_{att,tot} \cdot E_{pe} \cdot \mathrm{peADC},\right) \tag{5.2}$$

  where $\mathrm{S}_{A,B}$ is the number of ADCcounts after digitization on side A, B, $A_{l,A,B}$ is the attenuation factor calculated as in Equation 4.2, $f_{att,tot}$ is the ratio between the active and total deposited energy, obtained for electrons in Subsection 5.5.1, E_{pe} is the number of photo-electron per unit of energy and $peADC$ is the number of ADC counts per photo-electron.

- **Position**: For each of the barrel cells, y and z coordinates are taken as the geometrical center of the fired cell in the yz plane, while the x coordinate is reconstructed as $x = \frac{1}{2} v_{\mathrm{eff}} (t_a - t_b)$, where $t_{A,B}$ is the time of arrival of the light signal to the $\mathrm{PMT}_{A,B}$. For the endcap cells x and z coordinates are taken as the geometrical center of the cell, while the y is the one reconstructed.

- **Time**: The time t in each cell is reconstructed using $t = \frac{1}{2}(t_A + t_B) - \frac{L}{2v}$. where quantity t therefore represents the scintillation time in the cell after subtracting the light–propagation time to the photosensors. In the Monte Carlo configuration used in this thesis, where each event contains a single neutrino interaction, all TDC times are stored with respect to the true interaction time, so that t is measured relative to the neutrino interaction in the SAND volume. In a realistic beam–spill configuration, the same reconstruction formula would be applied to TDC values defined with respect to a global trigger or spill time; in that case t would give the cell scintillation time relative to that global reference, and the neutrino interaction time would have to be determined event by event from reconstruction or external timing.

[1] In this Chapter A, B represent the two PMTs located at the ends of each ECal module cell.

Per-cluster observables. Once the complete cells are reconstructed in a pre-cluster, global cluster observables are calculated as energy-weighted:

$$E_{\text{tot}} = \sum_i E_i, \tag{5.3}$$

$$\langle x \rangle = \frac{\sum_i E_i x_i}{E_{\text{tot}}}, \quad \langle y \rangle = \frac{\sum_i E_i y_i}{E_{\text{tot}}}, \quad \langle z \rangle = \frac{\sum_i E_i z_i}{E_{\text{tot}}}, \tag{5.4}$$

$$\langle t \rangle = \frac{\sum_i E_i t_i}{E_{\text{tot}}}. \tag{5.5}$$

The spread in position is calculated using the unbiased effective-statistics correction

$$n_{\text{eff}} \equiv \frac{(\sum_i E_i)^2}{\sum_i E_i^2}, \qquad \sigma_x = \sqrt{\frac{n_{\text{eff}}}{n_{\text{eff}} - 1} (\langle x^2 \rangle - \langle x \rangle^2)}, \tag{5.6}$$

and analogously for σ_y, σ_z, with $\langle x^2 \rangle \equiv \sum_i E_i x_i^2 / E_{\text{tot}}$.

Time-structure split. To resolve accidental merges of spatial-adjacent cells, for each pre-cluster the time dispersion is calculated. The times of the original energy deposition in the cell longitudinal coordinate, at the two ends, after propagation correction along the fiber, are calculated as follows:

$$t'_{A,i} \equiv t_{A,i} - \frac{d_{1,i}}{v_{\text{eff}}}, \qquad t'_{B,i} \equiv t_{B,i} - \frac{d_{2,i}}{v_{\text{eff}}}, \tag{5.7}$$

where $d_{1,2} = \frac{1}{2}\left(L \pm \frac{\Delta t}{v_{\text{eff}}}\right)$ are the distances of the original signal from thwe two ends of the modules.

Using the corresponding ADC values as weights, compute

$$\langle t'_A \rangle = \frac{\sum_i \mathrm{S}_{A,i}\, t'_{A,i}}{\sum_i \mathrm{S}_{A,i}}, \qquad \langle {t'_A}^2 \rangle = \frac{\sum_i \mathrm{S}_{A,i}\, {t'_{A,i}}^2}{\sum_i \mathrm{S}_{A,i}}, \tag{5.8}$$

$$\langle t'_B \rangle = \frac{\sum_i \mathrm{S}_{B,i}\, t'_{B,i}}{\sum_i \mathrm{S}_{B,i}}, \qquad \langle {t'_B}^2 \rangle = \frac{\sum_i \mathrm{S}_{B,i}\, {t'_{B,i}}^2}{\sum_i \mathrm{S}_{B,i}}. \tag{5.9}$$

With the correction defined from the ADC weights $n^A_{\text{eff}} = \frac{(\sum_i \mathrm{S}_{A,i})^2}{\sum_i \mathrm{S}^2_{A,i}}$ (and analogously for B), form the RMS values

$$t^A_{\text{RMS}} = \sqrt{\frac{n^A_{\text{eff}}}{n^A_{\text{eff}} - 1} \left(\langle {t'_A}^2 \rangle - \langle t'_A \rangle^2\right)}, \qquad t^B_{\text{RMS}} = \sqrt{\frac{n^B_{\text{eff}}}{n^B_{\text{eff}} - 1} \left(\langle {t'_B}^2 \rangle - \langle t'_B \rangle^2\right)}. \tag{5.10}$$

If

$$\sqrt{(t^A_{\mathrm{RMS}})^2 + (t^B_{\mathrm{RMS}})^2} \; > \; 5\,\mathrm{ns}, \tag{5.11}$$

the pre-cluster is split into up to four sub-clusters by the signs of the residuals $\left(t'_{A,i} - \langle t'_A \rangle, t'_{B,i} - \langle t'_B \rangle\right)$:

$$(+,+), \quad (+,-), \quad (-,+), \quad (-,-).$$

In this context the "time dispersion" is the RMS spread of the propagation-corrected times $t'_{A,i}$ and $t'_{B,i}$ over the cells of a pre-cluster on each side, i.e. to the intrinsic temporal width of the cluster as seen by each photosensor. For a relativistic particle ($\beta \simeq 1$) crossing the ECal, the time of flight difference between the earliest and latest cells that can still belong to a single shower is limited by the geometric size of a module and is therefore of order a few nanoseconds at most. A threshold of 5 ns corresponds to a path difference of about $c \times 5\,\mathrm{ns} \sim 1.5\,\mathrm{m}$, safely larger than the physical extension of an individual cluster inside a module. The choice $\Delta t_{\mathrm{split}} = 5\,\mathrm{ns}$ is thus a conservative working point: pre-clusters produced by a single particle are rarely split, whereas pre-clusters containing two or more time-separated components (for example overlapping showers or late nuclear activity) typically exceed the 5 ns dispersion and are split into sub-clusters. Per-cluster observables are recomputed for each sub-cluster, and the split test is iterated until no sub-cluster passes the 5 ns criterion.

Spatial–temporal merge. To correct for over-splits and add compatible sub-clusters, pair of clusters (i, j) are compared and merged if they are close both in space and time. A global pre-selection requires $\Delta t < 2.5\,\mathrm{ns}$. Then a module-aware spatial check is applied:

- Endcaps: require $|y_i - y_j| < 250\,\mathrm{mm}$ and $\sqrt{(x_i - x_j)^2 + (z_i - z_j)^2} < 250\,\mathrm{mm}$.
- Barrel: require $|x_i - x_j| < 250\,\mathrm{mm}$ and $\sqrt{(y_i - y_j)^2 + (z_i - z_j)^2} < 250\,\mathrm{mm}$.

When two clusters are merged, their cell lists are concatenated and cluster observables are recomputed. The procedure continues until no more merges are possible.

Choice of merge distance. The spatial merge parameter used in merge routine has been fixed to $\Delta r_{\mathrm{merge}} = 25\,\mathrm{cm}$ based on a scan of the mean energy bias $E_{\mathrm{true}} - E_{\mathrm{reco}}/E_{\mathrm{true}}$ versus merge distance shown in Figure 5.1. For each merge distance to check, the same 250 ν_e interaction sample, with a beam-like energy spectrum, forced to interact in the SAND tracker volume has been used. E_{true} is the total energy deposited in the ECal by the primary electron that has been selected

as the main generator of the cluster (see Section 5.3). For small merge values ($\lesssim 20\,\text{cm}$) the bias is negative, indicating under-merging (fragments of the same cluster remain split, so $E_{\text{reco}} < E_{\text{true}}$). At large values ($\gtrsim 30\,\text{cm}$) the bias turns positive, indicating over merging. The crossing region around 25 cm minimizes the bias and is consistent with zero within uncertainties, while remaining conservative against over-merging. This scan was performed with the time-split fixed at 5 ns; the two parameters are coupled and should be re-optimized together when PID is finalized.

Particle dependence. Both the merge and split threshold parameters are not constant: they depend on particle type and energy because the active–total response and topology differ and once particle identification is available in the framework, these parameters should be tuned per particle. For electrons, the calibration study of the active–passive factor presented in Section 5.5.1 provides the appropriate reference for such a tuning.

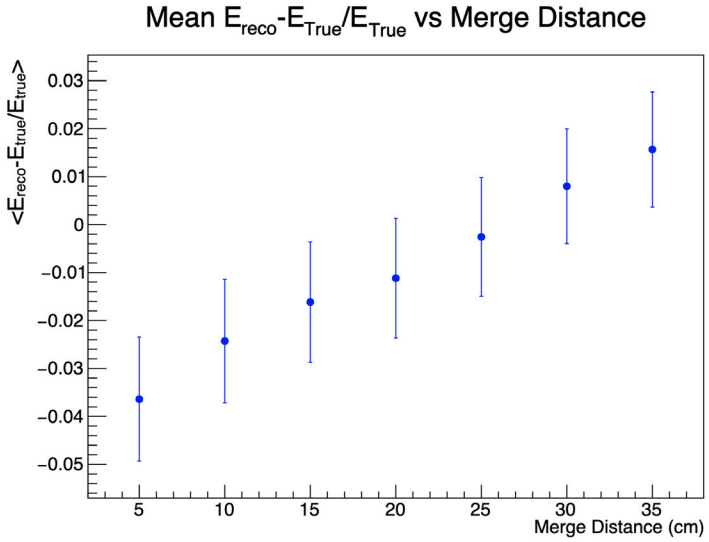

Figure 5.1: $(E_{\text{reco}} - E_{\text{true}})/E_{\text{true}}$ as a function of the merge distance. Points are from the same sample of 250 ν_e interactions, with beam-spectrum energies, interacting in the SAND tracker volume; all interactions are selected, no spill has been simulated. E_{true} is the energy deposited in the ECal by the primary electron selected as the main generator of the cluster. The bias crosses zero near 25 cm, motivating the choice $\Delta r_{\text{merge}} = 25\,\text{cm}$ used in the merge routine. Vertical error bars show the standard error on the mean.

Direction and apex. For clusters spanning multiple layers in the modules, per-layer energy-weighted positions are computed and fitted with a weighted least-

squares straight line versus the known layer coordinates. The fit uses energy-dependent weights and an energy-based depth offset to estimate an apex point (a_x, a_y, a_z) and a unit direction vector (s_x, s_y, s_z) for the cluster.

Recovery of incomplete cells. The final stage of the algorithm recover single-ended incomplete cells associating them to the nearest cluster using a tight range of space and time difference. An incomplete cell is linked to the closest cluster if its centroid is within $\Delta r < 15\,\text{mm}$ (in the appropriate module plane) and $|\Delta t| < 3\,\text{ns}$. The corresponding single-ended energy is estimated with a single value of ADC as

$$E = E^{(\text{single})}_{\text{fromADC}}(\text{S}; d, \text{layer}), \tag{5.12}$$

using a layer-dependent attenuation factor evaluated at the distance d to the firing photocathode, where d is inferred from the cluster centroid projected along the fiber axis (barrel: $d = \frac{L}{2} \pm x_{\text{cl}}$; endcaps: $d = \frac{L}{2} \pm y_{\text{cl}}$).

Cluster type tagging. Each final cluster is labeled as barrel, endcap, or mixed depending on whether its cells belong exclusively to a barrel module, exclusively to an endcap module, or to both. The tag is derived from the cell identifiers and is used in the following for analysis and quality control.

5.2 edep-reader tool

`edep-reader` is a `C++17` helper around the `edep-sim` truth output (`TG4Event` described in Section 4.1) that organizes the Monte Carlo record as a navigable tree (`EDEPTree`), where parent–child relations between particle trajectories are explicit and per–trajectory quantities are easy to query. Each event is represented as a collection of particle trees, with one tree rooted at each primary particle, built from four classes:

- `EDEPTree` (event–level container root): given a `TG4Event` and a `TGeoManager`, it (i) builds a per–track, per–subdetector (component) map of the trajectories and the hits deposited in the different detector volumes: `std::map<int, std::map<component, std::vector<EDEPHit>>>` from `SegmentDetectors`; (ii) instantiate one `EDEPTrajectory` for each GEANT4 `TG4Trajectory`; and (iii) links trajectories into a parent/children tree via `CreateTree`.
- `EDEPTrajectory` (nodes, one per GEANT4 `TG4Trajectory`): each instance stores identifiers (`id`, `parent_id`, `pdg_code`), parent/children links (`GetParent()`, `GetChildrenTrajectories()`), interaction metadata (`GetInteractionNumber()`, `GetReaction()`) and kinematics (`GetInitialMomentum()`). Geometry-aware

functions are present: `GetTrajectoryPoints()`, first/last points `GetFirstPointsInDetector(component)`, entering/exiting flags (`IsEntering(component)`, `IsExiting(component)`), and a hit map `GetHitMap()`.

- `EDEPTrajectoryPoint`: space–time samples along a trajectory, grouped per detector component. Each point provides access to the local four–position and four–momentum via `GetPosition()` and `GetMomentum()`. Points are owned by `EDEPTrajectory` inside per–component containers `std::map<component, std::vector<EDEPTrajectoryPoint>>`.

- `EDEPHit`: truth energy-deposition record with a unique `id`, start/stop four–vectors and deposited energy. Hits are are auxiliary data attached to each `EDEPTrajectory`, accessed through its hit map `GetHitMap()`, filtered by detector `component` and stored in time order as `std::map<component, std::vector<EDEPHit>>`.

Iteration pattern. `EDEPTree` provides depth–first iterators over the particle trees: starting from each primary, the iterator first descends to the first child if present, otherwise advances to the next sibling; when siblings are exhausted, it returns to the parent and continues. Helper methods used in this thesis include `GetTrajectory(int)`, `GetParentOf(int)` and `GetTrajectoryWithHitIdInDetector(int, component)`.

A scheme of the code is shown in Figure 5.2

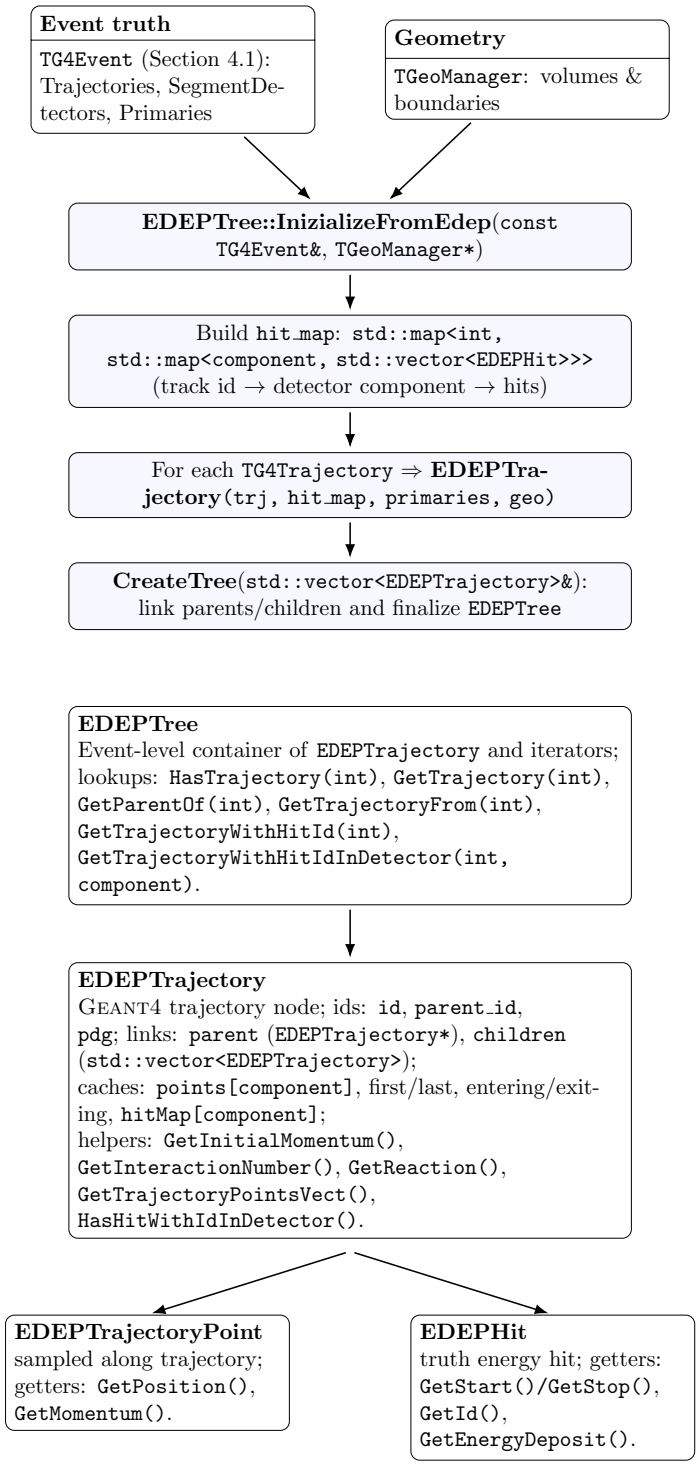

Figure 5.2: Illustrative scheme of *edep-reader*: inputs, minimal build pipeline, and core classes.

The backtracking algorithm described in Section 5.3 uses three operations that edep-reader provides in a unified interface: (i) association between hits and trajectory to collect all trajectories that produced photoelectrons in a reconstructed ECal cluster (`GetTrajectoryWithHitIdInDetector(int id, component::ECAL)`); (ii) tree navigation going backward from those trajectories to find the "entering" `cluster_generator`, using parent/child links (`GetParent()`, `GetChildrenTrajectories()`); (iii) truth observable computation by summing the hits of deposited energies in the ECal volumes over the relevant hits from `GetHitMap()` and by evaluating the generator's entry momentum at the first ECal point (`GetMomentum()` at the point returned by `GetFirstPointsInDetector(component component_name)`).

This design eliminates manual parsing of `TG4Event` and makes the reconstructed-truth matching reproducible and consistent with the SAND reconstruction data format used throughout this thesis and for further analysis.

5.3 Monte Carlo-cluster backtracking

Any use of reconstructed objects relies on a mapping to the underlying Monte Carlo information. A robust reconstructed-truth association at cluster level is essential to validate reconstruction algorithms, to calculate calibration constants, to build particle identification algorithms, to train machine-learning classifiers, and to study the detector effects that can affect physics analyses. In particular, it is necessary to know which simulated particles have contributed to a given cluster and how it develops in the ECal.

In the context of this thesis, the reconstructed ECal clusters are the common building block to all subsequent performance studies and physics applications. In this chapter they are the objects on which cluster–level observables are defined and studied, and from which the active–passive calibration factor and the intrinsic energy resolution of the calorimeter are extracted. In Chapter 6 the same clusters provide the input to the neutron–tagging algorithm for $\bar{\nu}_\mu p \to \mu^+ n$ interactions on hydrogen. To carry out these studies, for each reconstructed cluster, a well defined truth counterpart is needed, specifying also which Monte Carlo particles have contributed to its energy deposits and by how much.

A "true cluster" is built by collecting all Monte Carlo trajectories that produce photoelectrons in the cells belonging to that cluster, selecting one or more of them as so-called generators, and computing truth-level summary quantities[2].

[2]In this section, every time trajectories, trajectory points, hits and trees tterms are used they have to be referred to `EDEPTrajectory`, `EDEPTrajectoryPoint`, `EDEPHit` and `EDEPTree` objects defined in Section 5.2.

When several trajectories contribute, the true cluster explicitly stores the list of generators and their individual contributions.

The code is developed in C++17 and processes two ROOT input files. The first file contains the full simulated truth information produced by edep-sim (Section 4.1), and the second includes the reconstructed ECal clusters, provided by the clustering step described in Section 5.1.

The output consists of a ROOT file in which each entry represents an event in SAND, and, event by event, two TTrees are produced, as shown below:

```
KEY: TTree    tMC;  Monte Carlo clusters
KEY: TTree    tCluster;      reconstructed clusters
```

- The tCluster TTree contains one branch consisting of a std::vector<cluster>, each cluster holds the same structure described in Section 5.1.
- The tMC contains one branch consisting of a std::vector<true_cluster>, each true_cluster holds the following data format: where the cluster_generator

```
struct truecluster{
    int tid; /**< main generator particle identifier - \textsc{Geant4} track ID */
    double x; /** True cluster position */
    double y;
    double z;
    double t;
    double e; /** True cluster deposited energy in the active material */
    double vis_e; /** True cluster photo-electrons */
    int n_traj; /** Number of trajectories contributing to the cluster */
    double sx; /** True cluster direction cosines */
    double sy;
    double sz;
    int ntot_cell; /** Number of cells in the cluster */
    int cell_l0; /** Number of cells in layer x */
    int cell_l1;
    int cell_l2;
    int cell_l3;
    int cell_l4;
    double energy_l0; /** Energy deposited in layer x */
    double energy_l1;
    double energy_l2;
    double energy_l3;
    double energy_l4;
    double lay0_maxE; /** The maximum energy deposited between all the cells in layer */
    double lay1_maxE;
    double lay2_maxE;
    double lay3_maxE;
    double lay4_maxE;
    double asymmetry; /** (MaxE_all_layer - MinE_all_layer) / (MaxE_all_layer + MinE_all_layer) */
    double Eoverp; /** Cluster reco energy divided by main generator true momentum */
    bool moregens= false;
    std::vector<cluster_generator> vec_generator;  /** Generators that participate in the cluster*/
};
```

,

Listing 1: Definition of the truecluster structure.

owns the following data structure:

```
struct cluster_generator{
  int pdg_code;
  int parent_pdg_code; /** pdg code of the generator parent */
  int track_id; /** Geant track ID  */
  int parent_track_id; /** Geant generator parent track ID */
  double dep_energy; /** Energy deposited in the cluster active material  */
  double initial_energy; /** Monte Carlo energy in the first trajectory point in ECal */
  double initial_momentum; /** Monte Carlo momentum in the first trajectory point in ECal */
  double initial_x; /** First trajectory point coordinate in ECal cluster */
  double initial_y;
  double initial_z;
};
```

Listing 2: Definition of the `cluster_generator` structure.

To assign to each reconstructed cluster its truth Monte Carlo trajectories, called generators, the procedure involves the following key steps:

- **Cluster loop**: all the hits that have produced one or more photo-signals in the cluster and the corresponding trajectories associated are retrieved and saved.
- **Generator identification**: looping on the trajectories with hits in the cluster, each trajectory tree is navigated backward, until a generator is identified. For each trajectory, all the trajectory points are ordered following a time criterion, and starting from the latest one, going backward, each point's position is checked. When a point position is found to be out from a cluster cell volume, the trajectory is added as a generator. It is important to underline that in doing so, also neutral particles are taken into account.
- **True cluster quantities computation**: each `cluster_generator` quantity is computed and stored in the correspondent `truecluster`.

The `truecluster` in List 1 are calculated as follows:

- The main generator particle is chosen as the generator that has deposited the most visible energy in the cluster.
- `E/p`: E is the reconstructed cluster energy, p is the generator momentum, taken at the first trajectory point in the ECal, assuming this would be reconstructed by the tracker.
- `ntot_cell` and `cell_lx` are the same as the reconstructed cluster.
- `energy_lx`, `layx_maxE`, `asymmetry` are calculated using the reconstructed quantities.
- `moregens`: is set to `true` if more generators are present in the `truecluster`.

- `vec_generator`: collection of generators that have been identified. The order is energy increasing as a function of the position inside the `std::vector`.

The `cluster_generator` in List 2 are calculated as follows:

- `pdg_code` and `parent_pdg_code`: the pdg code of the trajectory and the parent selected as generator.
- `track_id` and `parent_track_id`: the unique track ID code of the trajectory and the parent selected as generator.
- `dep_energy`: the deposited energy in the cluster active material is calculated as the sum of the hit energy deposits of the generator. If the generator trajectory has at least one hit that has generated at least one photoelectron that is part of the cluster photo-signal, then all trajectory hits are checked. The hit energy deposits are summed up only if the hit start or hit middle, or the end point position, is inside a cluster cell volume.
- `initial_energy`: the Monte Carlo energy calculated in the first trajectory point of the trajectory, considering the whole detector.
- `initial_momentum`: the Monte Carlo momentum of the generator, calculated in the first trajectory point of the trajectory, considering the whole detector.
- $\vec{x}$: the position of the first trajectory point in the cluster.

5.4 Reconstructed vs. true variables

To validate the reconstructed-Monte Carlo cluster backtracking algorithm in choosing the correct generator particle associated with the cluster, the reconstructed variables from the clustering step and the true ones, computed using the algorithm, are compared. The performance of the algorithm is evaluated using particle gun simulations.

5.4.1 Particle guns

The particle gun simulation is performed using edep-sim 4.1, built upon GEANT4 v10.7.4 that simulates particle transport and physics interaction inside the detector *geometry*[3], specified by a `gdml` file. A configuration file specifies the parame-

[3]As described in Chapter 3, the final SAND geometry design is not yet fully defined, and several detector configurations are currently supported within the simulation framework. The simulation chain accommodates both STT-based and DRIFT-based tracker designs, each with multiple variants. The STT options differ by parameters such as the number of target and

ters, including particle type, energy, direction, and initial position of the GEANT4 General Particle Source primary particles.

In Figure 5.3, the plots of the reconstructed position for x, y, and z coordinates, as a function of the true ones, calculated using the position of the main generator particle, are shown. Each entry on the plots represents a cluster. The sample consists of 10^4 muons with initial position in SAND center $(0, -2384.73, 23910)$mm, with isotropic initial angle and uniform energy range between $[0.001, 6]$GeV. As expected, the distributions lay on the bisector. The same plots obtained a sample of 10^4 electrons with initial position in SAND center $(0, -2384.73, 23910)$mm, with isotropic initial angle and uniform energy range between $[0.001, 6]$GeV can be found in Figure 5.4.

In Figure 5.5, the tomography of the detector using the true cluster variable position in the three views can be observed. The greater density of events can be observed in all the views for the space regions where the ECal and barrel modules overlap. In Figure 5.6, the same plots with the reconstructed cluster apex variable are shown.

In Figure 5.7 and Figure 5.8, the plots of the reconstructed cluster energy as a function of the true one is reported for muons and electrons sample respectively; It has to be noticed that the reconstructed value is slightly higher than the true one because in the procedure of calculating the true energy of the generator, some hits can be missed. The requirement that for each generator trajectory (and children) the energy has to be summed up if there is at least one hit in the correspondent cluster, can exclude some hits. This is because, in principle, during the buildup of the photo-signal from the edepsim hits in the digitization step, described in Section 4.2, a hit in general produce N photons. Two things can then happen. The first issue is that not all photons reach the PMTs due to light attenuation in the fibers, resulting in a limit of 0 photoelectrons being produced by the PMT photocathode, which causes the true deposited energy calculated by the algorithm to be less than the actual deposited energy. The second is that photons of the same hit can contribute to different photo-signals in the same cells, which can contribute to different clusters. This scenario can show up if the decay time of the excited atom, summed to the propagation time to the PMTs, is greater than the acquisition time window of the PMTs (in this case 30 ns, see Section 4.2). Also, in this case, for some clusters, the true energy deposited calculated by the algorithm

tracking modules and the mechanical clearances between subdetectors. For the studies and results presented in this work, the geometry adopted is `SAND_opt3_DRIFT1.gdml`, which integrates 72 C_3H_6 and 8 C target modules and the DRIFT chamber tracking system. The ECal geometry includes a realistic description of the endcap and barrel modules; GRAIN has a 902 mm overall thickness.

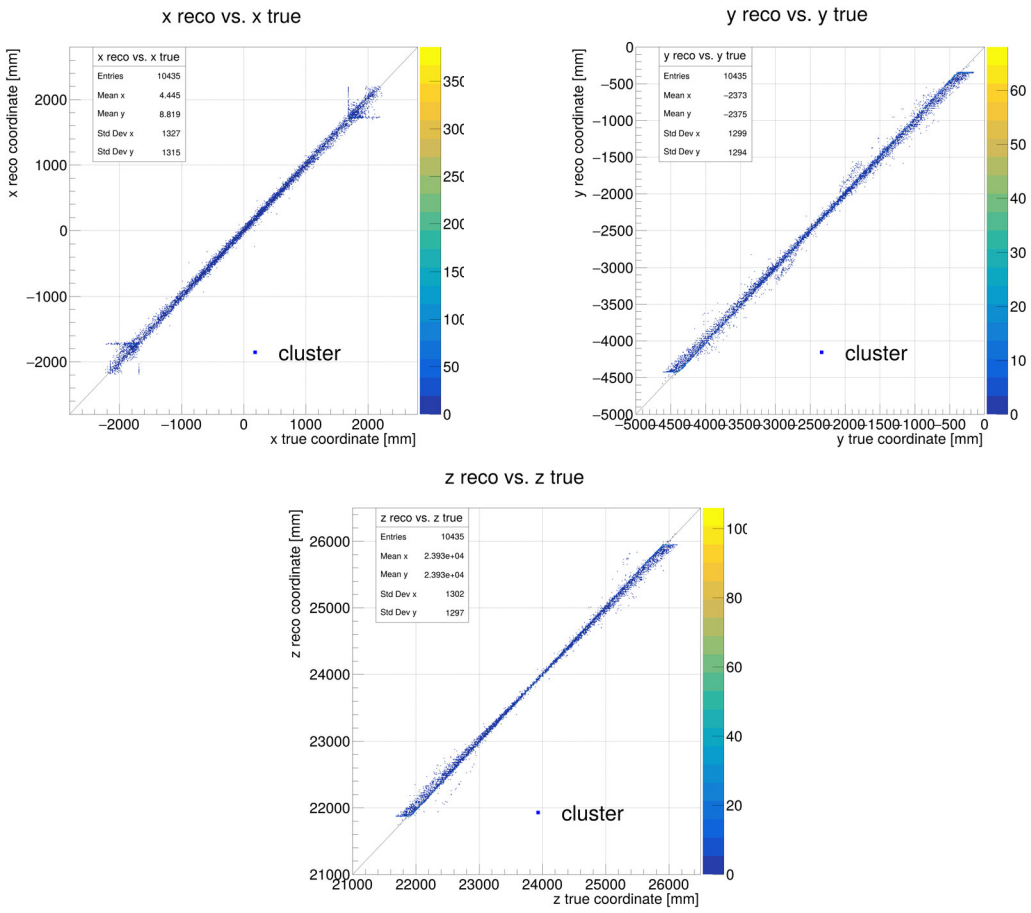

Figure 5.3: Reconstructed cluster position as a function of the true one for x, y, and z coordinates. The sample used is composed of 10^4 muons generated in the SAND center with isotropic initial angle and $E \in [0.001, 6]$GeV.

results in being less than the actual one. On the other hand, especially at low energies, when the hits produce a small number of photo-electrons, the average reconstructed energy is correct, due to the extraction of the photo-electron number from a Poisson distribution, the procedure is described in Section 4.2.

It has to be noticed that the energy here is calculated as deposited in the active material of the detector. To obtain the total deposited energy, it has to be corrected by the ratio of the energy deposition between active and passive material. The active-passive material calibration factor for energy deposition is different for different particles and different energy ranges and has to be tailored for each cluster, after particle identification algorithms identify the truth particle(s) associated with each reconstructed cluster, also using the information from the other

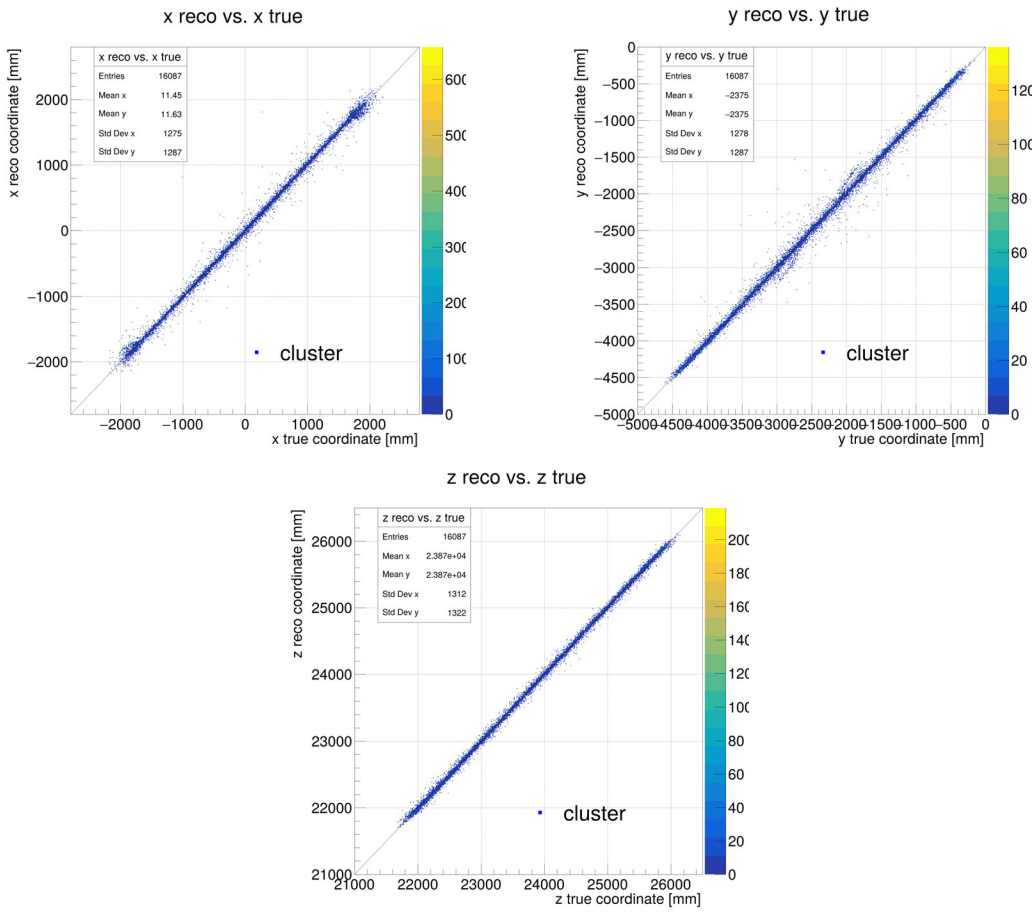

Figure 5.4: Reconstructed cluster position as a function of the true one for x, y, and z coordinates. The sample used is composed of 10^4 electrons generated in the SAND center with isotropic initial angle and $E \in [0.001, 6]$GeV.

two sub-detectors, GRAIN and the tracker. At the moment of this thesis writing, a complete code for particle identification has not yet been developed, while the calculation of the active-passive factor for electron and muons has been performed in the following Section 5.5 using the Monte Carlo-cluster backtracking algorithm developed in this thesis.

5.5 Active-passive material calibration factor

To convert the energy measured in the scintillating fibers (E_{active}) into the total energy deposited in each ECal cluster. The active-total factor has to be computed for each particle type, for different energies. In this thesis, samples of electrons and muons particle guns with several fixed initial energies E_{sim} have been simulated

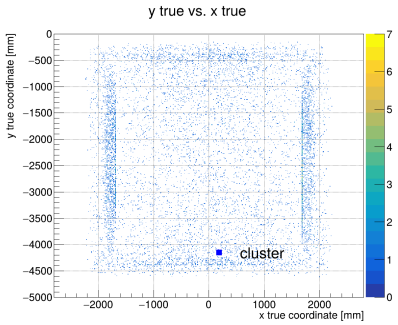

(a) yx view of SAND.

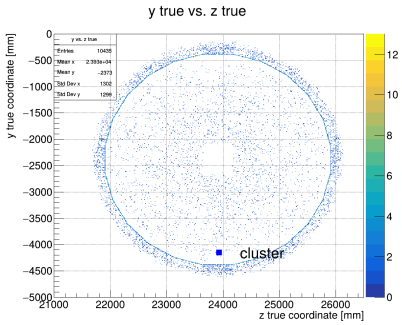

(b) yz view of SAND

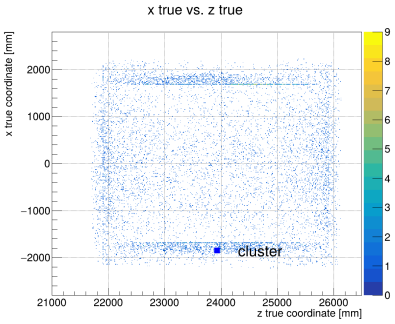

(c) xz view of SAND

Figure 5.5: Tomography of the detector using the true cluster variable position in the three views. The sample used is composed of muons 10^4 generated in the SAND center with isotropic initial angle and $E \in [0.001, 6]$GeV. Stats are reported only once in 5.5b.

and used to extract the conversion factor. The starting point of the particle guns is located at the end of the tracker in $(0, -2.38473, 25.81)$ m, with a uniform angular spectrum in the SAND hemisphere with $z > z_{\text{gen}}$.

For each particle the calibration factor is defined as

$$f(E) \equiv \frac{E_{\text{active}}}{E_{\text{initial}}}. \tag{5.13}$$

In Equation 5.13, E_{active} is the active energy deposited in the cluster and $E_{initial}$ is the energy of the particle generator at the first point in the cluster, requiring that the particle is fully contained; in this case $E_{\text{initial}} = E_{\text{tot, dep}}$, the total energy deposited by the particle in the ECal cluster.

To match the energy range that final state particle clusters will have, while exiting from the neutrino interaction vertex inside the detector, during DUNE data taking, two samples of ν_e and ν_μ are simulated. The neutrino interaction is simu-

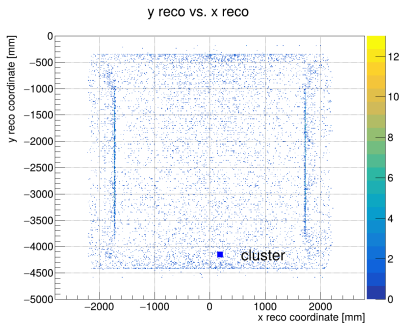

(a) yx view of SAND.

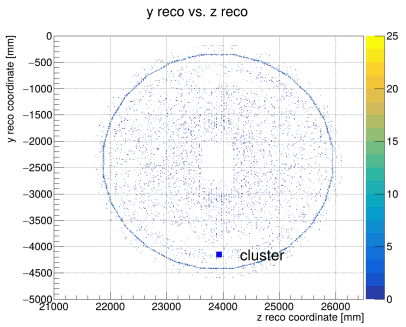

(b) yz view of SAND

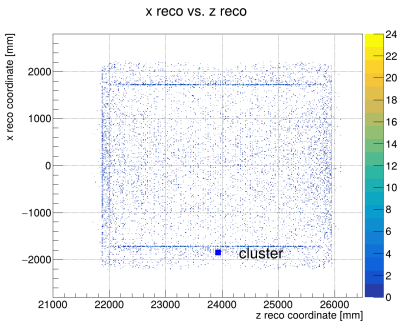

(c) xz view of SAND

Figure 5.6: Tomography of the detector using the reconstructed cluster variable apex position in the three views. The sample used is composed of muons 10^4 generated in the SAND center with isotropic initial angle and $E \in [0.001, 6]$GeV.

lated using the GENIE version 3.06.00. All the interaction modes are included, the flux template is the one developed by the DUNE collaboration, and the neutrino interactions are forced to happen in the SAND tracker volume. Particle transport and physics interaction inside the detectors is performed using edep-sim 4.1, built upon GEANT4 v10.7.4. The clusters are selected requiring that the main generator has deposited more than a fixed percentage of the total reconstructed deposited energy and that the `cluster_generator pdg_code` corresponds to the specific one of the chosen particle type under analysis.

5.5.1 Electrons

Energy range. In Figure 5.9, the plot of the initial energy for the electron generator particle as a function of the true deposited energy is shown. The sample shown is composed of $N_{\mathrm{e,tot}} = 47046$ electron generator particle clusters, arising from 30k ν_e interactions in the SAND tracker volume, with E_ν according to the official DUNE collaboration flux.

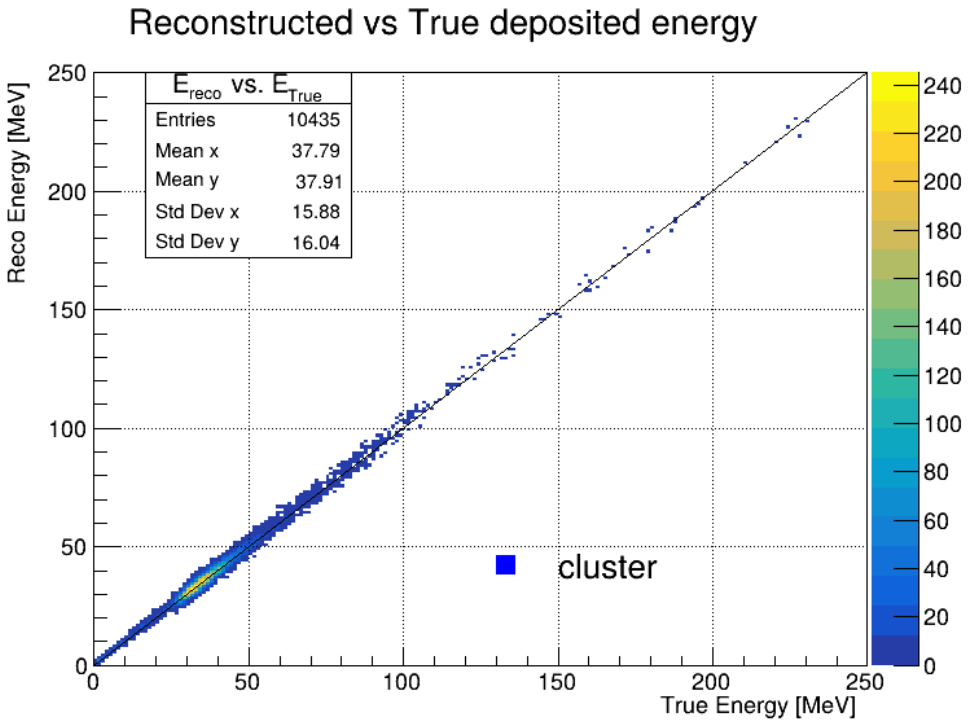

Figure 5.7: Cluster reconstructed as a function of the true deposited energy. The sample used is composed of muons 10^4 generated in the SAND center with isotropic initial angle and $E \in [0.001, 6]$GeV. The true energy is the sum of the deposited energy of all the generators.

The true energy is the sum of the deposited energy of all the generators, requiring that the main generator is an electron that has deposited at least 99.9% of the total cluster deposited energy. In the electron particle case $E_{\text{initial}} = E_{\text{tot, dep}}$ because electrons are always fully contained in this energy range, the outliers with $E_{active} > E_{initial}$ are explained in the Subsection 5.4.1.

The outliers with $E_{\text{initial}} > E_{\text{active}}$ correspond to cases where the same electron generator is associated with more than one cluster. In the backtracking, a generator is linked to a cluster whenever it has at least one trajectory point inside the corresponding cluster volume. If the shower from a given electron is split into two or more clusters by the time–splitting procedure, each of those clusters inherits the same E_{initial} (the generator energy at its first point in the ECal), but only a fraction of the total deposited energy ends up inside any given cluster. In the limit case where a particle interacts or decays almost immediately after entering the ECal, a cluster can be formed that contains only hits from the daughter trajectories, while still being tagged with the parent as generator. Such configurations

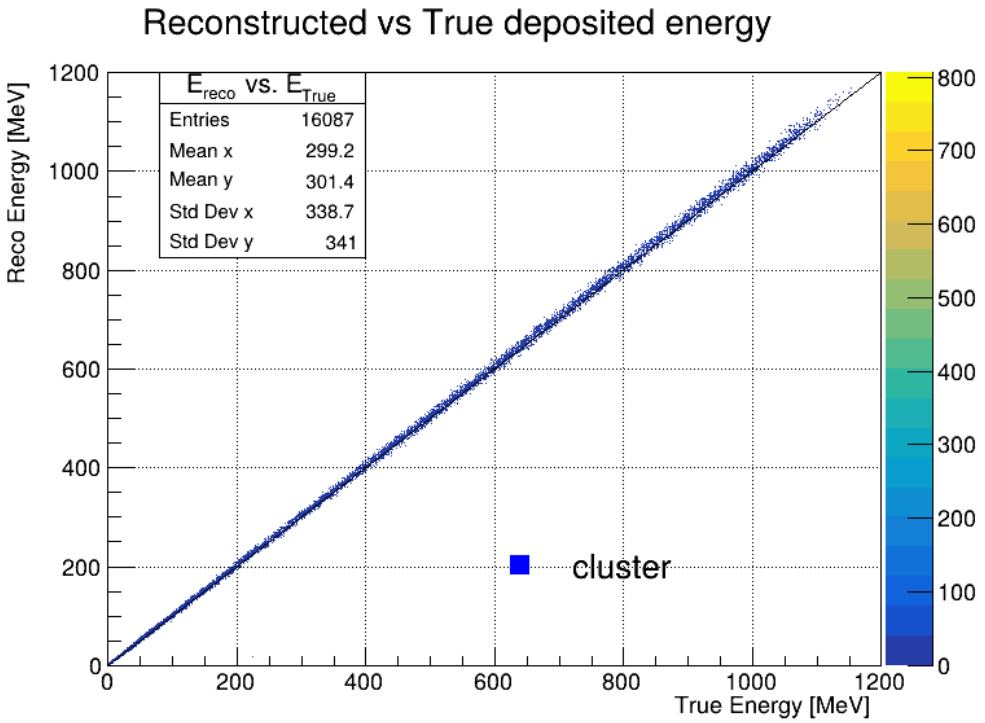

Figure 5.8: Cluster reconstructed as a function of the true deposited energy. The sample used is composed of electrons 10^4 generated in the SAND center with isotropic initial angle and $E \in [0.001, 6]$GeV. The true energy is the sum of the deposited energy of all the generators.

produce clusters with a large E_{initial} but relatively small E_{active}, giving rise to the outliers above the main proportional band.

Selection. The requirements for a cluster to pass the selection are to (i) have an electron as main generator, (ii) with contribution $> 99\%$ of the reconstructed deposited energy, and (iii) $|E_{\text{initial}} - E_{\text{sim}}| < 0.10\, E_{\text{sim}}$, where E_{initial} is the generator `EDEPTrajectory` energy at the first point in the cluster volume and E_{sim} the energy set by the simulation of the particle gun.

Fit strategy and uncertainties. For each E_{sim} a fit on the E_{active} distribution with a Gaussian to extract the mean $\langle E_{\text{active}} \rangle$ and width $\sigma_{E_{\text{active}}}$ is performed. Two representative gun samples are shown in Fig. 5.10; the relative widths are $\sigma/E \simeq 18.3\%$ at 100 MeV and $\simeq 6.18\%$ at 1 GeV.

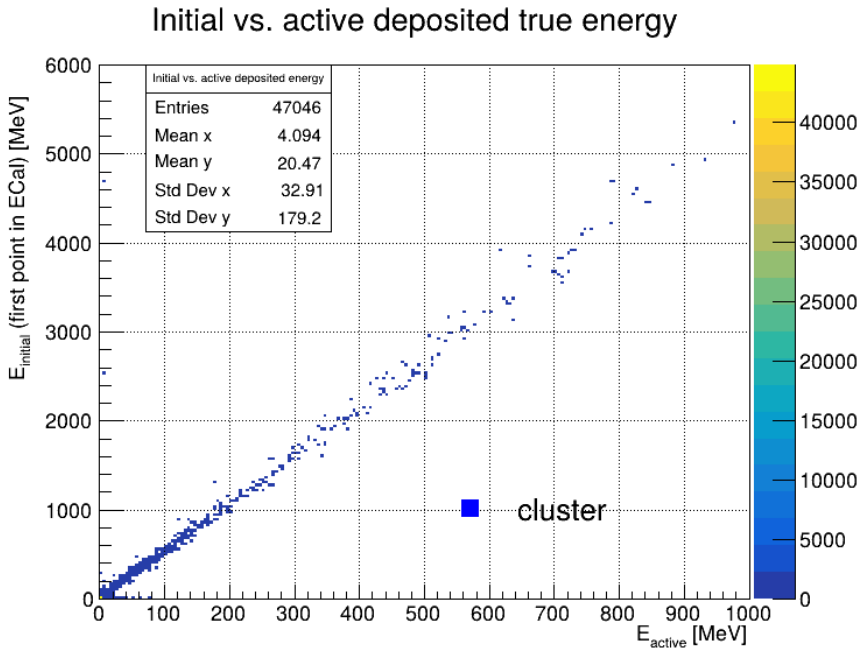

Figure 5.9: Initial energy for electron generator particle as a function of the true deposited energy. The sample shown is composed of 47046 electron generator particle clusters, arising from 30k ν_e interactions in the SAND tracker volume, with E_ν according to the official DUNE collaboration flux. The true energy is the sum of the deposited energy of all the generators, requiring that the electron is the main generator that has deposited at least 99.9% of the total cluster deposited energy.

Global calibration. Figures 5.11–5.12 show E_{sim} versus $\langle E_{\text{active}} \rangle$ in different energy ranges and the fit function obtained. A single global calibration factor is obtained with a linear fit of

$$E_{\text{sim}} \;=\; k\,\langle E_{\text{active}} \rangle .$$

Points are drawn with x–errors $\sigma_x^{\text{stat}} = \sigma_{E_{\text{active}}}/\sqrt{N_{\text{sel}}}$ and with y–errors set to

$$\sigma_y \;=\; \text{RMS}(E_{\text{init}})\,,$$

while the light–blue rectangles indicate a $\pm 10\%$ band in y and $\pm\sigma_{E_{\text{active}}}$ in x; the bands are not used in the fit.

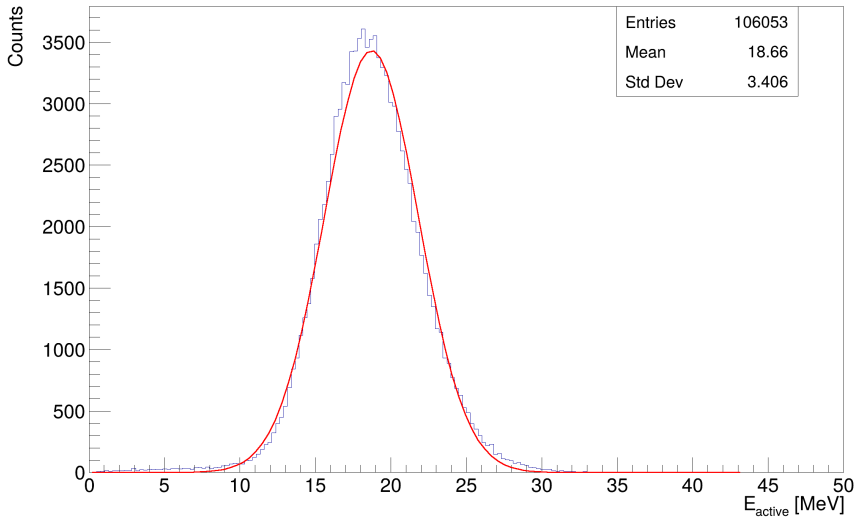

(a) $E_{\text{sim}} = 100$ MeV ($\sigma/E \approx 18.3\%$).

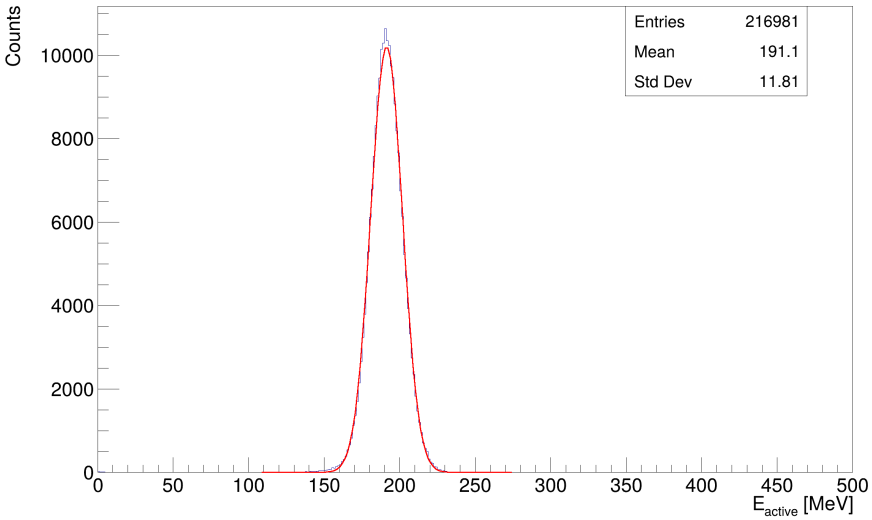

(b) $E_{\text{sim}} = 1$ GeV ($\sigma/E \approx 6.18\%$).

Figure 5.10: Distributions of E_{active} with Gaussian fits.

The global linear fit yields

$$k \;=\; 5.23036 \pm 0.00289 \quad \Rightarrow \quad f \;\equiv\; \frac{E_{\text{active}}}{E_{\text{tot,dep}}} = \frac{1}{k} \;=\; 0.191191 \pm 0.000106\,,$$

with $\chi^2/\text{ndf} = 543.33/10 = 54.33$. The large χ^2 reflects the tiny point uncertainties relative to residual non linearities; nevertheless, a single scale factor describes

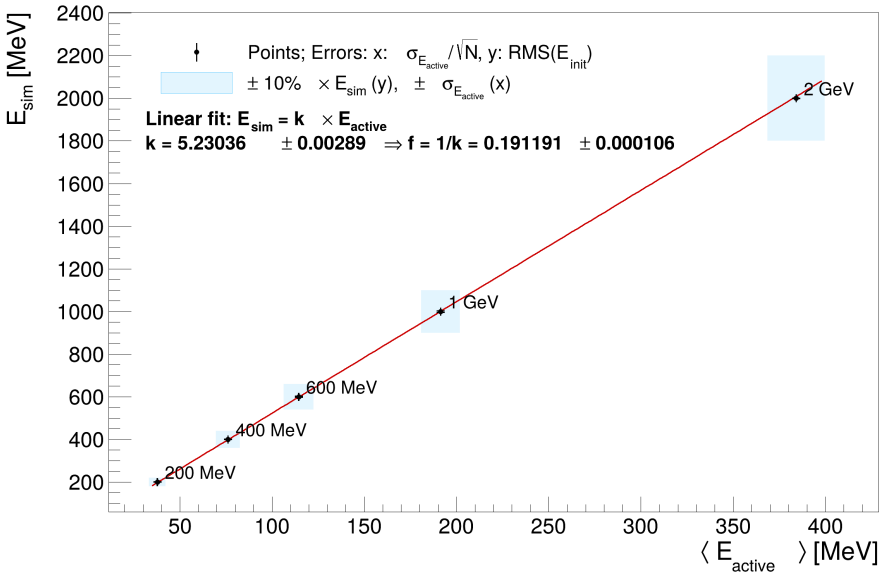

Figure 5.11: Calibration for $E_{\text{sim}} \geq 100$ MeV (same global fit as Fig. 5.12). Error bars in black: (x) $\sigma_{E_{\text{active}}}/\sqrt{N}$, (y) RMS(E_{init}). Blue rectangles: $\pm 10\%$ in y, $\pm\sigma_{E_{\text{active}}}$ in x.

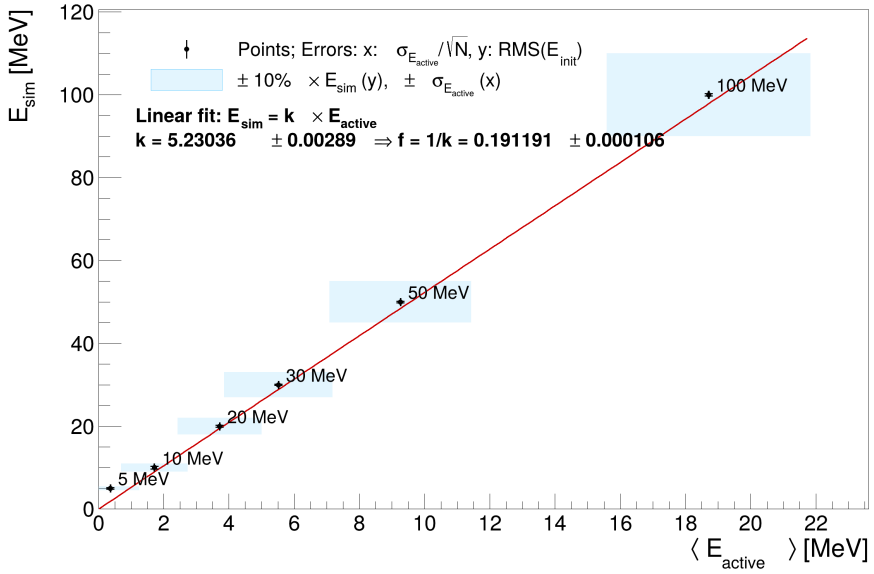

Figure 5.12: Same as Figure 5.11 for $E_{\text{sim}} \leq 100$ MeV.

the data better than the percent level across the full range, which is sufficient for the calibration used here.

5.5.2 Muons

Figure 5.13a shows, for clusters whose main generator is a primary muon, the energy of the muon at the first trajectory point inside the cluster volume (E_{initial}) versus the active energy deposited in the cluster. The sample contains 18368 clusters from 30k ν_μ interactions in the SAND tracker volume with the DUNE flux spectrum, requiring the muon to contribute at least 99% of the cluster energy. No other cuts are applied here.

Unlike electrons, which in the DUNE energy range are fully contained in the ECal and therefore populate a narrow proportional band (see Figure 5.9) muons exhibit three behaviors that are shown in Figure 5.13: (i) a broad band from through-going (not fully contained) muons with MIP-like ionization, where E_{active} depends mainly on path length; (ii) a low-E_{active} population at late times respect to the vertex time due to muon decays in the ECal; and (iii) a proportional band from fully contained, stopping muons, where E_{active} scales with E_{initial}.

To isolate the decay component, the cut in Figure 5.14 selects clusters with time $> 100\,\text{ns}$ respect to the vertex time and zero energy in the outermost ECal layer, ensuring the cluster originates from $\mu^- \to e^- + \bar{\nu}_e + \nu_\mu$ decay happening within the ECal, while the muon trajectory still enter the cluster having in it a trajectory point. The mean electron energy for a muon decaying at rest is $\sim 37\,\text{MeV}$ (see the review *"Muon Decay Parameters"* in [110]); applying the electron calibration factor of Equation 5.13 (Subsection 5.5.1) gives a value consistent with the mean active deposition of $\sim 6.8\,\text{MeV}$ of the observed distribution. Outliers are explained by incomplete containment of the decay electron or its secondaries.

The through-going, not-fully-contained muons, are shown in Figure 5.15 in which visible deposits in both the innermost and outermost ECal layers are required, using the threshold of $E_{\text{layer0,layer4}} > 4\,\text{MeV}$. The broad band is almost flat in E_{active}, and does not depend on E_{initial} above $300\,\text{MeV}$, as expected for a MIP-like ionization muon passing through different thickness.

Fully contained muons are selected by demanding a visible entrance and no exit: $E_{\text{layer0}} > 4\,\text{MeV}$ and $E_{\text{layer3}} = 0\,\text{MeV}$. Figure 5.16 shows a clear proportional trend between E_{active} and E_{initial}, as expected for stopping tracks where the total visible ionization follows the incident energy. Residual outliers away from the band are primarily due to large-angle scatters and side exits that bypass the outermost layer. The display of an interaction in which a muon is scattering not leaving energy in the outermost layer is shown in Figure 5.17.

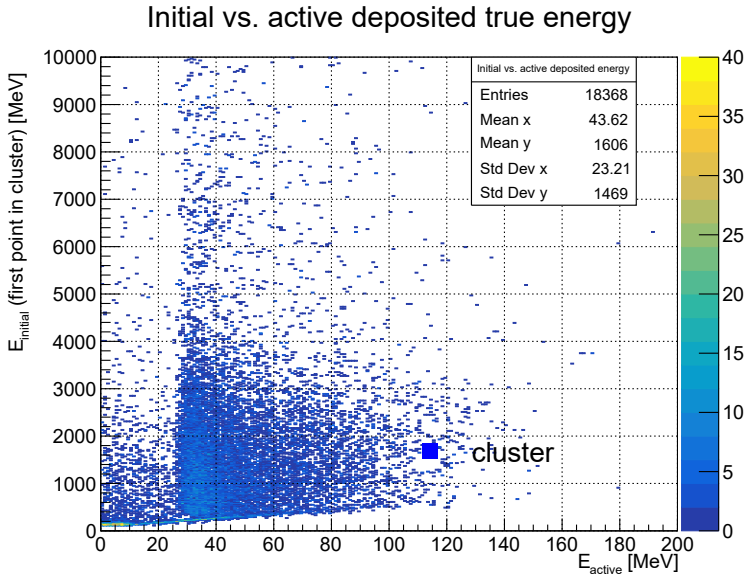

(a) Muon E_{initial} versus true active energy. Primary μ clusters with the muon contributing $\geq 99\%$ of the cluster energy; no further selection. The three regimes described in the text are visible.

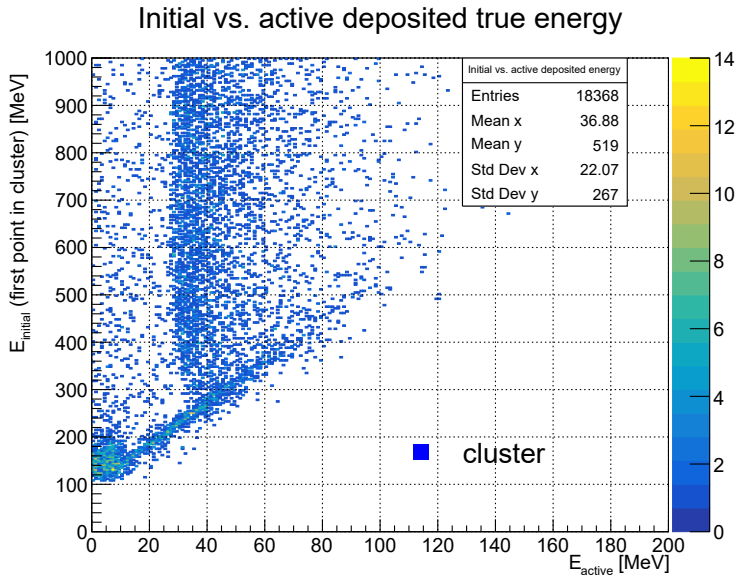

(b) Zoom to $E_{\text{initial}} \in [0, 1]$ GeV highlighting the low-energy structures.

Figure 5.13: Initial vs true active energy for primary muon clusters from ν_μ interactions in the SAND tracker volume. The lower panel 5.13b zooms the distribution in 5.13a.

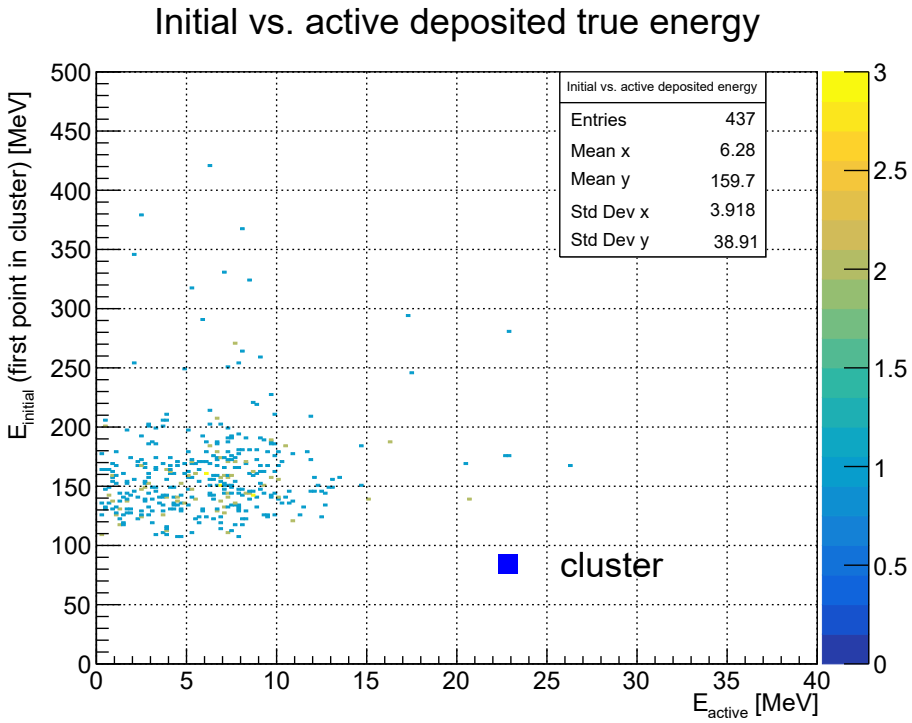

Figure 5.14: Muon-associated clusters enriched in decays: $t > 100\,\text{ns}$ and $E_{\text{layer4}} = 0\,\text{MeV}$. The mean E_{active} matches the expectation for a $\sim 37\,\text{MeV}$ Michel electron after applying the electron calibration factor.

5.6 Energy resolution

Definition and selection. For each electron–gun sample at fixed E_{sim} the residual is build as follows:

$$r \equiv E_{\text{init}} - k\,E_{\text{active}}, \tag{5.14}$$

where $k = \frac{1}{f}$ is the global active to total calibration calculated in Section 5.5. Events are required to pass the same quality selection used for the calibration: the cluster's main generator is an electron, it contributes $> 99\%$ of the reconstructed deposited energy, and $|E_{\text{init}} - E_{\text{sim}}| < 0.10\,E_{\text{sim}}$.

Fit strategy. For each energy r distribution is fit with a Double Sided Crystal Ball (DSCB). The DSCB core width, σ_{core}, is taken as the statistical energy resolution for the corresponding E_{sim} value. Two examples at 100 MeV and 1 GeV are shown in Fig. 5.18–5.19.

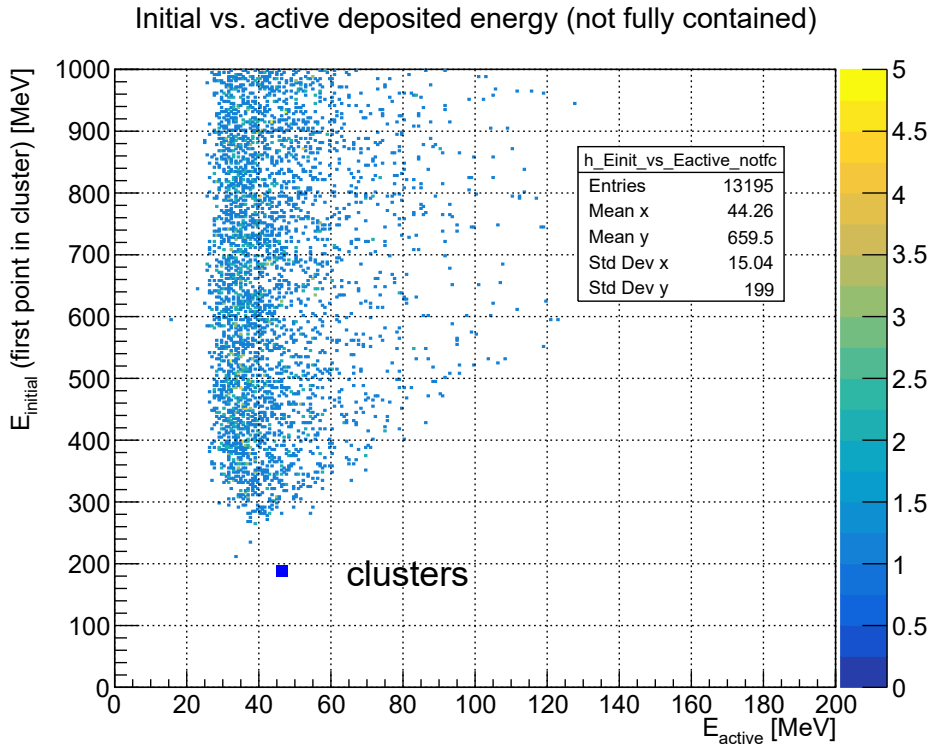

Figure 5.15: Passing, not-fully-contained muons selected with conditions $E_{\text{layer0}} > 4\,\text{MeV}$ and $E_{\text{layer4}} > 4\,\text{MeV}$. The broad band reflects MIP-like energy loss with different path lengths, independently by E_{initial} abbove $\simeq 300\,\text{MeV}$. See also the display of an event with not fully contained muon in Figure 5.17.

Resolution points and statistical uncertainties. For each particle gun energy

$$R(E) \equiv \frac{\sigma_{\text{core}}}{\langle E_{\text{init}} \rangle} \tag{5.15}$$

at $x = \langle E_{\text{init}} \rangle$ has been plotted. The statistical uncertainties are:

$$\delta x = \delta(\langle E_{\text{init}} \rangle) = \frac{\text{RMS}(E_{\text{init}})}{\sqrt{N_{\text{sel}}}}, \tag{5.16}$$

$$\delta R = \sqrt{\left(\frac{\delta\sigma_{\text{core}}}{\langle E_{\text{init}} \rangle}\right)^2 + \left(\frac{\sigma_{\text{core}}\,\delta(\langle E_{\text{init}} \rangle)}{\langle E_{\text{init}} \rangle^2}\right)^2}, \tag{5.17}$$

where $\delta\sigma_{\text{core}}$ is the fit uncertainty from the DSCB, and the uncertainty on the mean is purely statistical, Eq. (5.16). Systematic effects (as uncertainty on k) are not included in the error bars.

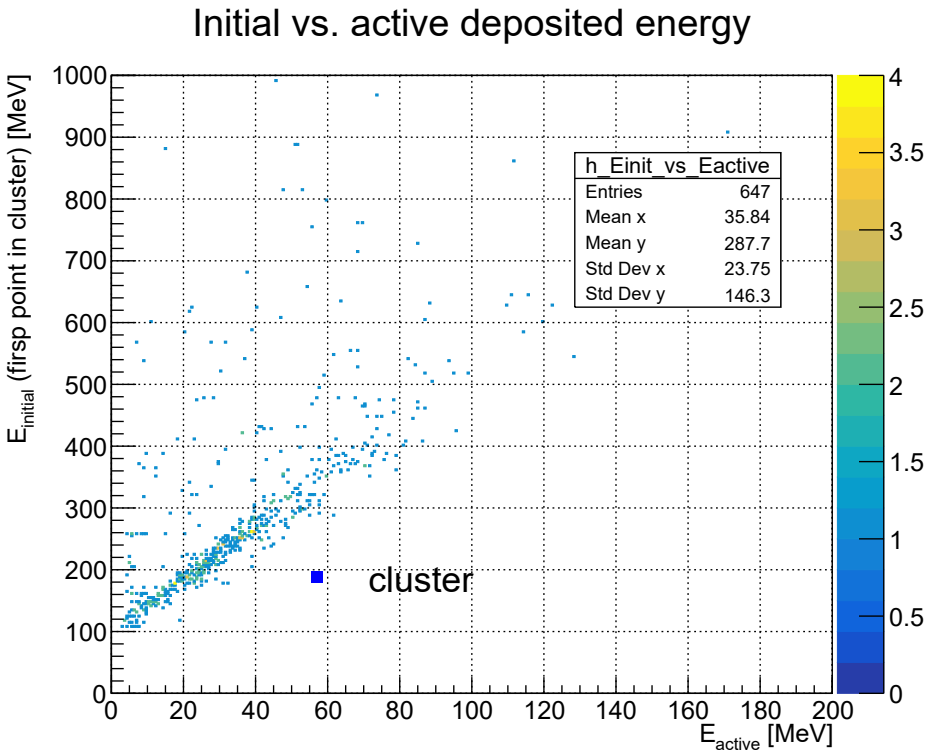

Figure 5.16: Fully contained muons selected with the conditions $E_{\text{layer0}} > 4\,\text{MeV}$ and $E_{\text{layer4}} = 0\,\text{MeV}$, requiring the muon to contribute $\geq 99\%$ of the cluster energy. A proportional band is visible; remaining outliers derive from hard scattering and side exits that do not leave energy deposits in the outermost layer cells.

Fit model and KLOE reference. The resolution points are fitted with:

$$\frac{\sigma}{E} = \sqrt{\frac{a^2}{E} + b^2}, \qquad \text{with } E \text{ in GeV}, \tag{5.18}$$

while the KLOE reference curve[4] is overlaid using the published parameters $a_{\text{KLOE}} = 0.057$, $b_{\text{KLOE}} = 0.006$ [111]. The resulting plot is shown in Fig. 5.20.

The fit returns parameters close to the KLOE measurements For this dataset, the fit gives

$$a = 0.0497 \pm 0.00009\ (\text{stat}), \qquad b = 0.0200 \pm 0.00024\ (\text{stat}).$$

A slightly smaller sampling term a and a larger constant term b than the KLOE

[4] Axes in Fig. 5.20 are labeled in MeV for convenience; E is converted to GeV before evaluating Eq. (5.18).

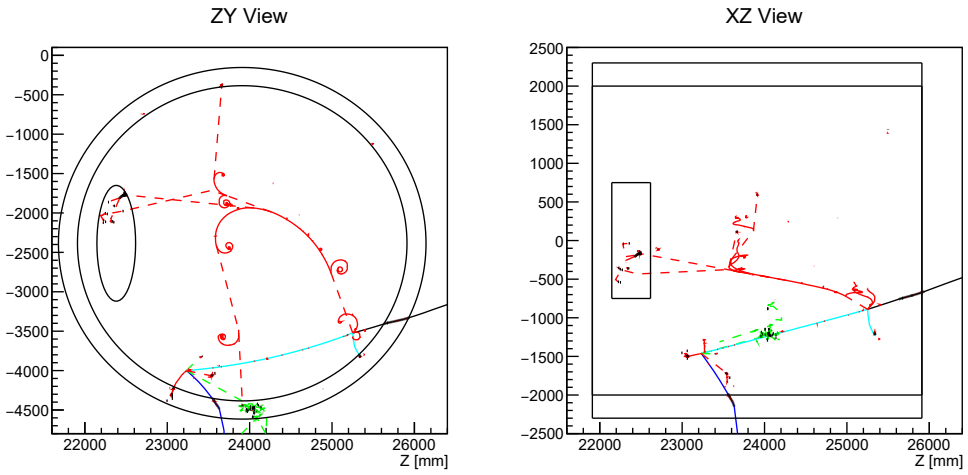

Figure 5.17: SAND event display of a ν_μ interaction with a not fully contained muon in the ECal undergoing hard scattering. Energy depositiion are present in the innermost but not in the outermost layer. Solid lines are charged particles while dashed are neutral: μ in blue, e/γ in red, π light blue, n green. ECal deposited energy hits: black dots.

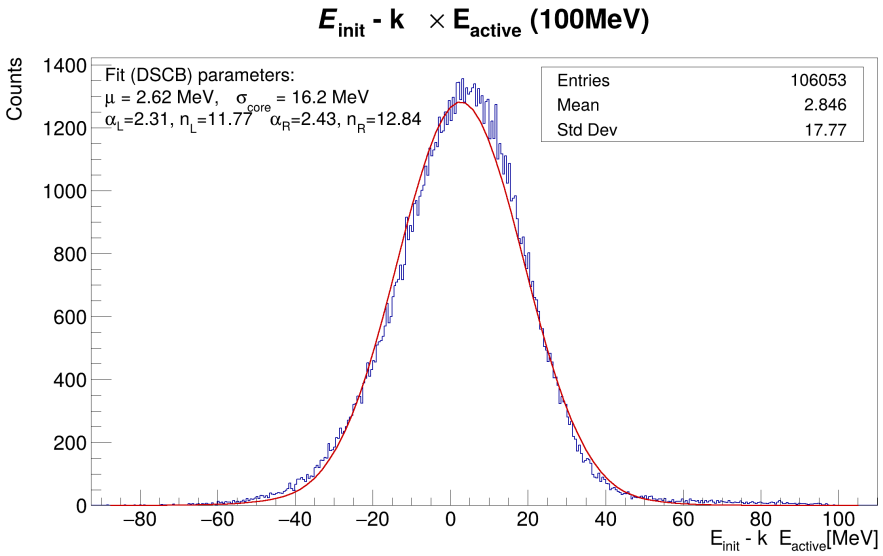

Figure 5.18: Residual distribution and DSCB fit for $E_{\text{sim}} = 100$ MeV. The quoted σ_{core} is used as the resolution numerator at this energy.

reference have been observed. Error bars reflect statistical uncertainties only. A study of systematics can be added in a subsequently.

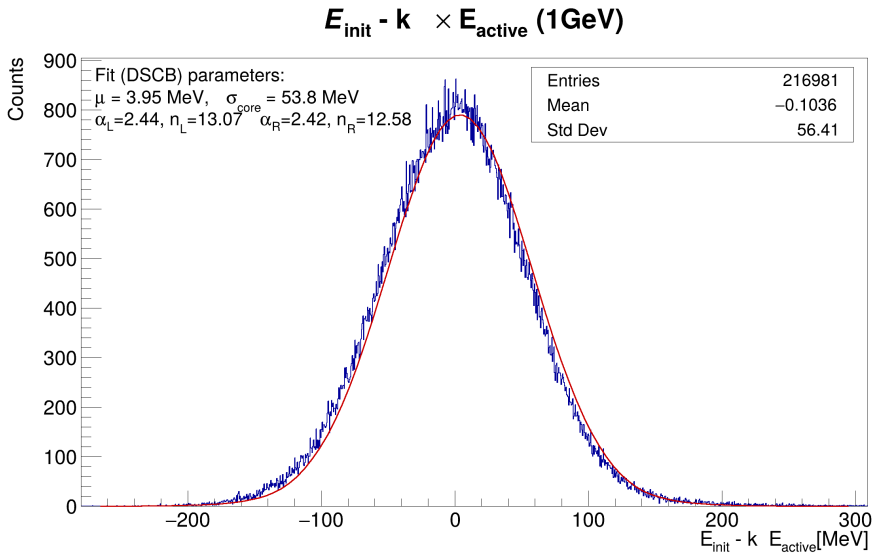

Figure 5.19: Residual distribution and DSCB fit for $E_{\text{sim}} = 1$ GeV.

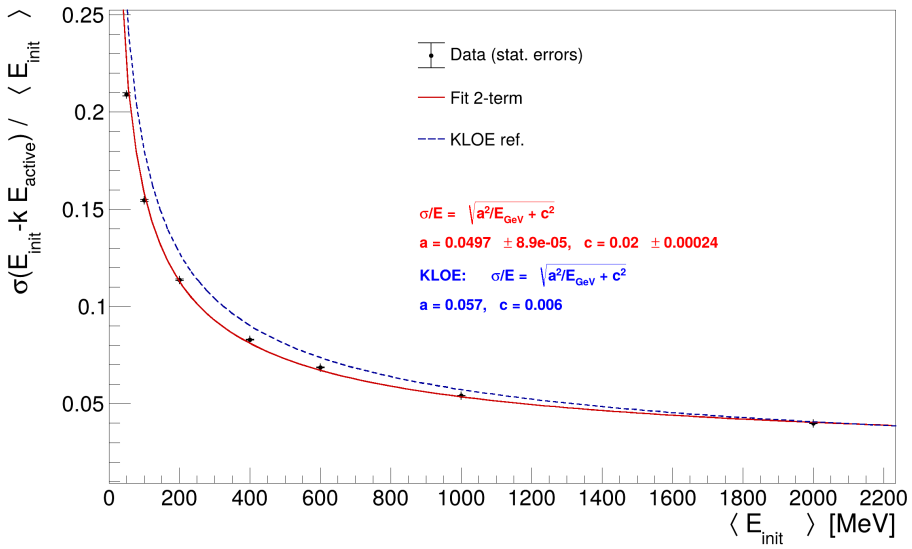

Figure 5.20: Resolution $R = \sigma_{\text{core}}/\langle E_{\text{init}}\rangle$, versus $\langle E_{\text{init}}\rangle$ with statistical error bars from Eqs. (5.16)–(5.17). The red line is a two–parameter fit to Eq. (5.18); the dashed curve is the KLOE reference ($a = 0.057$, $b = 0.006$).

Chapter 6

Neutron detection for $\bar{\nu}_\mu$-hydrogen interaction measurements

The physics potential of SAND to exploit $\bar{\nu}/\nu$ interactions on hydrogen in the tracker targets has been discussed in Section 3.2. In the SAND configuration, neutrino–electron elastic scattering and scattering on free protons in the CH_2 targets are the only processes that are essentially free from nuclear effects in the initial state. As such, they provide powerful handles for flux measurements, cross-section studies, and the control of systematic uncertainties [68].

Interactions on the hydrogen in the CH_2 targets can be isolated thanks to the excellent tracker resolution on the kinematic variables and to the data-driven subtraction procedure, the "solid hydrogen" technique [99], which removes the residual carbon background using events in the graphite targets. The ECal plays a fundamental role in the event reconstruction, being the main SAND sub-detector capable of detecting neutrons from $\bar{\nu}_\mu + p \to \mu^+ + n$ interactions on free protons.

In this chapter, building on the ECal digitization, clustering and Monte Carlo backtracking tools developed in Chapter 5, the signal selection for hydrogen interactions is described and the ECal response to neutrons is quantified. In particular, hit and cluster-level neutron detection efficiencies, the event selection efficiency and purity for the $\bar{\nu}_\mu + p \to \mu^+ + n$ channel, and the non-H interaction rejection achieved are evaluated. These results provide both the essential input and a complementary selection strategy for the solid-hydrogen analysis of $\bar{\nu}_\mu$ interactions in SAND.

To perform the study, a sample of 5.0×10^5 $\bar{\nu}_\mu$ interactions in the SAND tracker volume with the beam energy spectrum has been used. This sample corresponds to 5.73×10^{20} protons on target (POT), equivalent to 2545.67 h ($\simeq$ 106 d) of beam time.

6.1 Neutron detection efficiency in ECal

Figure 6.1 shows the distribution of the momentum p after final state interactions (FSI) of the primary neutrons from the interaction vertex. The total number

of neutrons produced is $N_{\mathrm{n,tot}} = 682912$ and for a compact characterization the spectrum has been fitted with a Landau curve obtaining MPV $= (287.2 \pm 0.3)$ MeV and $\sigma = (105.5 \pm 0.1)$ MeV. The Landau captures the asymmetric core and long tail.

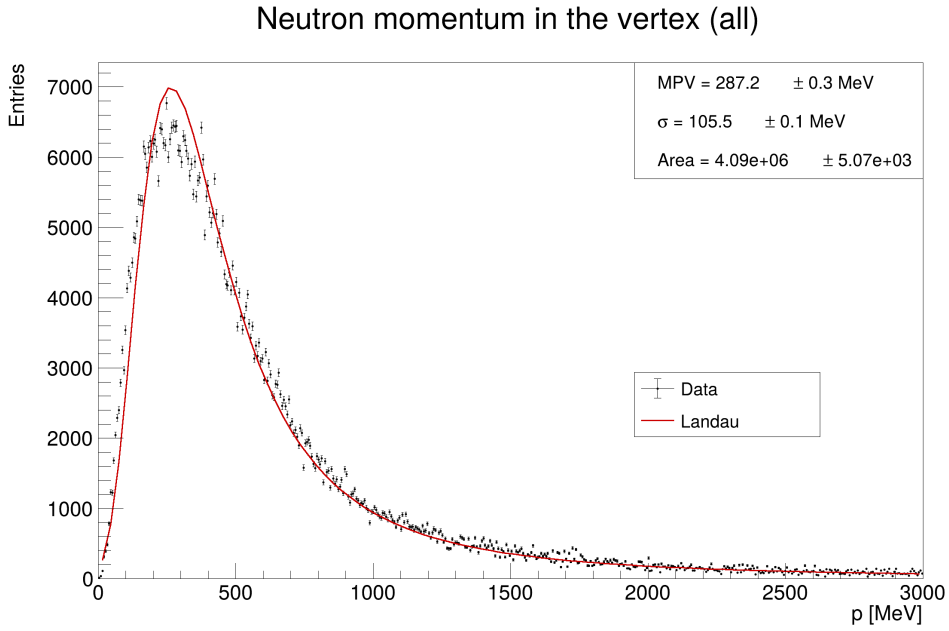

Figure 6.1: Initial momentum distribution (after FSI) for primary neutron exiting from the vertex for all kinds of neutrino interactions. $N_{\mathrm{n,tot}} = 682912$ is the total number of neutrons, the fit has been performed with a Landau curve.

The heat map in Figure 6.2 shows the neutron multiplicity in the stable final state after FSI, N_{neutrons}, as a function of the interaction mode record from the GENIE [103] reaction. As expected for an $\bar{\nu}_\mu$ beam, the CCQE ([CC], QES) row peaks at $N_{\mathrm{neutrons}} = 1$. On a free proton $\bar{\nu}_\mu + p \to \mu^+ + n$ produces exactly one neutron at the primary vertex, while for nuclear targets the intranuclear cascade can release more nucleons, producing a small tail with $N_{\mathrm{neutrons}} \geq 2$. Resonance (RES) and deep inelastic scattering (DIS) populate broader multiplicities due to hadronic re-interactions, and meson–exchange current (MEC, also called 2p2h) channels naturally enhance multi–nucleon knockout, populating $N_{\mathrm{neutrons}} \geq 2$.

Neutron ECal hit efficiency. The ECal hit efficiency can be defined for final–state neutrons as the fraction that produce at least one hit in the active scintillator:

$$\epsilon^{\mathrm{ECal}}_{n,\geq 1\,\mathrm{hit}} = \frac{N_n(\geq 1\,\mathrm{hit})}{N_n(\mathrm{produced})}\,. \tag{6.1}$$

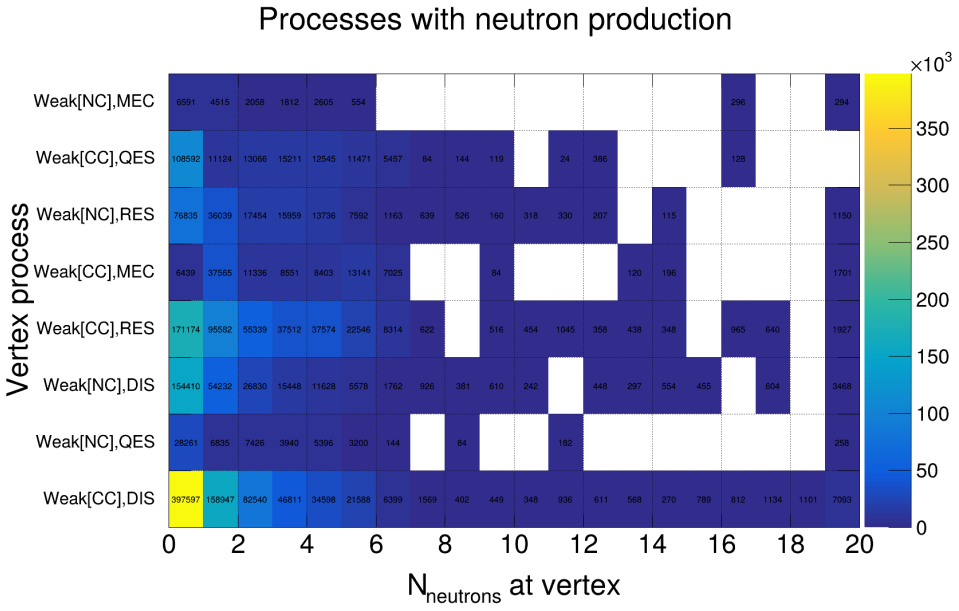

Figure 6.2: Neutrino interaction mode (from the GENIE reaction record) versus the number of neutrons in the stable final state at the vertex, N_{neutrons}, after FSI.

Figure 6.3 shows the distribution of the Monte Carlo hits of energy deposited in the ECal active material by the primary neutron `EDEPTrajectory` exiting the vertex, summed with all its `ChildrenTrajectories`[1]. Using the full sample size $N_{n,\text{tot}} = 682{,}912$ and the number with at least one ECal hit $N_{n,\text{hit}} = 528{,}677$, the global efficiency is

$$\epsilon^{\text{ECal}}_{n,\geq 1\,\text{hit}} \;=\; \frac{528{,}677}{682{,}912} \;=\; 0.774 \pm 0.0005_{\text{stat}} \;\approx\; 77.4\%\,.$$

As a function of the neutron kinetic energy at the vertex, the efficiency rises rapidly at low T_n^{true} and approaches a high plateau ($\gtrsim 90\%$) above a few hundred MeV (Figure 6.4). The efficiency at the hit level with at least one hit deposited in the ECal as a condition, $\epsilon^{\text{ECal}}_{n,\geq 1\text{ hit}}$, is higher than the cluster-level efficiency quoted later. The gap arises because neutrons often are fragmented into multiple small clusters that are affected both by attenuation and threshold on the readout; therefore, the cluster efficiency should be regarded as a stricter efficiency, while the hit efficiency is an upper limit for ECal detector efficiency.

As explained in Section 4.2, the energy deposited in each hit is attenuated for the path length in the fibers and converted into the corresponding number of photo-

[1] As defined in the `edep-reader` tool; see Sec. 5.2.

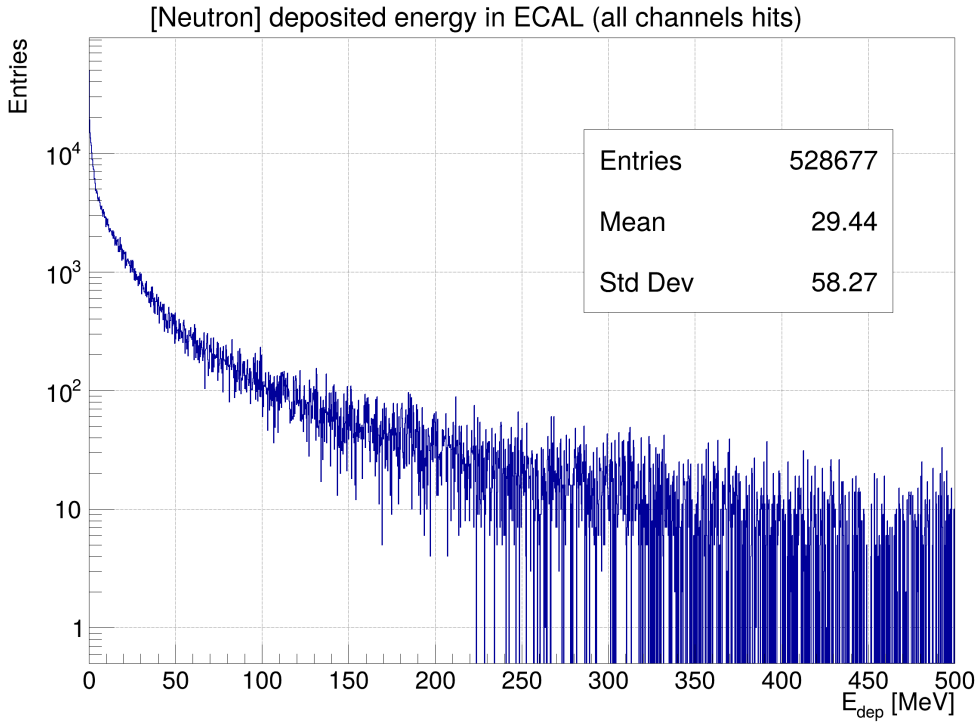

Figure 6.3: True energy deposited in the ECal active material (scintillating fibers) by the primary neutron, obtained by summing the energies of all `EDEPHit` objects in the ECal sensitive volumes associated with its `EDEPTrajectory` and with all its descendant trajectories in the `EDEPTree`.

electrons using Eq. 4.1. This value is used as the mean of a Poisson distribution from which the actual number of photoelectrons used in the digitization is drawn. For a 2.5 pe ADC threshold on the photosignal, the smallest energy producing a detectable hit in the ECal (and thus seeding a cluster) can be related to the mean of the Poisson distribution at a chosen efficiency. Requiring $P(N \leq 2; \mu_{pe}) = 0.10$ (i.e. 90% detection for a 2.5 pe discriminator) gives $\mu_{pe} = 5.32\, pe$. The corresponding energy threshold is

$$dE_{\text{thr}} = \frac{\mu_{pe}}{E_{pe} \cdot A_\ell}, \qquad E_{pe} = 18.5\,\text{pe/MeV}.$$

Using $A_{0\,\text{m}} = 1.00$ (no attenuation) and, for the far end of a 4.3 m barrel module,

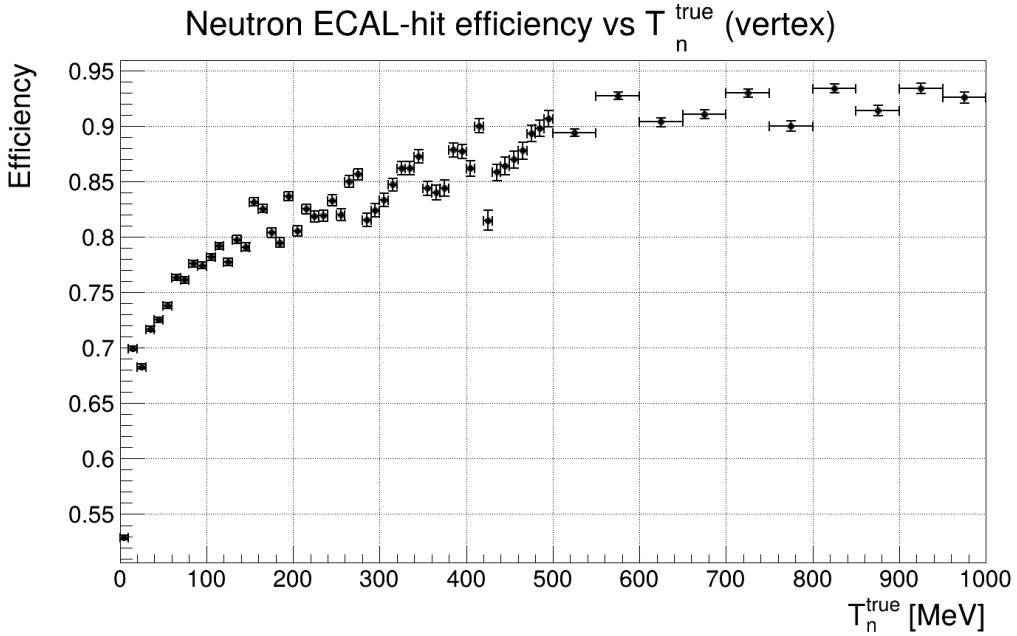

Figure 6.4: Neutron ECal hit efficiency $\epsilon^{\mathrm{ECal}}_{n,\geq 1\,\mathrm{hit}}$ versus true neutron kinetic energy at the vertex. Points show the binomial efficiency; vertical error bars indicate statistical uncertainties, and horizontal bars the bin widths.

the worst-plane value $A_{4.3\,\mathrm{m}} = 0.177$ (planes 4–5), one obtains

$$dE_{\mathrm{thr},\,A(0\,\mathrm{m})} = \frac{5.32}{18.5 \cdot 1.00} = 0.288\,\mathrm{MeV}, \tag{6.2}$$

$$dE_{\mathrm{thr},\,A(4.3\,\mathrm{m})} = \frac{5.32}{18.5 \cdot 0.177} = 1.626\,\mathrm{MeV}. \tag{6.3}$$

In Figure 6.5, the distribution in the low energy range of the cluster energy in the active material for clusters with a primary neutron as the main `cluster_generator`.

The first bin entry in the energy distribution for a neutron cluster results $E_{\mathrm{min,\,clu}} = 0.08\,\mathrm{MeV}$, and considering

$$E_{\mathrm{pe}} = 18.5\,\mathrm{pe/MeV}, \qquad \mu_{\mathrm{min,\,pe}} = E_{\mathrm{min,\,clu}}\,E_{\mathrm{pe}}\,A_{\ell}.$$

The detection probability can be computed as

$$P_{\mathrm{det}}(\mu_{\mathrm{min,\,pe}}) = P(N \geq 3; \mu_{\mathrm{min,\,pe}}) = 1 - e^{-\mu_{\mathrm{min,\,pe}}}\left(1 + \mu_{\mathrm{min,\,pe}} + \frac{\mu^2_{\mathrm{min,\,pe}}}{2}\right).$$

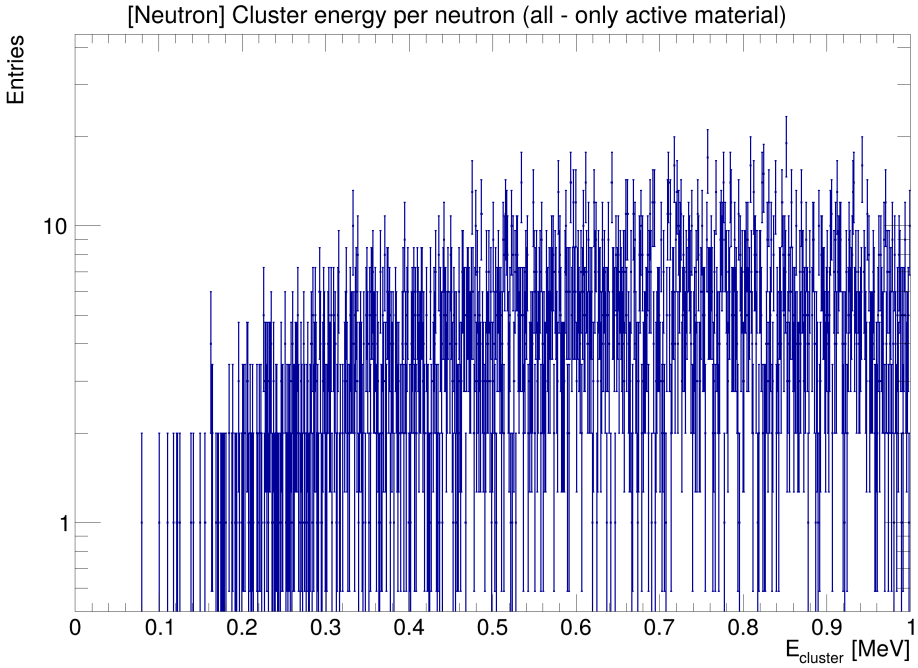

Figure 6.5: Deposited energy hit distribution in ECal for primary neutron exiting from the vertex for all kinds of neutrino interaction at low energies. Clusters are classified as neutron requiring a primary neutron as the main `cluster_generator`.

For a barrel module length $L = 4.3\,\mathrm{m}$ (midpoint at $\ell = 2.15\,\mathrm{m}$), the attenuation in Equation 4.2 gives:

$$\begin{aligned}
&\text{No attenuation, } A_{0\,\mathrm{m}} = 1: && \mu = 0.08 \times 18.5 = 1.48, && P_{\mathrm{det}} = 18.6\%.\\
&\text{Mid-module, } A_{2.15\,\mathrm{m}} \in [0.344,\, 0.399]: && \mu \in [0.508,\, 0.591], && P_{\mathrm{det}} \in [1.50\%,\, 2.22\%].\\
&\text{End of the module, } A_{4.3\,\mathrm{m}} \in [0.177,\, 0.239]: && \mu \in [0.261,\, 0.354], && P_{\mathrm{det}} \in [0.245\%,\, 0.568\%].
\end{aligned}$$

Thus, 0.08 MeV entries are expected: whenever the deposit occurs close to a photocathode, and by Poisson fluctuations at larger distances.

Neutron ECal cluster efficiency. In Figure 6.7, the cluster energy distribution in the active material for primary neutron exiting from the vertex for all kinds of neutrino interactions, considering clusters with a primary neutron as the main `cluster_generator`. $N_{n,\mathrm{clu}}$ is the number of final state neutrons that form at least one reconstructed cluster whose `cluster_generator` is the primary

neutron. Using the sample,

$$N_{n,\mathrm{tot}} = 682{,}912, \qquad N_{n,\mathrm{hit}} = 528{,}677, \qquad N_{n,\mathrm{clu}} = 206{,}775.$$

The ECal cluster efficiency (conditioned on having at least one hit) can be computed as

$$\epsilon^{\mathrm{ECal}}_{n,\mathrm{clu}\,|\,\mathrm{hit}} = \frac{N_{n,\mathrm{clu}}}{N_{n,\mathrm{hit}}} = 0.391 \pm 0.0007_{\mathrm{stat}},$$

equivalently, the global cluster efficiency is

$$\epsilon^{\mathrm{ECal}}_{n,\mathrm{clu}} = \frac{N_{n,\mathrm{clu}}}{N_{n,\mathrm{tot}}} = 0.303 \pm 0.0006_{\mathrm{stat}}.$$

To relate clustering to a realistic discriminator, we also consider a per–hit visible–energy threshold equal to the lowest bin populated by neutron clusters, $E_{\mathrm{min,clu}} = 0.08\,\mathrm{MeV}$ (active only). Counting neutrons with at least one hit above this value gives so that

$$\epsilon^{\mathrm{ECal}}_{n,\mathrm{clu}\,|\,>E_{\mathrm{min}}} = \frac{N_{n,\mathrm{clu}}}{N_{n,>E_{\mathrm{min}}}} = 0.408 \pm 0.0007_{\mathrm{stat}}.$$

All quoted uncertainties are binomial, $\sigma(\epsilon) = \sqrt{\epsilon(1-\epsilon)/N}$ where ϵ is the efficiency and N the corresponding denominator.

Figure 6.7 shows the visible energy of neutron-generated clusters (active material only). The fact that the mean of the cluster visible energy closely matches the mean of the hit deposited energy indicates that, on average, the reconstruction is unbiased for neutron-induced activity.

The resulting cluster efficiency versus true neutron kinetic energy at the vertex, $\epsilon^{\mathrm{ECal}}_{n,\mathrm{clu}}(T_n^{\mathrm{true}})$, is displayed in Figure 6.6: it is broadly flat at $\sim$ 30–35% in the 100–1000 MeV range. As expected, the efficiency is lower respect to the one calculated with the hits from Monte Carlo due to the attenuation of the light signal in the fibers, the threshold for ADC discriminator set to 2.5 pe and the requirement used in the sample that the cells of the clusters have to be complete (see Section 5.1).

The order of magnitude aligns with neutron–tag efficiencies reported in test-beam studies of the KLOE experiment's ECal module, as already discussed in 3.1.2.4. [94].

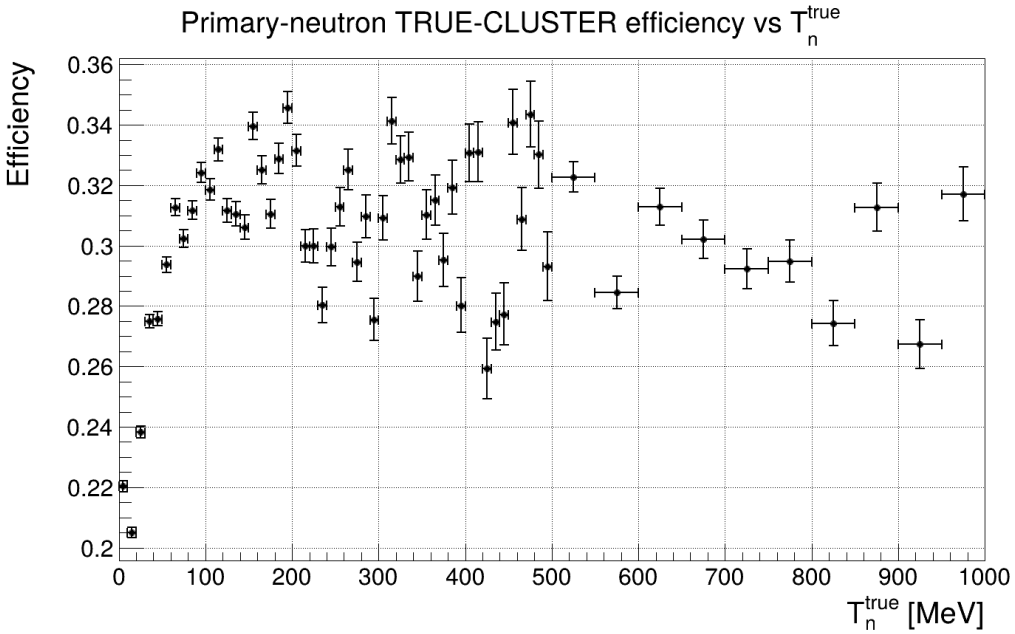

Figure 6.6: Primary neutron cluster efficiency $\epsilon_{n,\mathrm{clu}}^{\mathrm{ECal}}$ in the ECal as a function of true neutron kinetic energy at the vertex, T_n^{true}. Points show the binomial efficiency; vertical error bars indicate statistical uncertainties, and horizontal bars the bin widths.

6.2 $\bar{\nu}_\mu + p \to \mu^+ + n$ characterization

Table 6.1 summarizes the rate of CCQE (with $\mu^+ n$ in the stable final state) in the full sample of 5.0×10^5 neutrino interactions in the SAND tracker volume. Out of all interactions, 7.76% end in $\mu^+ n$; within this subset, about 82.9% occur on carbon and 16.6% on hydrogen, with all other isotopes contributing $\lesssim 0.5\%$. This composition anticipates that non-H (mostly C) backgrounds dominate and motivates the $(|\Delta t|, \Delta r)$ rejection of non-H interaction discussed later.

In Figure 6.8, the distribution of the initial momentum of the neutron exiting from the neutrino interaction vertex with $\mu^+ + n$ as a stable final state, with all the possible targets, the fit is done with a Landau curve only to show the most probable value. In Figure 6.9, the distribution of the deposited energy in the ECal, only in the active material, is obtained by summing the hits of the primary neutron `EDEPTrajectory` exiting from the vertex and of all the trajectories of the neutron children.

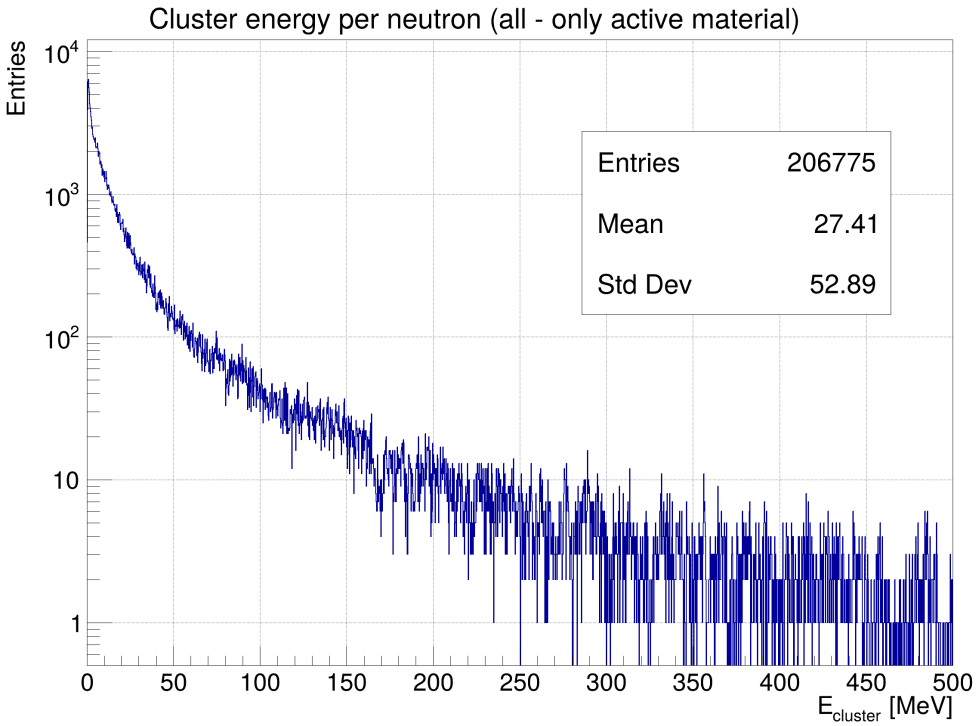

Figure 6.7: Cluster energy distribution in ECal for primary neutron exiting from the vertex for all kinds of neutrino interactions. Clusters are classified as neutron ones requiring a primary neutron as the main `cluster_generator`.

Table 6.1: Number of CCQE $\bar{\nu}_\mu$ interactions per target isotope in the sample of 5.0×10^5 neutrinos interacting in SAND tracker volume.

Target	**# Interactions**	**% of** 5.0×10^5
^{1}H	6451	1.2902
^{12}C	32143	6.4286
^{14}N	19	0.0038
^{16}O	9	0.0018
^{40}Ar	57	0.0114
^{197}Au	103	0.0206
Total	**38782**	**7.7564**

6.3 Kinematic selection

The good angular, vertex, momentum and timing resolutions of the highly segmented low-density tracker allow the determination of the interaction vertex posi-

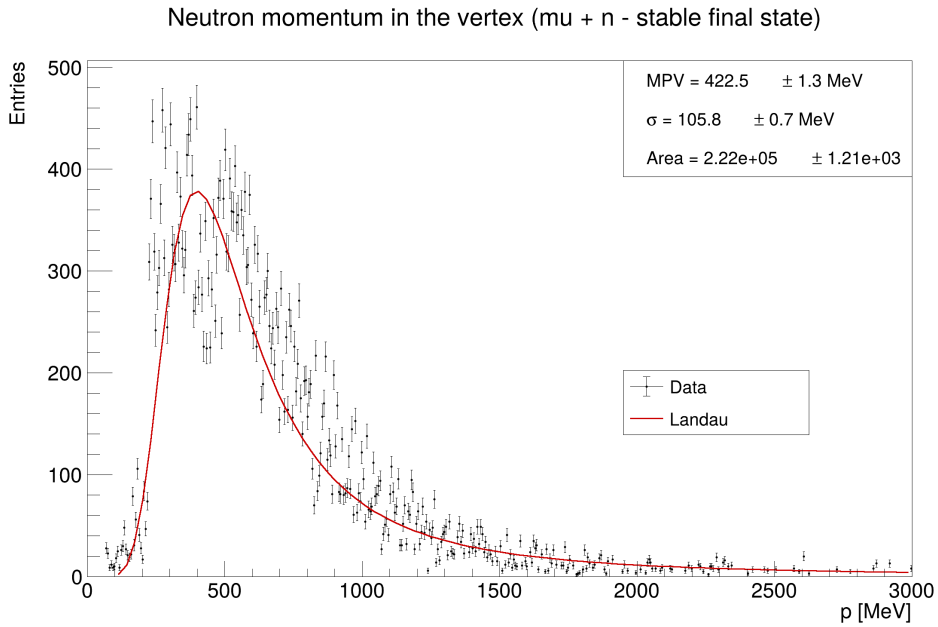

Figure 6.8: Momentum distribution for primary neutron exiting from the vertex with $\mu^+ + n$ as a stable final state. $N_{\mathrm{n},\mu^+ + n} = 38{,}782$

tion in the different modules and so in the different target materials. For interactions with a single charged track as the CCQE $\bar{\nu}_\mu + p \to \mu^+ + n$, the resolution on the neutrino vertex position is driven by the thickness of a single CH_2/C target plane, in which the detector wire located before the target layer does not present hits. Even if the vertex resolution is worse than for multi-track events it is still $<<$ 1 mm [112]. The uncertainty on the material assignment is given by the ratio between the thickness of the passive layers immediately upstream of the candidate target (drift chamber cathode foils or straw walls) and the thickness of the target, resulting in an efficiency >95% [100].

If the outgoing nucleon momentum is measured, one can, in principle, reconstruct the neutrino energy by summing the momenta of all final-state particles. On nuclear targets, the achievable accuracy in neutrino energy reconstruction event by event is intrinsically limited by the nucleon binding energy and Fermi motion that affect the initial state nucleon. In addition, the final-state hadron kinematics can be altered by the final-state interactions (FSIs) in which nucleon reinteracts with the cold nuclear medium before leaving the target nucleus that can be excited or even break up, releasing secondary particles that stop near the vertex and are not detected, biasing the reconstruction.

Hydrogen is the ideal target for reconstructing the initial neutrino energy because

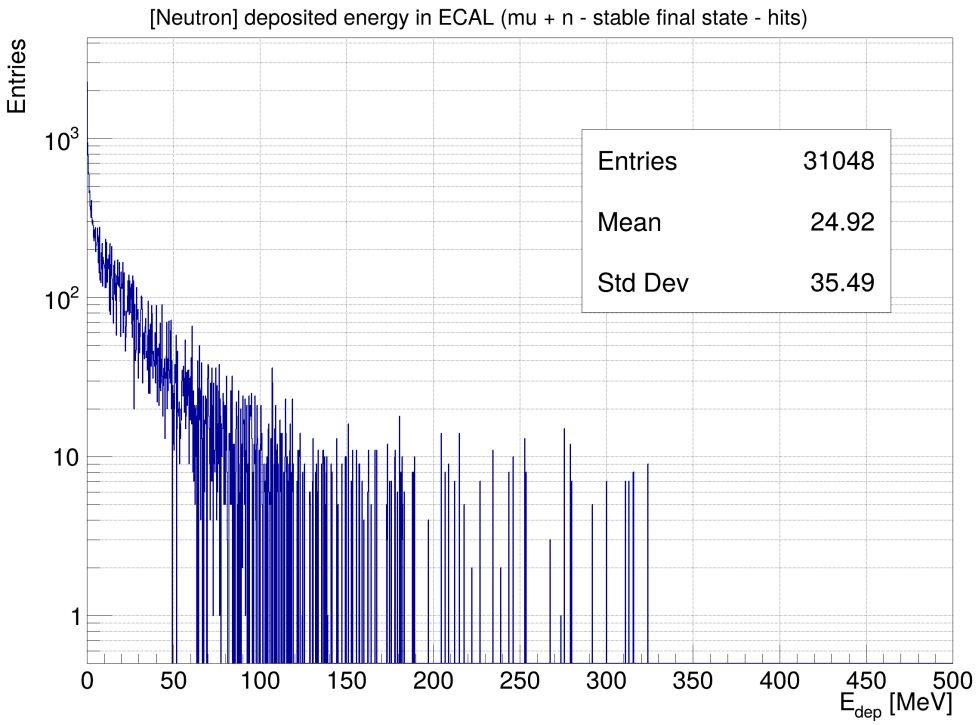

Figure 6.9: Deposited energy hit distribution in ECal for primary neutron from CCQE interaction with $\mu^+ + n$ as a stable final state.

nuclear effects are not present, and the reconstruction of the beam energy spectrum would be limited only by the knowledge of the cross section, which is much better understood than the nuclear ones. Once the correct target module is identified, the CH_2 interactions are separated from those in the other modules. Then, to isolate events on H in the mixture with the C nuclei of the polypropylene, the spatial symmetry in the final-state kinematics in CCQE can be exploited.

Since the H target is at rest, CCQE events are expected to be perfectly balanced in the plane transverse to the beam direction, and the muon and hadron vectors are back-to-back in the same plane. On the other hand, the nuclear effects give rise to a significant missing transverse momentum and a smearing of the transverse plane kinematics. The use of transverse plane variables and event kinematics to select various neutral and charged current (anti)neutrino interactions have been adopted in analyses by several experiments [113, 114] and is used in SAND as a powerful variable to select interactions on H.

If we consider the plane transverse to the neutrino direction, the missing transverse

momentum in Eq. 6.4

$$\delta p_T^m = \|\vec{p}_T^{\,H} + \vec{p}_T^{\,\ell}\| \tag{6.4}$$

is calculated as the sum of the projection in the transverse plane of the momenta of the hadronic state $\vec{p}_T^{\,H}$ and the leptonic one $\vec{p}_T^{\,\ell}$. In the hadron momentum vector, $\vec{p}^{\,H}$, the momenta of all the detectable particles in the final state are summed up, while particles absorbed after final state interactions, leptons and photons from decays and nuclear de-excitations are not considered. $\vec{p}^{\,\ell}$ takes into account the final-state leptons.

For the channel of this analysis, in case of interactions on the H target, $\vec{p}^{\,H}$ coincides with the momentum vector of the final state neutron. The leptonic momentum vector, despite the kind of nuclear target, is $\vec{p}^{\,\ell} = \vec{p}^{\,\mu}$ where neutrinos are not summed up. Only charged-current interactions are considered.

The antineutrino CCQE scattering on a free proton on hydrogen and the same process on a bound proton in carbon, using the missing transverse momentum $\delta p_T^m \equiv \|\vec{p}_T^{\,\ell} + \vec{p}_T^{\,H}\|$ are sketched in Figure 6.10 and described in the following:

Hydrogen (free p at rest).

$$\bar{\nu}_\mu + p(^1\mathrm{H};\, \vec{k}_F = 0) \;\rightarrow\; \mu^+ + n.$$

With the initial proton at rest (no Fermi motion $\vec{k}_F = 0$) the muon and neutron are back-to-back in the transverse plane, so

$$\delta p_T^m = \|\vec{p}_T^{\,\mu} + \vec{p}_T^{\,n}\| = 0.$$

Carbon (bound p with Fermi motion; no FSI).

$$\bar{\nu}_\mu + p\Big(^{12}\mathrm{C};\, \vec{k}_F\Big) \;\rightarrow\; \mu^+ + n + {}^{11}\mathrm{B}^*.$$

The initial proton carries a Fermi momentum $\vec{k}_F$ with transverse component $\vec{k}_{F,T}$. The momentum conservation in the transverse plane gives

$$\vec{p}_T^{\,\mu} + \vec{p}_T^{\,n} \;=\; \vec{k}_{F,T},$$

so the missing transverse momentum is

$$\delta p_T^m = \big\|\vec{p}_T^{\,\mu} + \vec{p}_T^{\,n}\big\| = \|\vec{k}_{F,T}\| \;>\; 0.$$

that for carbon is typical $\|\vec{k}_F\| \sim 200$–250MeV.

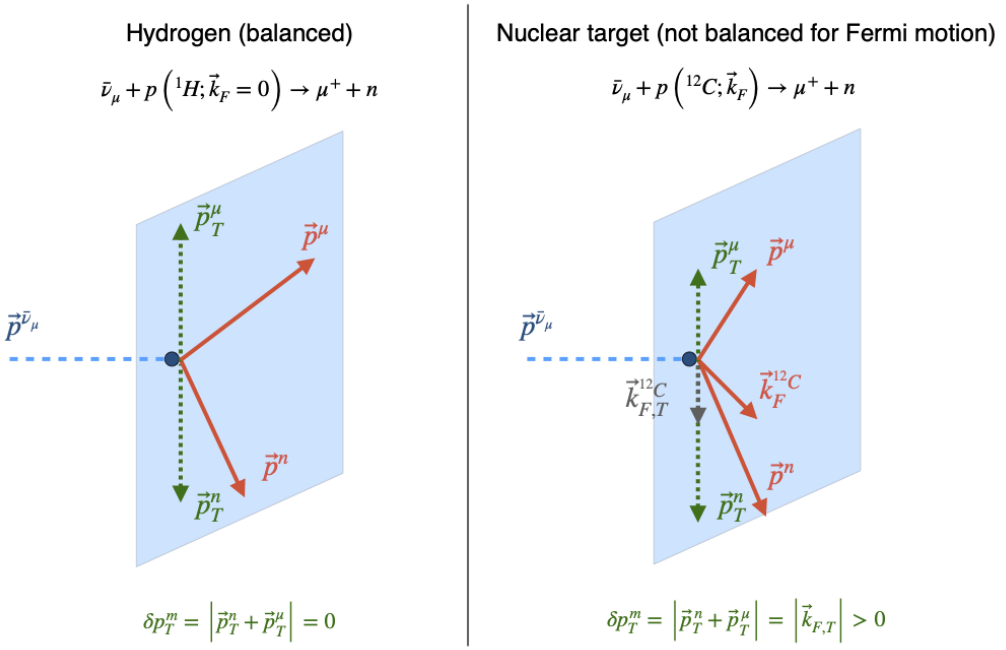

Figure 6.10: Transverse momentum balance in $\bar{\nu}_\mu$ CCQE scattering on hydrogen vs. carbon. **Left (H):** initial free proton at rest and the muon and neutron in the final state are back-to-back in the transverse plane, so $\delta p_T^m = \|\vec{p}_T^{\,\mu} + \vec{p}_T^{\,n}\| = 0$. **Right (C):** initial proton with Fermi momentum $\vec{k}_F$, giving $\vec{p}_T^{\,\mu} + \vec{p}_T^{\,n} = \vec{k}_{F,T}$ and $\delta p_T^m = \|\vec{k}_{F,T}\| > 0$. In both the situations, the only detectable particle for the hadronic state is the neutron, giving $\vec{p}_T^{\,H} \equiv \vec{p}_T^{\,n}$.

If the outgoing neutron re-scatters in the medium undergoing FSI, $n+N \to n'+N'$, an additional transverse shift Δ_T^{FSI} is introduced, increasing the missing transverse momentum:

$$\delta p_T^m = \|\vec{p}_T^{\,\mu} + \vec{p}_T^{\,n'}\| = \|\vec{k}_{F,T} + \Delta_T^{\text{FSI}}\| \; > \; 0,$$

where N denotes a nucleon belonging to the residual nuclear system and carrying its own Fermi momentum $\vec{k}_N$; N' is that same nucleon after the intranuclear collision.

In Figure 6.11b, the missing transverse momentum δp_T^m for all the charged-current $\bar{\nu}_\mu$ interactions on H and non-H targets. The sample used is the same as described in Section 6.1. As expected, CC interactions are perfectly balanced for the H target, while the variable is smeared for the other targets. In Figure 6.11a, the missing transverse momentum for the interaction on H and C is shown.

6.4 Prediction of the final–state neutron

If the interaction occurs on a hydrogen target, the final-state neutron quantities are fully determined once the muon track quantities are reconstructed. For the work of this thesis, the muon quantities are taken from the Monte Carlo, as the reconstruction tracking algorithms described in Section 4.3 are not completely validated yet.

How the prediction of the kinematics of the outgoing neutron of the $\bar{\nu}_\mu + p \to \mu^+ + n$ channel events is performed is described in the following.

Neutrino energy from final-state kinematics

The CCQE topology at the primary vertex with a single μ^+ and (at least) one neutron in the final state is selected, and on a proton at rest for hydrogen target, the momentum–energy conservation leads to the antineutrino energy in Eq. 6.5:

$$E_\nu^{\mathrm{QE}} \;=\; \frac{M_n^2 - m_\mu^2 - M_p^2 + 2\,M_p\,E_\mu}{2\,(M_p - E_\mu + p_\mu \cos\theta_\mu)}\,, \tag{6.5}$$

where the beam direction $\hat{n}_\nu$ is assumed to be known and it is taken from Monte Carlo information, the reconstructed muon momentum is denoted as $\vec{p}_\mu$, with magnitude $p_\mu = \|\vec{p}_\mu\|$ and energy

$$E_\mu = \sqrt{p_\mu^2 + m_\mu^2}\,. \tag{6.6}$$

θ_μ is the angle between $\vec{p}_\mu$ and $\hat{n}_\nu$, $\cos\theta_\mu = \hat{p}_\mu \cdot \hat{n}_\nu$ and the incident antineutrino three–momentum is along the beam,

$$\vec{p}_\nu \equiv E_\nu\,\hat{n}_\nu\,. \tag{6.7}$$

Predicted neutron momentum, energy, and speed

Assuming no nuclear effect are present, the neutron momentum is predicted from momentum conservation:

$$\vec{p}_n^{\,\mathrm{pred}} \;=\; \vec{p}_\nu - \vec{p}_\mu\,, \qquad p_n^{\mathrm{pred}} \equiv \|\vec{p}_n^{\,\mathrm{pred}}\|\,, \qquad \hat{u}_n \equiv \frac{\vec{p}_n^{\,\mathrm{pred}}}{p_n^{\mathrm{pred}}}\,. \tag{6.8}$$

The neutron total and kinetic energy follow from energy conservation:

$$E_n^{\mathrm{pred}} \;=\; E_\nu + M_p - E_\mu\,, \qquad T_n^{\mathrm{pred}} \;=\; E_n^{\mathrm{pred}} - M_n\,. \tag{6.9}$$

The predicted speed (in units of c) is

$$\beta_n^{\text{pred}} \;=\; \frac{p_n^{\text{pred}}}{E_n^{\text{pred}}} \;=\; \frac{p_n^{\text{pred}}}{T_n^{\text{pred}} + M_n}\,. \tag{6.10}$$

Neutron reference "flight line"

If the neutron does not interact in the tracker material before reaching the ECal, its trajectory is a straight line. The neutron "flight line" and the associated time–of–flight is defined from the vertex along the momentum unit vector $\hat{u}_n$ in Equation 6.11a

$$\vec{x}(s) = \vec{x}_0 + s\,\hat{u}_n\,, \qquad s \geq 0\,, \tag{6.11a}$$

$$t_{\text{pred}}(s) = t_0 + \frac{s}{\beta_n^{\text{pred}}}\,, \tag{6.11b}$$

where the primary vertex coordinates are $(\vec{x}_0, t_0)$.

Assuming that the neutron will interact in an ECal cell, for a generic reconstructed calorimeter cell at position $\vec{x}_i$ and time t_i, are defined

$$\vec{r}_i \equiv \vec{x}_i - \vec{x}_0\,, \qquad s_i \equiv \vec{r}_i \cdot \hat{u}_n \;= \left\|\vec{x}_{\text{pred}}\right\|, \qquad \Delta r_i \equiv \left\|\vec{r}_i - s_i\,\hat{u}_n\right\|, \tag{6.12}$$

with s_i the longitudinal projection of the reconstructed cell position along the "flight line" and Δr_i the perpendicular distance to it. The difference between the cell time with respect to the vertex time, and the time-of-flight along the "flight line" at s_i is

$$\Delta t_i \;\equiv\; t_i - t_{pred}(s_i) = (t_i - t_0) - \frac{s_i}{\beta_n^{\text{pred}}\, c}\,, \tag{6.13}$$

Matching and cut definition

For each reconstructed cluster, the cells are scanned and Δt_i is calculated. Among the cells, the one that minimizes $|\Delta t_i|$ is selected.

Given a pair of cut thresholds (τ, ρ) in time and space, respectively, a cell and hence its cluster passes the cut if

$$|\Delta t_i| \leq \tau \quad \text{and} \quad \Delta r_i \leq \rho\,. \tag{6.14}$$

Event-level quantities are calculated along with counters classifying each passing

cluster by its associated particle.

The following observables have been used for validation

$$\Delta\vec{x} \equiv \vec{x}_{\text{pred}}(s_i) - \vec{x}_i = \left(\vec{x}_0 + s_i\hat{u}_n\right) - \vec{x}_i, \tag{6.15}$$

$$\Delta t \equiv t_i - t_{pred}(s_i) = \Delta t_i\,. \tag{6.16}$$

The same construction is applied to the earliest Monte Carlo hit deposited in an ECal volume owned by a neutron trajectory[2]. $(\vec{x}_i, t_i)$ is taken from that hit and the distributions of $\Delta\vec{x}$, Δt, Δr are used to quantify the prediction accuracy.

Equations (6.5)–(6.10) are exact for CCQE interactions on hydrogen free proton while on nuclear targets they provide a biased prediction due to nuclear effects, which broaden Δt and Δr and may displace the ECal activity from the straight reference line. Moreover, even in CCQE events on hydrogen, the Δt and Δr distributions can broaden if the outgoing neutron undergoes hadronic interactions in detector material upstream of the ECal (elastic scattering, inelastic reactions, or capture), which kink the "flight line" path and delay the first ECal activity.

Residuals

Figures 6.12 and 6.13 show the distributions of the spatial $\Delta\vec{x}$ and of the timing residuals Δt between the "flight-line" prediction and the matched ECal cell for neutron clusters in CCQE events on nuclear targets and on hydrogen, respectively. On the distributions is performed a fit with a Double Crystal–Ball (DCB) function in Equation 6.17.

$$\begin{aligned}
t &\equiv \frac{x-\mu}{\sigma}, \qquad \alpha_L > 0,\ \alpha_R > 0,\ n_L > 1,\ n_R > 1,\ \sigma > 0,\\
f(x) &= \begin{cases} A_L\,(B_L - t)^{-n_L}, & t \le -\alpha_L,\\ \exp\!\left(-\tfrac{1}{2}t^2\right), & -\alpha_L < t < \alpha_R,\\ A_R\,(B_R + t)^{-n_R}, & t \ge \alpha_R, \end{cases}\\
A_L &= \left(\frac{n_L}{\alpha_L}\right)^{n_L} \exp\!\left(-\tfrac{1}{2}\alpha_L^2\right), \qquad B_L = \frac{n_L}{\alpha_L} - \alpha_L,\\
A_R &= \left(\frac{n_R}{\alpha_R}\right)^{n_R} \exp\!\left(-\tfrac{1}{2}\alpha_R^2\right), \qquad B_R = \frac{n_R}{\alpha_R} - \alpha_R.
\end{aligned} \tag{6.17}$$

The spatial residuals exhibit a narrow gaussian core centered near zero that corre-

[2]To refer to the `EDEPTrajectory` and `EDEPHit` objects, as defined in Sec. 5.2.

sponds to neutrons following the predicted straight path. The power-law tails represent both the facts that neutrons can undergo nuclear effects and interact before reaching the ECal. The core widths extracted from the DCB fits are, for nuclear targets, $\sigma_{\Delta x} \simeq 23.7 \pm 1.0$ mm, $\sigma_{\Delta y} \simeq 27.3 \pm 2.1$ mm, and $\sigma_{\Delta z} \simeq 24.0 \pm 1.1$ mm (see Figure 6.12); for interactions on hydrogen the gaussian core is narrowed due to the absence of nuclear effects reducing to $\sigma_{\Delta x} \simeq 13.6 \pm 0.8$ mm, $\sigma_{\Delta y} \simeq 12.8 \pm 0.8$ mm, and $\sigma_{\Delta z} \simeq 14.4 \pm 0.9$ mm (see Figure 6.13).

The σ values are comparable to the single cell spatial resolution: for y and z it is set by the cell granularity (44 mm to 52 mm) while for x longitudinal coordinate it is governed by the time of arrival difference between the two photo-signals (see Section 5.1),

$$x \;=\; \frac{v_{\text{fiber}}}{2}\left(t_{\text{A}} - t_{\text{B}}\right), \qquad \sigma_x \;=\; \frac{v_{\text{eff}}}{2}\sqrt{\sigma^2_{t_{\text{A}}} + \sigma^2_{t_{\text{B}}}} \;\overset{\sigma_{t_{\text{A}}}=\sigma_{t_{\text{B}}}=\sigma_t}{=}\; \frac{v_{\text{fiber}}}{\sqrt{2}}\,\sigma_t\,,$$

where the light speed along the fibers is $v_{\text{fiber}} = 17$ cm/ns and $t_{\text{A,B}}$ the time of the photo-signals at the photo-detector cell sides (see Section 4.2).

Assuming an average neutron deposited energy in the ECal of ~ 25 MeV and using the time resolution from KLOE calibration $\sigma_t(E) \simeq 54\,\text{ps}/\sqrt{E\,[\text{GeV}]} \oplus 140$ ps [115], one obtains $\sigma_t(0.025\,\text{GeV}) = 0.37$ ns .

$$\sigma_x \;=\; \frac{17\,\text{cm/ns}}{\sqrt{2}} \times 0.37\,\text{ns} \;=\; 44\,\text{mm}\,.$$

The time resolution above refers to a cluster timing that averages over multiple cells, and it has a smaller σ_t than the single cell one. Therefore, the σ_x obtained it is lower than the single–cell longitudinal resolution.

The timing residual Δt shows a peak with a bias respect to zero of $\simeq 1$ ns, compatible with the scintillation decay and the photo-sensor timing spread simulated in digitization 4.2. For nuclear targets (Figure 6.12d) tails are present on both sides, attributable both to nuclear effects and to interactions before the ECal. For hydrogen (see Figure 6.13d) the negative tail is suppressed, while the positive tail ($t_{\text{cell,match}} > t_{\text{pred}}$) remains, consistent with the neutron interacting before reaching the ECal, leading to a greater neutron time of flight respect to the "flight-line" one. From the DCB fits for nuclei interactions, $\mu_{\Delta t} = 0.89 \pm 0.01$ns and $\sigma_{\Delta t} = 0.70 \pm 0.01$ns are found; for hydrogen, $\mu_{\Delta t} = 0.91 \pm 0.01$ns and $\sigma_{\Delta t} = 0.30 \pm 0.01$ns.

6.5 Selection efficiency and purity

The measurement of $\bar{\nu}_\mu$–H interactions relies on identifying the neutron from $\bar{\nu}_\mu + p \to \mu^+ + n$ with minimal bias and background. While the tracker provides the kinematic handles used by the data-driven "solid hydrogen" subtraction (Section 3.2), the ECal can tag the neutron, so the performance of the neutron selection directly affects the systematic uncertainty on the H target event sample, that constrains the flux and cross-section measurements.

Two complementary figures of merit are required:

- the **selection efficiency**, which controls statistical power and biases from acceptance losses,
- the **purity** of the selected clusters, which governs the level of contamination from non-H neutrons or activity associated to different clusters, that would affect the C background subtraction [101].

For each CCQE event with a final state $\mu^+ + n$, for each cut pair $(|\Delta t|, \Delta r)$ defined in Equation 6.14, the following quantities are computed:

- **Efficiency** $\varepsilon(|\Delta t|, \Delta r) = N_{\text{events with } \geq 1 \text{ neutron pass}}/N_{\text{neutrons}}$: the fraction of primary neutrons for which at least one neutron cluster passes the cuts.
- **Purity** $P_{\text{clu}}(|\Delta t|, \Delta r) = P_{\text{clu}} = N_{\text{passing neutron clusters}}/N_{\text{passing generic clusters}}$: among all passing clusters, the fraction that are neutron-owned.
- **Best-is-neutron rate** $R_{\text{best}}(|\Delta t|, \Delta r) = N_{\text{events with neutron cluster as the best}}/N_{\text{neutrons}}$: the fraction event whose best passing cluster (smallest $|\Delta t|$, then smallest Δr) is a neutron cluster.

In Figures 6.14, 6.15, and 6.16 the map of the selection behaviour as a function of the cuts can be found. The efficiency grows mainly when increasing the spatial window Δr, while relaxing $|\Delta t|$ beyond $\sim$5 ns increases it only mildly. The cluster purity decreases with larger Δr, so tight spatial cuts can keep contamination low. The event-level R_{best} follows the efficiency trend but remains lower, as expected when multiple clusters pass and ranking can occasionally favour a non-neutron cluster.

Working points To guide analysis choices, three working points (WPs) can be defined depending on complementary priorities: **Baseline** ($|\Delta t|$, Δr) = (5 ns, 200 mm) gives $\varepsilon = 0.204$, $P = 0.493$, $R_{\text{best}} = 0.162$ for a balance between statistics and cleanliness; **Loose** (10 ns, 300 mm) gives $\varepsilon = 0.247$, $P = 0.329$, $R_{\text{best}} = 0.208$ requires less statistics giving a lower purity; **Tight** (5 ns, 100 mm) gives $\varepsilon = 0.121$,

$P = 0.628$, $R_{\text{best}} = 0.0099$ suppresses background with a signal-enriched selection. It as to be noticed that the background rejection can be performed using also different strategies combining the other SAND sub-detectors reconstructions.

Beam-time scaling Let N_{μ^+n} be the number of true CCQE events with final state $\mu^+ + n$. Define the per-interaction selection success probability (efficiency) at a working point as

$$\varepsilon_{\text{WP}} \;=\; \frac{N_{\text{sel}}}{N_{\mu^+n}}.$$

If $r_{\mu^+n} = N_{\mu^+n}/T_{\text{sample}}$ is the CCQE(μ^+n) interaction rate (events/hour), the expected number of selected events accumulated in beam time T_{WP} is

$$N_{\text{sel}} \;=\; r_{\mu^+n}\,\varepsilon_{\text{WP}}\,T_{\text{WP}}.$$

For a fixed N_{sel} number of events, times scale inversely with efficiency. Comparing any WP to the **Baseline** (Base) one has

$$\frac{T_{\text{WP}}}{T_{\text{Base}}} = \frac{\varepsilon_{\text{Base}}}{\varepsilon_{\text{WP}}}, \qquad \Delta T \equiv T_{\text{WP}} - T_{\text{Base}} = T_{\text{Base}}\left(\frac{\varepsilon_{\text{Base}}}{\varepsilon_{\text{WP}}} - 1\right). \tag{6.18}$$

Using the values read from the maps,

$$\varepsilon_{\text{Base}} = 0.204, \quad \varepsilon_{\text{Loose}} = 0.247, \quad \varepsilon_{\text{Tight}} = 0.121,$$

with $N_{\mu^+n} = 38{,}782$ and $T_{\text{Base}} = 2545.67$ h, Eq. (6.18) gives $T_{\text{Loose}}/T_{\text{Base}} = 0.204/0.247 = 0.826$ (about 17.4% less time, $\Delta T_{\text{Loose}} = -443.17$ h) and $T_{\text{Tight}}/T_{\text{Base}} = 0.204/0.121 = 1.686$ (about 68.6% more time, $\Delta T_{\text{Tight}} = +1746.20$ h).

A compact summary of the three working points and the beam-time scaling is reported in Table 6.2.

Table 6.2: Beam-time scaling at different working points assuming a fixed yield (N_{sel}) and taking **Baseline** as reference. Event counts use $N_{\mu^+n} = 38{,}782$. Times use $T_{\text{Base}} = 2545.67$ h.

WP	$(\lvert\Delta t\rvert, \Delta r)$	ε	P	R_{best}	T/T_{Base}	T [h]	N_{sel}
Loose	(10 ns, 300 mm)	0.247	0.329	0.208	0.826	2102.50	9,579
Baseline	(5 ns, 200 mm)	0.204	0.493	0.162	1.000	2545.67	7,912
Tight	(5 ns, 100 mm)	0.121	0.628	0.099	1.686	4291.87	4,693

Rejection power for non-H target interactions To quantify how much background from CCQEnon-hydrogen targets is removed by the selection before

applying the C subtraction procedure [99], the non-H rejection power is defined as

$$R_{\mathrm{rej}}^{\mathrm{nonH}}(|\Delta t|, \Delta r) = 1 - \varepsilon_{\mathrm{nonH}}(|\Delta t|, \Delta r) = 1 - \frac{N_{\mathrm{sel}}^{\mathrm{nonH}}}{N_{\mu^+ n}^{\mathrm{nonH}}}\,. \tag{6.19}$$

In Equation 6.19 $N_{\mu^+ n}^{\mathrm{nonH}}$ is the number of true CCQE($\mu^+ n$) interactions on non-H targets, that in SAND are dominated by carbon as shown in Table 6.1, and $N_{\mathrm{sel}}^{\mathrm{nonH}}$ is the subset that pass the $(|\Delta t|, \Delta r)$ cuts.

Figure 6.17 shows $R_{\mathrm{rej}}^{\mathrm{nonH}}$ as a function of the cuts: decreasing Δr makes rejection increasing quickly, while loosening $|\Delta t|$ beyond ∼5–10 ns brings only marginal changes.

At the three working points defined above, $R_{\mathrm{rej}}^{\mathrm{nonH}}$ results:

- **Tight** (5 ns, 100 mm): $R_{\mathrm{rej}} = 0.847$
- **Baseline** (5 ns, 200 mm): $R_{\mathrm{rej}} = 0.808$
- **Loose** (10 ns, 300 mm): $R_{\mathrm{rej}} = 0.760$

Thus, already at the **Baseline** point about four out of five non-H CCQE($\mu^+ n$) events are removed before applying the solid-hydrogen C–subtraction, cleaning the sample and reducing the statistics needed for the procedure. The working point should therefore balance this background reduction against the signal-efficiency discussed above.

Towards the full solid-hydrogen analysis

Towards the full solid-hydrogen analysis The analysis quantifies, for each $(\Delta t, \Delta r)$ working point, the selection efficiency for true $\bar{\nu}_\mu$ interactions on hydrogen, the corresponding acceptance for carbon events, and the fraction of carbon interactions that migrate into the hydrogen-enriched neutron-tag region. In a full solid-hydrogen analysis, these quantities enter the extraction of the $\bar{\nu}_\mu$–H signal. Starting from the CH_2 sample with a neutron tag, the number of selected events in each neutrino-energy bin is first corrected by subtracting the carbon contribution predicted from the graphite control sample under the same selection, and then divided by the $\bar{\nu}_\mu$–H selection efficiency to obtain an efficiency and background-corrected hydrogen yield, $N_H^{\mathrm{corr}}(E_\nu)$.

The resulting corrected yield, $N_H^{\mathrm{corr}}(E_\nu)$, is related to the differential $\bar{\nu}_\mu$ flux per POT, $\Phi_{\bar{\nu}_\mu}^{\mathrm{POT}}(E_\nu)$, by

$$N_H^{\mathrm{corr}}(E_\nu) = \Phi_{\bar{\nu}_\mu}^{\mathrm{POT}}(E_\nu)\, \sigma_{\bar{\nu}_\mu H}(E_\nu)\, N_{\mathrm{targets}}^{H}\, \mathrm{POT}, \tag{6.20}$$

so that the flux per POT can be obtained as

$$\Phi_{\bar{\nu}_\mu}^{\mathrm{POT}}(E_\nu) = \frac{N_H^{\mathrm{corr}}(E_\nu)}{\sigma_{\bar{\nu}_\mu H}(E_\nu)\, N_{\mathrm{targets}}^H\, \mathrm{POT}}. \tag{6.21}$$

Here $N_H^{\mathrm{corr}}(E_\nu)$ denotes the efficiency and background-corrected number of neutron-tagged $\bar{\nu}_\mu$–H interactions in the CH_2 sample in a given neutrino-energy bin, obtained after carbon subtraction using the graphite control sample. The quantity $\Phi_{\bar{\nu}_\mu}^{\mathrm{POT}}(E_\nu)$ is the differential $\bar{\nu}_\mu$ flux at the detector per proton on target (e.g. in units of $\mathrm{cm}^{-2}\,\mathrm{GeV}^{-1}\,\mathrm{POT}^{-1}$), $\sigma_{\bar{\nu}_\mu H}(E_\nu)$ is the $\bar{\nu}_\mu$ charged-current cross section on free protons, N_{targets}^H is the number of hydrogen targets in the fiducial mass, and POT is the integrated number of protons on target for the data set.

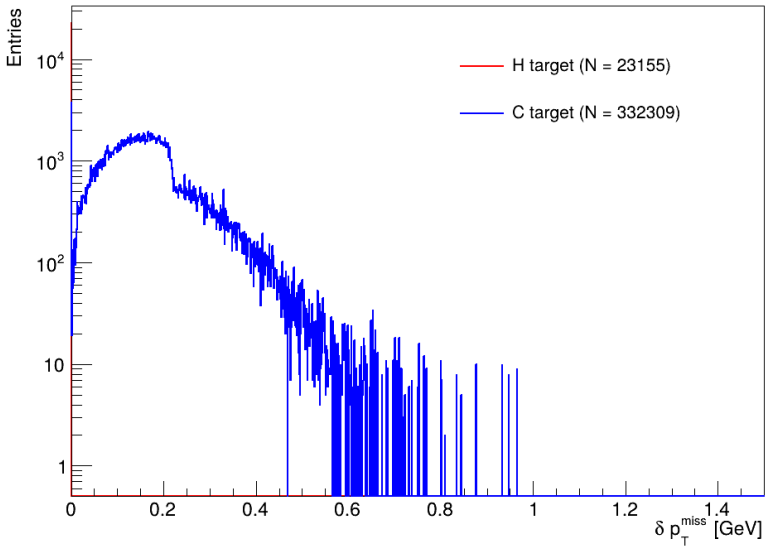

(a) δp_T^m for H (red) vs C (blue) interactions.

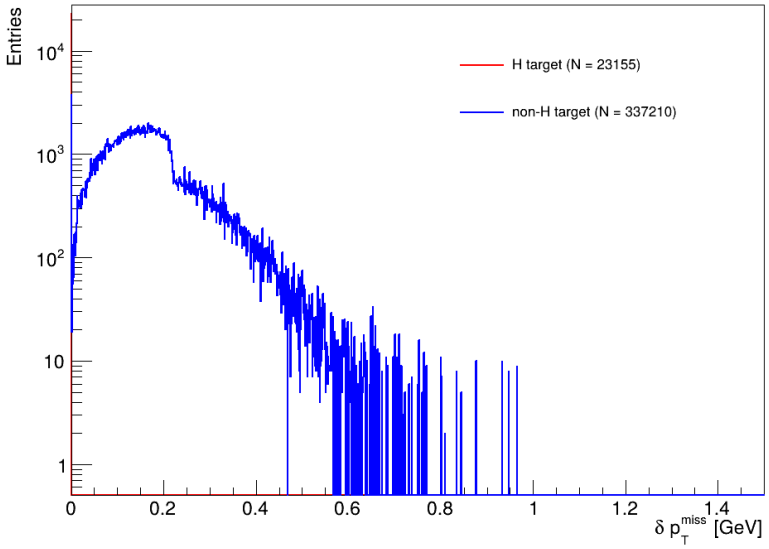

(b) δp_T^m H (red) vs all the other nuclei (blue) interactions.

Figure 6.11: Missing transverse momentum, $\delta p_T^m \equiv \left\|\vec{p}_T^{\,\mu} + \vec{p}_T^{\,\mathrm{H}}\right\|$, for charged-current $\bar{\nu}_\mu$ interactions in the sample described in Sec. 6.2. Panel (a) compares the interaction on hydrogen to the carbon ones. Panel (b) compares hydrogen interactions to the inclusive non-H sample. As expected, the H distribution is narrowly peaked near zero, while nuclear target interactions are smeared due to nuclear effects.

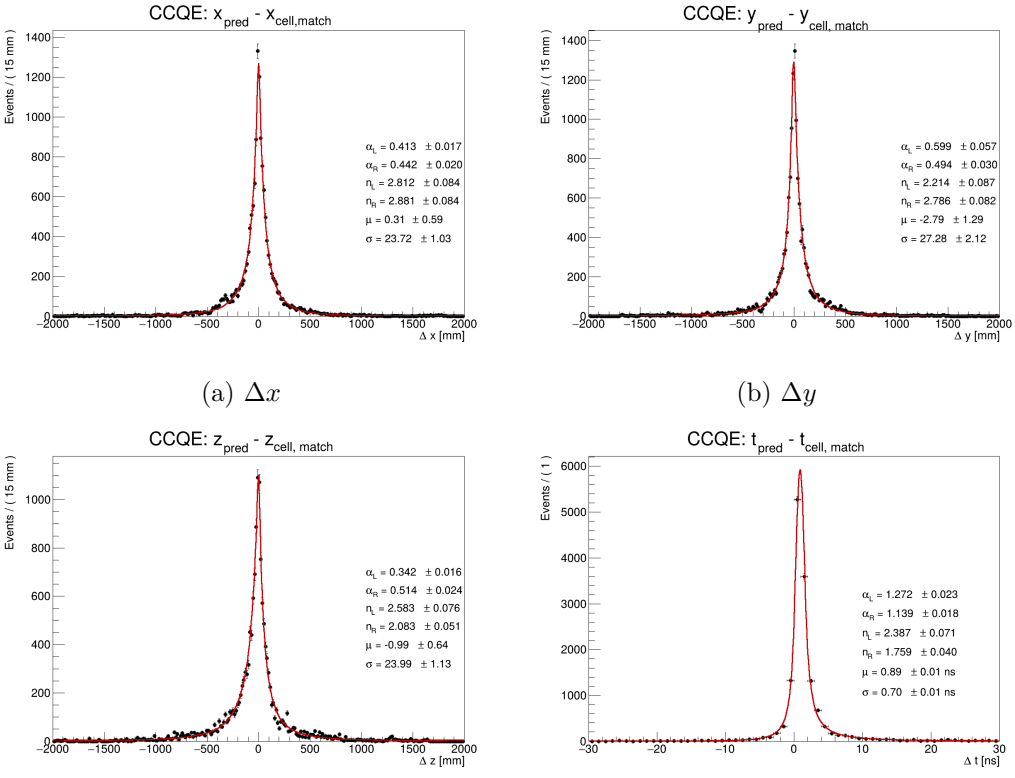

(a) Δx (b) Δy

(c) Δz (d) Δt

Figure 6.12: Residuals between "flight-line" prediction and reconstructed matched ECal cell for neutron associated cluster in CCQE events on nuclear targets. The distributions are fit with a Double Crystal Ball function (in red); $\Delta\vec{x}$ are fitted in $[-2, 2]$ m and Δt in $[-30, 30]$ ns.

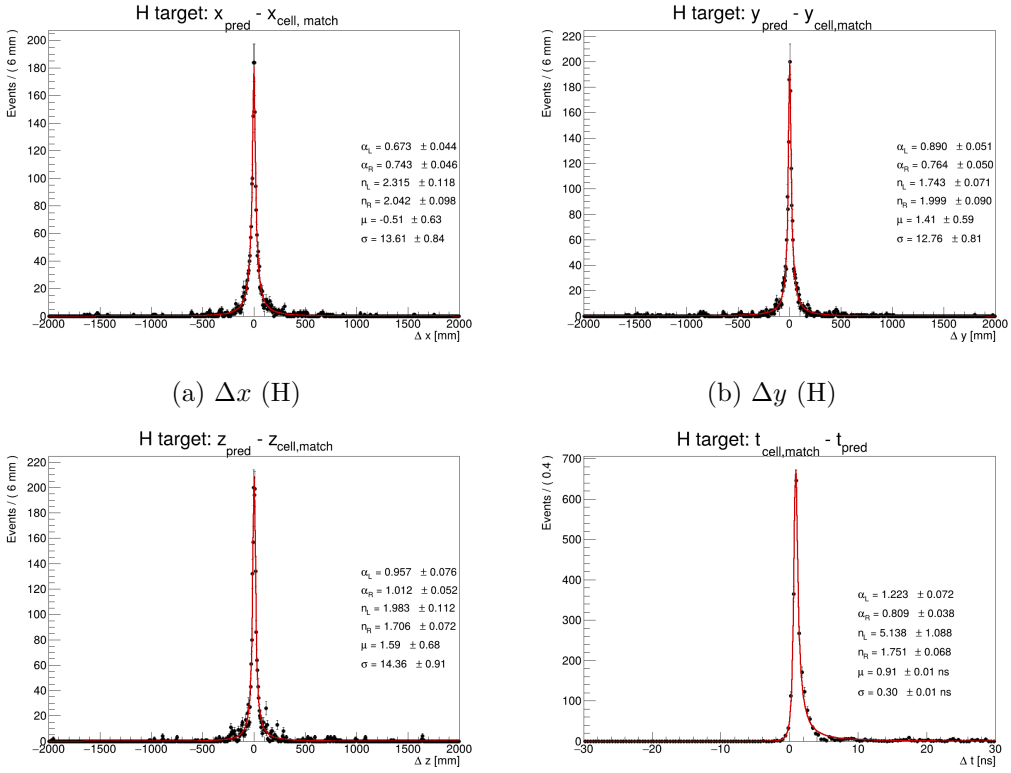

(a) Δx (H)

(b) Δy (H)

(c) Δz (H)

(d) Δt (H)

Figure 6.13: Same residuals as Figure 6.12 for neutron-associated clusters in CCQE events on hydrogen. The narrower gaussian cores and the reduced negative-time tail reflect the absence of nuclear effects.

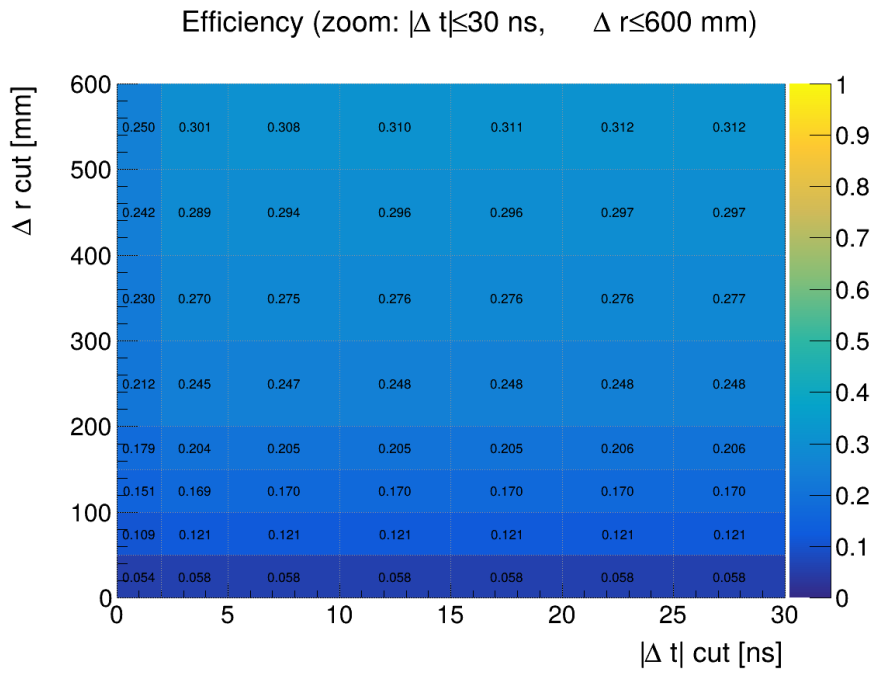

Figure 6.14: Efficiency map as a function of the cuts. In each bin $\varepsilon(|\Delta t|, \Delta r)$: the fraction of primary neutrons for which at least one neutron cluster passes the cuts. Zoom in the region $|\Delta t| \leq 30$ ns, $\Delta r \leq 600$ mm.

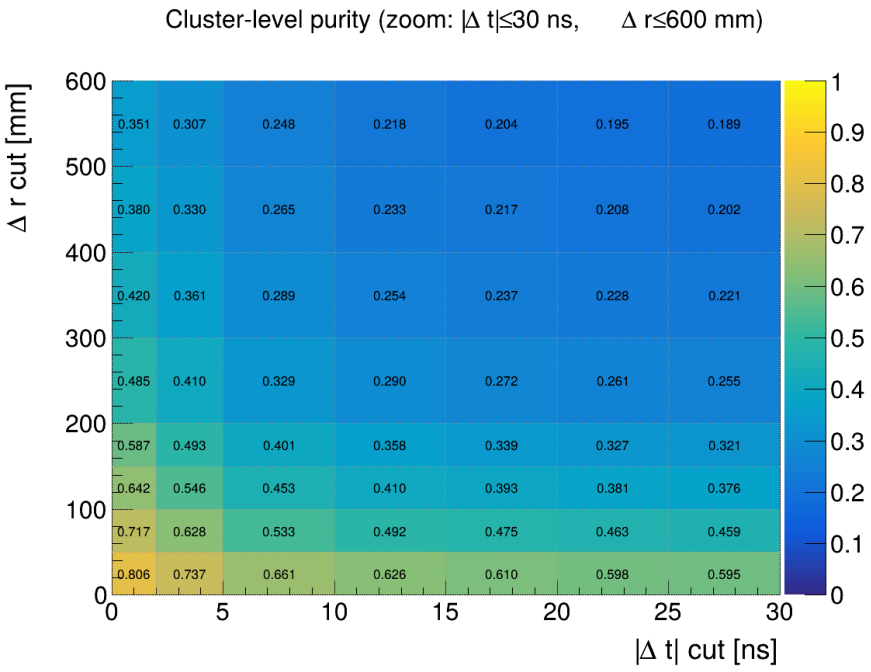

Figure 6.15: **Cluster-level purity** map as a function of the cuts. In each bin $P_{\text{clu}}(|\Delta t|, \Delta r)$: among all passing clusters, the fraction that are neutron-owned. Zoom in the region $|\Delta t| \leq 30$ ns, $\Delta r \leq 600$ mm.

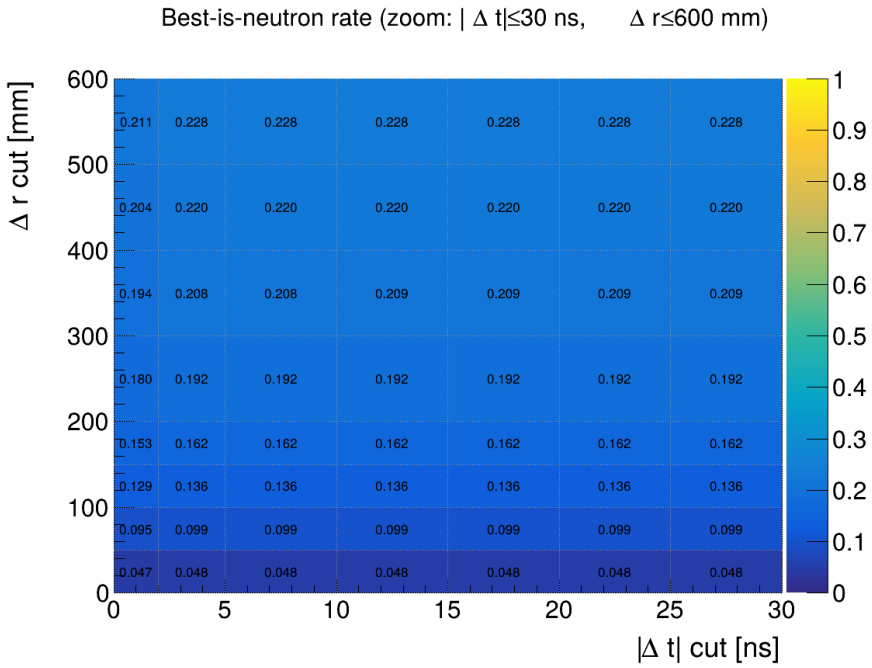

Figure 6.16: **Best-is-neutron rate** map as a function of the cuts. In each bin $R_{\text{best}}(|\Delta t|, \Delta r)$: the fraction event whose best passing cluster is a neutron cluster. Zoom in the region: $|\Delta t| \leq 30$ ns, $\Delta r \leq 600$ mm.

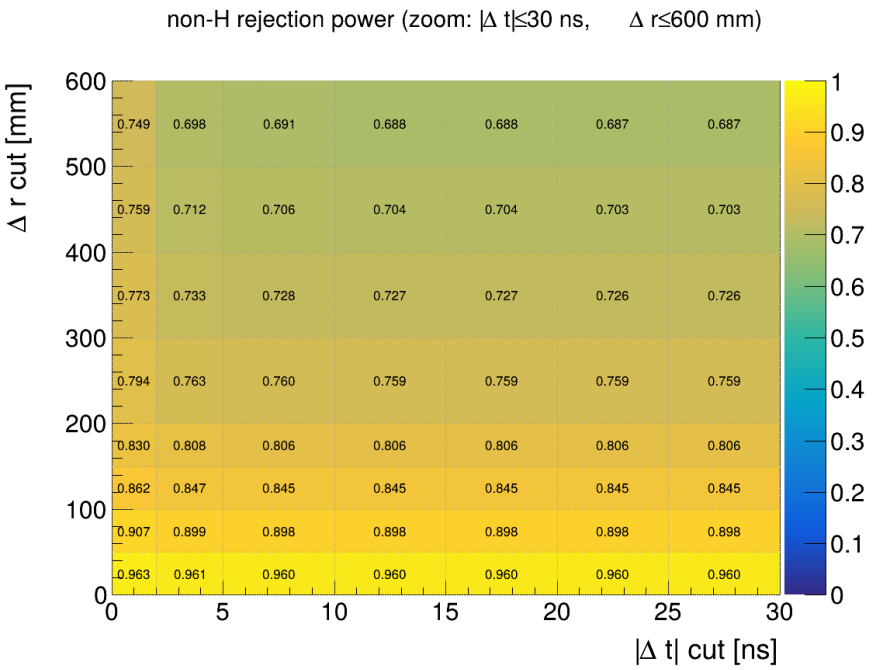

Figure 6.17: **non-H rejection power** $R_{\text{rej}}^{\text{nonH}}(|\Delta t|, \Delta r)$ as a function of the cuts. In each bin $R_{\text{rej}}^{\text{nonH}}$ defined in Eq. 6.19 as $R_{\text{rej}}^{\text{nonH}} = 1 - N_{\text{sel}}^{\text{nonH}}/N_{\mu^+n}^{\text{nonH}}$, shown as a heat map versus the cut pair $(|\Delta t|, \Delta r)$. Zoom in the region $|\Delta t| \leq 30$ ns and $\Delta r \leq 600$ mm.

Conclusions and future prospects

The studies presented in this thesis have established a coherent simulation-to-analysis chain for the SAND electromagnetic calorimeter, from the detailed modeling of energy deposits in the scintillating fibers to high-level reconstructed clusters and their association with Monte Carlo truth (see Chapters 4 and 5). The central outcomes of this work are the development of dedicated digitization, reconstruction and truth-matching algorithms for the ECal, their integration in the SAND software framework, and their validation through a series of performance and physics studies (Sections 4.2, 5.1, 5.2 and 5.3). On this basis, the neutron-tagging capability of the ECal has been quantified and the selection efficiency and background rejection have been studied in the specific context of the SAND hydrogen program (Chapter 6, in particular Sections 6.1, 6.2 and 6.5).

A C++ clustering algorithm has been developed (Section 5.1) that (i) classifies complete and incomplete cells, pairing the two photo-signals when both sides are fired; (ii) groups complete cells into pre-clusters by spatial adjacency; (iii) reconstructs energy, time, and position at the cell level, and builds energy-weighted cluster observables; (iv) splits time-dispersed pre-clusters using a time RMS corrected by the propagation and merges spatially and temporally compatible sub-clusters; and (v) recovers incomplete cells with a dedicated energy estimator.

A general truth matching algorithm, based on the `edep-reader` tool (Section 5.2), has been introduced: the Monte Carlo event from `edep-sim` is reorganized into a tree of trajectories, with explicit parent–child links so that the energy deposits in the ECal volumes can be traced back to the particles that produced them. For each reconstructed cluster, this infrastructure is used to build a corresponding *true_cluster* object, which provides its truth counterpart (see Section 5.3). The algorithm allows different performance and physics analyses to rely on the same, consistent reconstruction-truth association.

The complete simulation-to-analysis chain has been validated in Chapter 5 using muon and electron particle-gun samples and ν interactions in the SAND tracker volume. For electromagnetic showers, backtracking studies show a linear relationship between reconstructed and true cluster energies and allow the extraction of a global active–to–total calibration factor for electrons in the energy range relevant for the DUNE experiment (Section 5.5.1).

The analysis based on electron guns residuals yields an intrinsic energy resolution well described by

$$\frac{\sigma_E}{E} = \sqrt{\frac{(4.97 \pm 0.01)^2\%}{E_{\text{true}}\,[\text{GeV}]} + (2.00 \pm 0.02)^2\%}\,,$$

compatible with the KLOE experiment measurements (Section 5.6). For muons,

the same tools disentangle fully contained, through-going and decay populations, providing a consistent qualitative picture of their energy deposition in the ECal and setting the stage for a future, particle-dependent optimization of the split/merge clustering parameters and of the active–passive calibration.

As a result, the digitization, reconstruction, and Monte Carlo matching now form a single, self-consistent framework that serves as the baseline ECal model in SAND simulations and analyses.

A first extension is to compute particle-dependent calibration factors for different particles that contribute significantly to SAND observables, in particular charged pions, protons, and photons. This requires dedicated particle-gun samples and neutrino interactions, but can use the same backtracking tool and cluster selection developed in this work. Once particle-dependent calibrations are available, the clustering parameters could be re-optimized after a full particle identification chain is available.

The cluster observables defined in this thesis (i.e., longitudinal and transverse profiles, layer energies, asymmetries, and time structure) will be used for particle identification (PID) algorithms with ECal as the only detector to separate electromagnetic showers from MIP-like muon and pion tracks and showers. The reconstruction and backtracking tools developed here provide clean, truth-labeled samples for training and validating machine-learning models. The following step is to develop a PID framework that combines ECal information with tracker and GRAIN observables that can extend the separation power to the full charged-current sample and to suppress mis-associated or neutral activity. In addition to the use of track momenta (e.g. through E/p), also the spatial and angular matching between tracks and ECal clusters can be exploited as a powerful discriminant.

Chapter 6 applies the same framework to study neutron detection efficiency in ECal, and to perform the analysis of neutron tagging for $\bar{\nu}_\mu + p \to \mu^+ + n$ interactions on hydrogen.

The tools developed in this thesis are used both to characterize the neutron-induced response of the ECal and, via CCQE kinematics, to predict the location and timing of the final–state neutron reaching the calorimeter. Neutron candidates are then identified as clusters whose position and time are compatible with this prediction.

The ECal response to final state neutron from neutrino interaction has been studied, resulting in a hit-level efficiency of about $\sim 77\%$ using Monte Carlo information and a cluster-level efficiency of $\sim 35\%$ in the energy range relevant for DUNE (Section 6.1).

In addition, the spatial and timing residuals $(\Delta t, \Delta r)$ between the reconstructed neutron clusters and the kinematic prediction of the neutron path and time-of-flight from the interaction vertex exhibit narrow cores compatible with the expected detector resolutions (Section 6.4). This indicates that the reconstructed ECal activity is correctly associated with the underlying neutron kinematics.

Using these residuals as cut variables, a set of working points for the neutron tagging is defined and quantifies the trade-off between selection efficiency, purity, and non-H interaction background rejection (Section 6.5). At a chosen working point, the ECal neutron tag achieves an efficiency of order 20% on true μ^+n events, with neutron purities around 50% and a rejection of non-H CCQE(μ^+n)-like interactions at the level of $\sim$ 80%. The effective beam time required to reach a target event statistics is estimated for each working point (Table 6.2), illustrating how the ECal neutron tag can be used to balance statistical precision and background suppression for the SAND hydrogen measurements in the antineutrino channel.

The neutron-tagging study of Chapter 6 is therefore a first step towards a full solid-hydrogen analysis in SAND. The neutron-tagging procedure, together with a CCQE-like topology and transverse kinematic variables, will be used to collect a hydrogen-enriched signal in CH_2 modules for $\bar{\nu}_\mu + p \rightarrow \mu^+ + n$ interactions. In parallel, a pure-carbon control sample for the data-driven subtraction will be selected in the graphite modules with analogous topology and quality cuts, providing a general framework to extract $\bar{\nu}_\mu$-H samples. These samples form the basis for the measurements of the $\bar{\nu}_\mu$ flux at the SAND location, as well as for broader $\bar{\nu}_\mu$-H studies of cross sections and nuclear effects within the SAND antineutrino program.

Given the results discussed above, this thesis has provided a validated implementation of the ECal digitization, reconstruction, and truth backtracking for SAND, together with a quantitative characterization of its energy response and neutron-tagging capabilities. These elements form a solid technical and methodological basis on which future calibration, PID development, and hydrogen-based analyses of SAND at DUNE near detector complex can be performed.

Bibliography

[1] Wolfgang Pauli. *Open Letter to the Group of Radioactive People (Tübingen), 4 Dec 1930*. "Dear Radioactive Ladies and Gentlemen". 1930. URL: https://tildesites.bowdoin.edu/~naculich/280scans/pauli_letter.pdf.

[2] Enrico Fermi. "Tentativo di una teoria dei raggi β". In: *Il Nuovo Cimento* 11 (1934), pp. 1–19. DOI: 10.1007/BF02959820.

[3] C. S. Wu et al. "Experimental Test of Parity Conservation in Beta Decay". In: *Physical Review* 105 (1957), pp. 1413–1415. DOI: 10.1103/PhysRev.105.1413.

[4] E. C. G. Sudarshan and R. E. Marshak. "Chirality Invariance and the Universal Fermi Interaction". In: *Physical Review* 109 (1958), pp. 1860–1862. DOI: 10.1103/PhysRev.109.1860.2.

[5] R. P. Feynman and M. Gell-Mann. "Theory of the Fermi Interaction". In: *Physical Review* 109 (1958), pp. 193–198. DOI: 10.1103/PhysRev.109.193.

[6] S. Navas et al. "Electroweak Model and Constraints on New Physics". In: vol. 110. 3. Includes the definition of G_F and the weak scale relation $v = (\sqrt{2}G_F)^{-1/2}$. 2024. Chap. 10, p. 030001. DOI: 10.1103/PhysRevD.110.030001. URL: https://pdg.lbl.gov/2024/reviews/rpp2024-rev-standard-model.pdf.

[7] C. L. Cowan et al. "Detection of the Free Neutrino: A Confirmation". In: *Science* 124.3212 (1956), pp. 103–104. DOI: 10.1126/science.124.3212.103.

[8] A. Bettini. *Introduction to Elementary Particle Physics*. Cambridge University Press, 2008. DOI: 10.1017/CBO9780511809019.

[9] B. Pontecorvo. "Electron and Muon Neutrinos". In: *Zh. Eksp. Teor. Fiz.* 37 (1959). English transl.: Sov. Phys. JETP 10 (1960) 1236, pp. 1751–1757.

[10] G. Danby et al. "Observation of High-Energy Neutrino Reactions and the Existence of Two Kinds of Neutrinos". In: *Phys. Rev. Lett.* 9 (1962), pp. 36–44. DOI: 10.1103/PhysRevLett.9.36.

[11] K. Kodama et al. "Observation of tau neutrino interactions". In: *Phys. Lett. B* 504 (2001), pp. 218–224. DOI: 10.1016/S0370-2693(01)00307-0. arXiv: hep-ex/0012035.

[12] B T Cleveland et al. "Measurement of the solar electron neutrino flux with the Homestake chlorine detector". In: *The Astrophysical Journal* 496 (1998), pp. 505–526. DOI: https://doi.org/10.1086/305343. URL: https://doi.org/10.1086/305343.

[13] J N Abdurashitov et al. "Measurement of the solar neutrino capture rate with gallium metal. III. Results for the 2002–2007 data-taking period". In: *Physical Review C* 80.1 (2009), p. 015807. DOI: https://doi.org/10.1103/PhysRevC.80.015807. URL: https://doi.org/10.1103/PhysRevC.80.015807.

[14] W Hampel et al. "GALLEX solar neutrino observations: results for GALLEX IV". In: *Physics Letters B* 447.1 (1999), pp. 127–133. DOI: https://doi.org/10.1016/S0370-2693(98)01579-2. URL: https://doi.org/10.1016/S0370-2693(98)01579-2.

[15] Y. Fukuda et al. "Measurement of the solar neutrino energy spectrum using neutrino electron scattering". In: *Phys. Rev. Lett.* 82 (1999), pp. 2430–2434. DOI: http://doi.org/10.1103/PhysRevLett.82.2430.

[16] B Aharmim et al. "Measurement of the ν_e and Total ^{8}B Solar Neutrino Fluxes with the Sudbury Neutrino Observatory Phase-III Data Set". In: *Physical Review C* 87.1 (2013), p. 015502. DOI: https://doi.org/10.1103/PhysRevC.87.015502.

[17] B Pontecorvo. "Neutrino Experiments and the Problem of Conservation of Leptonic Charge". In: *Soviet Physics JETP* 26 (1968), pp. 984–988. URL: https://www.jetp.ras.ru/cgi-bin/dn/e_026_05_0984.pdf.

[18] V N Gribov and B Pontecorvo. "Neutrino astronomy and lepton charge". In: *Physics Letters B* 28.7 (1969), pp. 493–496. DOI: https://doi.org/10.1016/0370-2693(69)90525-5. URL: https://www.sciencedirect.com/science/article/pii/0370269369905255.

[19] Z Maki, M Nakagawa, and S Sakata. "Remarks on the Unified Model of Elementary Particles". In: *Progress of Theoretical Physics* 28 (1962), pp. 870–880. DOI: https://doi.org/10.1143/PTP.28.870. URL: https://doi.org/10.1143/PTP.28.870.

[20] Carlo Giunti and Chung W. Kim. *Fundamentals of Neutrino Physics and Astrophysics*. 2007. DOI: 10.1093/acprof:oso/9780198508717.001.0001.

[21] Mark Thomson. *Modern Particle Physics*. Cambridge: Cambridge University Press, 2013. DOI: 10.1017/CBO9781139525367.

[22] L. Wolfenstein. "Neutrino oscillations in matter". In: *Phys. Rev. D* 17 (1978), pp. 2369–2374. DOI: 10.1103/PhysRevD.17.2369.

[23] S. P. Mikheev and A. Yu. Smirnov. "Resonant amplification of neutrino oscillations in matter and solar neutrino spectroscopy". In: *Sov. J. Nucl. Phys.* 42 (1985). Yad. Fiz. 42 (1985) 1441–1448, pp. 913–917.

[24] K. Eguchi et al. "First Results from KamLAND: Evidence for Reactor Antineutrino Disappearance". In: *Phys. Rev. Lett.* 90 (2003), p. 021802. DOI: 10.1103/PhysRevLett.90.021802. arXiv: hep-ex/0212021.

[25] S. Abe et al. "Precision Measurement of Neutrino Oscillation Parameters with KamLAND". In: *Phys. Rev. Lett.* 100 (2008), p. 221803. DOI: 10.1103/PhysRevLett.100.221803. arXiv: 0801.4589.

[26] G. Bellini et al. "Precision Measurement of the ^{7}Be Solar Neutrino Interaction Rate in Borexino". In: *Phys. Rev. Lett.* 107 (2011), p. 141302. DOI: 10.1103/PhysRevLett.107.141302. arXiv: 1104.1816.

[27] M. Agostini et al. "Experimental Evidence of Neutrinos Produced in the CNO Fusion Cycle in the Sun". In: *Nature* 587 (2020), pp. 577–582. DOI: 10.1038/s41586-020-2934-0. arXiv: 2006.15115.

[28] K. S. Hirata et al. "Experimental study of the atmospheric neutrino flux". In: *Phys. Lett. B* 205 (1988), pp. 416–420.

[29] R. Becker-Szendy et al. "The electron- and muon-neutrino content of the atmospheric flux". In: *Phys. Rev. D* 46 (1992), pp. 3720–3724.

[30] Y. Fukuda et al. "Evidence for Oscillation of Atmospheric Neutrinos". In: *Phys. Rev. Lett.* 81 (1998), pp. 1562–1567. DOI: 10.1103/PhysRevLett.81.1562. arXiv: hep-ex/9807003.

[31] M. C. Sanchez et al. "Measurement of the L/E Distributions of Atmospheric Neutrinos in Soudan 2 and Their Interpretation as Neutrino Oscillations". In: *Phys. Rev. D* 68 (2003), p. 113004. DOI: 10.1103/PhysRevD.68.113004. arXiv: hep-ex/0307069.

[32] M. Ambrosio et al. "Measurement of the Atmospheric Neutrino-Induced Upgoing Muon Flux Using MACRO". In: *Phys. Lett. B* 434 (1998), pp. 451–457. DOI: 10.1016/S0370-2693(98)00885-5.

[33] S. Adrián-Martínez et al. "Measurement of Atmospheric Neutrino Oscillations with the ANTARES Neutrino Telescope". In: *Phys. Lett. B* 714 (2012), pp. 224–230. DOI: 10.1016/j.physletb.2012.06.058. arXiv: 1206.0645.

[34] M. G. Aartsen et al. "Measurement of Atmospheric Neutrino Oscillations with IceCube". In: *Phys. Rev. Lett.* 111 (2013), p. 081801. DOI: 10.1103/PhysRevLett.111.081801. arXiv: 1305.3909.

[35] S. Navas et al. "Review of Particle Physics". In: *Phys. Rev. D* 110.3 (2024), p. 030001. DOI: 10.1103/PhysRevD.110.030001. URL: https://pdg.lbl.gov.

[36] M. Jiang et al. "Atmospheric neutrino oscillation analysis with improved event reconstruction in Super-Kamiokande IV". In: *Prog. Theor. Exp. Phys.* 2019 (2019), 053F01. DOI: 10.1093/ptep/ptz015.

[37] M. G. Aartsen et al. "Measurement of Atmospheric Neutrino Oscillations at 6–56 GeV with IceCube DeepCore". In: *Phys. Rev. Lett.* 120 (2018), p. 071801. DOI: 10.1103/PhysRevLett.120.071801.

[38] M. H. Ahn et al. "Measurement of Neutrino Oscillation by the K2K Experiment". In: *Phys. Rev. D* 74 (2006), p. 072003. DOI: 10.1103/PhysRevD.74.072003. arXiv: hep-ex/0606032.

[39] P. Adamson et al. "Combined Analysis of ν_μ Disappearance and $\nu_\mu \to \nu_e$ Appearance in MINOS Using Accelerator and Atmospheric Neutrinos". In: *Phys. Rev. Lett.* 112 (2014), p. 191801. DOI: 10.1103/PhysRevLett.112.191801. arXiv: 1403.0867.

[40] K. Abe et al. "Indication of Electron Neutrino Appearance from an Accelerator-produced Off-axis Muon Neutrino Beam". In: *Phys. Rev. Lett.* 107 (2011), p. 041801. DOI: 10.1103/PhysRevLett.107.041801. arXiv: 1106.2822.

[41] P. Adamson et al. "First Measurement of Electron Neutrino Appearance in NOvA". In: *Phys. Rev. Lett.* 116 (2016), p. 151806. DOI: 10.1103/PhysRevLett.116.151806. arXiv: 1601.05022.

[42] K. Abe et al. "Measurements of neutrino oscillation parameters from the T2K experiment using 3.6×10^{21} protons on target". In: *Eur. Phys. J. C* 83 (2023), p. 782.

[43] M. A. Acero et al. “Improved measurement of neutrino oscillation parameters by the NOvA experiment”. In: *Phys. Rev. D* 106 (2022), p. 032004.

[44] F. P. An et al. “Observation of Electron-Antineutrino Disappearance at Daya Bay”. In: *Phys. Rev. Lett.* 108 (2012), p. 171803. DOI: 10.1103/PhysRevLett.108.171803. arXiv: 1203.1669.

[45] J. K. Ahn et al. “Observation of Reactor Electron Antineutrino Disappearance in the RENO Experiment”. In: *Phys. Rev. Lett.* 108 (2012), p. 191802. DOI: 10.1103/PhysRevLett.108.191802. arXiv: 1204.0626.

[46] Y. Abe et al. “Indication of Reactor Electron Antineutrino Disappearance in the Double Chooz Experiment”. In: *Phys. Rev. Lett.* 108 (2012), p. 131801. DOI: 10.1103/PhysRevLett.108.131801. arXiv: 1112.6353.

[47] Luca Stanco. “The next challenge for neutrinos: the mass ordering”. In: *EPJ Web Conf.* 164 (2017), p. 01031. DOI: 10.1051/epjconf/201716401031. arXiv: 1610.05533 [hep-ph].

[48] Mixing Neutrino Masses and Oscillations in S. Navas *et al.* (Particle Data Group). “Neutrino Masses, Mixing, and Oscillations”. In: vol. 110. 3. Section 14. 2024. Chap. 14, 14:1–14:72. DOI: 10.1103/PhysRevD.110.030001. URL: https://pdg.lbl.gov/2024/reviews/rpp2024-rev-neutrino-mixing.pdf.

[49] Ivan Esteban et al. “NuFit-6.0: Updated global analysis of three-flavor neutrino oscillations”. In: *J. High Energy Phys.* 2024.12 (2024), p. 216. DOI: 10.1007/JHEP12(2024)216. arXiv: 2410.05380 [hep-ph].

[50] Anatael Cabrera et al. “Synergies and prospects for early resolution of the neutrino mass ordering”. In: *Sci. Rep.* 12.1 (2022), p. 5393. DOI: 10.1038/s41598-022-09111-1. arXiv: 2008.11280 [hep-ph].

[51] Francesco Capozzi et al. “Neutrino masses and mixing: Entering the era of subpercent precision”. In: *Phys. Rev. D* 111 (2025), p. 093006. DOI: 10.1103/PhysRevD.111.093006. arXiv: 2503.07752 [hep-ph].

[52] B. Abi et al. “Deep Underground Neutrino Experiment (DUNE), Far Detector Technical Design Report, Volume I: Introduction to DUNE”. In: *JINST* 15.08 (2020), T08008. DOI: 10.1088/1748-0221/15/08/T08008. arXiv: 2002.02967 [physics.ins-det].

[53] B. Abi et al. *Deep Underground Neutrino Experiment (DUNE), Far Detector Technical Design Report, Volume II: DUNE Physics*. FERMILAB-PUB-20-025-ND. 2020. DOI: 10.48550/arXiv.2002.03005. arXiv: 2002.03005 [hep-ex].

[54] A. Abed Abud et al. “Snowmass Neutrino Frontier: DUNE Physics Summary”. In: *arXiv e-prints* (2022). DOI: 10.48550/arXiv.2203.06100. arXiv: 2203.06100 [hep-ex].

[55] B. Abi et al. “Long-baseline neutrino oscillation physics potential of the DUNE experiment”. In: *Eur. Phys. J. C* 80.10 (2020), p. 978. DOI: 10.1140/epjc/s10052-020-08456-z. arXiv: 2006.16043 [hep-ex].

[56] H.-T. Janka. "Explosion mechanisms of core-collapse supernovae". In: *Annual Review of Nuclear and Particle Science* 62 (2012), pp. 407–451. DOI: 10.1146/annurev-nucl-102711-094901. arXiv: 1206.2503 [astro-ph.SR].

[57] A. Mirizzi et al. "Supernova neutrinos: production, oscillations and detection". In: *Rivista del Nuovo Cimento* 39.1–2 (2016), pp. 1–112. DOI: 10.1393/ncr/i2016-10120-8. arXiv: 1508.00785 [astro-ph.HE].

[58] B. Abi et al. "Supernova neutrino burst detection with the Deep Underground Neutrino Experiment". In: *European Physical Journal C* 81 (2021), p. 423. DOI: 10.1140/epjc/s10052-021-09166-w. arXiv: 2008.06647 [hep-ex].

[59] F. Capozzi et al. "DUNE as the Next-Generation Solar Neutrino Experiment". In: *Phys. Rev. Lett.* 123 (2019), p. 131803. DOI: 10.1103/PhysRevLett.123.131803. arXiv: 1808.08232 [hep-ph].

[60] J. Kopp et al. "Sterile neutrino oscillations: the global picture". In: *Journal of High Energy Physics* 05 (2013), p. 050. DOI: 10.1007/JHEP05(2013)050. arXiv: 1303.3011 [hep-ph].

[61] B. Abi et al. "Prospects for beyond the Standard Model physics searches at the Deep Underground Neutrino Experiment". In: *European Physical Journal C* 81 (2021), p. 322. DOI: 10.1140/epjc/s10052-021-09007-w. arXiv: 2008.12769 [hep-ex].

[62] Y. Farzan and M. Tortola. "Neutrino oscillations and non-standard interactions". In: *Frontiers in Physics* 6 (2018), p. 10. DOI: 10.3389/fphy.2018.00010. arXiv: 1710.09360 [hep-ph].

[63] W. Altmannshofer et al. "Neutrino tridents at DUNE". In: *Physical Review D* 100.11 (2019), p. 115029. DOI: 10.1103/PhysRevD.100.115029. arXiv: 1902.06765 [hep-ph].

[64] V. De Romeri, K. J. Kelly, and P. A. N. Machado. "DUNE-PRISM sensitivity to light dark matter". In: *Physical Review D* 100.9 (2019), p. 095010. DOI: 10.1103/PhysRevD.100.095010. arXiv: 1903.10505 [hep-ph].

[65] H. Alhazmi et al. "Boosted dark matter at the Deep Underground Neutrino Experiment". In: *Journal of High Energy Physics* 04 (2017), p. 158. DOI: 10.1007/JHEP04(2017)158. arXiv: 1611.09866 [hep-ph].

[66] B. Abi et al. "Deep Underground Neutrino Experiment (DUNE), Far Detector Technical Design Report, Volume IV: The DUNE far detector single-phase technology". In: *JINST* 15 (2020), T08010. DOI: 10.1088/1748-0221/15/08/T08010. arXiv: 2002.03010 [physics.ins-det].

[67] A. Abed Abud et al. "The DUNE Far Detector Vertical Drift Technology, Technical Design Report". In: *JINST* 19 (2024), T08004. DOI: 10.1088/1748-0221/19/08/T08004. arXiv: 2312.03130 [physics.ins-det].

[68] A. Abed Abud et al. "Deep Underground Neutrino Experiment (DUNE) Near Detector Conceptual Design Report". In: *Instruments* 5.4 (2021), p. 31. DOI: 10.3390/instruments5040031. arXiv: 2103.13910 [physics.ins-det].

[69] N. Tosi. "The SAND detector of the DUNE experiment". In: *Nucl. Instrum. Meth. A* 1080 (2025), p. 170727. DOI: 10.1016/j.nima.2025.170727.

[70] A. Abed Abud et al. "DUNE Phase II: scientific opportunities, detector concepts, technological solutions". In: *JINST* 19 (2024), P12005. DOI: 10.1088/1748-0221/19/12/P12005. arXiv: 2408.12725 [hep-ex].

[71] A. Abed Abud et al. "A Gaseous Argon-Based Near Detector to Enhance the Physics Capabilities of DUNE". In: (2022). Contribution to Snowmass 2021. DOI: 10.48550/arXiv.2203.06281. arXiv: 2203.06281 [hep-ex].

[72] V. Papadimitriou et al. "Design of the LBNF Beamline". In: *arXiv preprint* (2017). DOI: 10.48550/arXiv.1704.04471. arXiv: 1704.04471 [physics.acc-ph].

[73] R. Acciarri et al. "Long-Baseline Neutrino Facility (LBNF) and Deep Underground Neutrino Experiment (DUNE), Volume 2: The Physics Program for DUNE at LBNF". In: *arXiv preprint* (2015). arXiv: 1512.06148 [hep-ex].

[74] Fermi National Accelerator Laboratory. *Neutrino Beam*. https://lbnf-dune.fnal.gov/how-it-works/neutrino-beam/. Accessed: 16 November 2025.

[75] S. Holmes et al. *The PIP-II Conceptual Design Report*. Tech. rep. Fermilab report PIP-II CDR. Fermilab, 2017. URL: https://pip2-docdb.fnal.gov/cgi-bin/ShowDocument?docid=113.

[76] R. Stanek et al. "PIP-III Project Overview and Status". In: *arXiv preprint* (2023). arXiv: 2311.05456 [physics.acc-ph].

[77] S. Tariq et al. "Design of the LBNF Beamline Target Station". In: *arXiv preprint* (2016). DOI: 10.48550/arXiv.1612.07293. arXiv: 1612.07293 [physics.acc-ph].

[78] J. Strait et al. "Long-Baseline Neutrino Facility (LBNF) and Deep Underground Neutrino Experiment (DUNE) Conceptual Design Report Volume 3: Long-Baseline Neutrino Facility for DUNE". In: *FERMILAB-DESIGN-2016-03* (2016). arXiv: 1601.05823.

[79] A. Abed Abud et al. "The DUNE Science Program". In: *arXiv e-prints* (2025). Submitted as input to the 2026 Update of the European Strategy for Particle Physics. arXiv: 2503.23291 [hep-ex].

[80] L. Paulucci et al. "The DUNE Vertical Drift Photon Detection System". In: *PoS* Neutrino2020 (2021), p. 178. DOI: 10.22323/1.387.0178. arXiv: 2112.09520 [physics.ins-det].

[81] S. Sacerdoti et al. "Signal and Power Transmission over Fiber in the DUNE Far Detector". In: *arXiv e-prints* (2024). arXiv: 2412.10177 [physics.ins-det].

[82] M. Auger et al. "A New Concept for Kilotonne Scale Liquid Argon Time Projection Chambers". In: *JINST* 14 (2019), P08009. DOI: 10.1088/1748-0221/14/08/P08009. arXiv: 1908.10956 [physics.ins-det].

[83] C. Hasnip et al. "DUNE-PRISM: Reducing neutrino interaction model dependence with a movable neutrino detector". In: *arXiv preprint* (2025). arXiv: 2501.14811 [hep-ex].

[84] S. Bertolucci. "DUNE Status and Outlook". Talk at the *nu@FNAL* meeting, Frascati, Italy. 2022.

[85] K. Abe et al. "T2K neutrino flux prediction". In: *Physical Review D* 87.1 (2013), p. 012001. DOI: 10.1103/PhysRevD.87.012001. arXiv: 1211.0469 [hep-ex].

[86] R. B. Patterson. "The NOvA experiment: status and outlook". In: *Nuclear Physics B - Proceedings Supplements* 235-236 (2013), pp. 151–157. DOI: 10.1016/j.nuclphysbps.2013.04.005. arXiv: 1209.0716 [hep-ex].

[87] K. Abe et al. "Search for CP violation in neutrino and antineutrino oscillations by the T2K experiment with 2.2×10^{21} protons on target". In: *Phys. Rev. Lett.* 121 (2018), p. 171802. DOI: 10.1103/PhysRevLett.121.171802. arXiv: 1807.07891 [hep-ex].

[88] Mario A. Acero et al. "New constraints on oscillation parameters from the NOvA experiment with neutrino and antineutrino beams". In: *Phys. Rev. D* 98 (2018), p. 032012. DOI: 10.1103/PhysRevD.98.032012. arXiv: 1806.00096 [hep-ex].

[89] M Adinolfi et. al. "The KLOE electromagnetic calorimeter". In: *Nuclear Instruments and Methods in Physics Research Section A: Accelerators, Spectrometers, Detectors and Associated Equipment* 482.1 (2002), pp. 364–386. DOI: https://doi.org/10.1016/S0168-9002(01)01502-9. URL: https://www.sciencedirect.com/science/article/pii/S0168900201015029.

[90] A. Montanari and the DUNE Collaboration. "Scintillation imaging in GRAIN liquid Argon detector of DUNE experiment". In: *JINST* 20 (2025), p. C05008. DOI: 10.1088/1748-0221/20/05/C05008.

[91] K. D. Smith et al. "Progress in the design and manufacture of the KLOE solenoid for the DAΦNE ring at Frascati". In: *IEEE Transactions on Applied Superconductivity* 7.2 (1997), pp. 630–632. DOI: 10.1109/77.614583.

[92] A. Antonelli et al. "Construction axnd performance of the lead–scintillating fiber calorimeter prototypes for the KLOE detector". In: *Nuclear Instruments and Methods in Physics Research Section A* 354.2–3 (1995), pp. 352–363. DOI: 10.1016/0168-9002(94)01058-7.

[93] Antonio Di Domenico and Danilo Domenici. *KLOE-to-SAND overview*. Contribution to the "Meeting Annuale della Collaborazione DUNE-Italia". INFN-LNF, Frascati, Italy, 10–12 November 2025. 2025. URL: https://agenda.infn.it/event/48150/contributions/278779/attachments/142202/215478/didomenico_DUNE_ITALIA_intro_20251110_5_web.pdf.

[94] M. Anelli et al. "Measurement of the detection efficiency of the KLOE calorimeter for neutrons between 22 and 174 MeV". In: *Nuclear Instruments and Methods in Physics Research Section A* 598.1 (2009), pp. 244–247. DOI: 10.1016/j.nima.2008.08.120.

[95] M. Andreotti et al. "Coded masks for imaging of neutrino events". In: *Eur. Phys. J. C* 81.11 (2021), p. 1011. DOI: 10.1140/epjc/s10052-021-09798-y. arXiv: 2105.10820 [physics.ins-det].

[96] Francesco Chiapponi. *Mid-Scale Drift Chamber Prototype: Design and Construction*. Presentation at the *Meeting Annuale della Collaborazione DUNE-Italia*, INFN–LNF, Frascati, Italy. Auditorium B. Touschek, 11 November 2025. Nov. 2025. URL: https://agenda.infn.it/event/48150/contributions/279681/.

[97] Matteo Tenti. "SAND at the DUNE ND complex". In: *Proceedings of Science*. Vol. PANIC2021. PoS. 2022, p. 282. DOI: 10.22323/1.380.0282.

[98] G. Adamov et al. *A Proposal to Enhance the DUNE Near Detector Complex*. Tech. rep. DUNE-doc-13262. Internal DUNE document. DUNE Collaboration, 2019. URL: https://docs.dunescience.org/cgi-bin/private/ShowDocument?docid=13262.

[99] H. Duyang et al. "A Precise Determination of (Anti)neutrino Fluxes with (Anti)neutrino-Hydrogen Interactions". In: *Phys. Lett. B* 795 (2019), pp. 424–431. DOI: 10.1016/j.physletb.2019.06.003.

[100] R. Petti. "Probing free nucleons with (anti)neutrinos". In: *Phys. Lett. B* 834 (2022), p. 137469. DOI: 10.1016/j.physletb.2022.137469.

[101] H. Duyang et al. "A novel approach to neutrino–hydrogen measurements". In: *Eur. Phys. J. Plus* 139 (2024), p. 1014. DOI: 10.1140/epjp/s13360-024-05783-y.

[102] L. Alvarez-Ruso et al. "NuSTEC White Paper: Status and Challenges of Neutrino–Nucleus Scattering". In: *Prog. Part. Nucl. Phys.* 100 (2018), pp. 1–68. DOI: 10.1016/j.ppnp.2018.01.006. arXiv: 1706.03621 [hep-ph].

[103] Costas Andreopoulos et al. "The GENIE Neutrino Monte Carlo Generator: Physics and User Manual". In: (2015). arXiv: 1510.05494 [hep-ph].

[104] Clark McGrew. *edep-sim: A generic Geant4-based detector simulation program*. https://github.com/ClarkMcGrew/edep-sim. GitHub repository, accessed 22 Nov 2025.

[105] DUNE Collaboration. *dunendggd: DUNE Near Detector geometry with gegede*. https://github.com/DUNE/dunendggd. GitHub repository, accessed 22 Nov 2025.

[106] DUNE Collaboration. *SANDReco: reconstruction framework for the SAND detector*. https://github.com/DUNE/sandreco. GitHub repository, accessed 22 Nov 2025.

[107] DUNE Collaboration. *ND_CAFMaker: Near Detector Common Analysis File producer*. https://github.com/DUNE/ND_CAFMaker. GitHub repository, accessed 22 Nov 2025.

[108] Valentina Cicero. "Imaging neutrino interactions with liquid Argon scintillation light at the DUNE near detector complex". In: *Nucl. Instrum. Meth. A* 1080 (2025), p. 170801. DOI: 10.1016/j.nima.2025.170801.

[109] R. Fruhwirth. "Application of Kalman filtering to track and vertex fitting". In: *Nuclear Instruments and Methods in Physics Research Section A* 262.2–3 (1987), pp. 444–450. DOI: 10.1016/0168-9002(87)90887-4.

[110] Muon Decay Parameters in S. Navas *et al.* (Particle Data Group). "Muon Decay Parameters". In: vol. 110. 3. 2024. Chap. 57, 57:1–57:6. DOI: 10.1103/PhysRevD.110.030001. URL: https://pdg.lbl.gov/2024/reviews/rpp2024-rev-muon-decay-params.pdf.

[111] Calorimeters in S. Navas *et al.* (Particle Data Group). "Particle Detectors at Accelerators". In: vol. 110. 3. 2024. Chap. 35, p. 35.10.2. DOI: 10.1103/PhysRevD.110.030001. URL: https://pdg.lbl.gov/2024/reviews/contents_sports.html#Calorimetry.

[112] M. Anfreville et al. "The Drift chambers of the NOMAD experiment". In: *Nucl. Instrum. Meth. A* 481 (2002), pp. 339–364. DOI: 10.1016/S0168-9002(01)01371-7.

[113] P. Astier et al. "Search for $\nu_\mu \to \nu_e$ oscillations in the NOMAD experiment". In: *Phys. Lett. B* 483 (2000), pp. 387–404.

[114] X. G. Lu et al. "Measurement of final-state correlations in neutrino muon-proton mesonless production on hydrocarbon at $<E_\nu> \simeq 3$ GeV". In: *Phys. Rev. Lett.* 121 (2018), p. 022504. DOI: 10.1103/PhysRevLett.121.022504.

[115] F. Ambrosino et al. "Calibration and performances of the KLOE calorimeter". In: *Nucl. Instrum. Meth. A* 598 (2009), pp. 239–243. DOI: 10.1016/j.nima.2008.08.097.